Exploring beyond the minimal supersymmetric model scenarios with dark matter and collider signals

Jack Yakup Araz

A Thesis
In the Department
of
Physics

Presented in Partial Fulfillment of the Requirements
For the Degree of
Doctor of Philosophy (Physics) at
Concordia University
Montréal, Québec, Canada

April 2020

CONCORDIA UNIVERSITY
SCHOOL OF GRADUATE STUDIES

This is to certify that the thesis prepared

By: **Jack Y. Araz**

Entitled: **Exploring beyond the minimal supersymmetric model scenarios with dark matter and collider signals**

and submitted in partial fulfillment of the requirements for the degree of

DOCTOR OF PHILOSOPHY (Physics)

complies with the regulations of the University and meets the accepted standards with respect to originality and quality.

Signed by the final Examining Committee:

______________________________ Chair
James Grant

______________________________ External Examiner
Geneviève Bélanger

______________________________ External to Program
Marco Bertola

______________________________ Examiner
Cherif Hamzaoui

______________________________ Examiner
Panagiotis Vasilopoulos

______________________________ Thesis Supervisor
Mariana Frank

Approved by ______________________________
Valter Zazubovits
Graduate Program Director

__________ 2020 ______________________________
André Roy, Dean
Faculty of Arts & Science

Abstract

Exploring beyond the minimal supersymmetric model scenarios with dark matter and collider signals

Jack Y. Araz, Ph.D.
Concordia University, 2020

This thesis presents a study on phenomenology of beyond the Standard Model (SM) in the context of extensions of supersymmetric realisations. This extended framework allows us to accommodate viable dark matter (DM) candidates which the SM do not have, and it offers a unified gauge structure for all three nuclear forces. With this motivation, we investigated two possible extensions of MSSM and their predictabilities in future collider experiments.

First, we presented an extension of MSSM via vector-like (VL) supermultiplets which can provide new annihilation channels for dark matter. We investigate a simple extension with two VL pairs of weak doublets (lepton and down-type quark) and a pair of VL-neutrino singlets. Both neutralino and sneutrinos can emerge as viable DM candidates in such a framework. A complete analysis has been conducted on the DM. Furthermore, we investigate specific collider signatures that such construction can bring and demonstrate the enhanced production of events fortified with tau leptons.

Secondly, we investigated $U(1)$ extensions of the MSSM framework within E_6 gauge structure by conducting a detailed analysis of the parameter space that can emerge through a variety of $U(1)'$ charge structures. Such a scenario predicts two DM candidates, neutralino and sneutrino. We presented a detailed analysis of low energy and cosmological observables. It is also vital to present the specific signatures that such gauge structure can bring into collider experiments. A heavy Z' boson is one of the identifying features of such a framework. We investigated possible loopholes in analyses where we observed that Z' mass bounds can be relaxed up to 300 GeV by changing the boundary conditions on the gauge couplings. We presented possible leptophobic scenarios which can be observed through supersymmetric cascade decays up to 7σ statistical significance at $\sqrt{s} = 14$ TeV with 3 ab^{-1} integrated luminosity.

Finally, we revisited the current LHC bounds on supersymmetric particles in the light of theoretical uncertainties and studied high luminosity predictions. We investigated the effects of these uncertainties on gluino, squark mass limits and on coupling sensitivity of simplified s-channel DM models.

To my mentor and the person whom I loved like a grandfather... Rest in peace...

"There are two things in life multiplied by sharing: love and knowledge...
I am trying to achieve this, in the last days of my life..."

Namık Kemal Pak
1947 - 2015

Acknowledgements

First of all, most of this thesis has been written while I was under precautionary quarantine in Glasgow, Scotland, due to COVID-19 pandemic. So probably I should be thankful that I can't leave the flat even if I wanted to.

This is going to be a long list which obviously will start with my supportive parents and little brother. All these long years, I always felt their constant support even when I lost hope towards certain things. Of course, I'm going to count my supervisor, Mariana Frank, as part of my family since her support was beyond a supervisor's care.

I can not stress enough the indisputable support and the strength that I've received from my partner, Maureen Holland. She was always there to encourage me to continue when I was powering through without even noticing the sunrise and supported every single decision I made no matter how hard it was for both of us. Also, I can not be thankful enough (although she said a bottle of wine was enough) for her help on correcting the language on my texts (yes she needed the entire bottle).

Next in line is, of course, my office mate and brother, Özer Özdal. Without him, none of this would be possible, and I can not deny the amount of physics that I've learned from him. I'll always miss his presence as a friend and a colleague.

I have a special thanks to a person who is my mentor and collaborator, but mostly to me, he was like a big brother that I envy. He showed me how a scientist should be with his idealistic scientific ethics and beyond that, he showed me how to be a father and a husband alongside the scientist persona. Benjamin Fuks, you are my Obi-Wan Kenobi...

Of course, I can not forget the person who taught me coding, Simon-Gabriel Beauvais. Although this ruined my dreams (I saw him in my nightmare for a week while he was explaining to me why the Earth is collapsing and destroying life as we know it), it seems totally worth it. He became one of the people that I would thrust with my life, when I came to Montréal.

Quite frankly, this journey was not possible without my amazing friends, climbing and workout team. No matter how many names I write, the list will not cover every single person that made this journey possible. Thank you all for making my life a better place, I am lucky to meet every single one of you and had the chance to expand my perspective towards life.

Finally, I would like to thank Innovative Training Network MCnetITN3 for giving me the chance to work at the University of Glasgow. Also, I acknowledge Ministére de l'Éducation et de l'Enseignement supérieur and J. W. McConnell Memorial Graduate Fellowship for the economic support during my PhD and academic visits to Europe. I also would like to acknowledge Sorbonne University, INFN – LNF, IPPP – Durham University for their hospitality and people who made those visits possible; Gennaro Corcella, Michael Spannowsky, Shankha Banerjee and Andy Buckley.

Contribution of the Author

The original research work presented in chapters 3, 4, 5 and 6. The research in chapter 3 is in collaboration with Mariana Frank, Benjamin Fuks, Shankha Banerjee and Andreas Goudelis and publication can be found in ref. [1]. Chapter 4 is in collaboration with Mariana Frank and Benjamin Fuks which can be found in ref. [2]. Chapter 5 has been conducted in collaboration with Mariana Frank, Benjamin Fuks and Gennaro Corcella and can be found in refs. [3, 4, 5]. Finally, the research in chapter 6 has been conducted with Mariana Frank and Benjamin Fuks and also can be found in ref. [6] which is currently under review.

All the figures in the review presented in chapter 1 and 2 have been prepared by the author to be presented in this thesis.

In chapter 3, 4, 5 the model building, computational calculations and production of the graphs were conducted by the author as a partial the fulfillment of the requirements for the degree of doctor of philosophy in the Concordia Physics Department, Montreal, Quebec.

In chapter 6 the part of the open-source software which is used to conduct the research has been built by the author as well as the production of the graphs and all the results presented in the paper as a partial the fulfillment of the requirements for the degree of doctor of philosophy in the Concordia Physics Department, Montreal, Quebec.

Contents

List of Figures

List of Tables

Acronyms

ATLAS	A Toroidal LHC Apparatus
BSM	beyond the standard model
BNL	Brookhaven National Laboratory
CERN	European Organization for Nuclear Research
CEDM	chromoelectric dipole moment
CMB	cosmic microwave background
CMDM	chromomagnetic dipole moment
CMS	Compact Muon Solenoid
DM	dark matter
FIMPs	feebly interacting particles
FNAL	Fermi National Accelerator Laboratory
EW	electroweak
EWSB	electroweak symmetry breaking
GUT	Grand Unified Theory
J-PARC	Japan Proton Accelerator Research Complex
LEP	The Large Electron-Positron Collider
LHC	The Large Hadron Collider
LSP	lightest supersymmetric particle
LO	leading order
LUX	The Large Underground Xenon experiment
NLO	Next-to-leading order
LSP	lightest supersymmetric particle
HL-LHC	High-Luminosity-LHC
MSSM	Minimal Supersymmetric Extension of the Standard Model
NMSSM	next-to-minimal supersymmetric standard model
NLSP	next-to-lightest supersymmetric particle
PDF	parton distribution functions
SBS	spontaneous symmetry breaking
SM	Standard Model
SMEFT	SM effective field theory
SUSY	Supersymmetry
SSM	Sequential Standard Model

SNO	The Sudbury Neutrino Observatory
QCD	quantum chromodynamics
UMSSM	$U(1)'$ extended MSSM
USM	$U(1)'$ extended SM
vev	vacuum expectation value
RGEs	renormalization group equations
FNAL	Fermi National Accelerator Laboratory
IMS	intermediate mass scale
WMAP	The Wilkinson Microwave Anisotropy Probe
2HDM	two Higgs doublet model

Chapter 1

High Energy Physics: Where do we stand?

Since the dawn of time, humanity is trying to understand "How" and "Why" the matter behaves as it does. The written history reveals the fact that we were using mathematics to understand our surroundings for more than 3000 years. However, the pillars of our axiomatic way of thinking have been built by Thales of Miletus (624 – 546 BC). During his visits to Egypt, he acquired the knowledge of advanced geometry and mathematics used to measure farmland and to understand the motions of "celestial objects" [7]. By migrating this knowledge to Ancient Greece and teaching it to his successor, Pythagoras of Samos (c. 570 – c. 495 BC), he planted the first seed which today became science and philosophy as we know it. Although today we know that Ancient Babylonians were using much more advanced mathematics than Pythagoreans [8], the so-called Western Philosophy's axiomatic approach to mathematics and philosophy has been build in the hands of Ancient Greeks [1].

Until Galileo, questions "How" and "Why" have been asked together to understand the mechanics and the reasons for this behaviour of the known matter. Today, we have **slightly** more sophisticated understanding of the Universe, which is based on a combination of different mechanics under one model.

---

[1] It is important to note that, due to the lack of resources, advancements in Babylonian mathematics and philosophy are still a source of debate. The modern philosophy classifies the entire pre-Socratic era as Oriental philosophy and bases the entire epistemological origins on the Ancient Greeks [9, 10]. Although there are debates on how should we interpret the Babylonian tablets [11], we encounter with multiple Greek philosopher's visiting ancient Egypt and Mesopotamia for knowledge exchange [12]. Thus, it is essential to keep an open-mind regarding today's epistemological origins. For more information on mathematics in ancient Egypt and Babylonia see refs. [13, 14, 15, 16, 17, 18].

The theoretical framework that describes the fundamental rules between subatomic particles is called the Standard Model (SM) of particle physics [19, 20, 21, 22, 23, 24, 25, 26]. It is, so far, the most powerful tool to describe the fundamental interactions that rule the universe, which can be summarized as electromagnetic, weak and strong nuclear forces. Gravity, on the other hand, is described by General Relativity, which is a different theoretical framework for celestial bodies and for which a quantum theory still eludes us. The SM explains the known matter with six quarks and six leptons, together with their antiparticles, all organized in three families. The interactions between particles are described via the exchange of gauge bosons. These bosons consist of eight gluons g for the strong force, three massive vector bosons ($W^{\pm}$ and Z) for the weak force, and a photon γ for the electromagnetic force. The mass of the particles is described by their interaction with the Higgs field, where the quantum is called the Higgs boson. Physicists have built dedicated facilities all over the world to be able to study the SM.

There are still many questions that the SM cannot answer. Supersymmetry (SUSY) is one of the frameworks, developed to resolve the major questions left unanswered by the SM, which we will further dwell upon in this thesis.

On the experimental side, the The Large Hadron Collider (LHC) is the most ambitious of the facilities built to understand the SM with high precision. It is operated by European Organization for Nuclear Research (CERN) at the border of France and Switzerland. The 26.7 km-circumference ring surrounded by superconducting magnets is designed to accelerate two counter-rotating proton beams to 14 TeV centre-of-mass energy and collide them in centre of the cylindrical detectors. In particular, Compact Muon Solenoid (CMS) and A Toroidal LHC Apparatus (ATLAS) are two detectors at LHC dedicated to find anything beyond the SM. The discovery of the last missing piece of the SM, Higgs boson, by the LHC has raised a variety of queries. With the collection of a massive amount of data, an integrated luminosity of 300 fb^{-1}, has been reached since the discovery of the Higgs boson. Although the current results suggest that the nature of this scalar is mostly SM-like, a few channels still have large uncertainties. These uncertainties may or may not be statistical artefacts, but it is clear that we need more precise measurements to ascertain the nature of the electroweak symmetry breaking (EWSB). Accessing the properties of the new physics, in particular, can be achieved through higher luminosities and centre-of-mass energies in LHC and it seems like an absolute necessity to understand the physics beyond the standard model (BSM).

In this chapter, from section 1.1, we will briefly introduce the SM and its shortcomings to describe the behaviour of the matter in the Universe, section 1.2. In section 1.3 we will summarize the different approaches in the literature to patch missing gaps of the SM.

1.1 The Standard Model of Particle Physics: A brief introduction

The SM is the most successful model which describes known particles and their interactions in four-dimensional space-time. The SM consists of two types of matter particles, quarks and leptons. Each of these types has three consecutive family (generations) which are only differing by their masses. An atom is only composed of a specific combination of the first generation particles, where the other generations can only be observed either through cosmic rays or high energy collision experiments. Both quarks and leptons are spin-1/2 fermions.

Table 1.1: *Summary of the fermionic particle content of the SM.*

	Quark		Charge [e]	Mass [GeV]	Lepton		Charge [e]	Mass [GeV]
1^{st} gen.	down	d	-1/3	0.5×10^{-2}	electron	e	-1	0.5×10^{-3}
	up	u	2/3	0.2×10^{-2}	e neutrino	ν_e	0	unknown
2^{nd} gen.	strange	s	-1/3	9.5×10^{-2}	muon	μ	-1	0.11
	charm	c	2/3	1.275	μ neutrino	ν_μ	0	unknown
3^{rd} gen.	bottom	b	-1/3	4.18	tau	τ	-1	1.78
	top	t	2/3	173	τ neutrino	ν_τ	0	unknown

The interactions between fermions are defined by an exchange of a mediator where these mediators are defined through a gauge symmetry. For the simplest case, the Lagrangian of a scalar field can be written as

$$\mathcal{L} = \partial_\mu \phi \, \partial^\mu \phi^* - V(\phi, \phi^*) \quad ; \qquad \mu = 0, 1, 2, 3 \ ,$$

where the first term is the kinetic term and V is some potential function of ϕ. For a field transformation $\phi \to e^{i\alpha(x)}\phi'$, the kinetic term of the Lagrangian can no longer be invariant under this specific transformation. However, by defining a covariant derivative which can also transform like the scalar field via a gauge potential, A_μ, the invariance of the Lagrangian can be achieved.

$$D_\mu\phi = \partial_\mu\phi + iA^a{}_\mu(T_a\phi) \quad \rightarrow \quad \mathcal{L} = D_\mu\phi\ D^\mu\phi^* - V(\phi,\phi^*)\ . \tag{1.1.1}$$

Here T^a is the generator of the corresponding group, which is 1 for this particular example. As a consequence of such transformation, one ends up with a coupling term between the gauge field and the scalar field, $A_\mu\phi A^\mu\phi$.

For a Dirac Lagrangian, on the other hand,

$$\mathcal{L} = -i\psi^{\dagger i}\bar{\sigma}^\mu D_\mu\psi_i\ ,$$

a generic covariant derivative can be defined as

$$D_\mu\psi_i = \partial_\mu\psi_i - igA^a{}_\mu(T_a\psi)_i\ .$$

This results in a three point interaction term with g being the interaction or coupling strength. Here σ^μ denotes the Pauli matrices and T^a is a generic hermitian matrix corresponding to the transformation of the chiral field ψ.

The SM consist of three types of gauge groups. The gauge structure of the SM can be described via two sets of gauge symmetries.

$$\mathcal{G}_{\rm SM} \equiv \underbrace{U(1)_{\rm Y}\otimes SU(2)_{\rm L}}_{\text{Electroweak}}\otimes\underbrace{SU(3)_{\rm C}}_{\text{Strong}}\ . \tag{1.1.2}$$

The first two groups refer to electroweak interactions of the standard model [19, 20, 21] where subindex Y refers to the hypercharge, which we will refer as Q_{Y_f}. Together with the isospin, they generate the electric charge of the corresponding particle, $Q_{Y_f} = 2(Q_f - I_f^3)$ where I_f^3 stands for the weak isospin. The mediator of $U(1)$ gauge is a photon with spin 1. The subindex L on $SU(2)_{\rm L}$ indicates that the SM is a left-handed field theory and does not preserve the parity transformation, meaning that right-handed chiral fields transform differently than left-handed chiral fields. The mediators of the $SU(2)_{\rm L}$ gauge group are heavy vector bosons $W^\pm$ and Z. The last term in Eq. (1.1.2) refers to the strong interactions of the quantum chromodynamics (QCD) [23, 24, 25], where subindex C indicates colour indices which are red, green and blue. $SU(3)_{\rm C}$ consists of 8, spin one gluons as mediators. The interactions and their mediators are summarized in Table 1.2.

Table 1.2: *Summary of the gauge bosons in the SM.*

Interaction	Gauge	Boson		Charge [e]	Mass [GeV]
Strong	$SU(3)_{\mathrm{C}}$	8 gluon	g	0	0
Weak	$SU(2)_{\mathrm{L}}$	2 W	$W^{\pm}$	±1	80.379 ± 0.012
		Z	Z	0	91.188 ± 0.002
Electromagnetic	$U(1)$	photon	γ	0	0

Up until 2012, there were no proof indicating the mass generation in the SM. That year both CMS [27] and ATLAS [28] collaborations announced the discovery of the Higgs boson which being the last missing piece of the SM. The Higgs mechanism describes the mass generation of the SM particles via spontaneous symmetry breaking (SBS) of gauge structure of the SM [29, 30, 31, 32, 33, 34].

$$SU(2)_{\mathrm{L}} \otimes U(1)_{\mathrm{Y}} \xrightarrow{\Lambda_{\mathrm{SM}} \approx 1\ \mathrm{TeV}} U_{\mathrm{EM}}(1)\ . \tag{1.1.3}$$

Due to the so-called "Mexican hat" shape of the Higgs potential, Fig. 1.1, the ground state of the potential is no longer symmetric, $\langle\phi\rangle \neq 0$. Instead there are two local minima where the location on the potential can be determined via the energy scale of the system.

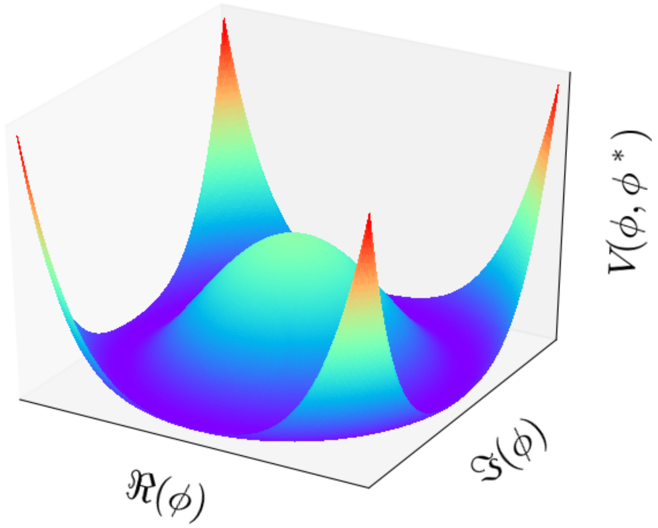

Figure 1.1: *Visual representation of the Higgs potential projected on the reel and imaginary plane. The colour code represents the numerical value of the potential where red being the largest and purple being the minimum value.*

Higgs is a spin zero isodoublet scalar field under $SU(2)_{\mathrm{L}}$. It couples to each fermion with mass m_f where the coupling strength is driven by the Yukawa coupling of the particular chiral field, Y_f. The mass of the Higgs boson consists of two parts,

$$m_h^2 \cong m_{h,\text{three}}^2 + \Delta m_h^2 \ , \tag{1.1.4}$$

where the first term is the three level Higgs mass coming from its self interaction. The first term can be determined by its vacuum expectation value (vev), $v \simeq 246$ GeV, and its self coupling, λ. The second term in Eq. (1.1.4) is the correction coming from fermionic loops.

$$m_{h,\text{three}}^2 = \sqrt{2\lambda v^2} \quad , \quad \Delta m_h^2 = \frac{|Y_f|^2}{16\pi^2}\left[-2\Lambda_{\text{SM}}^2 + 6m_f^2 \ln\frac{\Lambda_{\text{SM}}}{m_f} + \cdots\right] . \tag{1.1.5}$$

It is important to stress that the fermionic loop corrections of the Higgs mass are largely dependent on the ultraviolet cut-off scale, Λ_{SM} where weak group fuses into electromagnetic one as shown in Eq. (1.1.3). Since this contribution depends on the Yukawa coupling of the corresponding fermion, due to its large mass (see Table 1.1), the largest contribution would come from the top quark as shown in Fig. 1.2.

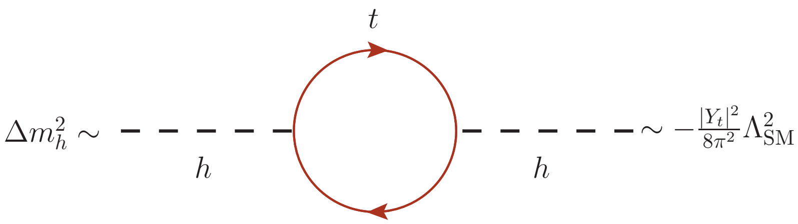

Figure 1.2: *Top quark loop correction to the Higgs mass, where Y_t is the Yukawa coupling of the top quark and Λ_{SM} is the ultraviolet cut-off scale of the SM. The diagram has been created via Jaxodraw package [35].*

Thus, if the SM was valid up to the Planck scale, $M_{\text{Planck}} = 2.435 \times 10^{18}$ GeV, the corrections to the Higgs mass would be at the order of $\mathcal{O}(10^{36})$ GeV^2. However, today we know that the Higgs mass is 125.09 ± 0.21 (stat.) ± 0.11 (syst.) GeV [27, 28]. The only way to explain this discrepancy between the theory and experiment is to state that the SM is only an effective field theory which can explain the nature of the known matter up to $\Lambda_{\text{SM}} \approx 1$ TeV. This brings us to the core motivation of beyond the SM, but more on this later.

The SM Lagrangian density can be written in three major parts. We will describe the kinetic interaction terms of all chiral fields in the $\mathcal{L}_{chiral}$, the gauge interaction terms will be written under $\mathcal{L}_{gauge}$ and finally, the Yukawa terms, Higgs potential and scalar kinetic part will be introduced. As shown above, $\mathcal{L}_{chiral}$ consists of nothing but the kinetic Dirac Lagrangian,

$$\mathcal{L}^{\mathrm{SM}}_{chiral} = -i\psi^{\dagger i}\bar{\sigma}^{\mu} D_{\mu}\psi_i \ . \tag{1.1.6}$$

Here ψ represents the chiral fields which are summarized in Table 1.3. The gauge interaction term of the Lagrangian density consists of field strength tensors for $SU(3)_{\mathrm{C}}$, $SU(2)_{\mathrm{L}}$ and $U(1)_{\mathrm{Y}}$ respectively,

Table 1.3: *Quantum numbers of the SM chiral fields and the Higgs isodoublet. The table shows the corresponding gauge charges, isospin and electric charge values respectively.*

	$SU(3)_C \otimes SU(2)_L \otimes U(1)_Y$	I_f^3
$L \equiv \begin{pmatrix} \nu_L \\ e_L \end{pmatrix}$	$(\mathbf{1}, \mathbf{2}, -1)$	$-\frac{1}{2}$ $\frac{1}{2}$
e_R	$(\mathbf{1}, \mathbf{1}, -2)$	0
$Q \equiv \begin{pmatrix} u_L \\ d_L \end{pmatrix}$	$(\mathbf{3}, \mathbf{2}, \frac{1}{3})$	$-\frac{1}{2}$ $\frac{1}{2}$
u_R	$(\overline{\mathbf{3}}, \mathbf{1}, \frac{4}{3})$	0
d_R	$(\overline{\mathbf{3}}, \mathbf{1}, -\frac{2}{3})$	0
$\phi \equiv \begin{pmatrix} \phi^{+} \\ \phi^{0} \end{pmatrix}$	$(\mathbf{1}, \mathbf{2}, 1)$	$\frac{1}{2}$ $-\frac{1}{2}$

$$\mathcal{L}^{\mathrm{SM}}_{gauge} = -\frac{1}{4}F^{a}_{\ \mu\nu}F_{a}^{\ \mu\nu} = -\frac{1}{4}\left\{G^{a}_{\ \mu\nu}G_{a}^{\ \mu\nu} + W^{a}_{\ \mu\nu}W_{a}^{\ \mu\nu} + B_{\mu\nu}B^{\mu\nu}\right\} \ . \tag{1.1.7}$$

The subindex a in $\mathcal{L}_{gauge}$ implies the gauge group index which has eight different values for $SU(3)_{\mathrm{C}}$ and three different values for $SU(2)_{\mathrm{L}}$. The generic field strength tensor is defined via the corresponding gauge potential,

$$F^{a}_{\ \mu\nu} = \partial_{\mu}A^{a}_{\ \nu} - \partial_{\nu}A^{a}_{\ \mu} + g_i f^{abc}A_{b\mu}A_{c\nu} \quad , \quad g_i \in \{g_1,\ g_2,\ g_3\} \ .$$

The coupling strength of the gauge groups are given by $g_{1,2,3}$ where numbers correspond to $U(1)$, $SU(2)_{\mathrm{L}}$ and $SU(3)_{\mathrm{C}}$ respectively. f^{abc} is the antisymmetric structure constant.

As mentioned above, since the SM does not preserve left and right chirality, the transformation of the covariant derivative for the right- and left-handed fields should be defined differently. The covariant derivative of the left-chiral fields can be defined as;

$$\begin{aligned} D_\mu L_i &= \partial_\mu L_i - i\frac{g_1}{2}B_\mu L_i + i\frac{g_2}{2}W^a_{\ \mu}T_a L_i \ , \\ D_\mu Q_i &= \partial_\mu Q_i - i\frac{g_1}{6}B_\mu Q_i + i\frac{g_2}{2}W^a_{\ \mu}T_a Q_i + ig_3 G^a_{\ \mu}T^a Q_i \ . \end{aligned} \tag{1.1.8}$$

The right-handed chiral fields, on the other hand, transform as follows;

$$\begin{aligned} D_\mu e_R &= \partial_\mu e_R - ig_1 B_\mu e_R \ , \\ D_\mu q_R &= \partial_\mu q_R - iY_q g_1 B_\mu q_R + ig_3 G^a_{\ \mu}T^a q_R \ , \end{aligned} \tag{1.1.9}$$

where q_R stands for u_R and d_R and Y_q is their corresponding hypercharge, as shown in Table 1.3. The gauge potential, corresponding to the gauge group has been given via the same notation used for the field strength tensor in Eq. (1.1.7).

Last but not least, as mentioned above, particles gain their masses through their coupling with the Higgs field. The coupling strengths are determined by their Yukawa coupling.

$$\mathcal{L}^{\rm SM}_{Higgs} \subset \mathcal{L}_{Yukawa} = -Y_e\ \bar{e}_R L\phi^\dagger - Y_d\ \bar{d}_R Q\phi^\dagger - Y_u\ \bar{u}_R Q\phi + h.c. \tag{1.1.10}$$

It is worthwhile to stress that the chiral fields only couple with the Higgs field through with their left and right chiral fields. The mass generation of the gauge bosons, on the other hand, are hidden in the transformation of the scalar field, Eq. (1.1.1). If we apply the generic expression for the SM group structure, we will end up with,

$$D_\mu\phi = \partial_\mu\phi + ig_1 B_\mu\phi + ig_2 W^a_{\ \mu}T_a\phi \ .$$

Expanding Eq. (1.1.6)'s first term using the definition of the covariant derivative above one ends up with the interaction terms of the gauge fields with the Higgs field. Finally, we need to add the Higgs potential, $V(\phi,\phi^*)$, as shown in Fig. 1.1, to be able to ensure the symmetry breaking mechanism and kinetic scalar terms in the Lagrangian.

$$\mathcal{L}^{\rm SM}_{Higgs} \subset V(\phi,\phi^*) = -a\phi\phi^* + b(\phi\phi^*)^2 \quad , \quad a,b \geq 0 \quad \text{and} \quad \mathcal{L}^{\rm SM}_{Higgs} \subset -D_\mu\phi^* D^\mu\phi$$

The Lagrangian density of the SM should be written with the combination of all these terms to include interactions of all matter fields,

$$\mathcal{L}_{\rm SM} = \mathcal{L}^{\rm SM}_{chiral} + \mathcal{L}^{\rm SM}_{gauge} + \mathcal{L}^{\rm SM}_{Higgs} \ .$$

Although this theoretical framework explains known, relatively low energy matter with extremely high accuracy, unfortunately (or maybe fortunately), nature requires a much larger framework to explain its beauty. In the following section, section 1.2, we summarized the missing ingredients of the SM. In section 1.3, we will discuss the recipes to be followed to fill the missing pieces of this jigsaw puzzle.

1.2 Why do we need to go beyond the Standard Model?

Whilst the SM is the most successful theoretical framework to explain experimental results; there are many queries that it can not explain or even it does not contain enough information to explain some discrepancies in the observed data.

First, we should mention the Hierarchy problem. As already introduced with Eq. (1.1.5) and Fig. 1.2, the SM can not be valid up to the Planck scale. Nevertheless, why do we need it to span such a wast energy scale? In order to explain the mass generation of the particles, $SU(2)_{\rm L} \otimes U(1)_{\rm Y}$ needs to be broken via Higgs vev. This has been shown to occur around $\Lambda_{\rm SM} \approx 1$ TeV, which is the scale that electroweak symmetry breaks down to weak and electromagnetic forces. However, this does not introduce an energy scale that can unify strong force to electroweak force and the SM does not have the tool-set to produce such unification (see Fig. 2.2). This so-called grand unification needs to happen around the Planck scale. This raises the question, why there is such a large gap between two energy scales,

$$M_{\rm Electroweak} = \Lambda_{\rm SM} \approx 1 \text{ TeV} \quad , \quad M_{\rm Planck} \approx 10^{15} \text{ TeV} \quad \Rightarrow \quad \frac{M_{\rm Planck}}{M_{\rm Electroweak}} \approx 10^{15} \ .$$

This brings us to the discussion of Grand Unified Theory (GUT). Such theories are designed to explain this energy gap between electroweak and Planck scale. This thesis will ponder on this notion and try to propose a framework to achieve this goal.

Neutrino mass is one of the most important problem of the SM. As shown in Table 1.3, neutrinos do not have a right-handed chiral field and as shown in Eq. (1.1.10), a mass term can only be achieved through a right-handed and a left-handed chiral field interacting with the

Higgs field. Due to the lack of a right-handed neutrino field, the SM does not include a mass term for neutrinos. However, in 2001 and 2002 The Sudbury Neutrino Observatory (SNO) Collaboration [36, 37], in 2013 T2K (Tokai to Kamioka, Japan) Collaboration [38][2] have shown that the neutrino mass eigenstates can change flavour [40] which rightfully become the Nobel prize-winning topic in 2015. Although we currently do not know the exact value, this discovery is an unprecedented proof of the existence of their masses.

$\mathcal{CP}$-violation[3] in Kaon systems has been known for over 50 years [41]. It has been shown that such mechanism can be added to the strong gauge term in the Lagrangian as $\alpha G^{a}{}_{\mu\nu} G_{a}{}^{\mu\nu}$, where $\mathcal{O}(\alpha) < 10^{-8}$. However, the SM does not generate such a symmetry violation naturally, its rather *ad hoc* [42]. Also our source of $\mathcal{CP}$-violation is quite small; in order to be able to explain the matter-antimatter asymmetry in the early universe one needs additional sources of $\mathcal{CP}$-violation[4] [43]. So far we don't have any explanations regarding $\mathcal{CP}$-violation through the SM.

The SM explains the dynamics of three nuclear forces relatively quite well. However, such a framework is "doomed" to remain microscopic. The effects of gravity are only effective in much larger energy scales and can only be non-negligible beyond the Planck scale. This requires an effective extension of the SM to include the effects of gravity, but as mentioned above the SM is valid only up to the TeV scale. Thus, the SM is not enough to explain the effects of gravity together with the nuclear forces.

From the observed cosmological data, we can see undeniable evidence of an unknown source that can not be explained via known matter in the Universe. The galaxy rotation data and mass distribution of various nebula reveal the fact that the known matter can not explain the observed phenomenon [44, 45, 46, 47]. Relatively most striking evidence comes from the cosmic microwave background (CMB) data [48]. To explain all this discrepancy one needs to introduce a particle[5] called dark matter. The CMB data shows that a specific density of dark matter and dark energy is necessary to end up with the observed data. Fig. 1.3 shows a simulation of the CMB data using a power spectrum with a different matter, dark matter and dark energy densities. Left panel was prepared with approximately observed values where the 5% of the Universe is assumed to be baryonic matter, 27.5% of the Universe assumed

---

[2] For more recent results see ref. [39].

[3] Charge conjugation and parity.

[4] This needs to occur with baryon number violation and deviation from thermal equilibrium, for more see ref. [43].

[5] It does not need to be a particle, but since this thesis is on particle physics, we will try to explain everything through that line of thought.

to be dark matter and 67.5% of the Universe assumed to be dark energy. This construction shows close enough match with the actual observed CMB spectrum showed on the upper right corner of the image. The right panel, on the other hand, shows a scenario assuming that the Universe is made up with 100% baryonic matter, quite frankly such construction dramatically diverges from the observed CMB spectrum. Unfortunately, the SM does not have a particle that can play the role of a dark matter candidate. It is natural to assume that the neutrino might be a dark matter candidate but the fact is the production rate of the neutrino is too large compared to the expected density of the dark matter. If neutrino was the dark matter, the dark matter density in the Universe should have been much larger than the observed value. For this reason, proposing a dark matter candidate will be one of the main objectives of this thesis.

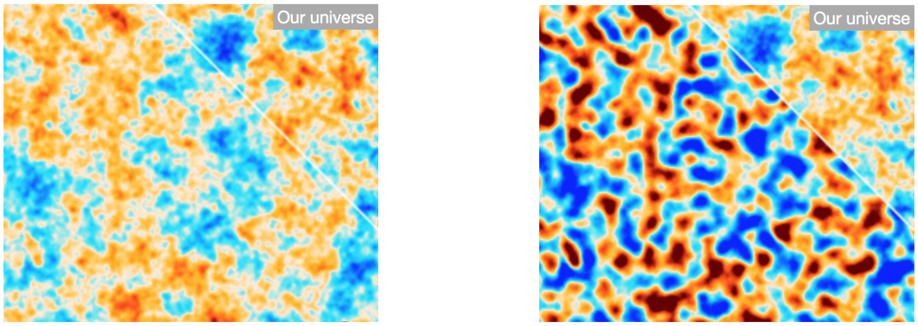

Figure 1.3: *CMB simulation to compare observed data with different dark matter and dark energy densities. Both simulations show the observed data on the upper right corner. The left panel simulates observed conditions where baryonic matter density is chosen to be* $\Omega_B = 0.05$, *dark matter density* $\Omega_{\rm DM} = 0.275$ *and the dark energy density is at* $\Omega_\Lambda = 0.675$ *which results in a flat universe. The right panel shows a universe with 100% baryonic matter. The simulation has been created via a modified version of* `planckapps` *[49].*

The origin of mass is another unknown in the SM. Using the Higgs mechanism, we can understand how particles gain their masses, but the actual values are determined by the observed data. As a matter of fact, we have no clue why there are three generations of particles and why their mass changes wildly from one generation to the next, as shown in Table 1.1.

We can ask even more questions such as; why we only have the group structure as defined in $\mathcal{G}_{SM}$? Why are quarks confined in hadronic structures such as protons and neutrons? Why there are about twenty completely free parameters determined only by the experimental data, *etc.* In section 1.3, we will describe different approaches presented in the literature to answer one or multiple problems of the SM.

1.3 Hitchhiker's guide to find new physics

In this rather short road map, we will summarize some of the ongoing attempts on solving the problems of the SM. There are two main paths to take, one can accept the SM as a basis and try to expand the Lagrangian piece by piece, or one can construct a broader framework which breaks down to the SM.

One way to approach such a vast set of problems is to add particles or interactions to the SM Lagrangian. This *ad hoc* technique doesn't have a single recipe, but can provide solid directions to the grand question of "Where to find new physics?". Extending the family structures in the SM or adding new particles such as new vector-like leptons or axions can lead to viable dark matter candidates and explain the mass of neutrinos. The large uncertainties, especially, in Higgs and top quark coupling strengths to other particles and themselves is an important starting point to develop such a theory. SM effective field theory (SMEFT) is another way of approaching to answer such queries. As mentioned earlier, LHC has entered into a precision era with High-Luminosity-LHC (HL-LHC). We will be able to observe billions of top quarks and Higgs bosons, which will quench our need for statistics in the data. Currently, we observe large uncertainties in the coupling strengths of these particles, which might be an additional source of $\mathcal{CP}$-violation. The Yukawa corrections to the couplings of these particles in SMEFT can be added as higher-order interaction terms in the Lagrangian,

$$\mathcal{L} = \mathcal{L}_{\rm SM} + \mathcal{L}_{\rm eff} = \mathcal{L}_{\rm SM} + \frac{1}{\Lambda}\mathcal{L}_1 + \frac{1}{\Lambda^2}\mathcal{L}_2 + \mathcal{O}(\Lambda^{-4}) + h.c. \quad , \quad \mathcal{L}_n = \sum_i C_i O_i \ ,$$

where $\mathcal{L}_1$ represents dimension five operators, $\mathcal{L}_2$ represents the dimension six operators and $\mathcal{O}(\Lambda^{-4})$ represents other higher dimensional operators. Λ is nothing but the cut-off scale of this new "extended" field theory which supposed to be beyond the TeV scale. Determining the variables in higher order terms with large precision can greatly help us to construct complete models that can describe the nature of the new physics at the Planck scale. Understanding these couplings and their high energy event shapes are essential for constructing a complete BSM model from a bottom-up approach. For instance, in the SM, top quark's chromomagnetic dipole moment (CMDM) arises at the one-loop level and chromoelectric dipole moment (CEDM) at the three-loop level which also hints new sources of $\mathcal{CP}$-violation. The impact of these higher dimensional corrections on top quarks, has already been studied in two Higgs doublet model (2HDM) [50], and has been discussed in supersymmetric scenarios in terms of QCD corrections to top quark production [51, 52] as well as electroweak corrections [53, 54]. In addition to the particle mass bounds, these coupling corrections can provide a distinct constraint on new physics scenarios.

Another, very well motivated, approach can be adapted by achieving more general symmetries. As we discussed earlier, the very foundation of the SM stands upon the shoulders of the Noether's theorem [55] where symmetries in a system ascertain the interactions between particles via the gauge principle. The idea of breaking from a larger gauge structure to the SM is considered under the title of *grand unified theories* (GUTs). This breaking mechanism can happen directly or in steps in which leads to the SM gauge structure,

$$\mathcal{G}_{\rm GUT} \quad \xrightarrow{M_{\rm GUT}\approx 10^{15}\ \rm TeV} \quad \mathcal{G}_{SM} \quad \xrightarrow{M_{\rm EWSB}\approx 1\ \rm TeV} \quad SU(3)_{\rm C}\otimes U(1)_{\rm EM}\ .$$

GUT models provide a framework which can describe the unification of the three nuclear forces and due to this unification, eliminate the free parameters of the standard model and force them to be dependent on a single variable at the Planck scale.

The SM relies on four-dimensional space-time symmetries where it is invariant under Lorentz transformations[6]. It is possible to extend the dimensionality of the SM and by doing so, extend its Poincaré symmetry[7]. Such theories are well motivated under Kaluza Klein Theory [56] which indicates that the SM originated from a higher dimensional "brane" and decouples from other dimensions at the low energy scale. Such an approach can provide solutions to the hierarchy problem and unify internal space-time symmetries.

Finally, let us converge this chapter to the topic that we will wrestle within this thesis. *Supersymmetry* (SUSY) [57, 58] proposes a different way of expanding the space-time symmetries of the SM. Using the Noether Theorem's lemma, which indicates that the temporal component of the current is a conserved entity, one can end up with a simple transformation relation between bosons and fermions as a virtue of spin-statistics. Such theoretical framework allows us to solve several problems of the SM. In the next following chapters, we will mention the motivation behind the *supersymmetry* and define the model within the borders of Minimal Supersymmetric Extension of the Standard Model (MSSM), chapter 2.

This thesis is organised as follows; in chapter 2 we will introduce MSSM and will discuss how to improve the missing ingredients of the SM and MSSM with an even more

---

[6] Translation in space-time.

[7] Including translation in space-time, rotation in space and boosts.

extended framework. In chapter 3, we will discuss the possibility of extending MSSM field structure via vector-like multiplets. In chapter 4 and chapter 5 we will investigate a gauge extention of MSSM and how to find its signature at the LHC. In chapter 6 we will discuss current bounds on the supersymmetric particles and effects of the theoretical uncertainties on these bounds and finally we will conclude in chapter 7.

Chapter 2

Minimal Supersymmetric Extention of the Standard Model (MSSM)

Despite the success of the SM, there is still a lot to unfold in the observed data. In the previous chapter, we saw that there are many issues that the SM cannot explain and it is unlikely that a simple extension will be able to cover all those issues. In this chapter we will introduce the minimal possible supersymmetric extension of the standard model [57, 58, 59, 60, 61]. The reason that we are starting from a minimal framework is to have least amount of free parameters and decide which direction we need to go from here, in more technical words the goal is to fix as many problems as possible using only one extra generator of the symmetry group. In the following, we discuss the motivation behind such framework, section 2.1, and then we will move on with the definition of the model in section 2.2.

2.1 Motivation

The goal of the MSSM is enhancing the space-time symmetries of the SM wihtout changing its gauge structure. By introducing a symmetry between bosons and fermions, we ensure that the Lagrangian is symmetric under Poincaré transformations.

The main motivation behind the supersymmetry is that, it can provide a natural solution to the hierarchy problem. As we described with the Fig. 1.2, fermionic loop corrections cause divergences in the Higgs mass. In supersymmetry these quadratic divergences receive opposite sign contributions from the supersymmetric partners of the corresponding particle, where in this specific case supersymmetric partner of top quark as shown in Fig. 2.1 [62].

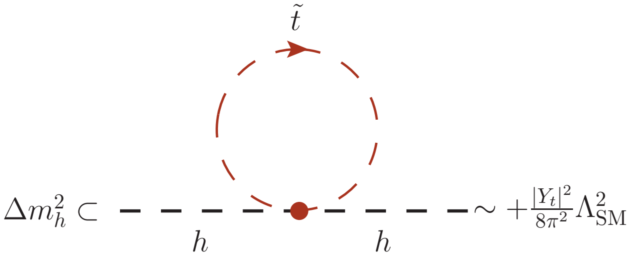

Figure 2.1: *Bosonic loop corrections to the Higgs boson mass coming from the supersymmetric partner of the top quark, $\tilde{t}$. The diagram has been created via Jaxodraw package [35].*

Furthermore, obtaining a theory that can describe the unification of all three nuclear forces has always been the goal [63, 64]. It is possible to achieve such unification in the SM by adding extra fields and interaction terms that can modify the renormalization group equations (RGEs). In MSSM such modification occurs naturally [65, 66, 67, 68, 69, 70, 71]. The RGEs of the gauge couplings, g_1, g_2 and g_3, evolve through energy scales via,

$$\beta_{g_i} = \frac{d}{d(\ln(Q/Q_0))} g_i = \frac{1}{16\pi^2} b_i g_i^3 \ .$$

Here Q is the varying energy scale, Q_0 is the relative energy scale which we will take as 1 GeV, b_i is a model and gauge dependent constant. Due to the modifications in the value of this constant in MSSM, we observe an "optimistic" unification in the gauge couplings. Fig. 2.2 shows the evolution of each gauge coupling through energy scales for both SM and MSSM which are represented with dashed and solid lines respectively. The red, green and blue colour codes represent $U(1)_Y$, $SU(2)_L$ and $SU(3)_C$ gauge couplings respectively. As seen in the behaviour of the dashed lines they deviate from the unification with $\mathcal{O}(10^2)$ TeV scale. On the other hand, one can observe the unification of all three gauge couplings for MSSM at $\mathcal{O}(10^{15})$ TeV which is approximately the order of the Planck scale. Dark red dashed lines show the reach of the corresponding experiment where The Large Electron-Positron Collider (LEP) has been conducted at 100 GeV centre-of-mass energy, LHC Phase I was at $\sqrt{s} = 8$ TeV and today LHC is moving towards $\sqrt{s} = 14$ TeV for Phase III. Although these LHC energies are massive achievements, at those energy levels the detectors need to be extremely sensitive to be able to observe the difference between SM and MSSM. Especially $SU(3)_C$ gauge coupling suffers from very large uncertainties with respect to other couplings and also QCD background is particularly overwhelming. Additionally it is important to stress

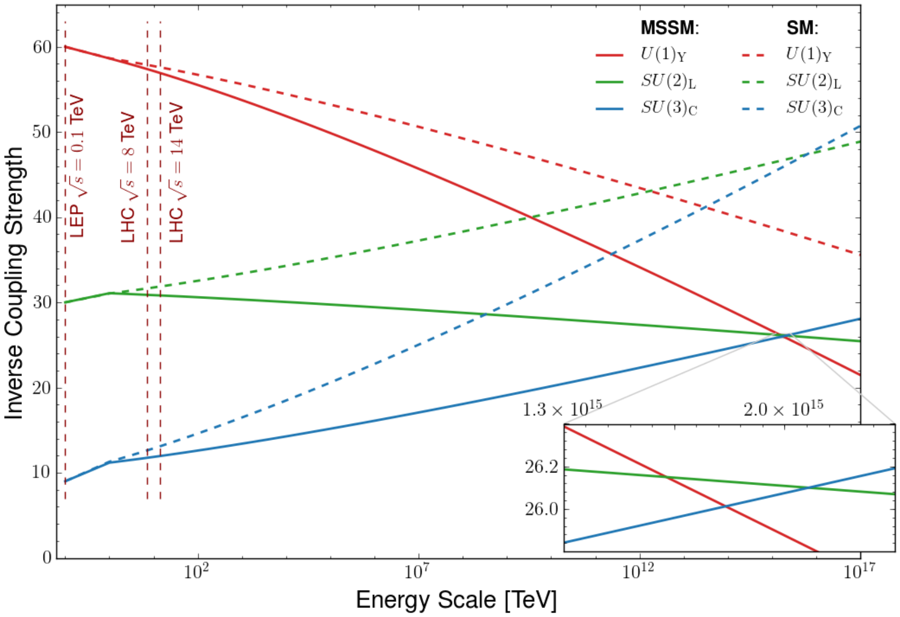

Figure 2.2: *Evolution of the inverse gauge couplings with two loop RGEs plotted against the energy scale. Coloured solid lines represent MSSM gauge coupling evolutions with red, green, blue being* $U(1)_Y$, $SU(2)_L$ *and* $SU(3)_C$ *coupling respectively. Coloured dashed lines represents the SM gauge coupling evolution with the same colour code. Dark red dashed lines show the reach of the experiments with LEP at 100 GeV, LHC phase I reach upto 8 TeV and LHC phase III will run at 14 TeV centre-of-mass energy. Bottom right plot shows 25 times zoomed-in version of the unification point.*

that, whilst we observe unification in the gauge couplings in a logarithmic energy scale, when zoomed in one can immediately see that the couplings do not quite unify. This has been shown in the lower right plot of Fig. 2.2. Despite this fact, MSSM can still achieve a major improvement to the gauge unification.

The SM Lagrangian that we presented earlier contains numerous variables that can only be fixed via experimental results. In the supersymmetric Lagrangian, on the other hand, terms are defined as interactions as much as possible. This introduces certain limitations and relations with each term and does not require free parameters as the SM Lagrangian does. The only downside is that we do not know at which scale supersymmetric particles gain their masses (in other words, where supersymmetry is spontaneously broken). Thus we require several free variables to define SUSY breaking at a certain scale and the amount of free variables is model dependent. Introducing a grand unified model can relate these variables via RGEs and set to a constant at GUT scale.

Finally, one of the most important achievements of MSSM is having a viable dark matter (DM) candidate [72]. The fermionic components of the gauge and Higgs sectors of the MSSM can mix with each other and generate neutral and charged mass eigenstates. One of the neutral mass eigenstates has the potential to be the lightest supersymmetric particle (LSP). Due to the conservation rules that we will mention later, a supersymmetric particle can only decay into one SM, and one supersymmetric particle, being LSP, constraints kinematic space and makes it stable. Depending on its production rate this particle can easily satisfy observable constraints on DM.

With these motivations in mind section 2.2 briefly describes the theoretical framework of MSSM and links its properties to the motivations mentioned above.

2.2 Definition of the model

The theoretical framework of MSSM is based on four-dimensional supersymmetric field theory of Wess and Zumino [57, 59, 73]. MSSM is the simplest case of the supersymmetric extensions where the gauge structure of the SM has been kept as it is but the field content has been extended. Under this framework we will talk about the notion of superfields. Superfields encode supermultiplets which include particles and their supersymmetric partners (sparticles), additionally it includes auxiliary fields for off-shell supersymmetry. In MSSM chiral-superfields contain SM's matter sector as well as supersymmetric fermions while vector-superfields contain SM's gauge fields and supersymmetric bosons. There are other types of superfields as well but they are not used in MSSM framework.

2.2.1 Field content

Requiring an extra symmetry between bosons and fermions as well as preserving all the SM quantum numbers requires an extention in the field content since it can not be described within the standard framework. In MSSM every fermion gets a supersymmetric partner where, quarks and leptons will have scalar squark and slepton pairs respectively. Due to the fact that the left- and right-handed fermions transform differently under the SM gauge group, as shown in Eq. (1.1.8) and Eq. (1.1.9), their supersymmetric partners also have left- and right-handed complex partners. Electroweak bosons and gluons, on the other hand, will get fermionic partners so-called gauginos and gluinos.

One important difference that has to occur in MSSM is the Higgs sector. As in two Higgs doublet models [74, 75], MSSM requires two Higgs doublets. The reason of such construction in MSSM is two folds. The first reason is the structure of the superpotential, which we will discuss in section 2.2.2. In short, to be able to get physical equation of motions with a superpotential one needs to require it to have a holomorphic structure. This means that it can not contain a field and its complex conjugate at the same time. In the SM, as shown in Eq. (1.1.10), up-type quark sector interacts with the Higgs field ϕ where down-type sector interacts with its complex conjugate. To be able to generate mass for both up-type and down-type quark sectors, as well as the lepton sector, MSSM requires two opposite sign Higgs fields. The second reason comes from the gauge anomalies[1] [76, 77, 78]. Fig. 2.3 shows possible diagrams that can emerge from a general Lagrangian. Such anomalies leads to inconsistencies, gauge currents, and must be cancelled out to have a consistent theory. For this reason it is obligatory to have another Higgs field with oposite $U(1)$ charge to satisfy the equation in Fig. 2.3. Table 2.1 shows the gauge structure of the MSSM Higgs sector. The rest of the fields are not shown since they are the same as in Table 1.3 with only extension of the field structure.

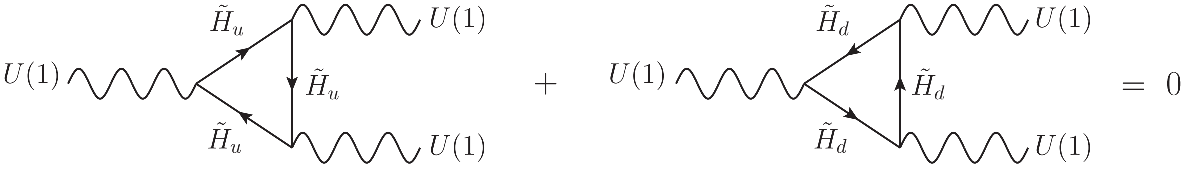

Figure 2.3: *Gauge anomaly diagrams for up- and down-type Higgs superfields. The diagram has been created via Jaxodraw package [35].*

Table 2.1: *Up- and down-type Higgs doublets in MSSM and their gauge structure.*

	$SU(3)_C \otimes SU(2)_L \otimes U(1)_Y$
$\tilde{H}_u \equiv \begin{pmatrix} H_u^+ \\ H_u^0 \end{pmatrix}$	$(\mathbf{1}, \mathbf{2}, 1)$
$\tilde{H}_d \equiv \begin{pmatrix} H_d^- \\ H_d^0 \end{pmatrix}$	$(\mathbf{1}, \overline{\mathbf{2}}, -1)$

Chiral and gauge supermultiplets are constructed with these superfields. Both of these supermultiplets contain same number of fermionic and bosonic degrees of freedom. To include the left(right)-handedness, the chiral supermultiplet contains a Weyl fermion and its scalar complex partner. To preserve off-shell supersymmetry, two auxiliary fields have been

---

[1] Gauge anomalies will be discussed with more detail in section 2.3.

introduced, F having two real fermionic degrees of freedom and D, having two real bosonic degrees of freedom. Both fields are eliminated for on-shell cases. Gauge supermultiplets are denoted as a massless gauge boson field ${A^a}_\mu$, its Weyl fermion partner λ^a and additionally the SM gauge fields, $\hat{W}^\pm$ and $\hat{Z}$ as shown before. The adjoint representation index a runs from one to eight for $SU(3)$, from one to three for $SU(2)$.

2.2.2 Lagrangian density

Following the prescription of the section 1.1, the MSSM Lagrangian can be written as a combination of $\mathcal{L}_{chiral}$, $\mathcal{L}_{gauge}$ and extra supersymmetric gauge interactions [79, 80]. Since we already built the SM on chiral representations, we can simply add the extra terms and define extended transformations.

The chiral part of the Lagrangian will mostly remain the same except the extention of the field contents as described in section 2.2.1. In addition to extended kinetic Dirac and kinetic scalar parts of the Lagrangian we need to add interaction terms of the chiral supermultiplets,

$$\mathcal{L}^{\text{MSSM}} \subset -\frac{1}{2}\left(W^{ij}\psi_i\psi_j + W^*_{ij}\psi^{\dagger i}\psi^{\dagger j}\right) - W^i W^*_i \ .$$

The interactions of the chiral and the gauge supermultiplets are introduced in the superpotential, W. W^i and W^{ij} is defined as,

$$W^i = \frac{\partial W}{\partial \phi_i} \quad \text{and} \quad W^{ij} = \frac{\partial^2 W}{\partial \phi_i \partial \phi_j} \ .$$

As can be inferred from the definition, generic W^i and W^{ij} are polynomials in the scalar field ϕ^i and ϕ^{*i}. Since the variation of the interaction Lagrangian must be zero (Euler-Lagrange equation), in order to $\delta\mathcal{L}_{int}$ to vanish one can show that W can not be a function of ϕ^i and ϕ^{*i} at the same time[2]. Thus W must be holomorphic (complex analytic) in order to preserve Euler-Lagrange equation.

The superpotential plays a major role in construction of a supersymmetric theory. The interactions between all particles and their masses can be defined by gauge transformations

---

[2] This can be observed using Fierz identity, since it does not apply to a mixture of a scalar field and its conjugate, such terms will not vanish in the $\delta\mathcal{L}_{int}$. For more information see ref. [58], section 3.2.

and a corresponding superpotential. A generic MSSM superpotential can be written as,

$$\begin{aligned} W_{\text{MSSM}} &= -\mathbf{Y}_e \hat{E}\hat{L}\hat{H}_d - \mathbf{Y}_u \hat{U}\hat{Q}\hat{H}_u - \mathbf{Y}_d \hat{D}\hat{Q}\hat{H}_d + \mu \hat{H}_u \hat{H}_d \ , \\ W_{SUSY} \subset W_{\text{MSSM}} &+ \underbrace{\lambda \hat{L}\hat{L}\hat{E}}_{\not{L}} + \underbrace{\lambda' \hat{L}\hat{Q}\hat{D}}_{\not{L}} + \underbrace{\lambda'' \hat{U}\hat{D}\hat{D}}_{\not{B}} - \underbrace{\mu' \hat{L}\hat{H}_u}_{\not{L}} \ . \end{aligned} \tag{2.2.1}$$

We will analyse the equation in two parts. In the first line $\mathbf{Y}_i$ is the corresponding Yukawa coupling of the chiral superfield denoted with the subindex. $\hat{E}$, $\hat{U}$, $\hat{D}$ are the right-handed superfield for leptons (sleptons), up-type quarks (squarks) and down-type quarks (squark) respectively. L and $\hat{Q}$ on the other hand are the left-handed superfields. μ is dimension-full Higgs self-interaction coupling. It is rather important to discuss the implications of this parameter. μ is a rather arbitrary constant where it can have any value from zero to M_{Planck}. However, zero would imply that there will be no interactions between two Higgs doublet and M_{Planck} will mean that there will be too much of it. In MSSM there is no possible physical bound that we can apply on this parameter, which causes so-called μ-problem.

The second line of Eq. (2.2.1) indicates the terms that violate Lepton (L) and Baryon (B) number conservation. Although SM does not have any renormalizable term in the Lagrangian that can violate L or B, those are violated in the nature by non-perturbative electroweak (EW) effects [81]. In order to prevent proton from decaying, due to these terms, an additional symmetry, so-called R-parity, imposed on MSSM.

$$R = (-1)^{3B+L+2S} \ ,$$

where S is the spin of the superfield. While the SM particles have positive R-parity, SUSY particles have negative R-parity. For this reason, in order to conserve R-parity a three-body vertex with supersymmetric particles has to have one SM particle. This symmetry also causes LSP to be stable, since it is not kinematically possible for such particle to decay into any supersymmetric particle(s) with a SM particle. Although we will assume that this symmetry is conserved for the purposes of this thesis R-parity violating models can be found in refs. [82, 83].

The gauge part of MSSM Lagrangian is also expanded with supersymmetric gauge terms,

$$\mathcal{L}^{\text{MSSM}}_{gauge} \subset -i\lambda^{\dagger a}\bar{\sigma}^{\mu} D_{\mu}\lambda_a + \frac{1}{2} D^a D_a \ .$$

$\mathcal{L}^{\text{MSSM}}_{gauge}$ includes Yang-Mills field strength term as before. The covariant derivative of a gaugino field and D^a are defined as

$$D_\mu \lambda_a = \partial_\mu \lambda_a + g_a f_{abc} A^{\mu b} \lambda^c \quad \text{and} \quad D_a = g_a(\phi^* T_a \phi)$$

respectively. It is important to note that D^a is not covariant derivative but it is so-called D-term. As before T^a denotes the hermitian matrices corresponding to the generator of that gauge group which satisfies the Lie algebra, $[T^a, T^b] = i f^{abc} T_c$.

Finally, we can add gauge interaction term to the MSSM Lagrangian as,

$$\mathcal{L}_{\text{MSSM}} \subset -\sqrt{2} g(\phi^* T^a \psi)\lambda_a - \sqrt{2} g \lambda^{\dagger a}(\psi^\dagger T^a \phi) + g(\phi^* T^a \phi) D_a \ .$$

As already been defined in the Lagrangian, F- and D-terms can be used to define scalar potential $V(\phi, \phi^*)$. This will generate a potetial which is completely defined by supersymmetric interactions instead of free variables as it so happens in the SM.

$$V(\phi, \phi^*) = \underbrace{W^*_i\, W^i}_{F\text{-term}} + \underbrace{\frac{1}{2}\sum_a g_a (\phi^* T^a \phi)^2}_{D\text{-term}} \ , \tag{2.2.2}$$

where using the equations of motion one can deduce that $F^i = -W^{*i}$ and $F^{*i} = -W^i$.

2.2.3 SUSY-breaking

Although we have access to 13 TeV centre-of-mass energy at the LHC, SUSY particles are yet to be observed. This implies that supersymmetric particle spectrum has to be heavy and SUSY has to be broken at a higher scale than EWSB. However SUSY breaking has to be "soft" so that it won't introduce new ultraviolet divergences to the Higgs mass [84, 85]. SUSY breaking Lagrangian for MSSM is given as,

$$\begin{aligned}
\mathcal{L}_{soft} \quad = \quad & -\frac{1}{2}(M_1 \tilde{B}\tilde{B} + M_2 \tilde{W}\tilde{W} + M_3 \tilde{g}\tilde{g} + c.c.) \\
& - \left(\tilde{Q}^\dagger \mathbf{m}^2_Q \tilde{Q} + \tilde{L}^\dagger \mathbf{m}^2_L \tilde{L} + \tilde{U} \mathbf{m}^2_U \tilde{U}^\dagger + \tilde{D} \mathbf{m}^2_D \tilde{D}^\dagger + \tilde{E} \mathbf{m}^2_E \tilde{E}^\dagger\right) \\
& - \left(\tilde{U} \mathbf{A}_U \tilde{Q} H_u - \tilde{D} \mathbf{A}_D \tilde{Q} H_d - \tilde{E} \mathbf{A}_E \tilde{L} H_d + c.c.\right) \\
& - \left(m^2_{H_u} H^*_u H_u + m^2_{H_d} H^*_d H_d\right) \\
& - \left(m^2_{H_u H_d} H_u H_d + c.c.\right) \ .
\end{aligned}$$

The first line corresponds to gaugino mass terms; bino mass (M_1), wino mass (M_2) and gluino mass (M_3) respectively. Second line consists of sfermionic soft-masses with m_i^2 being 3×3 hermitian matrices. They are squark soft-mass ($\mathbf{m}_Q^2$), slepton soft-mass ($\mathbf{m}_L^2$), right-handed up-type squark soft-mass ($\mathbf{m}_U^2$), right-handed down-type squark soft-mass ($\mathbf{m}_D^2$) and right-handed slepton soft-mass ($\mathbf{m}_E^2$). These mass terms can be complex but they have to be hermitian to have a real Lagrangian. Third line of the equation consists of trilinear couplings with $\mathbf{A}_f$ being complex 3×3 matrix in mass dimensions. The fourth line corresponds to non-holomorphic scalar squared mass terms and fifth line consists of holomorphic scalar squared mass terms ($m_{H_u H_d}^2$).

As mentioned before, MSSM Lagrangian is defined via interaction terms to be able to have a self-consistent theory. However, since we do not know at which scale MSSM breaks, terms in the $\mathcal{L}_{soft}$ have to be free. For a GUT theory on the other hand, these variables evolve via RGEs to the Planck scale and unify. Thus one can write them as,

$$\begin{aligned} M_1 = M_2 &= M_3 = M_{1/2} \ , \\ \mathbf{m}_E^2 = \mathbf{m}_Q^2 = \mathbf{m}_L^2 = \mathbf{m}_U^2 = \mathbf{m}_D^2 = M_0^2 \mathbf{1} \quad &; \quad m_{H_u}^2 = m_{H_d}^2 = m_{H_u H_d}^2 = M_0^2 \ , \\ \mathbf{A}_{\tilde{f}} &= A_0 \mathbf{Y}_{\tilde{f}} \ . \end{aligned}$$

The reason why we have two sets of mass terms namely one for gauginos ($M_{1/2}$) and one for sfermions and Higgsinos (M_0) is due to the breaking scheme. Gaugino fields arise from the decomposition of the adjoint representation whereas the matter fields and Higgs doublets arise from vector representation of the unified gauge group. In section 2.3 this notion is exemplified in more detail.

Unlike the supersymmetry preserving part of the Lagrangian, introduced in the previous section, soft-breaking part of the Lagrangian introduces a variety of new terms to the Lagrangian which can neither be rotated out nor have a counterpart in the SM. There are 105 new phases, masses and mixing angles introduced in the complete Lagrangian of the MSSM and these cannot be avoided [86] but can be reduced using GUT prescription.

2.2.4 Electroweak symmetry breaking and particle mixing

Compared to the SM's EWSB potential, MSSM's is slightly more complicated due to the necessity of having two complex Higgs doublets. The MSSM's symmetry breaking potential is given as;

$$\begin{aligned} V &= m^2_{H_u}|H^0_u|^2 + m^2_{H_d}|H^0_d|^2 + m^2_{H_uH_d}\left(H^0_uH^0_d + c.c.\right) \\ &\quad +|\mu|^2\left(|H^0_u|^2 + |H^0_d|^2\right) \\ &\quad +\frac{1}{8}\left(g_1^2+g_2^2\right)\left(|H^0_u|^2 + |H^0_d|^2\right)^2 + \frac{1}{2}g_2\left|H^+_uH^{0*}_d + H^0_uH^{-*}_d\right| \ , \end{aligned}$$

where first line is coming from $\mathcal{L}_{soft}$, second line from the F-term of Eq. (2.2.2) and the last line is from the D-term of Eq. (2.2.2). In order to satisfy the observed EWSB, $SU(2)_L \otimes U(1)_Y \rightarrow U(1)_{EM}$, one needs to minimize the potential. Since $SU(2)_L$ rotations alow us to rotate away one of the weak isospin components of Higgs doublet, without the loss of generality one can choose $H^+_u = 0$ which will automatically indicate $H^-_d = 0$ due to charge conservation. Thus one can simply rewrite the potential as,

$$V = \left(|\mu|^2 + m^2_{H_u}\right)|H^0_u|^2 + \left(|\mu|^2 + m^2_{H_d}\right)|H^0_d|^2 - (m^2_{H_uH_d}H^0_uH^0_d + c.c.) + \frac{1}{8}(g_1^2+g_2^2)\left((H^0_u)^2 + (H^0_d)^2\right) \ .$$

Since $\langle\phi_i\rangle$ and $m^2_{H_uH_d}$ need to be positive definite, due to the rotations in the $\mathcal{L}_{soft}$ part, in order to have non-zero minima, the potential needs to satisfy following conditions,

$$(m^2_{H_uH_d})^2 > \left(|\mu|^2 + m^2_{H_u}\right)\left(|\mu|^2 + m^2_{H_d}\right) \quad , \quad 2m^2_{H_uH_d} < 2|\mu|^2 + m^2_{H_u} + m^2_{H_d}$$

In order to generate mass for both down-type and up-type quarks the neutral portion of both Higgs doublet needs to gain a vev which will be denoted as $\langle H^0_i\rangle = v_i$. Using

$$\tan\beta = \frac{v_u}{v_d} \quad \text{and} \quad v^2 = v_u^2 + v_d^2 \ ,$$

where $v^2 = 174$ GeV^2 and $0 < \beta < \pi/2$. These lead to,

$$\begin{aligned} \left\langle\frac{\partial V}{\partial H^0_u}\right\rangle &\Rightarrow \quad 0 = 2\left(|\mu|^2 + m^2_{H_u}\right) - m^2_{H_uH_d}\ \cot\beta + \tfrac{1}{2}(g_1^2+g_2^2)\ v^2 \ , \\ \left\langle\frac{\partial V}{\partial H^0_d}\right\rangle &\Rightarrow \quad 0 = 2\left(|\mu|^2 + m^2_{H_d}\right) - m^2_{H_uH_d}\ \tan\beta + \tfrac{1}{2}(g_1^2+g_2^2)\ v^2 \ . \end{aligned}$$

Two Higgs doublets have eight degrees of freedom, but after EWSB only five of them gain mass. Namely two $\mathcal{CP}$-even Higgs with SM-like Higgs (h) and its heavier counter partner (H), one $\mathcal{CP}$-odd Higgs (A_0) and two charged Higgs ($H^\pm$). The rest of the degrees of freedom are absorbed by massless Goldstone bosons ($G^{0,\pm}$) [74, 87]. After the diagonalization of the mass eigenstates in the basis of (H_d, H_u) the tree-level masses are given as,

$$m^2_{A_0} = \frac{2m^2_{H_uH_d}}{\sin 2\beta} \quad , \quad m^2_{H^\pm} = m^2_{A_0} + \frac{1}{4}v^2 g_2^2 \, ,$$

$$m^2_{H,h} = \frac{1}{2}\left(m^2_{A_0} + \frac{1}{4}v^2(g_1^2 + g_2^2) \ \pm \ \sqrt{\left(m^2_{A_0} + \frac{1}{4}v^2(g_1^2+g_2^2)\right)^2 - m^2_{A_0}(v_d^2 - v_u^2)(g_1^2+g_2^2)} \right) ,$$

Note that the values of $m^2_{\phi_i}$, μ and $\tan\beta$ are free in this scenario and $m^2_{H_uH_d}$ can be written in terms of them. Although $m^2_{\phi_i}$ and $m^2_{H_uH_d}$ can be fixed at the GUT scale μ and $\tan\beta$ will still remain as free parameters of the model, but of course these parameters will be constrained via the observable masses.

The effects of EWSB, require higgsinos and electroweak gauginos to mix and yield 4 neutral and 2 charged mass eigenstates, called neutralinos and charginos respectively [58, 84, 87]. In the gauge eigenstate basis $\psi^0 = (\tilde{B}, \tilde{W}^0, \tilde{H}_d^0, \tilde{H}_u^0)$ the neutralino mass matrix is given as,

$$\mathcal{M}_{\tilde{\chi}^0} = \begin{pmatrix} M_1 & 0 & -\frac{1}{2}g_1 v_d & \frac{1}{2}g_1 v_u \\ 0 & M_2 & \frac{1}{2}g_2 v_d & -\frac{1}{2}g_2 v_u \\ -\frac{1}{2}g_1 v_d & \frac{1}{2}g_2 v_d & 0 & -\mu \\ \frac{1}{2}g_1 v_u & -\frac{1}{2}g_2 v_u & -\mu & 0 \end{pmatrix} .$$

Diagonalization of $\mathcal{M}_{\tilde{\chi}^0}$ by a unitary matrix N leads to four neutralinos, $N^* \mathcal{M}_{\tilde{\chi}^0} N^{-1} = diag(m_{\tilde{\chi}_1^0}, m_{\tilde{\chi}_2^0}, m_{\tilde{\chi}_3^0}, m_{\tilde{\chi}_4^0})$ with $\tilde{\chi}_1^0$ being the lightest one[3].

Similarly the chargino basis can be written as $\psi_i^\pm = (\tilde{W}^-, \tilde{H}_d^-)$, $(\tilde{W}^+, \tilde{H}_u^+)^\dagger$ and the corresponding mass matrix is given as,

$$\mathcal{M}_{\tilde{\chi}^\pm} = \begin{pmatrix} M_2 & \frac{1}{2}g_2 v_u \\ \frac{1}{2}g_2 v_d & \mu \end{pmatrix} .$$

Since $\mathcal{M}_{\tilde{\chi}^\pm}$ is not symmetric two unitary matrices are needed to diagonalize the matrix, $U\mathcal{M}_{\tilde{\chi}^\pm}V^{-1} = diag(m_{\tilde{\chi}_1^\pm}, m_{\tilde{\chi}_2^\pm})$. Simply diagonalizing $\mathcal{M}_{\tilde{\chi}^\pm}$ by absorbing all the complex phases one can deduce positive definite tree-level masses as

$$m^2_{\tilde{\chi}^\pm_{1,2}} = \frac{1}{2}\left(M_2^2 + \mu^2 + \frac{1}{2}g_2^2 v^2 \mp \sqrt{\left(M_2^2 + \mu^2 + \frac{1}{2}g_2^2 v^2\right)^2 - 4(\mu M_2 - g_2^2 v_u v_d)^2} \right) .$$

---

[3] For analytic solution of the diagonalization see ref. [88, 89].

The scalar fermion mass eigenstates can be determined by diagonalizing 6×6 mass matrices. This reduces to 3×3 for sneutrino since it does not have right-handed part. Sneutrino mass matrix can be constructed simpy from the left-handed neutrino superfield basis $(\tilde{\nu}_L)$, $(\tilde{\nu}_L^*)$.

$$\mathcal{M}_{\tilde{\nu}}^2 = \begin{pmatrix} m_{LL}^2 + (m_{\tilde{L}}^2)_{11} & 0 & 0 \\ 0 & m_{LL}^2 + (m_{\tilde{L}}^2)_{22} & 0 \\ 0 & 0 & m_{LL}^2 + (m_{\tilde{L}}^2)_{33} \end{pmatrix} ,$$

where $m_{LL}^2 = \frac{1}{8}(g_1^2 + g_2^2)(v_u^2 - v_d^2)$. For other fermions, due to the left-right interaction this changes slightly. In the basis of $(\tilde{\psi}_L,\ \tilde{\psi}_R)$, $(\tilde{\psi}_L^*,\ \tilde{\psi}_R^*)$; a generic sfermionic mass matrix can be written as,

$$\mathcal{M}_f^2 = \begin{pmatrix} m_{LL}^2 & m_{LR}^2 \\ m_{RL}^2 & m_{RR}^2 \end{pmatrix} ,$$

where

$$\begin{aligned} m_{LL}^2 &= m_F^2 + \frac{v_d^2 - v_u^2}{8}\left(I_f^3(1+\cos^2\theta_W) - Y_f \sin^2\theta_W\right)(g_1^2+g_2^2) + m_f^2 \ , \\ m_{RR}^2 &= m_{F'}^2 + \frac{v_d^2 - v_u^2}{2} Q_f \sin^2\theta_W (g_1^2+g_2^2) + m_f^2 \ , \\ m_{RL}^2 &= m_{LR}^{*2} = m_f^2(A_f^* - \mu f(\beta)) \ , \end{aligned}$$

where $f(\beta)$ corresponds to $\cot\beta$ for up-type sfermions and $\tan\beta$ for down-type sfermions. m_f, Y_f, I_f^3 and Q_f are fermion mass, hypercharge, isospin and electric charge of the corresponding sfermionic field. $m_{F,F'}$, on the other hand, is the mass term generated via F-term in the Lagrangian and A_f is the trilinear coupling.

A supersymmetric mass spectrum considered as "natural" if the contributions to the Higgs mass are relatively small,

$$\mathcal{N} = \frac{\Delta m_h^2}{m_h^2} \ ,$$

where $\mathcal{N}$ is called the fine-tuning parameter [90][4]. Naturally one expects to have an observable where every independent contributor to this observable is comparable or less than itself. For a contributor larger than the value of the observable, the model requires a same and opposite

---

[4] Note that there is also another approach through Z mass which is defined as follows; for all the free

value of fine-tuning for such a contributor. As we already mentioned in discussion of the Fig. 1.2, for if the SM is valid up to the Planck scale, using Eq. (1.1.4), one can show that $\mathcal{N} \sim 10^{30}$.

One of the most important motivations behind the supersymmetry was its elegant solution to the hierarchy problem and by doing so solving the issue of the naturalness. A so-called Natural mass spectrum of a supersymmetric model is shown in Fig. 2.4. The blue lines represents the Higgs masses with respect to the relatively small μ-parameter with h being the SM-like Higgs at 125.09 GeV. Green lines show the lightest three squark masses which give the largest contribution to the loop corrections of the Higgs mass. For heavier squark spectrum the logarithmic divergences of the Higgs loop corrections will grow. Thus to expect a "natural" spectrum, stop should be relatively light. The teal lines represents bino and wino relative mass which should represent the average chargino and neutralino masses. In such

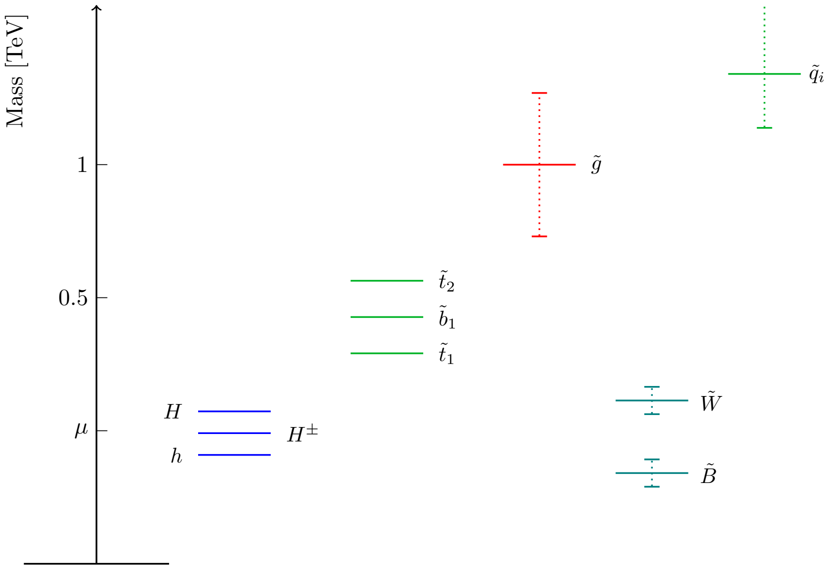

Figure 2.4: *Natural SUSY spectrum. The blue lines show the Higgs masses with the lightest being the SM-like Higgs, $H^\pm$ is the charged Higgs and H is the second lightest Higgs. Green lines represents squarks ($\tilde{q}_i$) with the lightest three squarks given separately, namely left-handed stop ($\tilde{t}_1$), left-handed sbottom ($\tilde{b}_1$) and right-handed stop ($\tilde{t}_2$) respectively. The red line represents gluino and teal lines show the gauginos; bino ($\tilde{B}$) and wino ($\tilde{W}$) respectively. Finally μ on the y-axis represents $H_u - H_d$ coupling introduced in Eq. (2.2.1).*

---

parameters defining the Z mass in a model, a_i,

$$\Delta \equiv \max \left| \frac{a_i \partial m_Z^2(a_i)}{m_Z^2 \partial a_i} \right| ,$$

where for a model Δ defines the fine-tuning parameter [91].

a construction, chargino and neutralino mass spectrum is compressed [92]. However, as we will show in chapter 6, the constraints on the supersymmetric particles are getting beyond the representative masses shown in Fig. 2.4. Although, there are large uncertainties our predictions show that even if we take uncertainties into account SUSY spectrum is unlikely to be "natural".

On the other hand, is it correct scientific approach to classify a model as "natural" or not by demanding a reasonable $\mathcal{N} = \Delta m_h^2/m_h^2$ ratio? How does this variable help us to understand the fundamental properties of the nature? Anthropic reasoning states that, there might be multiple universes with slightly different $\mathcal{N}$, but it might be possible that only this value of $\mathcal{N}$ can conclude with an observer [93, 94, 95]. Unfortunately, this thesis won't be able to propose a solution to this discussion so we will leave this topic as a cliff hanger.

2.3 How to build one model to rule them all?

In this section, we will discuss the principles of constructing a larger gauge structure which eventually breaks down to the SM gauge group at lower energy scales. As an example we will concentrate on $SU(5)$ and E_6 groups since our study in this thesis consists of this particular group structure.

As mentioned before, after we successfully merged the electromagnetic force and weak force into a unified framework, the idea of GUT gained a lot of support. The idea of unified symmetries forms the basis of superstring theories as well. In order to find the correct unification group, which eventually decomposes to $\mathcal{G}_{\rm SM}$, one has to make sure that such decomposition will satisfy all the SM quantum numbers. It has been shown that the only groups that can accommodate SM gauge and quantum-number structure are $SU(n)$ $(n \geq 5)$, $SO(4k + 2)$ $(k \geq 2)$ or E_6 [96, 97].

Starting from the minimum possible extension of the SM, our first option would be rank 4 $SU(5)$ group which already decomposes in to the SM gauge structure with a single intermediate mass scale (IMS), $SU(5) \xrightarrow{\Lambda_{SU(5)}} \mathcal{G}_{\rm SM}$ [98]. The irreducible vector representation of $SU(5)$, $\mathbf{10} \oplus \overline{\mathbf{5}}$, includes all 15 Weyl fermion states in the SM and MSSM. However, as revealed with Eq. (2.2.1), $SU(5)$ does not naturally generate a symmetry to prevent R-parity violating terms from appearing in the Lagrangian. Since this occurs for both SM extensions as well as in SUSY, such a unification structure will require an extra $B - L$ symmetry as described for the supersymmetric case earlier. Additionally, as shown in Fig. 2.2, $SU(5)$ does not yield a naturally unified gauge structure at any energy scale, which is the goal of the GUT approach [97].

The next would be investigating rank 5 groups for GUT, which are $SO(10)$ or $SU(6)$. But $SU(6)$ can not generate the SM quantum numbers naturally. Although it can be achieved via additional symmetries, we will not consider it in here. This leads us to $SO(10)$ as the second minimal extension of the SM group structures [99]. Due to its only few "exotic" fermions and multiple decomposition possibility, $SO(10)$ is one of the widely studied group structures [96, 97, 99, 71, 100, 101, 102]. Two main breaking schemes of $SO(10)$ gauge group are $SO(10) \rightarrow SU(4)_C \otimes SU(2)_L \otimes SU(2)_R$, so called Pati–Salam symmetry and $SO(10) \rightarrow SU(5) \otimes U(1)_\chi$. As one can see from different breaking patterns, $SO(10)$ gauge group can require up to three different IMS. The irreducible vector representations of $SO(10)$ can be written as $\mathbf{16} \oplus \mathbf{10}$ which include all fermionic content of SM within $\mathbf{16} = \mathbf{10}_1 \oplus \overline{\mathbf{5}}_{-3} \oplus \mathbf{1}_5$. Here sub-indices represent the $U(1)$ charge. $\mathbf{10}_1(\mathbf{16})$ includes[5] right-handed up–type quark chiral field and right-& left-handed lepton fields. $\overline{\mathbf{5}}_{-3}(\mathbf{16})$ covers right-handed down–type quark chiral fields and left-handed quark fields. Finally $\mathbf{1}_5(\mathbf{16})$ contains right-handed neutrino singlet. Other irreducible representations of $\mathbf{10}_1(\mathbf{16})$ are $\mathbf{5}_{-2} \oplus \overline{\mathbf{5}}_2$ which contain up- and down-type exotic fermions[6]. The inclusion of the $\mathbf{45}$ generator of $SO(10)$ completes the particle content of $\mathcal{G}_{SM}$, since $\mathbf{45} = \mathbf{24}_0 \oplus \mathbf{10}_{-4} \oplus \overline{\mathbf{10}}_4 \oplus \mathbf{1}_0$, it includes all $\mathbf{24}_0(\mathbf{45})$ generators of $SU(5)$ which are $\hat{B}$, $\hat{G}$, $\hat{W}^\pm$ and left right isospin triplets ($\hat{I}_{L,R}$) which form the generators of $\mathcal{G}_{SM}$ [96, 97, 101, 102]. Although, the decomposition of $SO(10)$ through Pati-Salam structure elegantly solves the proton decay problem, due to naturally occurring $U(1)_{B-L}$, its decomposition through $SU(5) \otimes U(1)_\chi$ still includes all problems of $SU(5)$.

Fig. 2.5 shows some of the breaking schemes that can originate from $SU(5)$, $SO(10)$ and E_6. The colour code represents the breaking of a particular group where blue is used for $SO(10)$, red for $SU(5)$, green for $SU(4)_C$, coral-red for $SU(2)_R$ and brown for $U(1)_{B-L} \otimes U(1)_R$. Some branches show conditions on their occurrence where the ones quote "only $SO(10)$" are not originated from E_6 and do not include $U(1)_\psi$. One important matter to discuss about Fig. 2.5 is that at the end it shows a decomposition into two different gauge structure one with the SM that we showed before and one with $U(1)'$ extended SM (USM). The main difference between these two gauge structure is that USM includes an extra gauge boson called Z' due to the extra $U(1)$ gauge group. In chapter 5 we will discuss the

---

[5] The notation $\mathcal{R}_1(\mathcal{R}_2)$ indicates the origin of the decomposition, in this particular case the irreducible representation $\mathcal{R}_1$ originating from the decomposition of $\mathcal{R}_2$.

[6] In supersymmetry, $\mathbf{5}(\mathbf{10})$ representations also include electroweak Higgs superfields.

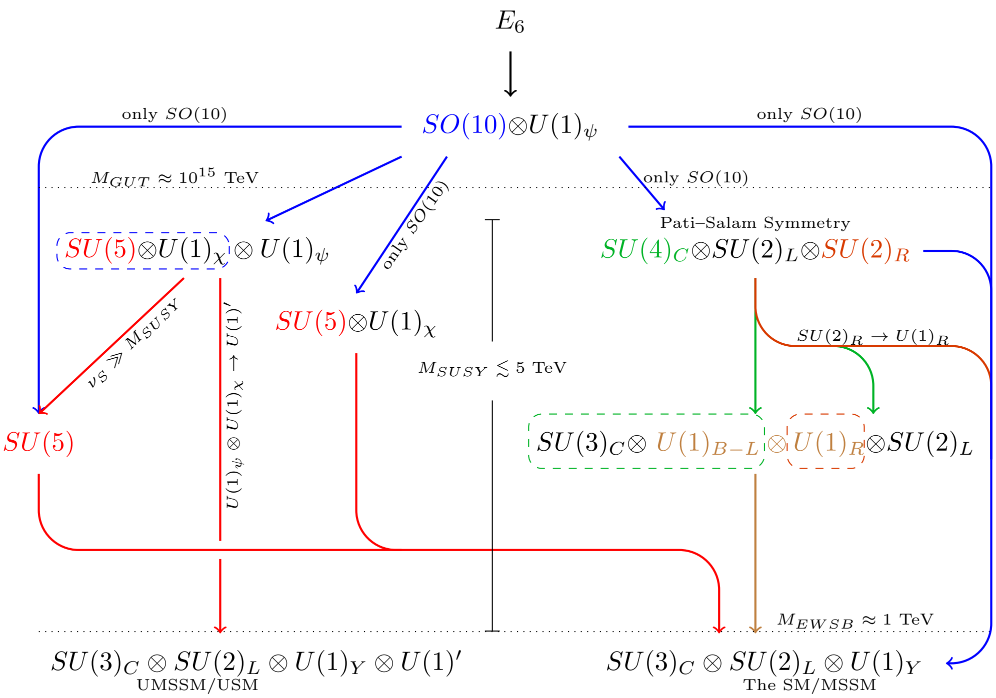

Figure 2.5: *Possible E_6 and $SO(10)$ decomposition schemes to the SM or $\mathcal{G}_{\rm SM} \otimes U(1)'$ gauge group. The colour code is as follows; red used for $SU(5)$ breaking, green for $SU(4)$, coral red for $SU(2)_{\rm R}$ and brown for $U(1)_{B-L} \otimes U(1)_R$. The branch with $v_S \gg M_{SUSY}$ shows that $SU(5) \otimes U(1)'$ can truncate to $SU(5)$ with a heavy vev. Representative energy levels are included for EWSB at 1 TeV, SUSY breaking from 1 to 5 TeV and GUT scale at $\mathcal{O}(10^{15})$ TeV.*

implications of such extention. One justification to have two different gauge groups is that, we are considering a heavy Z' which is out of the reach of the current detector capabilities.

The next in the line to discuss is the E_6 gauge group. Being supersymmetric due to its possible origins from superstring, $E_8 \to E_6 \otimes U(1)$, it is also a desirable group structure for heterotic string theories [97, 103]. In addition to one that has been shown in Fig. 2.5, possible E_6 decomposition channels are

$$E_6 \to \begin{cases} SU(2) \otimes SU(6) \\ SU(3)_C \otimes SU(3)_L \otimes SU(3)_R \\ SO(10) \otimes U(1)_\psi \end{cases} . \qquad (2.3.1)$$

As mentioned before, since first decomposition involves $SU(6)$, it can not satisfy correct quantum numbers for $\mathcal{G}_{SM}$. Due to the exact compactification to $\mathcal{G}_{SM}$, the $[SU(3)]^3$ decomposition is one of the possible GUT scenarios. $[SU(3)]^3 \rightarrow \mathcal{G}_{SM}$ proceeds as:

$$\begin{aligned} E_6 \;&\underset{\Lambda_1}{\longrightarrow}\; SU(3)_C \otimes SU(3)_L \otimes SU(3)_R \\ &\underset{\Lambda_2}{\longrightarrow}\; SU(3)_C \otimes SU(2)_L \otimes SU(2)_R \otimes U(1)_L \otimes U(1)_R \\ &\underset{\Lambda_3}{\longrightarrow}\; SU(3)_C \otimes SU(2)_L \otimes SU(2)_R \otimes U(1)_{B-L} \underset{\Lambda_4}{\longrightarrow} \mathcal{G}_{SM}\ , \end{aligned}$$

where Λ_i indicates different IMS [97]. Requiring four different IMS makes this decomposition structure very complicated to work with, where each breaking scale requires different vev to break a particular symmetry. Thus, in this thesis we will focus on the third breaking scheme shown in Eq. (2.3.1).

Due to the fact that $E_6 \subset SO(10)$, this breaking scheme accommodates all the features of $SO(10)$. Fig. 2.6 shows the **27**-plet vector representation decomposition of supersymmetric E_6. As before the colour code represents breaking of a specific group where blue is for $SO(10)$ and red is for $SU(5)$. All matter fields of the SM (or MSSM) are represented under $\mathbf{16}_1$ with one extra field, namely right-handed neutrino chiral superfield, $\hat{N}$. In addition to the EW Higgs superfields, $\mathbf{10}_{-2}$ also contains two exotic quark supermultiplets. It is important to note that these exotic multiplets can couple with other quark superfields and depending on their mass, this can cause proton decay. There are two ways to prevent such mechanism: one is to make them massive, the second is to introduce Z_2 parity, forbidding some explicit

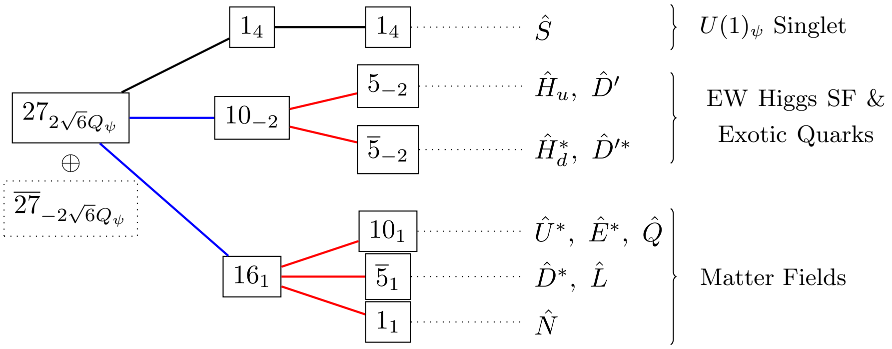

Figure 2.6: *Decomposition of E_6 through* **27***–plet vector representation where subindices represent corresponding normalized $U(1)$ charges. The colours representation is as follows: blue represents $SO(10)$, and red represents $SU(5)$ breaking. The right hand side of the diagram shows the superfields represented by the corresponding number of irreducible representations.From $\mathbf{16}_1 = \mathbf{10}_1 \oplus \overline{\mathbf{5}}_1 \oplus \mathbf{1}_1$ decomposition we get: $\hat{U}^*$, $\hat{D}^*$ the right-handed color triplets, $\hat{E}^*$ the right-handed spin doublet, $\hat{Q}$ two left-handed color triplets, $\hat{L}$ two left-handed spin doublets, and $\hat{N}$ the right-handed singlet field. The $\mathbf{10}_{-2} = \mathbf{5}_{-2} \oplus \overline{\mathbf{5}}_{-2}$ decomposition yields two Higgs doublets and $\mathbf{1}_4$ yields a $U(1)_\psi$ singlet.*

couplings. The first case, requires the vev of the singlet field S to be very heavy. Such scenario will cause a very heavy Z' as well, which is not desirable. Thus, we will decouple them from the model by giving them Z_2-odd charge.

In order to break SUSY in the E_6 gauge group, the singlet field needs to gain vev where we will call this energy scale M_{SUSY} or $M_{Z'}$[7]. After $SO(10)$ breaking, as shown in Fig. 2.5, we end up with two $U(1)$ gauge groups which end up mixing with each other to generate $U(1)'$. All fields are charged under $U(1)'$ which gives a natural symmetry to prevent R-violating terms in the Lagrangian.

The generators of E_6, $SO(10)$ and $SU(5)$ are coming from **78**–plet adjoint representation of E_6, as shown in Fig. 2.7. The main generators, the gauge fields, are shown within the corresponding irreducible representations. The inclusion of $U(1)_\chi$ charge is visible only in the adjoint representation, as shown in $SO(10)$ decomposition. The mixture of $\mathbf{78} \otimes (\mathbf{27} \oplus \overline{\mathbf{27}})$ generates the mixing of $U(1)_\psi \otimes U(1)_\chi$ to induce $U(1)'$.

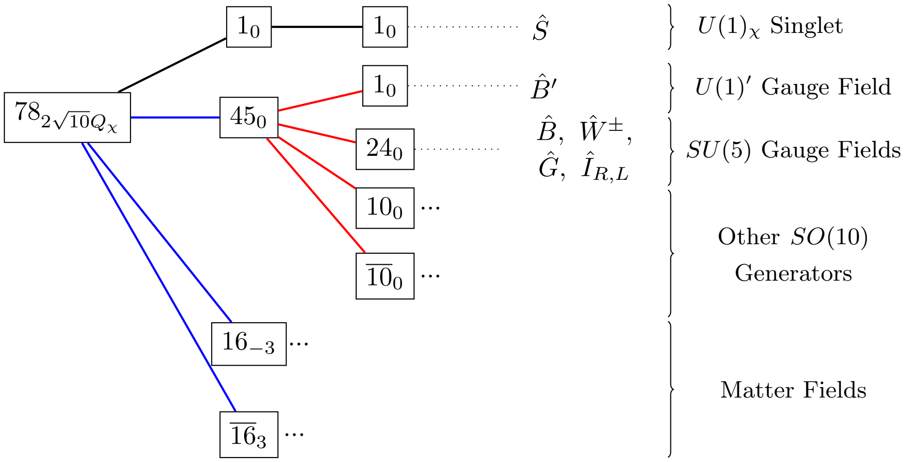

Figure 2.7: *Decomposition of E_6, through* **78**–*plet adjoint representation, for the same configuration as in Fig. 2.6. The* **45** *adjoint representation includes the generators of $SO(10)$ and from the decomposition of $\mathbf{45} = \mathbf{1} \oplus \mathbf{24} \oplus \mathbf{10} \oplus \overline{\mathbf{10}}$ we obtain the generators of $SU(5)$ where $\hat{B}, \hat{W}^\pm$ are $SU(2)$ generators, $\hat{G}$ $SU(3)$ colour triplets, $\hat{I}_{R,L}$ is the isospin generator and $\hat{B}'$ is the generator of $U(1)'$. Two* **16** *yield the other generations of fermionic matter which mix with the $\mathbf{16}(\mathbf{27})$ at lower energy to become the SM fermion spectrum.*

The charges of the superfields under $U(1)'$ are assigned via series of rules. First, for the superpotential to satisfy the Fierz identity all terms in W have to obey $\sum_i Q_{\psi_i} = 0$. However since this depends on the choice of superpotential, we will mention it after

---

[7] The energy scale where Z' gains its mass.

presenting W. Second rule comes from gauge anomaly currents which are induced by first order loop corrections. Fig. 2.8 shows the possible triangle diagrams for anomaly currents, if such diagrams exist for a global symmetry, they violate the Noether current conservation associated with it. This violates the corresponding gauge symmetry and induce unphysical terms. Fig. 2.8 summarizes all these anomaly currents and shows the equations that charges have to satisfy, where n_ψ represents the number of generation, Y_ψ is hypercharge, Q_ψ is $U(1)'$ charge of the corresponding field. T^a is the trace of the generator of the corresponding group and the chiral field. The first line in Fig. 2.8 represents $U(1) - U(1) - U(1)$ gauge anomaly

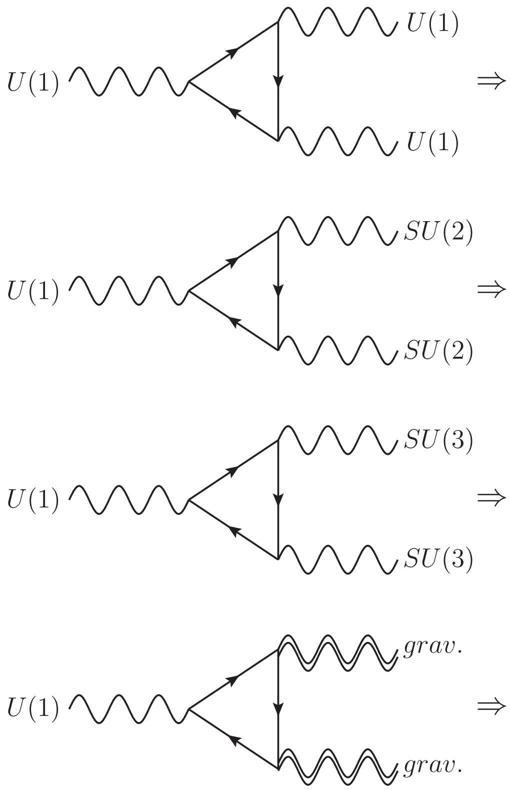

$$\Rightarrow \sum_\psi n_\psi Q_\psi^3 = 0 \ , \ \sum_\psi n_\psi Q_\psi Y_\psi^2 = 0 \ , \ \sum_\psi n_\psi Q_\psi^2 Y_\psi = 0$$

$$\Rightarrow \sum_\psi n_\psi Q_\psi T_\psi^{SU(2)} = 0$$

$$\Rightarrow \sum_\psi n_\psi Q_\psi T_\psi^{SU(3)} = 0$$

$$\Rightarrow \sum_\psi n_\psi Q_\psi = 0$$

Figure 2.8: *$U(1)$ Gauge anomaly currents with respect to each gauge group. First diagram shows $U(1)$ gauge current with either itself or with $U(1)_\mathrm{Y}$. Second diagram shows possible gauge currents occurring between $U(1) - SU(2) - SU(2)$. Third and forth diagram are same as before but with $SU(3)$ and gravity. n_ψ represents the number of generations of the corresponding chiral field, Q_ψ is the $U(1)'$ charge and Y_ψ represents the $U(1)_\mathrm{Y}$ charge of the chiral field. T_ψ^i is the trace of the corresponding chiral field under gauge i. Finally, grav. stands for the gravitational field. Diagrams are created via Jaxodraw package [35].*

currents, where it should satisfy all permutations of possible $U(1)$ currents in the model. Since we have one additional $U(1)$ group it is $U(1)' - U(1)' - U(1)'$, $U(1)' - U(1) - U(1)$ and $U(1)' - U(1)' - U(1)$ respectively. Second (third) line shows it for $U(1)' - SU(2) - SU(2)$

$(U(1)' - SU(3) - SU(3))$ anomaly currents and finally the last line shows the interaction with gravity.

We can derive these rules for the case of E_6-inspired $U(1)'$ extended MSSM (UMSSM) the equations where the first line of Fig. 2.8 reads[8],

$$\begin{aligned} 3(6Q_Q^3 + 3Q_U^3 + 2Q_L^3 + Q_E^3 + Q_N^3) + 2(Q_{H_u}^3 + Q_{H_d}^3) + Q_S^3 &= 0 \ , \\ Q_Q + 8Q_U + 2Q_D + 3Q_L + 6Q_E + 2(Q_{H_u} + Q_{H_d}) &= 0 \ , \\ 3(Q_Q^2 - 2Q_U^2 - Q_D^2 - Q_L^2 + Q_E^2) + Q_{H_u}^2 - Q_{H_d}^2 &= 0 \ , \end{aligned} \tag{2.3.2}$$

respectively. From the second line in Fig. 2.8 we get,

$$3(3Q_Q + Q_L) + Q_{H_u} + Q_{H_d} = 0 \ , \tag{2.3.3}$$

and the third line gives

$$2Q_Q + Q_U + Q_D = 0 \ . \tag{2.3.4}$$

Finally the last line of Fig. 2.8 reads,

$$3(6Q_Q + 3Q_U + 3Q_D + 2Q_L + Q_E + Q_N) + 2(Q_{H_u} + Q_{H_d}) + Q_S = 0 \ . \tag{2.3.5}$$

In order to write a consistent E_6-inspired UMSSM theory, the relations between $U(1)'$ charges, as shown above, have to be satisfied.

---

[8] We are not going to repeat the same exercise for vector-like extentions of MSSM because vector-like multiplets cancel each other's anomalies as shown for the Higgs doublet case in Fig. 2.3.

Chapter 3

MSSM extension with vector-like multiplets

During the past few decades, supersymmetry has gained the status of one of the best theoretically-motivated scenarios for physics beyond the Standard Model (SM). Under specific conditions it can address the hierarchy problem, achieve gauge coupling unification and, when R-parity is conserved, provide natural dark matter candidate(s). However, supersymmetric models of particle physics have been under assault both from collider searches and from direct and indirect dark matter detection experiments. The measured value of the Higgs-boson mass seems to require TeV-scale scalar quarks, a fact further strengthened by the results of direct sparticle searches at the LHC. The null results from dark matter searches have put substantial pressure on (light) neutralino dark matter and, since long ago, have wiped out left-handed sneutrinos as phenomenologically-viable dark matter candidates. Furthermore, in its minimal version, supersymmetry fails to explain neutrino masses. Before, however, abandoning low-scale supersymmetry, one may ask if some of these outstanding issues can be addressed in MSSM, while maintaining the attractive features of the latter and giving rise to novel signals at colliders and elsewhere.

A large variety of MSSM extensions have been studied in the past, including (but not limited to) effective approaches [104, 105], as well as minimal modifications of the MSSM particle content [106, 107] or gauge group structure [108, 109]. In Ref. [110], a less minimal approach was proposed, extending the MSSM particle content by additional pairs of vector-like supermultiplets. The advantage of this choice is that the Higgs-boson mass can be raised while maintaining perturbative gauge coupling unification. The suggested models involve either $\mathbf{5} + \overline{\mathbf{5}}$ complete representations of $SU(5)$ (the 'LND' scenario) or $\mathbf{10} + \overline{\mathbf{10}}$ complete representations of $SU(5)$ (the 'QUE' scenario). Additionally, a 'QDEE' setup which does not contain complete multiplets of $SU(5)$ but still leads to gauge coupling unification has also been envisaged. In this notation scheme, the capital letters denote the nature of the extra supermultiplets relatively to their MSSM counterparts carrying the same charge, colour and $B - L$ quantum numbers.

The dark matter phenomenology of the QUE and QDEE models was already studied in Refs. [111, 112]. In both cases, the dark matter candidate is the lightest neutralino, much like in the MSSM, albeit with some interesting twists, and their phenomenology is rather similar. In this work we will focus on the third scenario, the so-called LND model. Although in this scenario the little hierarchy problem of the MSSM cannot be resolved [110], the LND model presents some other attractive features. As above-mentioned, it can lead to gauge coupling unification, although this necessitates that the vector-like fermions have masses in the 600-1000 GeV window [110]. The field content contains a pair of vector-like neutrino singlets, whose fermionic components can be seen as a sterile neutrino. This could consequently provide explanations for the hints of neutrino oscillations at a higher frequency and for the differences between the neutrinos and antineutrinos measured by the LSND and MiniBooNE experiments [113, 114]. The model moreover features two potential dark matter candidates, the lightest neutralino as well as the lightest singlet-like sneutrino. Furthermore, under a specific configuration, it could give rise to additional contributions to the anomalous magnetic moment of the muon, and large mixings between the new fermions and the third generation SM fermions are allowed and can lead to distinctive signals at the LHC. With this as motivation, we expect the phenomenology of this model to differ from that of the QUE and QDEE models, and in this paper we perform an analysis of the dark matter constraints and collider implications for this model.

This paper is structured as follows. In section 3.1 we present the superfield content of the LND model, its superpotential and soft supersymmetry-breaking Lagrangian, and detail the particle mixings that are relevant for dark matter. In section 3.2 we describe the setup of our parameter space exploration, and provide information on the experimental constraints that are imposed within our scan and the computational tools that have been employed. In section 3.3 we study the dark matter phenomenology of our model, separately for the case of a neutralino and a sneutrino LSP. The consequences of the model at the LHC are explored in section 3.4.

3.1 Theoretical Framework

3.1.1 Field content and Lagrangian

The LND model is an extension of the MSSM inspired by $SU(5)$ Grand Unification (GUT) considerations. We begin with the MSSM chiral superfield content that contains three generations of quark (Q) and lepton (L) weak doublets, as well as three generations of up-type quark ($\bar{U}$), down-type quark ($\bar{D}$) and charged lepton ($\bar{E}$) weak singlets. In our notations, the fermionic and scalar components of these supermultiplets read

$$\begin{aligned} Q \equiv (q_L, \tilde{q}_L) \sim \left(\mathbf{3}, \mathbf{2}, \frac{1}{6}\right) \quad &, \quad L \equiv \left(\ell_L, \tilde{\ell}_L\right) \sim \left(\mathbf{1}, \mathbf{2}, -\frac{1}{2}\right) \ , \\ \bar{U} \equiv \left(u^c_R, \tilde{u}^\dagger_R\right) \sim \left(\bar{\mathbf{3}}, \mathbf{1}, -\frac{2}{3}\right) \quad &, \quad \bar{D} \equiv \left(d^c_R, \tilde{d}^\dagger_R\right) \sim \left(\bar{\mathbf{3}}, \mathbf{1}, \frac{1}{3}\right) \ , \\ \bar{E} \equiv \left(e^c_R, \tilde{e}^\dagger_R\right) \quad &\sim \quad (\mathbf{1}, \mathbf{1}, 1) \ , \end{aligned} \tag{3.1.1}$$

where we also indicate their representation under the $G_{\text{MSSM}} \equiv SU(3)_c \times SU(2)_L \times U(1)_Y$ gauge group. The ^{c} superscript indicates charge conjugation while the $_{L,R}$ subscripts refer to the left- and right-handedness of the fermion.

In the model considered in this work, the MSSM matter sector of Eq. (3.1.1) is extended by vector-like pairs of supermultiplets forming a complete $\mathbf{5} \oplus \bar{\mathbf{5}}$ representation of $SU(5)$. Such a configuration allows to keep a reasonable level of simplicity and to maintain perturbative gauge coupling unification at high energy, with new states appearing at the TeV scale [115, 116, 117, 118]. Decomposing the $\mathbf{5} \oplus \bar{\mathbf{5}}$ GUT supermultiplets in terms of the G_{MSSM} gauge group, the chiral content of the model includes one pair of vector-like leptons $(L_5, \bar{L}_5)$ in the fundamental representation of $SU(2)_L$ and one pair of vector-like down-type quarks $(D_5, \bar{D}_5)$ in the trivial representation of $SU(2)_L$,

$$\begin{aligned} L_5 \equiv (\ell_{5L}, \tilde{\ell}_{5L}) \sim \left(\mathbf{1}, \mathbf{2}, -\frac{1}{2}\right) \ , \qquad & \bar{L}_5 \equiv (\ell^c_{5R}, \tilde{\ell}^\dagger_{5R}) \sim \left(\mathbf{1}, \mathbf{2}, \frac{1}{2}\right) \ , \\ D_5 \equiv (d_{5L}, \tilde{d}_{5L}) \sim \left(\mathbf{3}, \mathbf{1}, -\frac{1}{3}\right) \ , \qquad & \bar{D}_5 \equiv (d^c_{5R}, \tilde{d}^\dagger_{5R}) \sim \left(\bar{\mathbf{3}}, \mathbf{1}, \frac{1}{3}\right) \ . \end{aligned} \tag{3.1.2}$$

As in many GUT-inspired supersymmetric models, we also add a pair of vector-like gauge singlets[1],

$$N \equiv \big(N_L, \tilde{N}_L\big) \sim \Big(\mathbf{1}, \mathbf{1}, 0\Big) \;, \qquad \bar{N} \equiv \big(N_R^c, \tilde{N}_R^\dagger\big) \sim \Big(\mathbf{1}, \mathbf{1}, 0\Big) \;, \tag{3.1.3}$$

that can be mapped to a pair of extra (s)neutrinos and find motivation in dark matter and neutrino physics [119]. With respect to the MSSM, the model features one extra down-type quark and two extra down-type squarks, one extra charged lepton and two additional charged sleptons as well as two more neutrinos along with their accompanying four extra sneutrinos. The Higgs sector is identical to the MSSM one and consists of two weak doublets of Higgs supermultiplets

$$H_d \equiv \big(\tilde{H}_d, h_d\big) \sim \Big(\mathbf{1}, \mathbf{2}, -\frac{1}{2}\Big) \;, \qquad H_u \equiv \big(\tilde{H}_u, h_u\big) \sim \Big(\mathbf{1}, \mathbf{2}, \frac{1}{2}\Big) \;, \tag{3.1.4}$$

that are sufficient to break G_{MSSM} down to $U(1)_{\text{em}}$ and generate supersymmetric masses for all particles. Finally, the model includes three gauge supermultiplets (as the gauge group is the same as in the MSSM) that we denote by

$$\begin{aligned} G \equiv \big(g, \lambda_{\tilde{G}}\big) \sim \Big(\mathbf{8}, \mathbf{1}, 0\Big) \quad &, \quad W \equiv \big(w, \lambda_{\tilde{W}}\big) \sim \Big(\mathbf{1}, \mathbf{3}, 0\Big) \;, \\ B \equiv \big(b, \lambda_{\tilde{B}}\big) \;\; &\sim \;\; \Big(\mathbf{1}, \mathbf{1}, 0\Big) \;, \end{aligned} \tag{3.1.5}$$

for the QCD (G), weak (W) and hypercharge (B) gauge groups.

The supersymmetry-conserving (non-gauge) interactions of the model are driven by the superpotential W_{LND} that is written, assuming R-parity conservation, as [110]

$$\begin{aligned} W_{\text{LND}} = &\;\mu\, H_u \cdot H_d + \mathbf{y_u}\, \bar{U}\, Q \cdot H_u - \mathbf{y_d}\, \bar{D}\, Q \cdot H_d - \mathbf{y_e}\, \bar{E}\, L \cdot H_d \\ &+ \mu_D\, D_5\, \bar{D}_5 + \mu_L\, L_5 \cdot \bar{L}_5 + \mu_N\, N\, \bar{N} + k_N\, \bar{N}\, L_5 \cdot H_u - h_N\, N\, \bar{L}_5 \cdot H_d \\ &- \varepsilon_{\mathbf{D}}\, \bar{D}_5\, Q \cdot H_d - \varepsilon_{\mathbf{E}}\, \bar{E}\, L_5 \cdot H_d + \varepsilon_{\mathbf{N}}\, \bar{N}\, L \cdot H_u + \kappa_{\mathbf{D}}\, D_5\, \bar{D} + \kappa_{\mathbf{L}}\, L \cdot \bar{L}_5 \;, \end{aligned} \tag{3.1.6}$$

where all flavour indices have been explicitly omitted for simplicity. The first terms correspond to the MSSM superpotential in which μ denotes the MSSM off-diagonal Higgs(ino) mass contribution and $\mathbf{y_u}$, $\mathbf{y_d}$ and $\mathbf{y_e}$ stand for the up-type quark, down-type quark and charged lepton Yukawa matrices in flavour space. Moreover, μ_D, μ_L and μ_N are explicit masses for the non-MSSM fields and h_N and k_N stand for the Yukawa interactions of the non-coloured vector-like superfields. The terms of the last line of the superpotential include

---

[1] This choice is consistent with minimal representations which do not violate lepton number.

new Yukawa couplings driving the mixing of the Standard Model fermions with their vector-like counterparts (the $\varepsilon_{\mathbf{D}}$, $\varepsilon_{\mathbf{E}}$ and $\varepsilon_{\mathbf{N}}$ vectors in flavour space) as well as direct mass mixing terms (the $\kappa_{\mathbf{D}}$ and $\kappa_{\mathbf{L}}$ vectors in flavour space). While these are strongly constrained by flavour data, such mixings have to be non-vanishing to prevent the existence of unwanted cosmologically stable relics. For consistency with both flavour and cosmology constraints, in the following we will assume the existence of a small mixing with the third generation of Standard Model fermions only.

As in any realistic supersymmetric model, supersymmetry has to be softly broken. The Lagrangian thus includes gaugino and scalar mass terms, as well as bilinear and trilinear scalar interactions whose form is obtained from the superpotential. The gaugino mass contributions read

$$\mathcal{L}_{\text{soft}}^{(\lambda)} = -\frac{1}{2}\Big(M_1\lambda_{\tilde{B}}\cdot\lambda_{\tilde{B}} + M_2\lambda_{\tilde{W}}\cdot\lambda_{\tilde{W}} + M_3\lambda_{\tilde{g}}\cdot\lambda_{\tilde{g}} + \text{h.c.}\Big)\ , \tag{3.1.7}$$

where the M_1, M_2 and M_3 parameters represent the bino, wino and gluino masses, and the scalar mass Lagrangian is given by

$$\begin{aligned}\mathcal{L}_{\text{soft}}^{(\phi)} = \quad & -m^2_{H_d}h_d^\dagger h_d - m^2_{H_u}h_u^\dagger h_u - \mathbf{m^2_{\tilde{Q}}}\,\tilde{q}_L^\dagger\,\tilde{q}_L - \mathbf{m^2_{\tilde{d}}}\,\tilde{d}_R^\dagger\,\tilde{d}_R - \mathbf{m^2_{\tilde{u}}}\,\tilde{u}_R^\dagger\,\tilde{u}_R - \mathbf{m^2_{\tilde{L}}}\,\tilde{\ell}_L^\dagger\,\tilde{\ell}_L \\ & -\mathbf{m^2_{\tilde{e}}}\,\tilde{e}_R^\dagger\,\tilde{e}_R - m^2_{\tilde{L}_5}\,\tilde{\ell}_{5L}^\dagger\,\tilde{\ell}_{5L}\ - m^2_{\tilde{\tilde{L}}_5}\,\tilde{\ell}_{5R}^\dagger\,\tilde{\ell}_{5R} - m^2_{\tilde{D}_5}\,\tilde{d}_{5R}^\dagger\,\tilde{d}_{5R} - m^2_{\tilde{\tilde{D}}_5}\,\tilde{d}_{5L}^\dagger\,\tilde{d}_{5L} \\ & \qquad -m^2_{\tilde{N}}\,\tilde{N}_L^\dagger\,\tilde{N}_L - m^2_{\tilde{\tilde{N}}}\,\tilde{N}_R^\dagger\,\tilde{N}_R - \Big[\mathbf{m^2_{\tilde{L}_5,\tilde{L}}}\,\tilde{\ell}_L^\dagger\,\tilde{\ell}_{5L} + \text{h.c.}\Big] \\ & \qquad\qquad -\Big[\mathbf{m^2_{\tilde{D}_5,\tilde{D}}}\,\tilde{d}_R^\dagger\,\tilde{d}_{5R} + \text{h.c.}\Big]\ ,\end{aligned} \tag{3.1.8}$$

where m_i^2 represent the various mass parameters, in flavour space. Moreover, the superpotential-induced soft terms are written as

$$\begin{aligned}\mathcal{L}_{\text{soft}}^{(W)} = \quad & \Big[-b\,h_u\cdot h_d\ + \mathbf{T}_d\,\tilde{d}^\dagger\,\tilde{q}\cdot h_d\ + \mathbf{T}_e\,\tilde{e}^\dagger\,\tilde{l}\cdot h_d\ - \mathbf{T}_u\,\tilde{u}^\dagger\,\tilde{d}\cdot h_u\ - b_D\,\tilde{d}_{5R}^\dagger\,\tilde{d}_{5L} \\ & -b_L\,\tilde{\ell}_{5R}^\dagger\cdot\tilde{\ell}_{5L}\ - b_N\,\tilde{N}_R^\dagger\,\tilde{N}_L\ - a_{k_N}\,\tilde{N}_R^\dagger\,\tilde{\ell}_{5L}\cdot h_u\ + a_{h_N}\,\tilde{N}_L\,\tilde{\ell}_{5R}^\dagger\cdot h_d\ + \mathbf{a}_{\varepsilon_{\mathbf{D}}}\,\tilde{d}_{5R}^\dagger\,\tilde{q}_L\cdot h_d \\ & +\mathbf{a}_{\varepsilon_{\mathbf{E}}}\,\tilde{e}_R^\dagger\,\tilde{\ell}_{5L}\cdot h_d\ - \mathbf{a}_{\varepsilon_{\mathbf{N}}}\,\tilde{N}_R^\dagger\,\tilde{\ell}_L\cdot h_u\ - \mathbf{b}_{\kappa_{\mathbf{D}}}\,\tilde{d}_R^\dagger\tilde{d}_{5L}\ - \mathbf{b}_{\kappa_{\mathbf{L}}}\,\tilde{\ell}_{5R}^\dagger\cdot\tilde{\ell}_L + \text{h.c.}\Big]\ ,\end{aligned} \tag{3.1.9}$$

where the first four terms are the usual MSSM soft terms, b denotes the bilinear Higgs interaction strength and $\mathbf{T_i}$ the various squark-Higgs trilinear interactions in flavour space. The a_{k_N} and a_{h_N} parameters represent the trilinear couplings of the vector-like sneutrinos and sleptons to the Higgs fields, whilst the $\mathbf{a}_{\varepsilon_\mathbf{i}}$ and $\mathbf{b}_{\kappa_\mathbf{i}}$ parameters are three-dimensional vectors describing the mixing of the vector-like and MSSM scalars. Similarly to their superpotential term counterparts, the latter will be assumed vanishing for the first two generations, and small for the third generation.

Once electroweak symmetry is broken, all particles with the same electric charge and lying in the same colour and spin representations mix. The neutralino sector is identical to the MSSM one, consisting of four Majorana fermions χ_i^0, $i = 1, \ldots, 4$, which are linear combinations of the four neutral gaugino and higgsino gauge eigenstates. The lightest neutralino, χ_1^0 is the first dark matter candidate we shall consider. The model also contains five physical neutrinos which are admixtures of the usual MSSM neutrinos with the fermionic neutral components of L_5 and $\bar{L}_5$ as well as with the fermionic components of the gauge singlet chiral superfields N and $\bar{N}$. The two heaviest exotic states are not stable, since they can decay through the Yukawa-like $\varepsilon_{\mathbf{E}}$ and $\varepsilon_{\mathbf{N}}$ terms in Eq. (3.1.6), and thus they cannot be potential dark matter candidates. The second dark matter candidate considered is in the sneutrino sector, which in the LND model consists of seven physical scalars. The sneutrino mixing is described by the symmetric mass matrix $M^2_{\tilde{\nu}}$. In the $(\tilde{\nu}_{5L}, \tilde{N}_L, \tilde{\nu}_e, \tilde{\nu}_\mu, \tilde{\nu}_\tau, \tilde{\nu}^\dagger_{5R}, \tilde{N}^\dagger_R)$ basis, matrix elements in the 7×7 symmetric matrix include soft terms, supersymmetric contributions as well as D-term contributions and are given by

$$
\begin{aligned}
\left(M^2_{\tilde{\nu}}\right)_{11} &= \frac{1}{8}\left[\frac{e^2}{s^2_w}+\frac{e^2}{c^2_w}\right]\left[v_d^2-v_u^2\right]+\mu_L^2+m^2_{\tilde{L}_5}+\frac{1}{2}k_N^2 v_u^2 \ , \\
\left(M^2_{\tilde{\nu}}\right)_{12} &= \frac{1}{\sqrt{2}}\left[h_N\mu_L v_d+k_N\mu_N v_u\right] \ , \\
\left(M^2_{\tilde{\nu}}\right)_{1(2+f)} &= \mu_L\left(\kappa_{\mathbf{L}}\right)_f+\frac{1}{2}k_N v_u^2\left(\varepsilon_{\mathbf{N}}\right)_f+\left(\mathbf{m^2_{\tilde{L}_5,L}}\right)_f \ , \\
\left(M^2_{\tilde{\nu}}\right)_{16} &= b_L \ , \\
\left(M^2_{\tilde{\nu}}\right)_{17} &= \frac{1}{\sqrt{2}}\left[a_{k_N}v_u-\mu k_N v_d\right] \ , \\
\left(M^2_{\tilde{\nu}}\right)_{22} &= \mu_N^2+m^2_{\tilde{N}}+\frac{1}{2}h_N^2 v_d^2 \ , \\
\left(M^2_{\tilde{\nu}}\right)_{2(2+f)} &= \mu_N v_u\left(\varepsilon_{\mathbf{N}}\right)_f+h_N v_d\left(\kappa_{\mathbf{L}}\right)_f\Big] \ , \\
\left(M^2_{\tilde{\nu}}\right)_{26} &= \frac{1}{\sqrt{2}}\left[a_{h_N}v_d-\mu h_N v_u\right] \ , \\
\left(M^2_{\tilde{\nu}}\right)_{27} &= b_N \ , \\
\left(M^2_{\tilde{\nu}}\right)_{(2+f)(2+f')} &= \frac{1}{8}\left[\frac{e^2}{s^2_w}+\frac{e^2}{c^2_w}\right]\left[v_d^2-v_u^2\right]\delta_{ff'}+\left(\mathbf{m^2_{\tilde{L}}}\right)_{ff'}+\frac{1}{2}v_u^2\left(\varepsilon_{\mathbf{N}}\right)_f\left(\varepsilon_{\mathbf{N}}\right)_{f'}+\left(\kappa_{\mathbf{L}}\right)_f\left(\kappa_{\mathbf{L}}\right)_{f'} \ , \\
\left(M^2_{\tilde{\nu}}\right)_{(2+f)7} &= \frac{1}{\sqrt{2}}\left[v_u\left(\mathbf{a}_{\varepsilon_{\mathbf{N}}}\right)_f-\mu v_d\left(\varepsilon_{\mathbf{N}}\right)_f\right] \ , \\
\left(M^2_{\tilde{\nu}}\right)_{66} &= \frac{1}{8}\left[\frac{e^2}{s^2_w}+\frac{e^2}{c^2_w}\right]\left[v_u^2-v_d^2\right]+\mu_L^2+m^2_{\tilde{\bar{L}}_5}+\frac{1}{2}h_N^2 v_d^2+\sum_{f=1}^{3}\left(\kappa_{\mathbf{L}}\right)_f^2 \ , \\
\left(M^2_{\tilde{\nu}}\right)_{67} &= \frac{1}{\sqrt{2}}\left[h_N v_d\mu_N+k_N v_u\mu_L+v_u\sum_{f=1}^{3}\left(\kappa_{\mathbf{L}}\right)_f\left(\varepsilon_{\mathbf{N}}\right)_f\right] \ , \\
\left(M^2_{\tilde{\nu}}\right)_{77} &= \mu_N^2+m^2_{\tilde{\bar{N}}}+\frac{1}{2}k_N^2 v_u^2+\frac{1}{2}v_u\sum_{f=1}^{3}\left(\varepsilon_{\mathbf{N}}\right)_f^2 \ ,
\end{aligned}
$$

where $f, f' = 1$, 2 and 3 are generation indices, $\left(M^2_{\tilde{\nu}}\right)_{ij} = \left(M^2_{\tilde{\nu}}\right)_{ji}$ and all other elements vanish.

3.2 Parameter Space Exploration

3.2.1 Parameter space

As indicated in the Lagrangian introduced in the previous section, the LND model parameter space is defined from a large set of beyond the SM free parameters. Assuming unification conditions and relying on the minimisation of the scalar potential, this list can be further reduced. In the following, we define the range of value allowed for each parameter relevant for our study. We have verified that wider ranges did not yield any new phenomenology. We fixed the values of all input parameters at the supersymmetry-breaking scale, with the exception of the common MSSM sfermion and Higgs mass M_0 and their common soft trilinear coupling A_0 that are defined at the GUT-scale. This particular choice allows us to analyse a large set of different scalar spectra, concentrating in particular on scenarios with light electroweak scalars and heavier strongly-interacting ones (that are only marginally relevant for our dark matter study). For the supersymmetry-breaking scale we have taken the geometric mean of the masses of the lightest ($M_{\tilde{u}_1}$) and heaviest ($M_{\tilde{u}_6}$) up-type squarks, $M_{\text{SUSY}} \sim \sqrt{M_{\tilde{u}_1} M_{\tilde{u}_6}}$, and restricted it to be smaller than 5 TeV.

We start with the superpotential parameters appearing in Eq. (3.1.6). While the SM first and second generation Yukawa couplings are neglected, we fix the third generation ones to the value given in the Particle Data Group Review [120]. All other parameters are left free and will be scanned over, with the exception of the off-diagonal Higgs mixing parameter μ whose absolute value is fixed from the scalar potential minimisation conditions. The supersymmetric masses of the three pairs of vector-like supermultiplets μ_D, μ_L and μ_N are taken as varying in the GeV - TeV range,

$$\mu_D \in [1, 8] \text{ TeV} , \qquad \mu_L \in [0, 3] \text{ TeV} \qquad \text{and} \qquad \mu_N \in [0, 5] \text{ TeV} ,$$

whilst the vector-like Yukawa couplings are taken of $\mathcal{O}(1)$,

$$k_N \in [-1, 1] \qquad \text{and} \qquad h_N \in [-1, 1] \ .$$

As previously stated, we forbid any mixing between the vector-like sector and the first two SM generations, so that the supersymmetric mass mixing parameters and ε Yukawa couplings solely involve the third generation,

$$\kappa_{\mathbf{D}} = \begin{pmatrix} 0 \\ 0 \\ \kappa_D \end{pmatrix} , \ \kappa_{\mathbf{L}} = \begin{pmatrix} 0 \\ 0 \\ \kappa_L \end{pmatrix} , \ \varepsilon_{\mathbf{D}} = \begin{pmatrix} 0 \\ 0 \\ \varepsilon_D \end{pmatrix} , \ \varepsilon_{\mathbf{E}} = \begin{pmatrix} 0 \\ 0 \\ \varepsilon_E \end{pmatrix} \ \text{and} \ \ \varepsilon_{\mathbf{N}} = \begin{pmatrix} 0 \\ 0 \\ \varepsilon_N \end{pmatrix} ,$$

with

$$\kappa_D \in [-10^{-6}, 10^{-6}] \text{ TeV} \ , \ \kappa_L \in [-1, 1] \text{ TeV} \ ,$$
$$\varepsilon_N \in [-0.1, 0.1] \ , \ \varepsilon_E \in [-1, 1] \text{ and } \ \varepsilon_D \in [-5, 5] \times 10^{-3} \ .$$

The parameters in the down-type quark sector are restricted to be small by flavour constraints. The quoted intervals have been determined after scanning over larger ranges and restricting the parameters responsible for flavour-changing effects in the down-type quark and charged lepton sectors according to the constraints in Table 3.2. The soft gaugino mass terms of Eq. (3.1.7) are allowed to vary independently in the GeV - multi-TeV range,

$$M_1 \in [0, 2] \text{ TeV} \ , \qquad M_2 \in [0, 3] \text{ TeV} \qquad \text{and} \qquad M_3 \in [0, 4] \text{ TeV} \ ,$$

whilst the MSSM squark and Higgs mass parameters appearing in Eq. (3.1.1) are imposed to unify to a common M_0 value,

$$M_0 \in [0, 5] \text{ TeV} \ .$$

The extra squark mass and mixing parameters are chosen to vary independently,

$$m_{\tilde{D}_5} \in [0, 5] \text{ TeV} \ , \quad m_{\tilde{\bar{D}}_5} \in [0, 5] \text{ TeV} \ , \quad \mathbf{m^2_{\tilde{D}_5, \tilde{D}}} = \begin{pmatrix} 0 \\ 0 \\ m^2_{\tilde{D}_5, \tilde{D}} \end{pmatrix}$$
$$\text{with} \quad m^2_{\tilde{D}_5, \tilde{D}} \in [-0.1, 0.1] \text{ TeV}^2 \ .$$

These new states introduce some of the specific features of the LND model, but our dark matter analysis and collider signals are largely independent of this choice. By contrast, the mass parameters of the extra sneutrinos and sleptons are also specific parameters of the model, but very relevant for what concerns cosmology. We keep all of them free and allow them to vary independently, again in the multi-TeV range,

$$m_{\tilde{N}} \in [0, 6] \text{ TeV} \ , \qquad m_{\tilde{\bar{N}}} \in [0, 6] \text{ TeV} \ , \qquad m_{\tilde{L}_5} \in [0, 1] \text{ TeV} \qquad \text{and} \qquad m_{\tilde{\bar{L}}_5} \in [0, 1] \text{ TeV} \ ,$$

and we fix the mass mixing between the MSSM and the vector-like sleptons as

$$\mathbf{m}^{\mathbf{2}}_{\mathbf{\tilde{L}_5,\tilde{L}}} = \begin{pmatrix} 0 \\ 0 \\ m^2_{\tilde{L}_5,\tilde{L}} \end{pmatrix} \quad \text{with} \quad m^2_{\tilde{L}_5,\tilde{L}} \in [-0.1, 0.1] \text{ TeV}^2 \ .$$

The rest of the soft parameters involving the MSSM sfermions and Higgs bosons are assumed to unify at the GUT scale, so that all squark trilinear couplings to the Higgs sector are set to a common A_0 value multiplied by the relevant SM fermion Yukawa coupling. In addition, all trilinear scalar couplings involving two vector-like sfermions are taken vanishing. Moreover, all bilinear terms are fixed to a common B_0 value, with the exception of the Higgs mixing parameter b whose value is driven by the scalar potential minimisation. We thus choose

$$B_0 \in [-5, 5] \text{ TeV} \ , \qquad A_0 \in [-2, 2] \qquad \text{and} \qquad a_{k_N} = a_{h_N} = 0 \ .$$

As for all other interactions involving the mixing of a vector-like and an MSSM particle, we enforce the soft ones to vanish for the first two generations,

$$\mathbf{a}_{\varepsilon_\mathbf{D}} = \begin{pmatrix} 0 \\ 0 \\ a_{\varepsilon_D} \end{pmatrix} \ , \qquad \mathbf{a}_{\varepsilon_\mathbf{E}} = \begin{pmatrix} 0 \\ 0 \\ a_{\varepsilon_E} \end{pmatrix} \qquad \text{and} \qquad \mathbf{a}_{\varepsilon_\mathbf{N}} = \begin{pmatrix} 0 \\ 0 \\ a_{\varepsilon_N} \end{pmatrix} \ ,$$

and, for simplicity, fix the input values of the three remaining free parameters to zero,

$$a_{\varepsilon_D} = a_{\varepsilon_E} = a_{\varepsilon_N} = 0 \ .$$

Since the SM Higgs-boson mass is taken equal to its measured value, the Higgs sector is fully defined from the conditions stemming from the minimisation of the scalar potential, once one extra parameter is fixed, as all parameters contributing at the one-loop order and beyond are already defined above. The ratio of the vacuum expectation values of the neutral components of the two Higgs doublets, $\tan\beta$, is allowed to vary in the following range,

$$\tan\beta \in [1, 60] \ .$$

The parameter space is now defined by the 25 new physics parameters and one sign is listed in Table 3.1, where we summarise the free parameters and the range over they are scanned.

Table 3.1: *Range of the free parameters of the model scans. The SM parameters are fixed to the values reported in the Particle Data Group Review [120] and all non-listed parameters are fixed to zero.*

Parameter	Scanned range	Parameter	Scanned range
μ_D	$[1,8]$ TeV	M_1	$[0,2]$ TeV
μ_N	$[0,5]$ TeV	M_2	$[0,3]$ TeV
μ_L	$[0,3]$ TeV	M_3	$[0,4]$ TeV
$\mathrm{sgn}(\mu)$	± 1	$m_{\tilde{L}_5}$, $m_{\bar{\tilde{L}}_5}$	$[0,1]$ TeV
h_N, k_N	$[-1,1]$	$m_{\tilde{D}_5}$, $m_{\bar{\tilde{D}}_5}$	$[0,5]$ TeV
κ_L	$[-1,1]$ TeV	$m_{\tilde{N}}$, $m_{\bar{\tilde{N}}}$	$[0,6]$ TeV
κ_D	$[-1,1]\times 10^{-6}$ TeV	$m^2_{\tilde{L}_5,\tilde{L}}$, $m^2_{\tilde{D}_5,\tilde{D}}$	$[-0.1,0.1]$ TeV^2
ε_N	$[-0.1,0.1]$	A_0	$[-2,2]$ TeV
ε_E	$[-1,1]$	B_0	$[-5,5]$ TeV
ε_D	$[-5,5]\times 10^{-3}$	$\tan\beta$	$[1,60]$
M_0	$[0,5]$ TeV		

3.2.2 Analysis setup and experimental constraints

In order to explore the parameter space defined in section 3.2.1, we have implemented the LND model in the SARAH 4.12.2 package [136], which we have used to generate the corresponding SPHENO (version 4.0.3) output [137]. With this last code, we derive the value of the model parameters at the electroweak scale through their renormalisation group running from the input scale, and extract the particle spectrum. In order to assess the phenomenological viability of the different scenarios probed during the scan, we enforce the compatibility with several flavour, collider and low-energy physics observables calculated by SPHENO and summarised in Table 3.2. The scenarios considered in our study must satisfy rare B-decay constraints [121, 123, 122],

$$\mathrm{BR}(B^0 \to X_s\gamma) \in [2.99, 3.87]\times 10^{-4} \quad , \quad \mathrm{BR}(B_s^0 \to \mu^+\mu^-) \in [1.1, 6.4]\times 10^{-9}$$
$$\text{and} \quad \frac{\mathrm{BR}(B \to \tau\nu_\tau)}{\mathrm{BR}_{\mathrm{SM}}(B \to \tau\nu_\tau)} \in [0.15, 2.41] \ ,$$

rare tau-decay constraints [124, 125, 126],

$$\mathrm{BR}(\tau \to e\gamma) \in [0, 3.3]\times 10^{-8} \ , \ \mathrm{BR}(\tau \to \mu\gamma) \in [0, 4.4]\times 10^{-8} \ , \ \mathrm{BR}(\tau \to e\pi) \in [0, 8.0]\times 10^{-8} \ ,$$
$$\mathrm{BR}(\tau \to \mu\pi) \in [0, 1.1]\times 10^{-7} \ , \qquad \mathrm{BR}(\tau \to 3\mu) \in [0, 2.1]\times 10^{-8} \ ,$$

Table 3.2: *Set of low-energy and flavour physics constraints imposed within our LND model scanning procedure (upper) and mass bounds imposed on the Higgs boson and new physics states (lower).*

Observable	Constraint	Observable	Constraint
$\mathrm{BR}(B^0 \to X_s\gamma)$	$[2.99, 3.87] \times 10^{-4}$ [121]	$\frac{\mathrm{BR}(B\to\tau\nu_\tau)}{\mathrm{BR}_{SM}(B\to\tau\nu_\tau)}$	$[0.15, 2.41]$ [122]
$\mathrm{BR}(B_s^0 \to \mu^+\mu^-)$	$[1.1, 6.4] \times 10^{-9}$ [123]	$\mathrm{BR}(\tau \to e\gamma)$	$[0, 3.3] \times 10^{-8}$ [124]
$\mathrm{BR}(\tau \to \mu\gamma)$	$[0, 4.4] \times 10^{-8}$ [124]	$\mathrm{BR}(\tau \to e\pi)$	$[0, 8.0] \times 10^{-8}$ [125]
$\mathrm{BR}(\tau \to \mu\pi)$	$[0, 1.1] \times 10^{-7}$ [125]	$\mathrm{BR}(\tau \to 3\mu)$	$[0, 2.1] \times 10^{-8}$ [126]
ΔM_s	$[10.2, 26.4]\ \mathrm{ps}^{-1}$ [127]	ΔM_d	$[0.29, 0.76]\ \mathrm{ps}^{-1}$ [127]
$\mathrm{BR}(Z \to e\mu)$	$[0, 7.5] \times 10^{-7}]$ [128]	$\mathrm{BR}(h \to e\mu)$	$[0, 3.5] \times 10^{-4}$ [129]
EWPO tests	$\leq 2\sigma$ [130, 131, 132]	$\chi^2(\hat{\mu})$	≤ 111.6

Mass	Constraint	Mass	Constraint
$M_{\chi_2^0}$	> 62.4 GeV [120]	$M_{\chi_1^\pm}$	> 103.5 GeV [120]
$M_{\chi_3^0}$	> 99.9 GeV [120]	$M_{\tilde{e}}$	> 107 GeV [120]
$M_{\chi_4^0}$	> 116 GeV [120]	$M_{\tilde{\mu}}$	> 94 GeV [120]
$M_{\tilde{g}}$	> 1.75 TeV [133]	$M_{\tilde{\tau}}$	> 81 GeV [120]
$M_{\tilde{t}}$	> 750 GeV [134]	$M_{\tau'}$	> 103 GeV [135]
M_h	125.09 ± 3 GeV [27]		

B-meson oscillation constraints [127],

$$\Delta M_s \in [10.2, 26.4]\ \mathrm{ps}^{-1}\ , \qquad \Delta M_d \in [0.29, 0.76]\ \mathrm{ps}^{-1}\ ,$$

and flavour-violating Z-boson [128] and Higgs-boson [129] decay bounds,

$$\mathrm{BR}(Z \to e\mu) \in [0, 7.5] \times 10^{-7} \qquad \text{and} \qquad \mathrm{BR}(h \to e\mu) \in [0, 3.5] \times 10^{-4}\ .$$

Moreover, we impose the compatibility with electroweak precision observables (EWPO) at the 2σ level [130], using a correlation function based on the oblique parameters [131, 132]. Thanks to the interface of SPheno with HiggsBounds version 4.3.1 [138] and HiggsSignals version 1.4.0 [139], we verify the consistency of the Higgs sector with experimental measurements of LHC Run 1. In practice, we check that the Higgs-boson mass, gluon and vector-boson fusion production cross sections (computed with the SusHi program version 1.5 [140]) and signal strengths agree with data up to deviations corresponding to a global $\chi^2(\hat{\mu})$ quantity of at most 111.6, which corresponds to a 2σ level of agreement for the number of considered observables.

Additionally, we constrain superpartners masses (of the MSSM sector) from direct search bounds [120, 133, 134]. We impose that the gluino mass ($M_{\tilde{g}}$), the neutralino and chargino masses ($M_{\tilde{\chi}_i^0}$ and $M_{\tilde{\chi}_i^\pm}$), the slepton masses ($M_{\tilde{e}}$, $M_{\tilde{\mu}}$ and $M_{\tilde{\tau}}$) and the stop mass ($M_{\tilde{t}}$) satisfy

$$\begin{gathered} M_{\tilde{g}} > 1.75 \text{ TeV} \ , \ M_{\tilde{\chi}_2^0} > 62.4 \text{ GeV} \ , \ M_{\tilde{\chi}_3^0} > 99.9 \text{ GeV} \ , \ M_{\tilde{\chi}_4^0} > 116 \text{ GeV} \ , \\ M_{\tilde{\chi}_1^\pm} > 103.5 \text{ GeV} \ , M_{\tilde{e}} > 107 \text{ GeV} \ , \ M_{\tilde{\mu}} > 94 \text{ GeV} \ , \ M_{\tilde{\tau}} > 81 \text{ GeV} \ , \ M_{\tilde{t}} > 750 \text{ GeV} \ , \end{gathered}$$

and enforce the vector-like lepton mass $M_{\tau'}$ to obey the LEP bound [135],

$$M_{\tau'} > 103 \text{ GeV}.$$

We now proceed to our analysis. We perform a scan of the parameter space by relying on the Metropolis-Hastings sampling method [141] in which the model free parameters vary as in Table 3.1 and are restricted by the constraints of Table 3.2, with the additional requirement that the LSP has to be neutral. For each point, we perform the dark matter analysis with MICROMEGAS version 4.3.1 [142], which allows us to calculate all DM observables used in the analysis of section 3.3 from the LND CALCHEP [143] model file generated by SARAH. In section 3.4, we perform a collider analysis of a few benchmark scenarios representative of the different spectra favoured by cosmology, by relying on the MG5_AMC@NLO [144] platform and an LND UFO model file [145] generated by SARAH. The interfacing of the various programmes and our numerical analysis have been performed with a modified version of the PYSLHA package version 3.1.1 [146].

3.3 Dark matter phenomenology

Having presented our model, the leading experimental constraints that we subject it to, and the methodology that we use in order to explore and assess the viability of the parameter space, we now proceed to present the results of our dark matter analysis. We divide the discussion into two parts, depending on the nature of the dark matter candidate (neutralino or sneutrino).

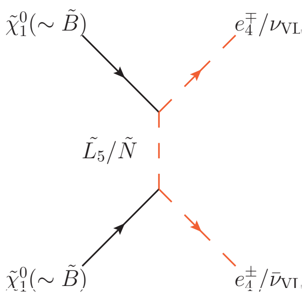

Figure 3.1: *Representative dark matter annihilation diagram into vector-like fermions.*

3.3.1 Neutralino dark matter

The lightest neutralino has, since long, been the most celebrated dark matter candidate of the MSSM. However, in the MSSM, barring co-annihilations and funnels, the possibilities for neutralino dark matter with an $\mathcal{O}(10^2)$ GeV mass are now severely constrained. In particular, almost pure higgsinos and winos tend to be under-abundant, unless their mass lies above about 1 TeV, as the cosmologically-attractive possibility of a pure higgsino with a mass below the W-boson mass M_W is excluded from chargino searches at LEP [147, 148, 149, 150]. Binos, on the other hand, tend to be overabundant by a few factors, unless either they can annihilate through the t-channel exchange of a sufficiently light sfermion into SM fermions, or they contain a substantial higgsino or wino fraction. The former case is disfavoured by sfermion searches at the LHC, whereas direct detection experiments [151] strongly constrain the mixed bino-higgsino scenario. The mixed bino-wino case is less constrained and constitutes one of the remaining possibilities for sub-TeV natural neutralino dark matter[2]. We refer to Ref. [155] for a recent detailed account of existing constraints.

In the context of MSSM extensions with vector-like fermions, however, the possibility of an almost pure bino dark matter with a mass of up to a few hundreds of GeV can be viable [111, 112]. In such scenarios, binos can annihilate into vector-like fermions through the t-channel exchange of the corresponding sfermion as illustrated in Fig. 3.1. In the QUE and QDEE models, these annihilation channels can constitute an efficient-enough mechanism for depleting binos in the early Universe due to the interplay of two effects. First, binos can annihilate into vector-like weak-singlet leptons E carrying hypercharge $Y_E = 1$. Since the sfermion-mediated annihilation cross section of binos into fermions scales as Y^4, this annihilation channel is particularly enhanced. Second, although $SU(2)_L$ singlet fermions

---

[2] Natural in the sense of how rapidly the predicted dark matter abundance changes with small variations of the model parameters [152, 153, 154].

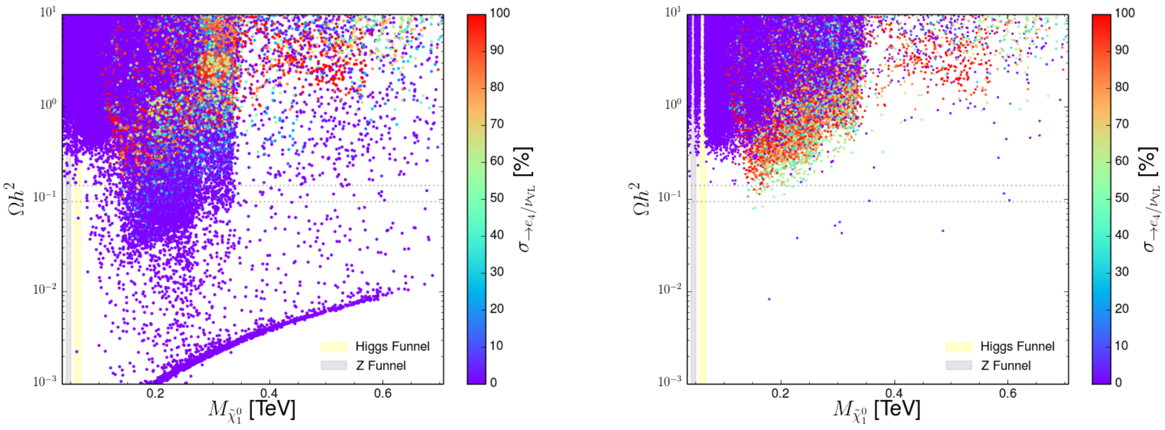

Figure 3.2: *Relic abundance of neutralino dark matter in the LND model as a function of the dark matter mass, with all known funnels and co-annihilation channels (left) or without those channels (right). The different colours correspond to the relative importance of the contributions from annihilations into vector-like fermions to the total dark matter annihilation cross section (blue to red for increasing contribution). The horizontal dashed lines indicate the region favoured by Planck data [156].*

also exist in the MSSM, the corresponding annihilation cross section is suppressed by the masses of the light SM fermions. The vector-like fermions present in MSSM extensions, on the other hand, are (necessarily) much heavier, hence this suppression is no longer present. It is the interplay of these two factors that renders heavier bino dark matter a viable option in the QUE and QDEE models, making it possible to achieve masses as high as ~ 450 GeV in the former case and ~ 600 GeV in the latter [111, 112]. In the LND model, however, the situation is slightly different. Although, in this model too the binos can annihilate into heavy electron (and neutrino) pairs through the t-channel exchange of the corresponding sfermions, now the new leptons belong to an $SU(2)_L$ doublet with an hypercharge $Y_L = 1/2$. This implies that, all other parameters being identical, the bino annihilation cross section is suppressed by a factor 1/16 relatively to the QUE and QDEE models. We thus expect the phenomenology of neutralino dark matter to be more similar to the MSSM one than that of the other two GUT-inspired MSSM extensions with vector-like fermions.

In Fig. 3.2 we present the neutralino relic abundance as a function of the dark matter mass, highlighting in different colours the contribution of these novel annihilation channels to the total dark matter annihilation cross section. In the left panel we show all the scenarios probed in our scanning procedure that respect the constraints described in section 3.2.2, whereas in the right panel we exclude scenarios in which dark matter depletion is dominated by funnels ($Z/h/H/A$) or co-annihilations. Several comments are in order.

First, we recover the well-known result that sub-TeV higgsinos and winos lie below the Planck region (with $\Omega h^2 \sim 0.12$ [156]), *i.e.* the predicted relic density is smaller by one or two orders of magnitude than the observed one. This is illustrated on the bottom of the left subfigure as a line-like accumulation of scenarios. In contrast, almost pure bino dark matter that does not annihilate into vector-like fermions can be either overabundant or under-abundant, depending on whether or not co-annihilations and funnels are efficient in depleting DM. The blue parameter space points for which the Planck measurements are exactly met correspond to scenarios of bino dark matter either annihilating through a quasi on-shell $Z/h/H$ or A boson, or co-annihilating with MSSM sparticles. Such configurations are also present in the MSSM. The novel feature appearing in the LND model are the red points, which correspond exactly to situations in which binos annihilate into vector-like leptons. While co-annihilations with the corresponding sfermions are also possible, they are not necessary to reproduce the Planck measurements.

Second, we observe the existence of a lower bound in the predicted dark matter abundance for binos annihilating exclusively into vector-like leptons. This limit is due to the fact that the interactions involved in annihilation diagrams such as the one depicted in Fig. 3.1 result from gauge couplings, which implies that their magnitude is essentially fixed. Then, in the absence of additional annihilation processes, these interactions can be efficient only up to a certain point in depleting dark matter, which corresponds to the observed lower bound in Ωh^2. This lower limit scales roughly as the squared bino mass, which is a consequence of the fact that, for large enough dark matter masses, $\langle \sigma v \rangle$ is roughly proportional to the inverse square of the dark matter mass, a dependence which reflects upon the predicted relic density. The situation is fairly similar to the scaling of the wino and/or higgsino abundance as a function of the neutralino mass.

Third, the rather sharp cut-off observed in the red points around a mass of 100 GeV is simply due to the fact that the vector-like leptons (and, in particular, the heavy electrons) cannot be lighter than about 100 GeV, because of the experimental constraints on their mass discussed in section 3.2.2.

So, as anticipated, the neutralino dark matter phenomenology we recover is fairly similar to the MSSM one. Due to the hypercharge suppression of processes such as the one depicted in Fig. 3.1, annihilation into vector-like fermions is not as efficient in the LND model as in the QUE and QDEE ones. It is, hence, not possible to reach bino masses larger than ~ 200 GeV while imposing all existing experimental constraints and explaining the observed dark matter density in the Universe. Although the dark matter annihilation channels might differ drastically, the accessible masses are at the end comparable to those that would be obtained in the MSSM. However, as we will see in section 3.4, the existence of the vector-like (s)fermions can give rise to interesting, novel phenomenological signatures at the LHC and provide additional handles for collider dark matter searches.

3.3.2 Sneutrino dark matter

As already explained in section 3.1, LND sneutrinos can be a random admixture of the MSSM ($SU(2)$ doublet) left-handed sneutrinos and the vector-like left- and right-handed $SU(2)$ doublet or singlet ones. A first finding from our parameter space scan is that, as expected (*cf. e.g.* Ref. [106]), mostly doublet-like sneutrino dark matter can be perfectly compatible with the requirement to reproduce the observed dark matter abundance in the Universe, but is excluded by direct detection experiments due to the strong coupling to the Z boson. This is a well-known feature in the MSSM which persists in the LND model. In order to illustrate it, in the left panel of Fig. 3.3 we show the sneutrino relic abundance as a function of its mass, highlighting in different colours (red to blue) the increasing doublet fraction. For simplicity, we ignore scenarios with MSSM-like sneutrinos. We observe that mostly doublet-like scenarios (blue points) can satisfy the Planck constraint for sneutrino masses around $600 - 800$ GeV, a range which is comparable to the usual MSSM sneutrino dark matter scenario [106]. These scenarios are, nonetheless, found to be in severe conflict with direct detection constraints.

In principle, the presence of additional light leptonic doublets could also provide the necessary contributions to tame down the discrepancy between the measured and predicted values of the anomalous magnetic moment of the muon, despite the fact that mixing is only allowed with the third generation of SM fermions [157]. This appealing option turns out to be strongly disfavoured by cosmology, so that one ends up with a situation similar to the MSSM one. From now on, we will not analyse further doublet-like sneutrino DM candidates.

Singlet-like scenarios (red points), on the other hand, offer much more freedom both from the viewpoint of the Planck-allowed sneutrino masses and as far as direct detection constraints are concerned. The abundance of singlet-like scenarios is determined through the interplay of several dark matter depletion processes including direct annihilations into Higgs boson pairs, annihilations through quasi-on-shell s-channel scalars and sfermion ex-

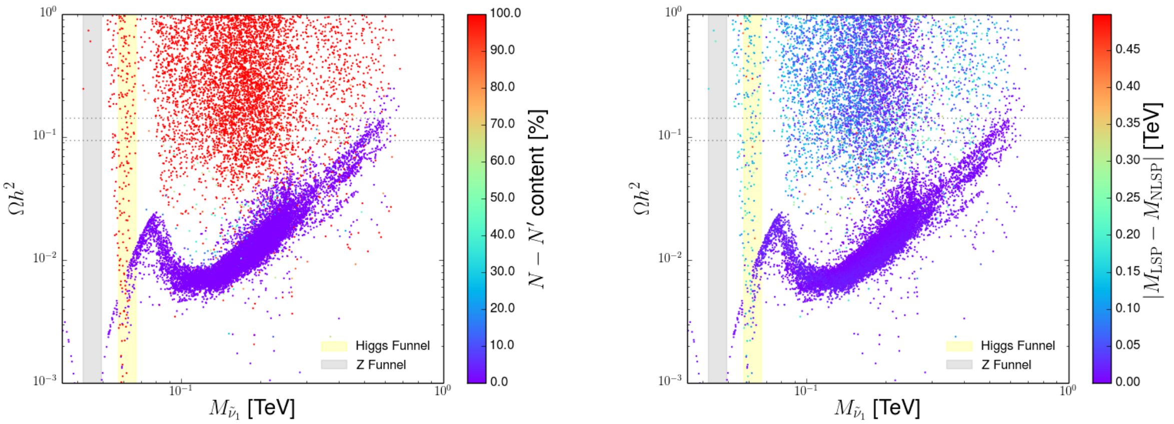

Figure 3.3: *Sneutrino relic abundance as a function of its mass. In the left panel we highlight in blue the parameter space points for which the lightest sneutrino is dominated by a doublet component, whereas red points are essentially singlet-like. In the right panel, we indicate which of the parameter space points are characterised by large (red) or small (blue) mass splittings between the lightest sneutrino and the NLSP.*

change, and co-annihilations. The impact of the latter is in particular illustrated in the right panel of Fig. 3.3, in which we highlight in different colours (red to blue) scenarios with decreasing mass splitting between the lightest sneutrino and the next-to-lightest supersymmetric particle (NLSP) and which indicate increasing co-annihilation contributions. The observed relic abundance in the Universe can be reproduced for a large range of mass splittings, which implies that sneutrinos can be a cosmologically viable option with or without co-annihilations.

The impact of the DM direct and indirect detection constraints for sneutrino dark matter on the LND model is shown in Fig. 3.4. In the left panel we present the DM-proton spin-independent scattering cross section against the sneutrino mass and compare it with the latest exclusion bounds from The Large Underground Xenon experiment (LUX) [158, 159] (red-dashed line) and XENON1T [160] (black-dashed line and shaded 3σ band). In order to account for the possibility of sneutrinos comprising only a subleading dark matter component, the scattering cross section has been rescaled according to the predicted dark matter abundance for each scenario, which we assume to scale identically to its present-day local density, an we ignore configurations yielding over-abundant dark matter. In the right panel we instead show the predicted zero-velocity thermally averaged self-annihilation cross section and compare it with the latest bounds from the Fermi satellite mission [161] for different annihilation channels. Although the exact nature of the annihilation products

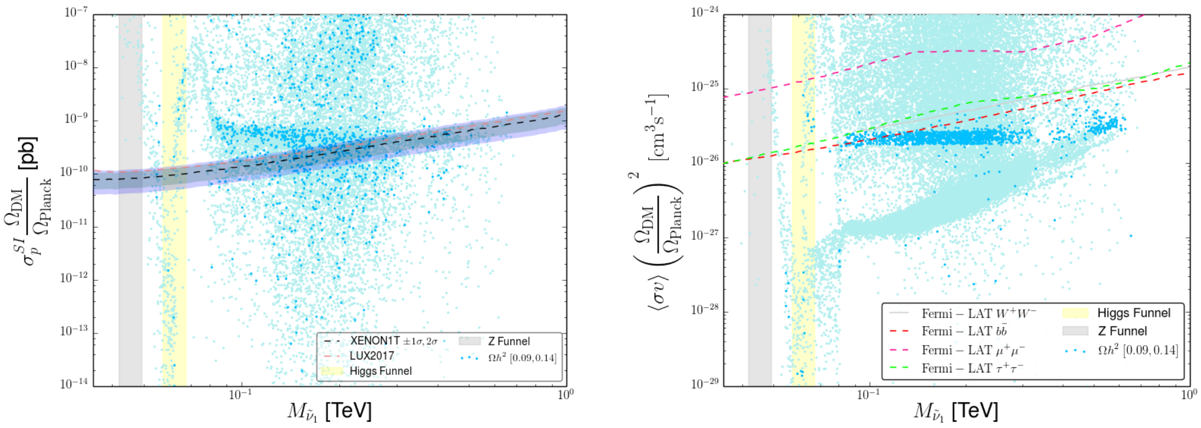

Figure 3.4: *Direct (left panel) and indirect (right panel) detection constraints on sneutrino dark matter in the LND model as a function of the dark matter mass. In both cases we highlight, in darker blue, the parameter space points for which the two-sided Planck constraint can be satisfied.*

may vary substantially, the constraints for hadronic (quarks/gauge bosons) channels tend to correspond more to the actual constraints on our scenarios. The self-annihilation cross section has in this case been rescaled by $\Omega^2_{\rm pred}/\Omega^2_{\rm Planck}$, again in order to account for the possibility of under-abundant scenarios. In both panels, the parameter space points satisfying both the upper and the lower Planck bound are highlighted in darker blue and we omit points for which dark matter would be over-abundant.

As we can observe from the left panel of Fig. 3.4, the parameter space points for which $M_{\tilde{\nu}_1} \sim M_h/2$ and which satisfy the relic density constraint lie within a band that exhibits a rather standard "funnel"-like behaviour. Below this mass value, efficient annihilation of singlet-like sneutrinos into light SM fermions requires rather large couplings to the Standard Model particles, especially the Higgs boson, which in turn implies that the corresponding scenarios are characterised by relatively large spin-independent scattering cross sections. This brings them in conflict with the recent LUX and XENON1T constraints, which are only satisfied if the sneutrinos annihilate through a quasi-resonant Higgs boson in the early Universe. Once the W-boson mass threshold is crossed, we observe another abrupt drop in σ_p^{SI} since for $M_{\tilde{\nu}_1} > M_W$ the sneutrinos can annihilate directly into a pair of W (and, eventually, Z) bosons. Still, direct detection constraints exclude most of the parameter space lying within this band for sneutrino masses roughly up to 200 GeV. For larger masses, the present-day sensitivity of direct detection experiments is no longer sufficient to exclude these scenarios.

Essentially the same structure is observed in the right panel of Fig. 3.4, without the sudden drop around M_W since the total dark matter self-annihilation cross section remains roughly constant in order to satisfy the Planck bounds. Besides, the occasional scattered points that lie outside the main dark blue band correspond to scenarios with large co-annihilation contributions or to cases in which dark matter annihilates predominantly into Higgs boson pairs or vector-like leptons. The larger spread of the dark blue points in the left panel of the figure with respect to the right one is due to the fact that, with the exception of co-annihilation, indirect detection probes *the same* processes that determine the dark matter abundance in the Universe. For instance, if dark matter annihilates predominantly into Higgs boson pairs, its direct detection prospects are rather modest whereas its indirect detection perspectives are almost identical to scenarios with a WW final state, since the final annihilation products are similar and the total thermally averaged self-annihilation cross section is roughly the canonical one.

The DM detection perspectives of the model are hence good, since most of the parameter space that has not yet been excluded by direct or indirect detection lies within a factor of a few from current bounds. We can expect that at least the most "canonical" scenarios will be probed with in the next decade or so. However, LND sneutrino dark matter candidates behave rather similarly to usual sneutrino dark matter in the MSSM augmented with a right-handed neutrino chiral supermultiplet. Most of the features discussed here are present in this scenario too, with the most important differences coming from the existence of a few additional annihilation channels (the contribution of which we have, however, found to be rather modest) and the presence of a handful of additional co-annihilation channels. Both of these features do not alter the global picture of sneutrino dark matter with respect to more conventional scenarios. Despite this, we should remind that given the current experimental constraints, essentially all neutralino dark matter scenarios necessitate a μ parameter that lies at the TeV scale or above. As it has been pointed out [152, 153, 154], since the μ parameter is related to the Z-boson mass already at tree-level, this introduces high levels of fine-tuning pushing the theory towards unnatural territories. In sneutrino dark matter scenarios such as the one we just studied, the μ parameter is decoupled from the dark matter mass and can be fixed much closer to the Z-boson mass as required by naturalness. In this respect, the presence of a second dark matter candidate in the form of the (mostly singlet-like) sneutrino in the LND model constitutes of an interesting novelty both with respect to the MSSM and to the QUE and QDEE setups.

3.4 Prospects at the HL-LHC

The results presented in the previous sections show that there exist LND configurations compatible with cosmological constraints as well as with flavour, Higgs and low-energy physics observables. We therefore single out several representative benchmark scenarios to study the corresponding LHC phenomenology in more depth, and turn our focus on setups featuring substantial cross sections for vector-like (s)fermion production at the LHC connected to potential novel LHC signatures worthy of investigation. Even though the LND model has some semblance with the MSSM, it exhibits differences due to the existence of additional vector-like leptons and down-type quark. Owing to flavour physics constraints, the vector-like down quark has to be massive and its coupling to the SM quarks has to be small, which reduces its corresponding LHC production cross section significantly. Typical LND signals therefore involve leptonic and often cleaner final states.

We concentrate on vector-like τ' production, in which each extra lepton dominantly decays into a neutral SM-like Higgs-boson h or Z-boson and a tau lepton,

$$pp \to \tau' \; \bar{\tau}' \to \tau\bar{\tau}XX \qquad \text{with} \qquad X = h, Z \; .$$

After accounting for h and Z-boson decays, this process could give rise to a copious production of multileptonic events with small SM backgrounds. We analyse the four benchmark points defined in Table 3.3, that leads to the production of events containing four first and second generation leptons (e or μ) at the LHC. The tables include the 20 parameters relevant for collider physics, the most relevant ones being $\varepsilon_{N,3}$, k_N, $\kappa_{L,3}$, h_N and ε_E as the considered signal involves vector-like τ' states. The corresponding particle spectra are presented in Table 3.4.

As soon as all branching ratios are properly included, final states containing four leptons (e or μ), at least one hadronic tau and no b-tagged jets could yield the largest signal sensitivity, highlighted in particular by a low associated background. We make use of MG5_aMC@NLO (version 2.6.1) [144] to generate leading-order hard-scattering events for both the signal for the four considered benchmarks, and for the different components of the SM background, for proton-proton collisions at a centre-of-mass energy of 14 TeV. We generate events for diboson production (including off-shell effects, once accounting for weak boson leptonic decays), as well as for the subdominant $t\bar{t}h$, $t\bar{t}Z$ and $t\bar{t}WW$ background contributions. We have additionally verified that triboson background contributions were

Table 3.3: *Parameters defining our four representative LND benchmark scenarios* **BP1-BP4**. *The sign of the μ parameter has been taken positive in all cases.*

	μ_L [GeV]	$\tan\beta$	$\varepsilon_{N,3}$	k_N	M_0 [TeV]	M_1 [GeV]	B_0 [GeV]	μ_D [TeV]
BP1	144.9	41.6	-0.045	0.013	2.2	160.8	584.64	7.22
BP2	128.9	42.6	-0.06	-0.18	1.57	168.25	481.79	5.47
BP3	132.42	40.52	-0.049	-0.13	1.65	156.39	452.09	6.03
BP4	162.96	25.36	-0.035	0.0888	1.05	206.24	1306.38	4.12

	M_2 [TeV]	$\kappa_{L,3}$ [GeV]	h_N	ε_E	A_0[GeV]	$m^2_{L',3}$ [TeV^2]	$m^2_{D',3}$ [TeV^2]	$m^2_{L,3}$ [TeV^2]
BP1	1.5	-11.9	-0.038	-0.29	95.26	0.15	1.76	4.78×10^{-3}
BP2	1.05	1.28	-6.8×10^{-3}	-0.16	-743.38	2.91×10^{-3}	1.29	6.86×10^{-3}
BP3	1.01	1.16	-4.9×10^{-3}	-0.16	-516.61	2.09×10^{-3}	1.55	7.58×10^{-3}
BP4	0.45	15.74	-0.106	2.47×10^{-3}	5.51×10^{-4}	0.25	23.68	0.20

	$m^2_{N,3}$ [TeV^2]	$m^2_{N',3}$ [TeV^2]	μ_N[GeV]	$m^2_{D,3}$[TeV^2]	κ_D [GeV]	ε_D	$m^2_{L_5,L,\ 3}$ [TeV^2]	$m^2_{D_5,D,\ 3}$ [TeV^2]
BP1	0.32	2.28×10^{-2}	748.84	10.59	0.0	-2.38×10^{-4}	-9.16×10^{-5}	7.89×10^{-5}
BP2	1.32×10^{-3}	1.11×10^{-3}	984.28	2.46×10^{-3}	0.0	-9.47×10^{-4}	-4.41×10^{-5}	-2.91×10^{-5}
BP3	1.24×10^{-3}	8.29×10^{-4}	975.48	3.31×10^{-3}	0.0	-1.08×10^{-3}	-4.50×10^{-5}	-2.69×10^{-5}
BP4	0.29	0.12	1499.71	14.89	0.0	-3.06×10^{-4}	-9.81×10^{-5}	3.86×10^{-5}

Table 3.4: *Masses of the particles lighter than 2.5 TeV for our four representative LND benchmark scenarios* **BP1-BP4**.

	$M_{\tau'}$ [GeV]	$M_{\tilde{\chi}_1^0}$ [GeV]	$M_{\nu_1'}$ [GeV]	$M_{\nu_2'}$ [GeV]	$M_{b'}$ [TeV]	$M_{\tilde{\chi}_2^0} \cong M_{\tilde{\chi}_1^\pm}$ [TeV]	$M_{\tilde{e}_1}$ [GeV]
BP1	150.87	157.48	146.71	748.95	7.36	1.53	175.73
BP2	133.98	164.91	130.22	985.49	5.64	1.09	188.66
BP3	137.41	153.33	133.68	976.16	6.16	1.05	175.47
BP4	168.72	202.55	164.21	1500.53	4.28	0.48	221.56

	$M_{\tilde{e}_2}$ [GeV]	$M_{\tilde{\nu}_1}$ [GeV]	$M_{\tilde{\nu}_2}$ [GeV]	$M_{\tilde{\nu}_3}$ [GeV]	$M_{\tilde{\nu}_4}$ [TeV]	$M_{\tilde{\nu}_5}$ [TeV]	$M_{\tilde{\nu}_6}$ [TeV]
BP1	516.31	169.23	520.67	633.22	1.02	1.47	1.81
BP2	401.71	193.82	401.03	491.87	1.31	1.78	2.39
BP3	399.22	182.70	396.97	459.45	1.31	1.38	1.99
BP4	691.04	219.54	691.25	1537.79	1.59	1.80	2.39

negligible. In our simulations, we rely on the four-flavour number scheme, making use of the leading-order set of NNPDF2.3 parton densities [162]. We include taus when enforcing weak boson leptonic decays, and allow for the presence of up to two extra partons in the final state. The multipartonic contributions are then merged following the MLM prescription [163]. Parton showering and hadronisation are performed within the PYTHIA8 (version 8.230) framework [164] and we simulate the response of the detector by means of DELPHES 3 (version 3.4.1) [165]. We modify slightly the default CMS detector parameterisation that relies on the FASTJET program (version 3.2.1) [166] for jet reconstruction on the basis of the anti-k_T algorithm [167], with a radius parameter set to $R = 0.5$. Our modifications imply a tau-tagging efficiency fixed to 60%, for a mistagging rate of a light-jet as a hadronic tau set to 1% (this configuration matches average performances after the object selection enforced below). In contrast, we consider standard b-tagging performance as implemented in the default CMS parameterisation [168].

We define the relevant reconstructed object candidates by imposing transverse momentum (p_T) and pseudorapidity (η) conditions on the leptons ($\ell = e, \mu$), hadronic taus (τ_h) and light and b-tagged jets (j and b),

$$\begin{aligned} p_T^\ell \geq 10 \text{ GeV and } |\eta^\ell| < 2.5 \ , \quad p_T^{\tau_h} \geq 20 \text{ GeV} \quad \text{and} \quad |\eta^\tau| < 2.5 \ , \\ p_T^{j,b} \geq 30 \text{ GeV} \ , \qquad |\eta^j| < 4.5 \quad \text{and} \quad |\eta^b| < 2.5 \ . \end{aligned} \tag{3.4.1}$$

We moreover require lepton isolation by imposing that the total hadronic activity within a cone of radius $\Delta R = 0.5$ around any electron (muon) is smaller than 12% (25%) of the lepton p_T, and that all reconstructed leptons are separated from each other by an angular distance, in the transverse plane, of at least $R = 0.5$. We then preselect events by constraining the number of reconstructed final-state electrons and muons (N^ℓ), hadronic taus (N^{τ_h}) and b-tagged jets (N^b), to be

$$N^\ell \geq 4 \ , \qquad N^b = 0 \qquad \text{and} \qquad N^{\tau_h} \geq 1 \ . \tag{3.4.2}$$

We then investigated a large set of observables and found that the most discriminatory ones are the total transverse activity H_T (the scalar sum of the p_T of all reconstructed visible objects), a modified version of the effective mass M_{eff} (the scalar sum of the p_T of all jets and the missing transverse energy $\not{E}_T$), and the invariant mass $M_{4\ell}$ of the system made of the four hardest leptons. The distributions in these variables are shown in Fig. 3.5 for both the different background contributions and the illustrative **BP1** benchmark scenario. Upon

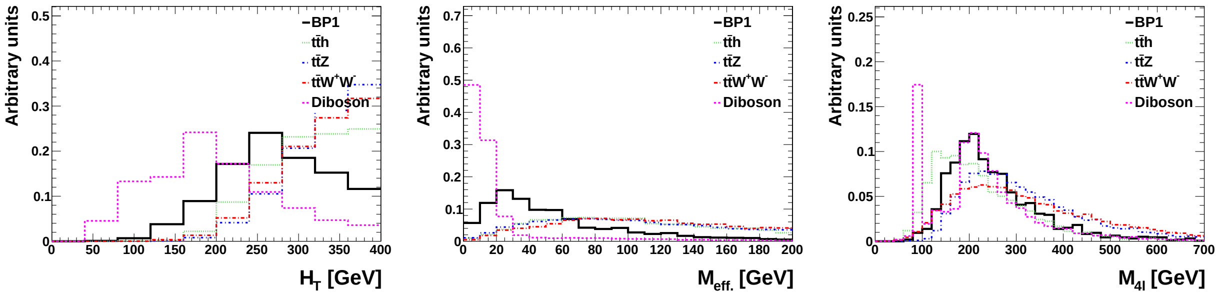

Figure 3.5: *Distributions in the H_T, $M_{\rm eff}$ and $M_{4\ell}$ observables for the* **BP1** *benchmark scenario and the dominant contributions to the SM background, once the preselection cuts of Eq. (3.4.2) have been imposed. The normalisation is arbitrary.*

scrutinising these variables, we select events for which

$$H_T > 250 \text{ GeV}, \qquad M_{\rm eff} > 30 \text{ GeV} \qquad \text{and} \qquad M_{4\ell} > 200 \text{ GeV}.$$

Whilst further optimisation is possible, these choices allow for a good enough background rejection in the context of the four considered benchmark selections, as illustrated by the detailed cutflow charts shown in Table 3.5 for 3 ab^{-1} of LHC collisions at 14 TeV.

We evaluate the sensitivity of the high-luminosity LHC to our different benchmark scenarios by computing two significance indicators s and Z_A defined by [169]

$$\begin{aligned} s &= \frac{S}{\sqrt{B+\sigma_B^2}} \qquad \text{and} \\ Z_A &= \sqrt{2\left((S+B)\ln\left[\frac{(S+B)(S+\sigma_B^2)}{B^2+(S+B)\sigma_B^2}\right] - \frac{B^2}{\sigma_B^2}\ln\left[1+\frac{\sigma_B^2 S}{B(B+\sigma_B^2)}\right]\right)}\ , \end{aligned} \tag{3.4.3}$$

with S and B being respectively the total number of signal and background events surviving the selection. Our results assume a 20% systematic uncertainty on the SM background, $\sigma_B = 0.2 \times B$. In Table 3.5 we compare the expectation for both 300 fb^{-1} and 3 ab^{-1} of LHC collisions. The discovery prospects are in all cases very promising, so that the presence of the vector-like leptons offers good handles on LND models. It will, however, be challenging to conclude about the realisation of the model in nature without getting a grip on the supersymmetric part of the spectrum with the LHC alone.

This could for instance be achieved by investigating the impact of the searches for supersymmetry through its monojet and multijet plus missing energy signatures [170, 171, 172, 173]. In all cosmologically-favoured LND setups analysed in section 3.3, such signals

Table 3.5: *Impact of our event selection strategy on the SM background and the four considered benchmark scenarios. For each cut, we provide the expected number of surviving events for $\mathcal{L} = 3$ ab^{-1} of LHC collisions at a centre-of-mass energy of 14 TeV. We also quote the corresponding significances s and Z_A defined in Eq. (3.4), including a 20% systematic uncertainty on the background. We additionally indicate, in parentheses, the significances for a lower luminosity of 300 fb^{-1}.*

Step	Requirements	Background	**BP1**	**BP2**	**BP3**	**BP4**
0	Initial	5.3×10^9	1.4×10^8	2.0×10^8	2.1×10^8	1.7×10^8
1	Preselection	149	241	336	336	282
2	$H_T > 250$ GeV	101	183	240	247	236
3	$M_{\text{eff}} > 30$ GeV	39	117	120	125	156
4	$M_{4\ell} > 200$ GeV	34	90	95	100	118
	3 ab^{-1} (300 fb^{-1})	s	10.06σ (4.59σ)	10.57σ (4.82σ)	11.13σ (5.08σ)	13.16σ (6.00σ)
		Z_A	6.70σ (3.39σ)	6.94σ (3.53σ)	7.22σ (3.68σ)	8.14σ (4.19σ)

arise from the pair production of squarks and/or gluinos. However, the lightest squarks have generally masses of about 2 TeV or more, so that the corresponding cross sections are negligibly small, especially after imposing the presence of at least one very hard jet in the final state. Exceptional scenarios nevertheless exist, in which lighter coloured superpartners are featured. In this case, the relevant cross sections are of $\mathcal{O}(1)$ fb, which is too small to yield any hope of observing a hint for the signal. We have, in addition, evaluated the cross sections associated with electroweakino pair production. For all scenarios favoured by cosmological data, they reach at most 0.1 fb, when the branching-ratio-favoured hadronic final states are considered. The direct observation of a supersymmetric signal at the LHC will, hence, be very unlikely. Thankfully, as demonstrated in this work, the presence of vector-like leptons in the LND model provides additional observational handles which are complementary to cosmological and astrophysical probes.

Our collider analysis focused on decays into vector-like τ' leptons, yielding signals with four leptons (electrons or muons), one hadronic tau and no b-jets. This constitutes a rather unique signature that is neither probed by multilepton analyses, which target final states with three or more leptons but no taus [174], nor by conventional searches for vector-like leptons, which include either three or more light leptons and no taus, or two light leptons and a single tau, as in Ref. [175]. Perhaps the closest experimental study to our proposal is the ATLAS analysis of Ref. [176]. However, the information provided in their Tables 4 and 6 indicate that not a single one of their signal region matches ours. Hopefully, further analyses at the LHC will allow for the investigation of a wider range of parameter space and probe additional multilepton signals.

Chapter 4

E_6–inspired $U(1)'$ extended MSSM

Supersymmetry is one of the most attractive theories of physics beyond the SM. It introduces a viable space-time extension, provides a natural solution to the hierarchy problem, allows for gauge coupling unification at a single Grand Unified scale, and, last but not least, it predicts a stable, neutral LSP as a realistic weakly interacting massive particle DM candidate. But despite the numerous appealing aspects, low-energy SUSY is plagued by one overwhelming failure: no compelling evidence for it is seen at the LHC. This imposes stringent constraints on the masses of any supersymmetric coloured particle. Under simplified assumptions, gluino and first and second generation squark masses of less than 2 TeV are for instance excluded for a large variety of LSP masses [177, 178, 179]. The absence of any light superpartners so far hence puts the theory in serious conflict with electroweak naturalness [91, 180]. However, most searches are based on the minimal supersymmetric scenario whose parameter space left to explore at the LHC is rapidly shrinking. In addition, the minimal model suffers from serious fine-tuning problems induced by the discovery of ATLAS [28] and CMS [27] collaborations of a scalar particle with a mass of 125 GeV and with the expected properties of a Standard Model Higgs boson. On one hand, it is important to be precise enough in the measurements of the properties of the new scalar particle in order to confirm its nature as the SM Higgs boson responsible for EWSB. On the other hand, the Higgs boson mass must be compatible with the requirements imposed by supersymmetry at the expense of moving the SUSY scale above TeV energies. This relatively heavy Higgs boson mass imposes indirect pressures on the supersymmetric spectrum. For instance, there is a strong tension between LHC measurements and the need for a fine-tuning that can be as large as 300 or more to accommodate a viable EWSB mechanism in case of heavy higgsinos. It is nonetheless possible to get viable scenarios with lighter higgsinos and a less extreme fine-tuning in some corners of the parameter space [181, 182].

One could assume that supersymmetry does not manifest itself as the MSSM, but feature instead an extended gauge symmetry. This implies the presence of additional new particles that could alter the exclusion limits derived in particular from measurements at the LHC in proton-proton collisions at centre-of-mass energies $\sqrt{s}$ of 7, 8 and 13 TeV. Ideally, the new model would preserve all the attractive features of the MSSM, resolve some of its outstanding issues, and allow for a parameter space distinct for that of the MSSM in some regions. One possible source of difference between an extended SUSY model and the MSSM could be in the viable options for the LSP. In its minimal incarnation, supersymmetry has one possible dark matter candidate, the neutralino which can be an arbitrary admixture of binos, winos and higgsinos.

Dark matter searches can play an important role as probes for physics beyond the SM, especially as providers of indirect information on the spectrum of the models under investigation. We rely on these observations to investigate the opportunities for natural DM candidates offered by extended supersymmetric scenarios and to make use of dark matter data as a testing ground for extended SUSY models. In one of the simplest extensions of the MSSM, the gauge group is enlarged by an extra $U(1)'$ symmetry. This model minimally introduces a new gauge boson, a new singlet Higgs field, and a right-handed neutrino, together with their superpartners. The right-handed sneutrino can be the LSP and a viable DM candidate in particular thanks to its interactions with the new gauge boson. This contrasts with the MSSM where left-handed scalar neutrinos, which do not partake in strong and electromagnetic interactions, cannot be possible candidates for DM as their interactions with the Z boson yield too high annihilation cross sections [119]. In addition, the lightest neutralino, that can also be an acceptable DM candidate, can exhibit novel properties due to its possible $U(1)'$ bino component. This would lead to additional annihilation channels which may imply some dissimilarities with the MSSM neutralino LSP.

The possibility of adding an extra $U(1)'$ gauge symmetry to the SM is well-motivated in superstring constructions [183], GUTs [184], models of dynamical symmetry breaking [185], little Higgs models [186, 187], and setups with large extra dimensions [188]. Extra $U(1)'$ groups generally arise from the breaking of an $SO(10)$ or E_6 symmetry to the SM gauge symmetry. In supersymmetry, $U(1)'$ models also offer a solution to the MSSM fine-tuning issue that is mainly driven by the bilinear μ term of the superpotential. This term is indeed simultaneously responsible for the Higgs boson mass and for the higgsino masses. In the MSSM, higgsinos are expected to be light, of $\mathcal{O}(100)$ GeV, while predictions for a Higgs boson mass of about 125 GeV require supersymmetric masses of $\mathcal{O}(1)$ TeV or more. This raises questions about the nature of the μ parameter. UMSSM suggest a solution to the so-called μ-problem by the introduction of an effective μ_{eff} parameter dynamically generated by the vev of a new scalar field S responsible for breaking the $U(1)'$ symmetry [189, 190]. While this resolution of the μ problem is similar to the one provided in the next-to-minimal supersymmetric standard model (NMSSM) [107], the $U(1)'$ symmetry additionally prevents from the appearance of cosmological domain walls [191]. Moreover, extra desirable features of UMSSM models are the absence of rapid proton decay operators (of dimension four), the protection of all fields by chirality and supersymmetry from acquiring high-scale masses, consistency with anomaly cancellation, gauge-coupling unification, as well as family universality that allow us to avoid flavour-changing neutral current constraints [192].

The aim of this article is to present a comprehensive study of all $U(1)'$ models emerging from the breaking of an E_6 symmetry in contexts where either a scalar neutrino or the lightest neutralino is the LSP. The former is not a possibility available in the MSSM, and, as we shall see, not the most natural solution in UMSSM models. There however exists a large variety of UMSSM realisations where the lightest sneutrino, which contains a dominant right-handed sneutrino component, is the LSP and where the observed dark matter abundance can be explained while satisfying other experimental constraints. This contrasts with left-handed sneutrino LSP scenarios which are excluded, as in the MSSM, by a non-zero sneutrino hypercharge that leads to a too efficient DM annihilation via a Z-boson exchange in the early Universe, and thus to a relic abundance lower than the $\Omega_{\text{DM}}h^2$ value measured by the The Wilkinson Microwave Anisotropy Probe (WMAP) [193] and Planck [194] satellites. We explore the UMSSM parameter space consistent with either a sneutrino or a neutralino LSP, impose constraints from dark matter relic abundance and direct detection experiments, and then investigate potential signals of the viable scenarios at the LHC. We also address the compatibility of acceptable setups with measurements of the anomalous magnetic moment of the muon $(g-2)_\mu$. The differences between the two (sneutrino and neutralino LSP) scenarios are outlined and we especially emphasise the challenges originating from the fact that for most of the parameter space for which dark matter constraints are satisfied, the expected LHC signals are not visible, while benchmark setups yielding LHC signals that could be extracted from the SM background fail to satisfy dark matter constraints.

Whereas previous phenomenological studies in specific UMSSM constructions have appeared in Refs. [195, 196, 197, 198, 199, 200, 201, 202, 203, 204, 205], our analysis features new ingredients. It encompasses *all* possible $U(1)'$ symmetries arising from the breaking of an E_6 symmetry, with the goal of determining characteristic signals which discriminate them. We moreover include all constraints arising from low-energy phenomena, updated results from the Z' boson searches and from Higgs boson signal strength data. More practically, we first perform a scan of the parameter space and then derive the regions of the parameter space consistent with a viable sneutrino or neutralino dark matter candidate. We then investigate the various signals that could arise from dark matter experiments in order to pinpoint possible genuine differences between the UMSSM realisations.

Our work is organised as follows. We review the properties of the supersymmetric models featuring an extra $U(1)$ symmetry, or UMSSM models, in section 4.1. We then explore the corresponding parameter space and determine the regions that exhibit a compatibility with the Higgs boson signal strength and low-energy data in section 4.2, imposing the LSP to be either a sneutrino or a neutralino. We next consider the associated Z' boson phenomenology in section 4.2.3 and the implications for the anomalous magnetic moment of the muon in section 4.2.4. In section 4.3, we focus on scenarios with a right sneutrino LSP and analyse the dependence of the DM relic density on the Z' boson mass as well as direct and indirect DM detection experiment signals. In section 4.4, we investigate cases where the neutralino is the LSP and again put an emphasis on the DM relic density, direct and indirect detection constraints. We finally discuss the prospects for observing UMSSM scenarios at colliders in section 4.5.

4.1 UMSSM Models

In this section, we briefly review the theoretical framework of minimal $U(1)'$-extended supersymmetric models that has been extensively discussed in Refs. [103, 190, 197]. The presence of the additional gauge group introduces one extra neutral gauge boson Z' of mass $M_{Z'}$ together with the corresponding gaugino superpartner $\lambda_{\tilde{Z}'}$. In their simplest incarnations, UMSSM models also requires the presence of an additional electroweak singlet superfield $S \equiv (s, \tilde{s})$, charged under the $U(1)'$ symmetry, that is responsible for the breaking of the extended symmetry group down to the electroweak group. The model field content moreover includes two weak doublets of quark ($Q \equiv (q, \tilde{q})$) and lepton ($L \equiv (l, \tilde{l})$) chiral supermultiplet as well as four weak singlets of up-type quark ($U \equiv (u, \tilde{u})$), down-type quark ($D \equiv (d, \tilde{d})$),

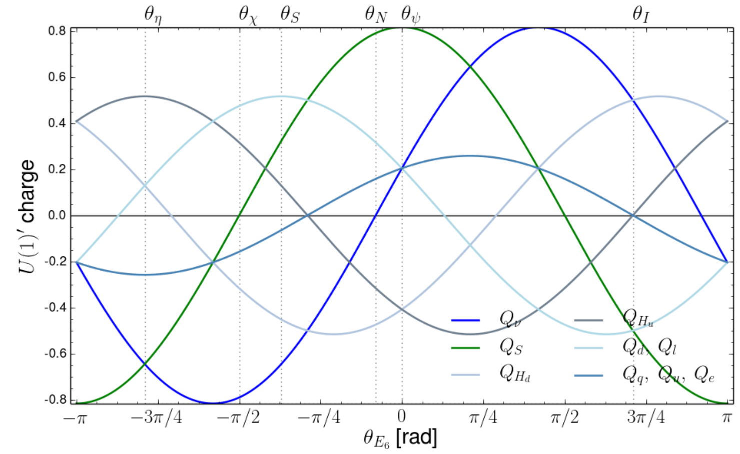

Figure 4.1: *Variation of the $U(1)'$ charges of the various UMSSM superfields as a function of the θ_{E_6} mixing angle. The standard $U(1)'_\eta$, $U(1)'_\chi$, $U(1)'_S$, $U(1)'_N$, $U(1)'_\psi$ and $U(1)'_I$ models are identified by dotted vertical lines.*

charged lepton ($E \equiv (e, \tilde{e})$) and right neutrino ($N \equiv (\nu_R, \tilde{\nu}_R)$) chiral supermultiplets. The Higgs sector contains, in addition to the S singlet, two weak doublets of Higgs supermultiplets ($H_u \equiv (\tilde{h}_u, h_u)$ and $H_d \equiv (\tilde{h}_d, h_d)$), and the gauge sector is similar to the one of the MSSM except for the $U(1)'$ field. It thus includes a QCD ($G \equiv (g, \lambda_{\tilde{G}})$), weak ($W \equiv (w, \lambda_{\tilde{W}})$) and hypercharge ($B \equiv (b, \lambda_{\tilde{B}})$) gauge supermultiplets.

There are several possibilities for defining the extra $U(1)'$ symmetry. The most commonly used parameterisation emerges from considering a linear combination of the maximal subgroups $U(1)'_\psi$ and $U(1)'_\chi$ resulting from the breaking of a grand unified E_6 gauge group [100],

$$E_6 \longrightarrow SO(10) \otimes U(1)'_\psi \longrightarrow \Big(SU(5) \otimes U(1)'_\chi\Big) \otimes U(1)'_\psi \ .$$

Introducing a mixing angle θ_{E_6}, a general $U'(1)$ charge operator can be written from the respective $U(1)'_\psi$ and $U(1)'_\chi$ charge operators Q'_ψ and Q'_χ as

$$Q'(\theta_{E_6}) = Q'_\psi \cos\theta_{E_6} - Q'_\chi \sin\theta_{E_6} \ .$$

In Fig. 4.1 we present the variation of the $U(1)'$ charges of the UMSSM quark, lepton and Higgs superfields as functions of the mixing angle θ_{E_6} that will be a key parameter of our analysis. We identify by vertical lines the anomaly-free $U(1)'$ group choices denoted by $U(1)'_\eta$, $U(1)'_\chi$, $U(1)'_S$, $U(1)'_N$, $U(1)'_\psi$ and $U(1)'_I$, and give the corresponding charge and mixing angle values in Table 4.1.

Table 4.1: *$U(1)'$ charges of the UMSSM quark (Q_q, Q_d, Q_u), lepton (Q_l, Q_e, Q_ν) and Higgs (Q_{H_u}, Q_{H_d}, Q_S) supermultiplets for the anomaly-free abelian group that could arise from the breaking of an E_6 symmetry. The value of the mixing angle $\theta_{E_6} \in [-\pi, \pi]$ is also indicated.*

	$2\sqrt{10}Q'_\chi$	$2\sqrt{6}Q'_\psi$	$2\sqrt{15}Q'_\eta$	$2\sqrt{15}Q'_S$	$2Q'_I$	$2\sqrt{10}Q'_N$
θ_{E_6}	$-\pi/2$	0	$\arccos(\sqrt{5/8}) - \pi$	$\arctan(\sqrt{15}/9) - \pi/2$	$\arccos(\sqrt{5/8}) + \pi/2$	$\arctan\sqrt{15} - \pi/2$
$Q_{q,u,e}$	-1	1	-2	-1/2	0	1
$Q_{d,l}$	3	1	1	4	-1	2
Q_ν	-5	1	-5	-5	1	0
Q_{H_u}	2	-2	4	1	0	2
Q_{H_d}	-2	-2	1	-7/2	1	-3
Q_S	0	4	-5	5/2	-1	5

The UMSSM superpotential contains usual quarks and lepton Yukawa interactions and reads, in the presence of a right-handed neutrino superfield N,

$$W = \mathbf{Y}_u \, U \, Q \, H_u \, - \mathbf{Y}_d \, D \, Q \, H_d \, - \mathbf{Y}_e \, E \, L \, H_d \, + \mathbf{Y}_\nu \, L \, H_u \, N \, + \lambda \, H_u \, H_d \, S \ , \tag{4.1.1}$$

where the four Yukawa couplings $\mathbf{Y}_u$, $\mathbf{Y}_d$, $\mathbf{Y}_l$ and $\mathbf{Y}_\nu$ are 3×3 matrices in flavour space and λ represents the strength of the electroweak Higgs singlet and doublet interactions. All indices are understood but explicitly suppressed for simplicity. After the breaking of the $U(1)'$ symmetry, the scalar component s of the singlet superfield gets a VEV v_S and the last superpotential term of Eq. (4.1.1) induces an effective μ-term with $\mu_{\rm eff} = \lambda v_S/\sqrt{2}$, allowing for the resolution of the μ-problem inherent to the MSSM [206, 207, 208, 209, 210]. As in the MSSM, SUSY is softly broken via the introduction of gaugino mass terms,

$$- \mathcal{L}_{\rm soft}^{\lambda} = \frac{1}{2}\Big(M_1 \lambda_{\tilde{B}} \cdot \lambda_{\tilde{B}} + M_2 \lambda_{\tilde{W}} \cdot \lambda_{\tilde{W}} + M_1' \lambda_{\tilde{Z}'} \cdot \lambda_{\tilde{Z}'} + M_3 \lambda_{\tilde{g}} \cdot \lambda_{\tilde{g}} + \text{h.c.} \Big) \ ,$$

where the M_i variables denote the various mass parameters, scalar mass terms m_i,

$$\begin{aligned} -\mathcal{L}_{\rm soft}^{\Phi} &= m_{H_d}^2 h_d^\dagger h_d + m_{H_u}^2 h_u^\dagger h_u + m_S^2 s^2 + m_{\tilde{Q}}^2 \tilde{q}^\dagger \tilde{q} + m_{\tilde{d}}^2 \tilde{d}^\dagger \tilde{d} \\ &\quad + m_{\tilde{u}}^2 \tilde{u}^\dagger \tilde{u} + m_{\tilde{L}}^2 \tilde{l}^\dagger \tilde{l} + m_{\tilde{e}}^2 \tilde{e}^\dagger \tilde{e} + m_{\tilde{\nu}}^2 \tilde{\nu}_R^\dagger \tilde{\nu}_R \ , \end{aligned}$$

and trilinear interactions featuring a structure deduced from the one of the superpotential,

$$-\mathcal{L}_{\rm soft}^{W} = A_\lambda \, s \, h_u \, h_d \, - A_d \, \tilde{d}^\dagger \, \tilde{q} \, h_d \, - A_e \, \tilde{e}^\dagger \, \tilde{l} \, h_d \, + A_u \, \tilde{u}^\dagger \, \tilde{d} \, h_u \, + \text{h.c.} \ ,$$

where the A_i parameters stand for the soft couplings.

After the breaking of the UMSSM gauge symmetry down to electromagnetism, all neutral components of the scalar Higgs fields get VEVs, $\langle h_u^0 \rangle = v_u/\sqrt{2}$, $\langle h_d^0 \rangle = v_d/\sqrt{2}$ and $\langle s \rangle = v_S/\sqrt{2}$. As a consequence, UMSSM models can easily lead to neutrino masses that are consistent with neutrino oscillation data through an implementation of a see-saw mechanism [211, 212, 213, 214]. The exact details depend on the form of the extra $U(1)'$ symmetry [215], and viable models can be constructed to contain Dirac-type [216] or Majorana neutrino masses [217]. The symmetry breaking mechanism additionally induces the mixing of fields carrying the same spin, colour and electric charge quantum numbers, and the gauge eigenbasis has to be rotated to the physical basis. Contrary to the MSSM where the tree-level SM-like Higgs-boson mass is bound by the Z-boson mass M_Z so that large stop masses and/or trilinear A_t couplings are required for pushing the loop corrections to a large enough value [218], the singlet field provides new tree-level F-term contributions that naturally stabilise the SM-like Higgs boson mass M_h to a greater value more easily in agreement with the measured experimental value of 125 GeV [219]. For any further details on the resulting particle spectrum, we refer to Refs. [189, 190, 198].

The UMSSM Lagrangian introduced above exhibit numerous parameters, in particular within its soft SUSY-breaking part. To reduce the dimensionality of the parameter space, we assume that the SUSY-breaking mechanism originates from minimal supergravity so that unification relations amongst the soft masses can be imposed at the GUT scale where an E_6 gauge symmetry is realised. We however deviate from the most minimal model by maintaing the freedom to choose the details of the lepton and neutrino sector, which guarantees that a sneutrino could be the LSP. More details are given in the following section.

4.2 Parameter Space Scan and Constraints

4.2.1 Technical setup

We perform a scan of the UMSSM parameter space in order to determine regions in which either a sneutrino or a neutralino is the LSP and thus a potential dark matter candidate. We focus on the six anomaly-free UMSSM realisations introduced in the previous section. More precisely, we generate the particle spectrum by making use of SARAH version 4.6.0 [136] and SPHENO version 3.3.8 [137]. Predictions for the dark matter observables are then achieved with MICROMEGAS version 4.3.1 [142], and the properties of the Higgs sector are evaluated with HIGGSBOUNDS version 4.3.1 [138] and HIGGSSIGNALS version 1.4.0 [139]. The interfacing of the various programmes and our numerical analysis have been implemented within the PYSLHA package, version 3.1.1 [146].

We make use of GUT-inspired relations to simplify the size of the parameter space. The considered set of free parameters is given by

$$\begin{aligned} &M_{1/2}, \quad M_0, \quad m_{\tilde{e}}, \quad m_{\tilde{L}}, \quad m_{\tilde{\nu}}, \quad \tan\beta = \frac{v_u}{v_d}, \quad \mu_{\rm eff}, \\ &\qquad\qquad A_0, \quad A_\lambda, \quad Y_\nu, \quad M_{Z'} \quad \text{and} \quad \theta_{E_6}\ , \end{aligned} \tag{4.2.1}$$

Table 4.2: *Ranges over which we allow the free parameters of Eq. (4.2.1) to vary.*

Parameter	Scanned range	Parameter	Scanned range
M_0	$[0,3]$ TeV	μ	$[-2,2]$ TeV
$M_{1/2}$	$[0,5]$ TeV	A_λ	$[-7,7]$ TeV
A_0	$[-3,3]$ TeV	$M_{Z'}$	$[1.98,5.2]$ TeV
$\tan\beta$	$[0,60]$	$m^2_{\tilde\nu}$	$[-6.8,9]$ TeV^2
θ_{E_6}	$[-\pi,\pi]$	$m^2_{\tilde e,\tilde l}$	$[0,1]$ TeV^2

Table 4.3: *Experimental constraints imposed within our scanning procedure in order to determine the parameter space regions of interest.*

Observable	Constraints	Ref.	Observable	Constraints	Ref.
M_h	125.09 ± 3 GeV (theo)	[27]	$\chi^2(\hat\mu)$	≤ 70	-
$\lvert\alpha_{ZZ'}\rvert$	$O(10^{-3})$	[220]	$M_{\tilde g}$	> 1.75 TeV	[133]
$M_{\chi^0_2}$	> 62.4 GeV	[120]	$M_{\chi^0_3}$	> 99.9 GeV	[120]
$M_{\chi^0_4}$	> 116 GeV	[120]	$M_{\chi^\pm_i}$	> 103.5 GeV	[120]
$M_{\tilde\tau}$	> 81 GeV	[120]	$M_{\tilde e}$	> 107 GeV	[120]
$M_{\tilde\mu}$	> 94 GeV	[120]	$M_{\tilde t}$	> 900 GeV	[134]
$\text{BR}(B^0_s \to \mu^+\mu^-)$	$[1.1, 6.4] \times 10^{-9}$	[123]	$\dfrac{\text{BR}(B\to\tau\nu_\tau)}{\text{BR}_{SM}(B\to\tau\nu_\tau)}$	$[0.15, 2.41]$	[122]
$\text{BR}(B^0 \to X_s\gamma)$	$[2.99, 3.87] \times 10^{-4}$	[121]			

where we have enforced a unification relation at the GUT scale relating the $U(1)'$, hypercharge, weak and QCD gaugino soft masses $M_1' = M_1 = M_2 = M_3 = M_{1/2}$ as well as the hypercharge, weak and $U(1)'$ gauge couplings $g_1 = g_2 = g'\sqrt{3/5}$. Constraining the SUSY scale to be below 5 TeV, renormalization group evolution implies, at the SUSY scale, that $6M_1 \approx 3M_2 \approx M_3$. We have moreover required that all squark soft masses and trilinear couplings respectively unify to common values M_0 and $A_0 Y_q$ at the GUT scale, the slepton and sneutrino masses $m_{\tilde e}$, $m_{\tilde L}$ and $m_{\tilde\nu}$ being kept independent whereas the leptonic trilinear coupling A_e is taken vanishing. The neutrino Yukawa matrix is finally fixed to a diagonal matrix with entries equal to 10^{-11}.

Our parameter space investigation relies on the Metropolis-Hasting sampling method where the free parameters of Eq. (4.2.1) are allowed to vary in the ranges given in Table 4.2, the lower bound on the mass of the Z' boson being the minimum value allowed for any choice of the $U(1)'$ symmetry (and corresponds to the $U(1)'_\eta$ case). This mass has been taken smaller than the one quoted in the 2016 Particle Data Group review [120] in order to allow for significant branching fractions for the Z' boson decays into a pair of supersymmetric particles [221]. We have retained scenarios for which the predictions for the observables listed in Table 4.3 agree with the experimental data. Constraints arising from the Higgs sector, namely a theory-experiment agreement for the Higgs boson mass, the gluon and vector boson fusion Higgs boson production cross-sections, and the Higgs signal strengths, have been applied by using HIGGSBOUNDS and HIGGSSIGNALS. This is achieved by evaluating the Higgs boson production rate in the gluon and vector boson fusion channels with the SUSHI program version 1.5 [140] and by then comparing the predictions to $\sigma(gg \to h) = 19.27^{+1.76}_{-4.44}$ pb and $\sigma(VV \to h) = 1.55^{+0.058}_{-0.039}$ pb for a centre-of-mass energy of 8 TeV and $\sigma(gg \to h) = 50.74^{+4.68}_{-11.6}$ pb for a centre-of-mass energy of 14 TeV [222]. We next derive a $\chi^2(\hat{\mu})$ quantity for each, estimating the deviation from the experimental data, the sum of which we enforce to be smaller than 70. We have moreover severely restricted any possible kinetic mixing between the Z and the Z' bosons, and required that the associated mixing angle $\alpha_{ZZ'}$ is of the order of 10^{-3}. We have additionally verified that predictions for the gluino mass $M_{\tilde{g}}$, the neutralino and chargino masses $M_{\tilde{\chi}^0_i}$ and $M_{\tilde{\chi}^\pm_i}$, the slepton masses $M_{\tilde{e}}$, $M_{\tilde{\mu}}$ and $M_{\tilde{\tau}}$ and the stop mass $M_{\tilde{t}}$ satisfy the experimental bounds [120]. We have also imposed constraints arising from B-physics that are related to rare B-meson decays, and checked that the three branching ratios $\mathrm{BR}(B^0_s \to \mu^+\mu^-)$, $\mathrm{BR}(B \to \tau\nu_\tau)$ and $\mathrm{BR}(B^0 \to X_s\gamma)$ agree with existing data.

4.2.2 General considerations and phenomenology of the Higgs sector

In Fig. 4.2 we present the results of our scan. We project the ensemble of accepted scenarios onto four two-dimensional planes in order to exhibit possible correlations between the $U(1)'$ mixing angle and the $U(1)'$ coupling g' (upper left panel), the superpotential parameter λ (upper right panel), $\tan\beta$ (lower left panel) and the effective μ_{eff} parameter (lower right panel). We moreover distinguish the classes of scenarios for which the LSP is a sneutrino (light blue points) and a neutralino (dark blue points).

In the upper left panel of Fig. 4.2, we observe that the g' coupling is in general large, which indicates that the $U(1)'$ interactions must be strong to satisfy all the imposed constraints. Whereas the value of g' is maximal in the context of $U(1)'_\psi$ models, it is generally highly dependent on many other parameters so that a large range of values can be probed, regardless of the precise choice of θ_{E_6}. We however observe that θ_{E_6} values around $\pm\pi/2$ do not offer any option for a phenomenologically viable scenario. This in particular disfavours the $U(1)'_S$ and $U(1)'_\chi$ models, as already suggested by the results of Fig. 4.1 where the $U(1)'$ charge of the electroweak singlet approaches zero for $\theta_{E_6} \approx \pm\pi/2$. In this case, the scalar

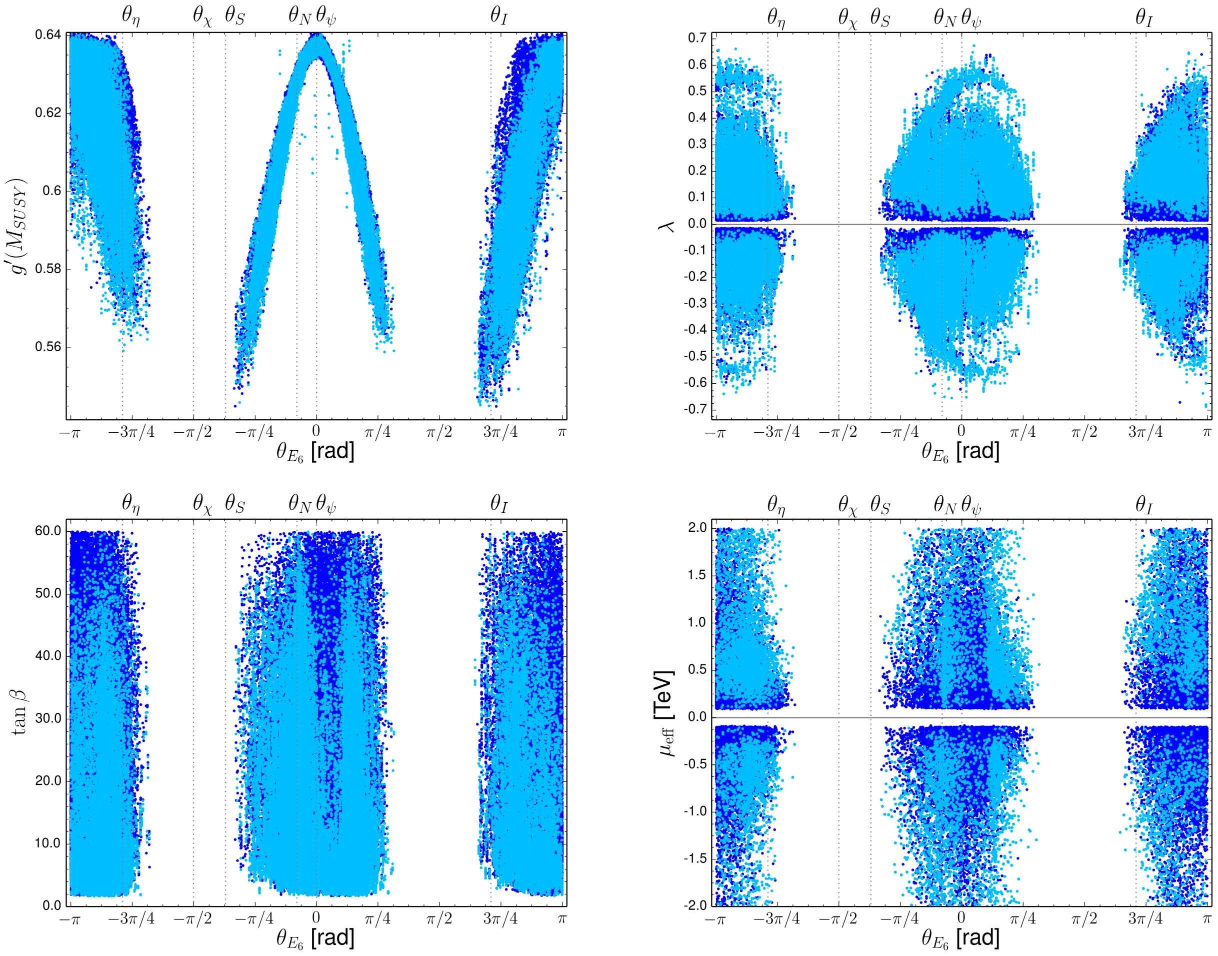

Figure 4.2: *Distributions in the UMSSM parameter space of the scenarios in agreement with the constraints imposed on section 4.2.1. Results are projected into the* (θ_{E_6}, g') *(upper left panel),* (θ_{E_6}, λ) *(upper right panel),* $(\theta_{E_6}, \tan\beta)$ *(lower left panel) and* $(\theta_{E_6}, \mu_{\rm eff})$ *planes. The light and dark blue points respectively represent scenarios in which the lightest sneutrino and the lightest neutralino is the LSP.*

field s is not sufficient to break the $U(1)'$ symmetry and one cannot construct any predictable scenario.

The general features of the Higgs sector are then analysed in the three other panels of Fig. 4.2. The distribution of the λ parameter as a function of the θ_{E_6} angle depicts how the weak singlet and doublets of Higgs fields mix. This information is also represented in the lower right panel of the figure where the λ parameter is traded for the effective μ_{eff} parameter to which it is proportional. While all possible values (different enough from zero and below 0.6 in absolute value) are in principle possible regardless of the mixing angle value, the anomaly-free $U(1)'_I$ model has the particularity to forbid $|\lambda| \gtrsim 0.3$. This stems from the structure of the $U(1)'$ charges that are small or vanishing for several supermultiplets and the lower bound on the Z' mass in the scanning procedure that both forbid λ to be too large. A similar effect being also observed for $\theta_{E_6} \approx -\pi/4$. The λ parameter must additionally be sufficiently large, in absolute value, to induce a successful EWSB so that λ values close to zero are forbidden.

While in general a sneutrino LSP can be obtained for any value of $\tan\beta$, this turns out to be easier in the case of $U(1)'_N$ models. These are scenarios where the right neutrino supermultiplet is not charged under the extended gauge symmetry, and right sneutrino masses do not therefore receive any contribution from the D-terms and mostly arise from the independent soft mass terms. As a result, one gets more freedom on $\tan\beta$ that can be consequently lower. A similar feature, but less pronounced, can be observed for other θ_{E_6} values where a combination of several zero $U(1)'$ charges leads to the same conclusions.

We further investigate the properties of the Higgs sector in Fig. 4.3 where we present both the mass difference between the SM-like Higgs boson and the next-to-lightest Higgs boson, $|M_{h_1} - M_h|$, in the left panel of the figure and the dependence of M_{h_1} on the Z'-boson mass in the right panel of the figure. As the singlet VEV drives the Z' boson mass, the second lightest Higgs boson has a mass of at most roughly the Z'-boson mass and is in this case singlet-dominated. In the lighter cases, it is mostly a doublet admixture and thus MSSM-like. There are a few scenarios featuring a sneutrino LSP where the second Higgs and the Z' bosons are almost degenerate, but any hierarchy can however be realised. The second Higgs boson is however at least 500 GeV heavier than the SM-like Higgs boson, which originates from the Higgs mixing pattern and the minimum value of the singlet VEV v_S (that stems from the $M_{Z'}$ lower limit imposed in our scan). Once again, smaller λ values obtained for the case of the $U(1)'_I$ scenario impact the spectrum and M_{h_1} is in general consequently

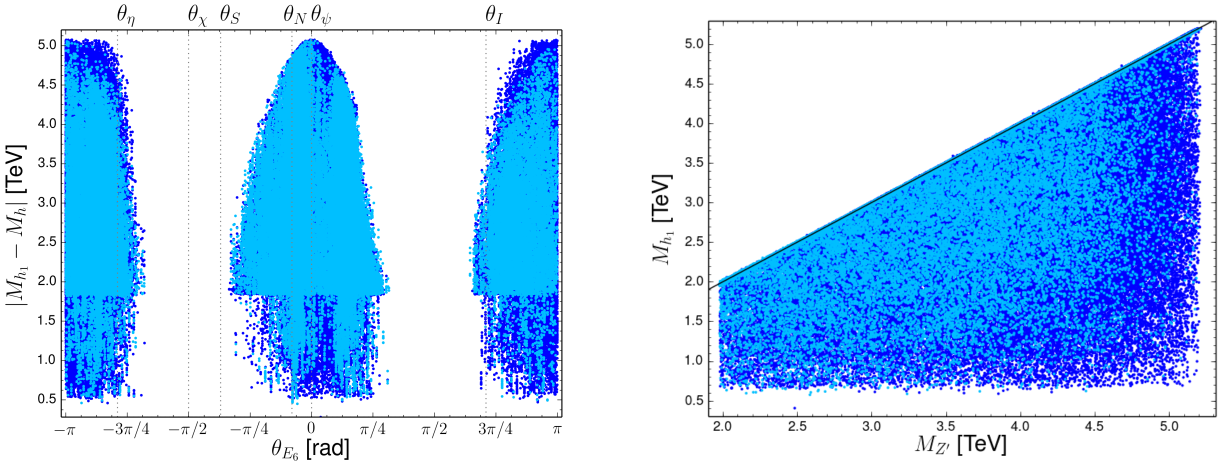

Figure 4.3: *Same as in Fig. 4.2 but for projection in the* $(\theta_{E_6}, |M_{h_1} - M_h|)$ *(left panel) and* $(\theta_{E_6}, M_{Z'})$ *(right panel) planes.*

smaller, the effects driven by the large v_S value being tamed by the smaller λ value.

4.2.3 Z' phenomenology

Typical Z' phenomenology can be dramatically different in the presence of supersymmetry, in particular due to the existence of new Z' decay channels into pairs of SUSY particles. This is illustrated in Fig. 4.4 where we analyse different options for the Z' decays as a function of the mixing angle θ_{E_6}.

Our results show that there is very little hope to be able to use Z' decay rates to differentiate $U(1)'$ models. Decays into slepton pairs are consistently small, while leptonic channels, that are also present in non-supersymmetric cases, exhibit branching ratios ranging from 0 to about 50%. A leptophobic behaviour emerges for specific mixing angles, but these features can be reproduced for other realisations where a large leptonic Z' branching fraction is as well common. This nevertheless leads to one of the most promising channels to look for a sign of $U(1)'$ new physics, by bump hunting in the dilepton mass distribution for LHC events featuring two opposite-sign final state leptons, provided the branching is large enough. The same conclusion holds for the dijet decay mode that corresponds to the preferred Z' decay mode, regardless of the value of θ_{E_6}. The only limiting factor is, both for the dilepton and dijet case, the Z' mass driving the production cross section and the associated phase space suppression in the heavy case.

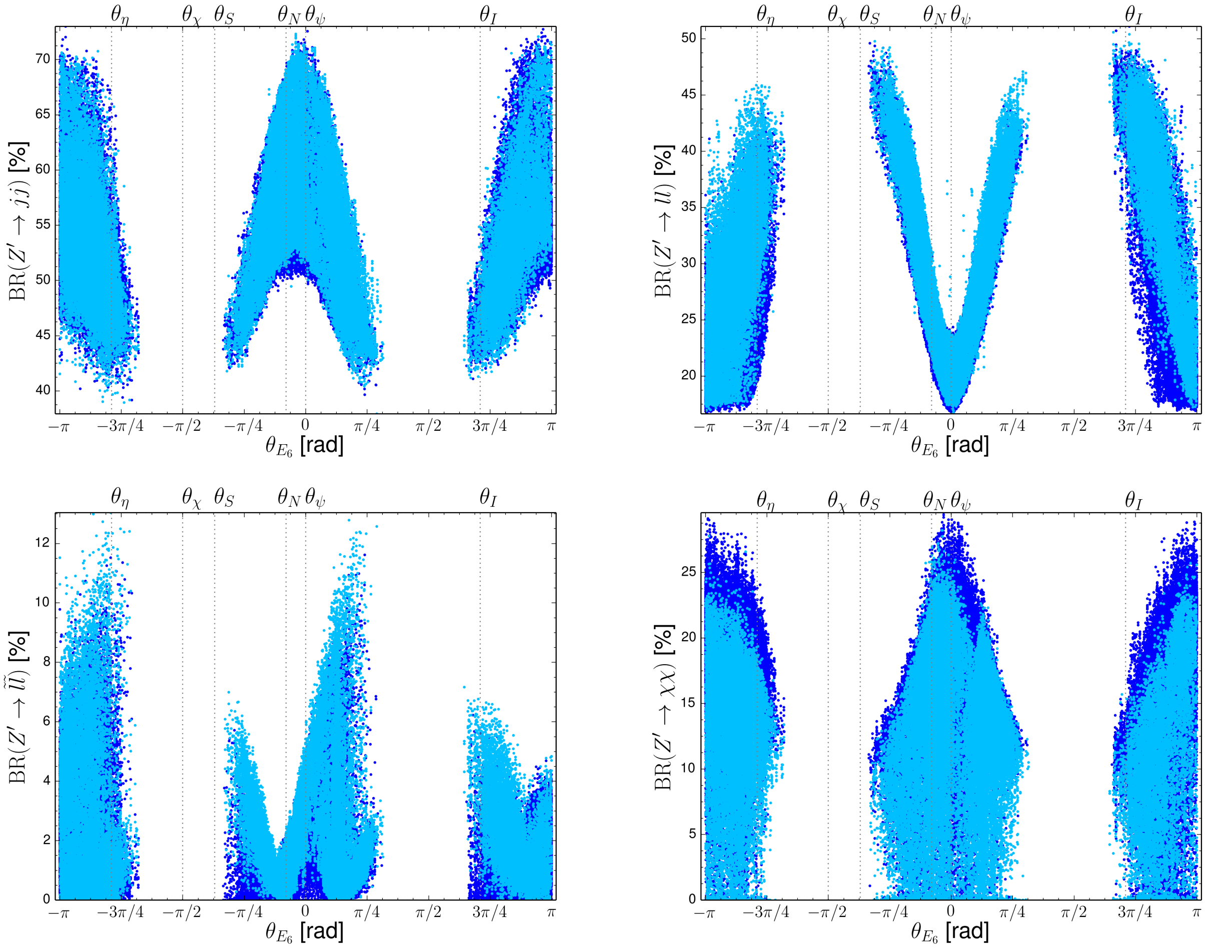

Figure 4.4: *Same as in* Fig. 4.2 *but for the branching ratios of the Z' boson for several decay channels, namely the Z' decays into a pair of jets (upper left), a pair of leptons (upper right), a pair of sleptons (lower left) and a pair of neutralinos or charginos (lower right).*

In the lower right panel of the figure, we investigate the magnitude of the Z' branching fraction into a pair of neutralinos or charginos. Such decays can often be abundant, with a branching ratio reaching about 20%, and yield a Z' signature made of both leptons and missing energy. This potentially allows for the distinction of SUSY and non-SUSY Z'-bosons.

4.2.4 The anomalous magnetic moment of the muon

Pioneering results from the Brookhaven National Laboratory (BNL) E821 experiment [223], their improvements at the Fermi National Accelerator Laboratory (FNAL) E989 experiment [224] and the anticipated results obtained from the Japan Proton Accelerator Research Complex (J-PARC) E34 experiment [225] have provided a very precise measurement of the anomalous magnetic moment of the muon $(g-2)_\mu$. The measured value departs by about 3σ from the SM expectation,

$$a_\mu^{\rm SM} = 116591828(2)(43)(26) \times 10^{-11} \ ,$$

which constitutes a challenge for beyond the SM model building. In the UMSSM framework, both the presence of the extra gauge boson and a neutral and charged (s)lepton sector in the presence of a sneutrino or neutralino LSP can have a drastic impact on the anomalous magnetic moment of the muon via loop-induced contributions. As the LSP is often much lighter than the Z' boson, the corresponding SUSY contributions are expected to be more important than any additional Z' contribution. As in the MSSM, new physics effects on $(g-2)_\mu$ are therefore mostly depending on $\tan\beta$ and the effective $\mu_{\rm eff}$ parameter, which determine the higgsino masses and the fermion and sfermion interactions with the higgs(ino) sector.

For each point of our parameter space scan, we present in the upper panel of Fig. 4.5 the UMSSM contributions to $(g-2)_\mu$, that we denote by Δa_μ, and that is expected to fill the gap between the theoretical predictions and $(g-2)_\mu$ data. The dependence of Δa_μ on the $\mu_{\rm eff}$ parameter is depicted on the left panel of the figure, and we observe that the gap between the experimental measurement and the theoretical prediction can only be filled for positive value of $\mu_{\rm eff}$. As in the MSSM, this originates from neutralino and slepton loop contributions that are proportional to $\mu_{\rm eff}$, so that a negative $\mu_{\rm eff}$ value would increase and not decrease the discrepancy between theory and experiment. Sneutrino LSP scenarios mostly feature a small

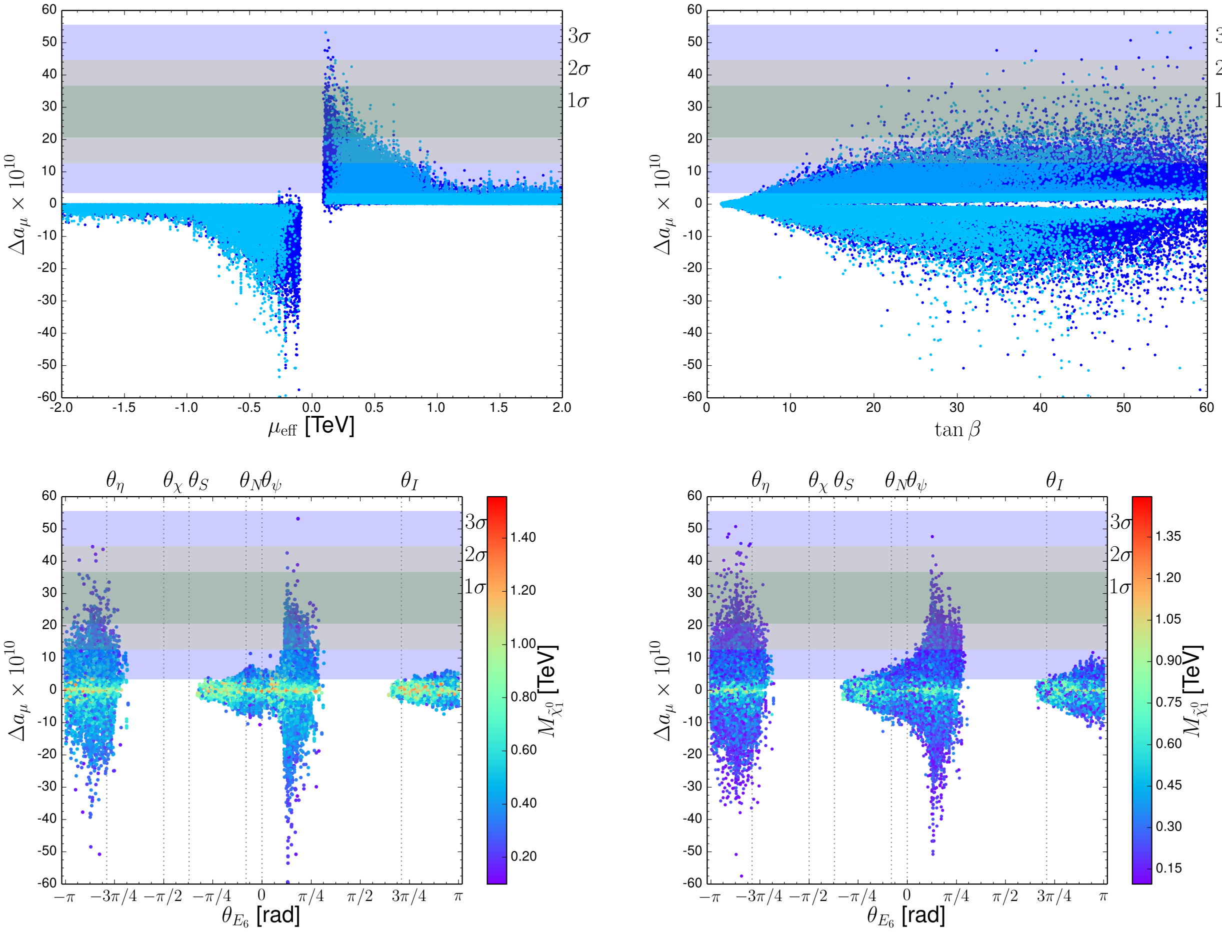

Figure 4.5: *UMSSM contributions to the anomalous magnetic moment of the muon, Δa_μ shown as a function of the effective $\mu_{\rm eff}$ parameter (upper left) and $\tan\beta$ (upper right). The light (dark) blue points represent scenarios in which the lightest sneutrino (neutralino) is the LSP. On the lower panels of the figure, we present the θ_{E_6} dependence of Δa_μ and depict by a colour code the mass of the lightest neutralino for scenarios with a sneutrino (lower left panel) and with a neutralino (lower right panel) LSP. On all figures, we moreover indicate by a green, grey and purple band the Δa_μ values for which we get an agreement at the 1σ, 2σ and 3σ level with the experimental value, respectively.*

μ_{eff} value, as already found in Fig. 4.2, which implies that the lightest neutralino is in general not too heavy. As a consequence, the corresponding contributions to $(g-2)_\mu$ are sizable and theoretical predictions agree better with data (for cases where $\mu_{\text{eff}} > 0$). This agreement is in addition facilitated for large $\tan\beta$ values, as shown in the right panel of the figure. Neutralino LSP scenarios in contrast allow for intermediate μ_{eff} values, so that resulting Δa_μ new physics contributions are not large enough to entirely fill the experiment-theory gap due to a heavy neutralino mass suppression.

These conclusions are further confirmed by the lower panel of Fig. 4.5 in which we show the variation of Δa_μ as a function of the $U(1)'$ mixing angle θ_{E_6} and correlate the results with the value of the mass of the lightest neutralino for sneutrino LSP scenarios (left panel) and neutralino LSP scenarios (right panel). We observe that in contrast to the other models, $U(1)'_I$ scenarios are unable to provide an explanation for the $(g-2)_\mu$ observations. This is connected to the larger $M_{1/2}$ mass parameter typical of these scenarios. The contributions from $U(1)'$ supersymmetric models to Δa_μ are dominated by slepton-neutralino loop diagrams, and are maximal for light sleptons. This occurs when the D-terms proportional to Q_l in the slepton mass matrix are zero as in Fig. 4.1, which corresponds to the peaks appearing in the lower panel graphs of Fig. 4.5.

4.3 Sneutrino Dark Matter

In this section we concentrate on scenarios exhibiting a sneutrino LSP and show that sneutrinos are UMSSM viable dark matter candidates, in contrast to the MSSM possibly extended with right sneutrinos. Unlike in a theory featuring only the SM gauge group, right sneutrinos can reach, in the UMSSM, thermal equilibrium thanks to their $U(1)'$ interactions with extra vector and/or scalar fields. Moreover, the sneutrino pair annihilation cross section is possibly enhanced by s-channel resonant (or near-resonant) exchanges, and the elastic scattering cross section of a dark matter particle with a SM parton is suppressed by several orders of magnitude as sneutrino couplings to the SM Z and Higgs bosons are reduced and the would-be dominant Z' exchange is mass-suppressed.

Our thorough investigation of the MSSM parameter space has revealed that, when allowing the model parameters to be small and run freely, the lightest neutralino naturally emerges as the LSP. Requiring a sneutrino to be the LSP implies more specific and less general corners of the parameter space, which is not necessarily an issue as the absence of any beyond the SM signal at the LHC could be an indication for a non-natural new physics setup. We now focus on the dark matter implications for all scanned scenarios exhibiting a sneutrino LSP in the $U(1)'_\psi$, $U(1)'_\eta$ and $U(1)'_I$ models, that are the three-anomaly free UMSSM setups satisfying so far all current constraints, and investigate constraints originating from the dark matter relic abundance in section 4.3.1 and direct detection and neutrino fluxes in section 4.3.2.

4.3.1 Relic Density

In order to analyse the constraints that could originate from the relic density on the UMSSM models, we explicitly choose two possibilities for the Z'-boson mass, a light Z'-boson case with $M_{Z'} = 2$ TeV and a heavier Z'-boson case with $M_{Z'} = 2.5$ TeV. Although the former option is slightly less than the Z'-boson limits presented in the 2016 Particle Data Group review [120], we recall that such light extra bosons are allowed in UMSSM scenarios where Z' decays into pairs of supersymmetric particles contribute significantly. Moreover, we use the results of our scan to enforce the values for other parameters to lead to a viable Higgs boson mass and a fair agreement with all other experiment constraints. The relic density contributions stemming from the presence of a Z' boson are crucial for models such as the UMSSM where the field content of the theory includes right sneutrinos that are not sensitive to the SM gauge interactions. Whilst a full parameter space scan could be in order, the above procedure allows us to study and understand the impact of specific parameters on the relic density, and in particular of the effective μ_{eff} parameter and the trilinear coupling A_λ, as in general, sneutrino DM is usually overabundant as a result of an inefficient sneutrino annihilation mechanism. We use as experimental bounds for the relic density the conservative range provided from the older WMAP data [226, 227] and including a 20% uncertainty,

$$\Omega_{\text{DM}} h^2 = 0.111^{+0.011}_{-0.015} \ .$$

Fixing first $M_{Z'}$ to 2 TeV, we investigate the dependence of the relic density on the mass of the lightest sneutrino, after selecting varied choices of $M_{\tilde{\chi}_1^0}$, μ_{eff} and A_λ. In addition, the $\tan\beta$, M_0 and A_0 parameters are modified correspondingly to recover a correct lightest Higgs boson mass of 125 GeV, and agreement with all the previously discussed experimental constraints. We consider, in our analysis, three parameter space regions on the basis of the mass of the lightest neutralino, which is most often the next-to-lightest superpartner (NLSP),

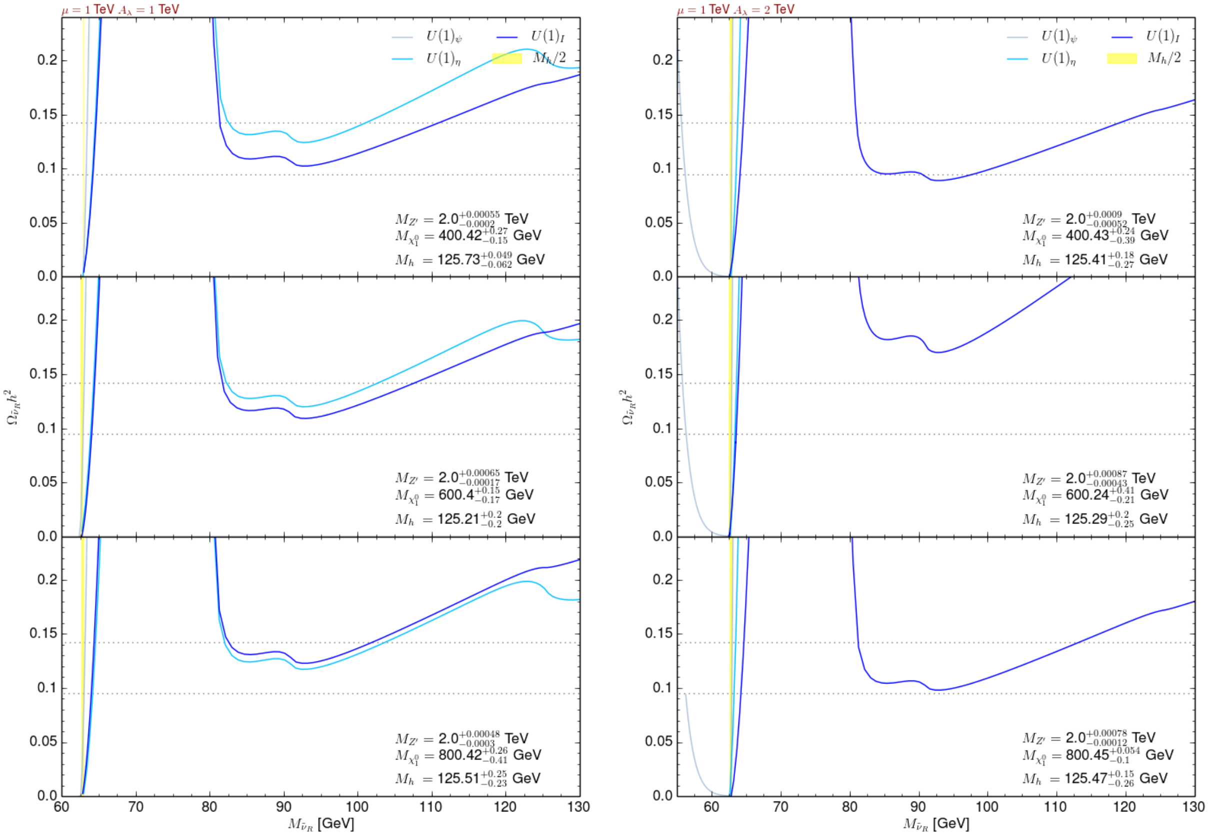
$\mu = 1$ TeV $A_\lambda = 1$ TeV
$\mu = 1$ TeV $A_\lambda = 2$ TeV
$U(1)_\psi$
$U(1)_\eta$
$U(1)_I$
$M_h/2$
$\Omega_{\tilde{\nu}_R} h^2$
$M_{\tilde{\nu}_R}$ [GeV]
$M_{Z'} = 2.0^{+0.00055}_{-0.0002}$ TeV
$M_{\chi_1^0} = 400.42^{+0.27}_{-0.15}$ GeV
$M_h = 125.73^{+0.049}_{-0.062}$ GeV
$M_{Z'} = 2.0^{+0.0009}_{-0.00052}$ TeV
$M_{\chi_1^0} = 400.43^{+0.24}_{-0.39}$ GeV
$M_h = 125.41^{+0.18}_{-0.27}$ GeV
$M_{Z'} = 2.0^{+0.00065}_{-0.00017}$ TeV
$M_{\chi_1^0} = 600.4^{+0.15}_{-0.17}$ GeV
$M_h = 125.21^{+0.2}_{-0.2}$ GeV
$M_{Z'} = 2.0^{+0.00087}_{-0.00043}$ TeV
$M_{\chi_1^0} = 600.24^{+0.41}_{-0.21}$ GeV
$M_h = 125.29^{+0.2}_{-0.25}$ GeV
$M_{Z'} = 2.0^{+0.00048}_{-0.0003}$ TeV
$M_{\chi_1^0} = 800.42^{+0.26}_{-0.41}$ GeV
$M_h = 125.51^{+0.25}_{-0.23}$ GeV
$M_{Z'} = 2.0^{+0.00078}_{-0.00012}$ TeV
$M_{\chi_1^0} = 800.45^{+0.054}_{-0.1}$ GeV
$M_h = 125.47^{+0.15}_{-0.26}$ GeV
0.0
0.05
0.1
0.15
0.2
60
70
80
90
100
110
120
130

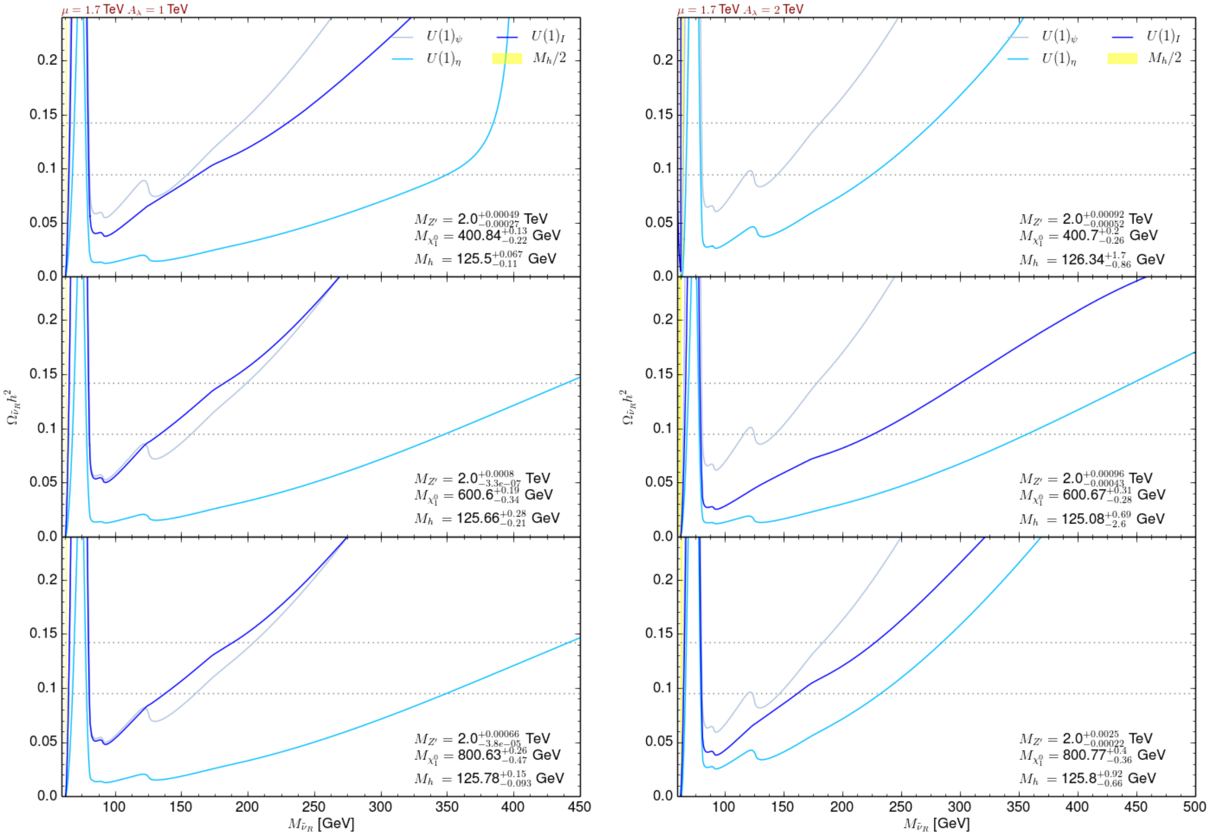

Figure 4.6: *Dependence of the relic density for UMSSM scenarios featuring a right sneutrino LSP and* $M_{Z'} = 2$ *TeV. We fix* $\mu_{\rm eff}$ *to 1 TeV (upper panels) and 1.7 TeV (lower panels), as well as* A_λ *to 1 TeV (left panels) and 2 TeV (right panels). In each of the four figures, the lightest neutralino mass has been respectively fixed to 400 GeV (upper inset), 600 GeV (middle inset) and 800 GeV (lower inset) and we focus on the the* $U(1)'_\psi$ *(grey),* $U(1)'_\eta$ *(light blue) and* $U(1)'_I$ *(dark blue) models.*

here taken to be 400 GeV, 600 GeV and 800 GeV respectively. Alongside the neutralino mass, μ_{eff} and A_λ are set to 1 or 1.7 TeV and 1 or 2 TeV respectively, this restricted set of values being sufficient to investigate the effects on these parameters on the dark matter relic density. The results are presented in Fig. 4.6.

In the upper right panel of the figure, we set $\mu_{\text{eff}} = A_\lambda = 1$ TeV and show that regardless of the value of the lightest neutralino mass and depending on the class of $U(1)'$ model, there exist two regimes where the predicted relic density matches the observations. First, in a region where the sneutrino mass is close to 65 GeV, one can design $U(1)'_\eta$, $U(1)'_\psi$ and $U(1)'_I$ UMSSM models where the relic density bounds are satisfied. A correct dark matter annihilation cross section can be achieved thanks to the enhanced contributions of Higgs-boson exchange diagrams that proceed in a resonant or near-resonant production mode ($M_{\tilde{\nu}_1} \approx M_h/2$). This configuration, also known as a Higgs funnel configuration, is achievable for any value of the μ_{eff} and A_λ parameters, as shown in the other panels of Fig. 4.6, although the value of A_λ affects its size. The Higgs funnel region is indeed narrower for larger A_λ values. While a similar regime could be expected for $M_{\tilde{\nu}_1} \approx M_{Z'}/2$, this latter setup implies very heavy sneutrinos that are then incompatible with the requirement of a sneutrino being the LSP.

A second kinematical regime allows for the recovery of a proper relic density, with a sneutrino mass lying in the $[80, 110]$ GeV window for $\mu_{\text{eff}} = A_\lambda = 1$ TeV (upper left panel of the figure). In this regime, both dark matter annihilation into a pair of Z-bosons and LSP-NLSP co-annihilations are important, as noticed by the size of the region depending on the mass of the lightest neutralino. Investigating the other panels of the figure, one observes that the exact details of this region of the parameter space, as well as its existence, strongly depend on the values of the μ_{eff} and A_λ parameters. The latter indeed directly affect the nature of the lightest neutralino and the properties of the heavier part of the Higgs sector, h_1 exchange contributions being very relevant for a not too heavy next-to-lightest Higgs boson (see Fig. 4.3).

Z'-boson exchange contributions play nevertheless a key role in the calculation of the relic density. For instance, in $U(1)'_\psi$ scenarios, the new gauge interactions of the sneutrinos are relatively weaker (due to the involved $U(1)'$ charges), the corresponding branching ratio being three times smaller than for the two other cases. As a result, the existence of the heavier sneutrino regime itself, in which the relic density constraints are correctly satisfied, is more challenging. This feature is emphasised on Fig. 4.7 where the Z'-boson mass is pushed

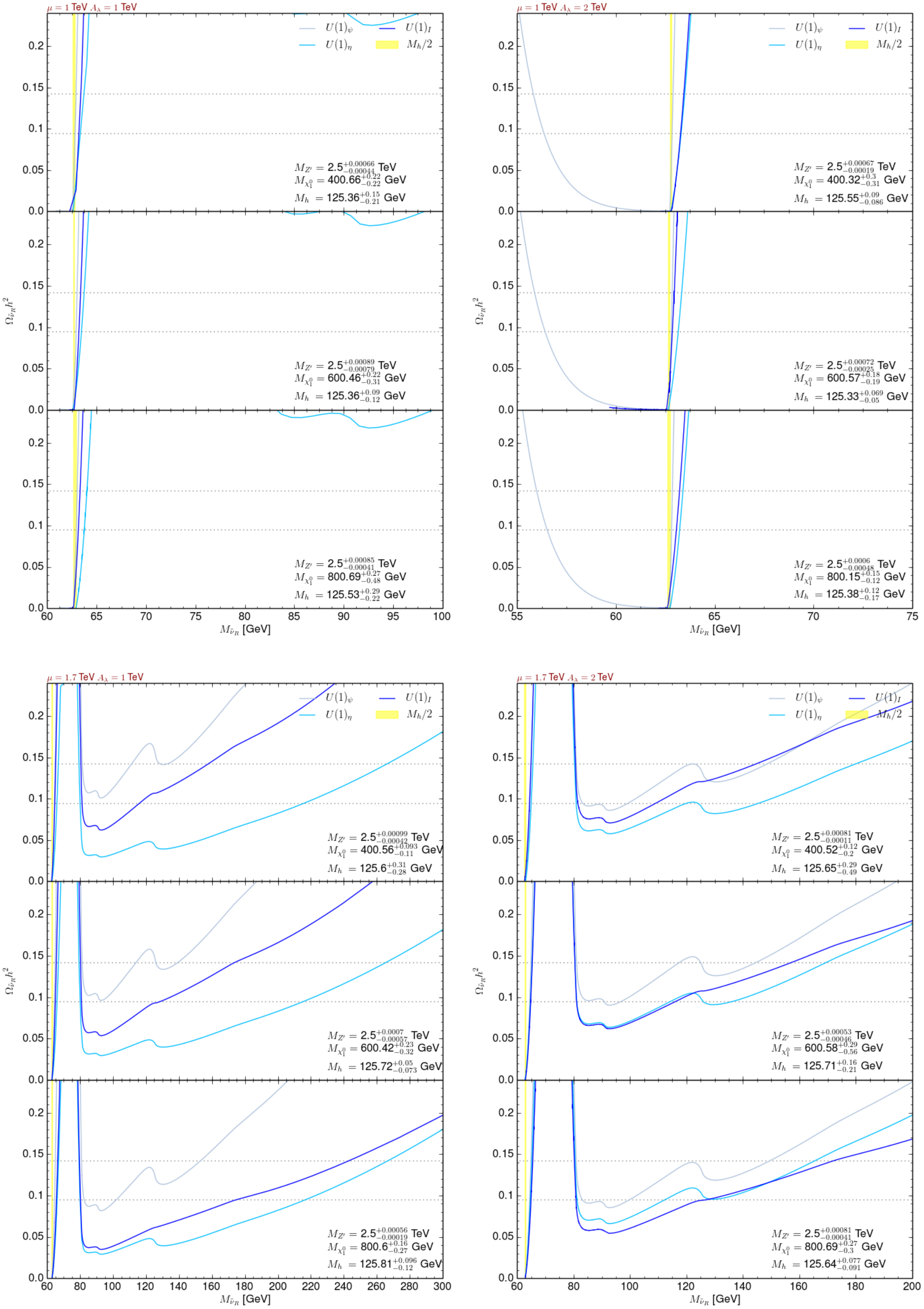

Figure 4.7: *Same as in Fig. 4.6 but for* $M_{Z'} = 2.5$ *TeV.*

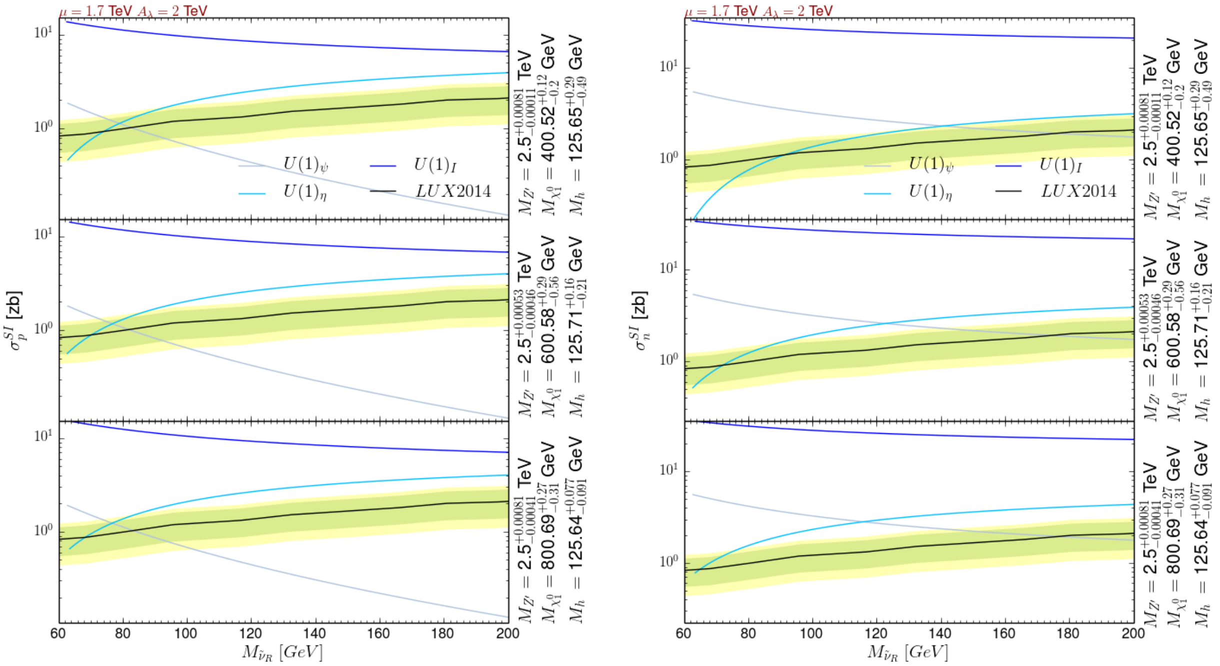

Figure 4.8: *Spin independent cross section associated with the scattering of dark matter off protons (left) and neutrons (right) presented as functions of the dark matter mass. We fix* $\mu_{\rm eff}$ *to 1.7 TeV and* A_λ *to 2 TeV. In each of the subfigures, the lightest neutralino mass has been respectively fixed to 400 GeV (upper inset), 600 GeV (middle inset) and 800 GeV (lower inset) and we focus on the* $U(1)'_\psi$ *(grey),* $U(1)'_\eta$ *(light blue) and* $U(1)'_I$ *(dark blue) models. The band corresponds to the* 2σ *limits extracted from LUX data [158, 159].*

to 2.5 TeV, the other $M_{\tilde\chi_1^0}$, A_λ and $\mu_{\rm eff}$ parameters being varied as before whereas the $\tan\beta$, M_0 and A_0 parameters are once again adjusted to reproduce all previously considered constraints. Although the existence of the Higgs funnel regime is barely affected by the changes, this regime may be shifted towards lighter sneutrino masses in the $[50, 65]$ GeV regime. In addition, heavier sneutrino LSP scenarios are more difficult to accommodate, which directly prevents the heavy sneutrino regime with a consistent relic density from existing, in particular if the $\mu_{\rm eff}$ parameter is not large enough.

4.3.2 Constraints from dark matter direct detection and neutrino fluxes

Direct detection experiments aim to detect DM scattering off nuclear matter and to measure its properties. While the DM interactions with nuclear matter can be generally classified as spin-dependent or spin-independent, only the latter is relevant for sneutrino dark matter. We

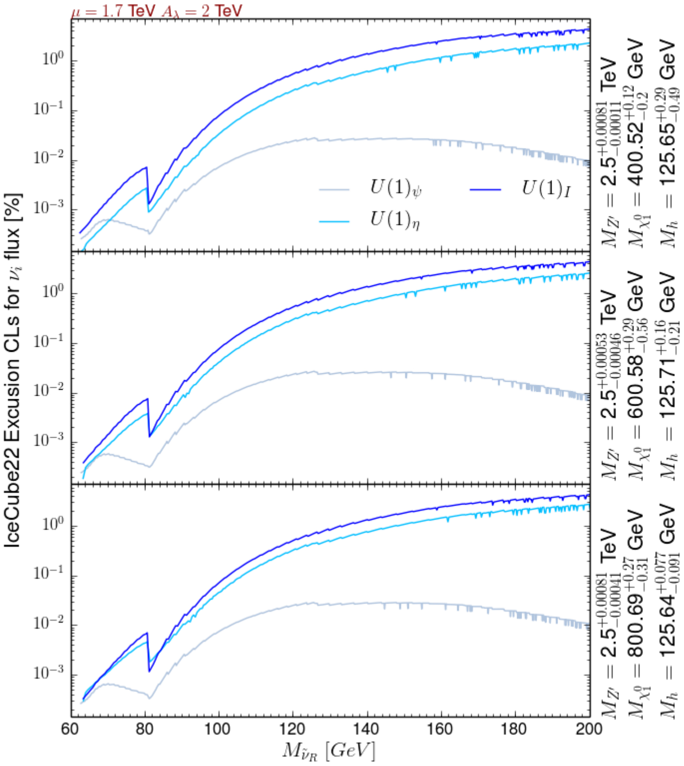

Figure 4.9: *Exclusion bounds, given as a confidence level, extracted from the neutrino flux observed in the IceCube experiment and presented as a function of the lightest sneutrino mass. The UMSSM scenario is fixed as in Fig. 4.8.*

present, in Fig. 4.8, UMSSM predictions for the spin-independent cross section associated with the scattering the LSP with protons (left panel) and neutrons (right panel), and compare them with the experimental results from the LUX experiment [158]. We adopt UMSSM scenarios in which $\mu_{\rm eff} = 1.7$ TeV and $A_\lambda = 2$ TeV, and the Z' mass is fixed to 2.5 TeV. As in the previous section, the results are given for lightest neutralino masses of 400 GeV (top inset), 600 GeV (central inset) and 800 GeV (lower inset).

Our results demonstrate the discriminating power of the spin-independent DM-nucleon scattering cross section as its behaviour as a function of the mass of the sneutrino LSP highly depends on the $U(1)'$ model. For a given LSP mass, cross section values obtained in $U(1)'_I$ models are one order of magnitude larger than for the two other classes of models, $U(1)'_\eta$ cross sections increasing in addition with the sneutrino mass. The results of the LUX experiment introduce strong constraints on wide regions of the parameter space, and our specific $\mu_{\rm eff}$ and A_λ choice are typical from the parameter space region in which both the relic density and the direct detection constraints can be easily accommodated. This however introduces tensions with the parameter space regions favoured by the anomalous magnetic moment of the muon results (see section 4.2.4), and only the Higgs funnel region in which the sneutrino mass is half of the Higgs-boson mass survives too all constraints.

While $U(1)'_I$ models are clearly disfavoured by direct detection data, $U(1)'_\psi$ scenarios cannot feature a viable light sneutrino DM, whilst $U(1)'_\eta$ setups in contrast prefer light LSP configurations with a sneutrino mass of about 60 GeV to 100 GeV depending on the neutralino mass. These results stem from the interaction of the lightest sneutrino with the Z, Z' and Higgs bosons. As the lightest sneutrino only very weakly couples to the SM sector, the scattering cross section mostly depends on the vectorial couplings of the LSP and of the SM quarks to the Z'-boson. These quark vectorial couplings being vanishing in the $U(1)'_\psi$ model, the resulting cross section is largely suppressed and those scenarios can survive more easily to LUX data. The neutron cross section, being larger as expected [198], however drastically reduces the size of the allowed region of the parameter space and future improvements in direct detection experiments may directly challenge the studied UMSSM setups.

Recent observations of ultra-high energy neutrino events at the IceCube experiment [228] indicate a possible deficit in the amount of observed muon tracks, which is known as the muon deficit problem, and an apparent energy gap in the three-year high energy neutrino data. This challenges any explanation based on atmospheric neutrinos, and suggests an extra-terrestrial origin that could involve dark matter. Data being however consistent with the SM expecta-

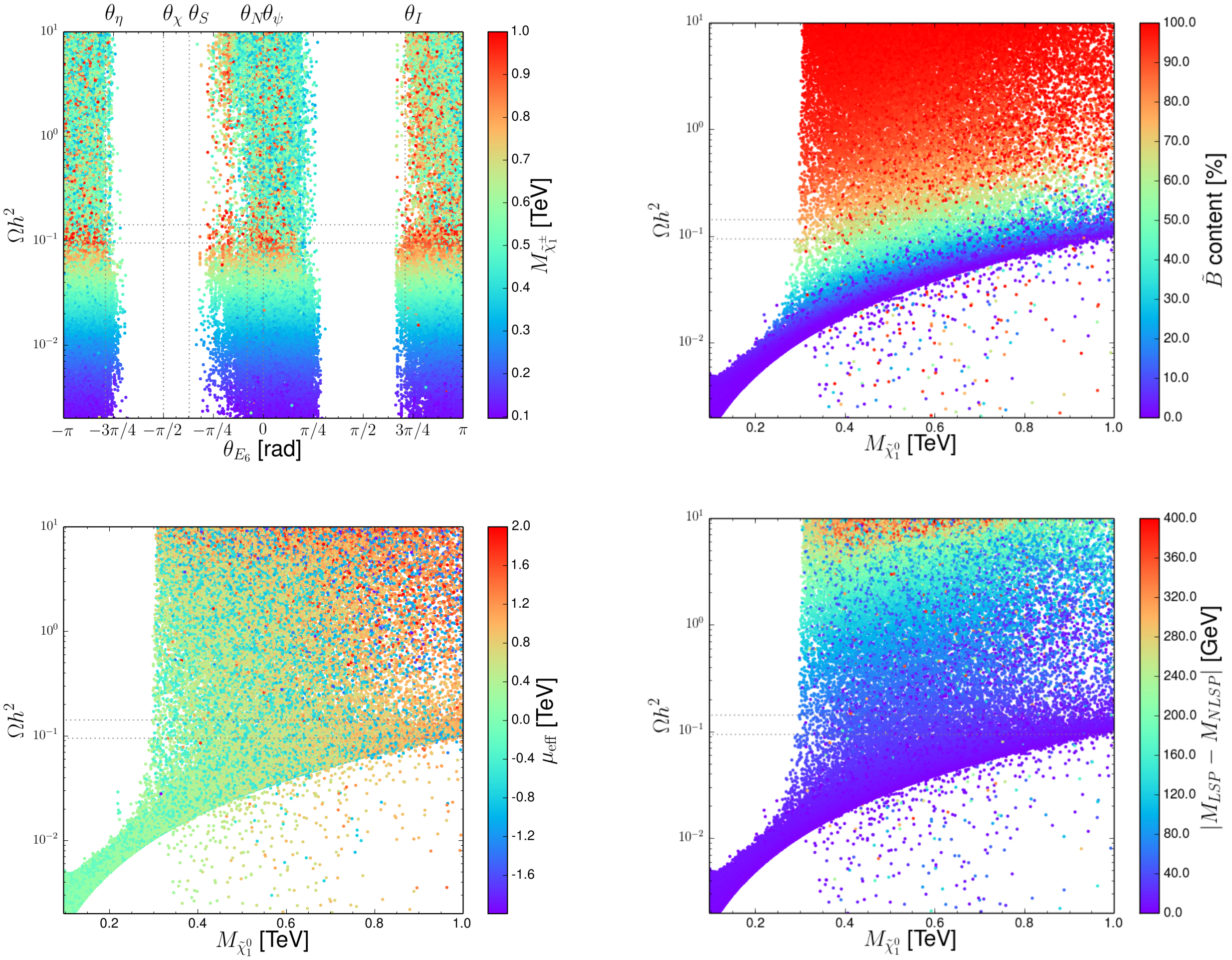

Figure 4.10: *DM relic density obtained for UMSSM scenarios featuring a neutralino LSP, presented as a function of the LSP mass and the* $U(1)'$ *mixing angle (upper left panel), the neutralino bino component (upper right panel), the* μ_{eff} *parameter (lower left panel) and the mass difference between the LSP and the NLSP (lower right panel).*

tion, this may introduce extra constraints when DM model building is at stake. We present, in Fig. 4.9, the corresponding exclusion as obtained in the UMSSM setup considered in this section with the help of MICROMEGAs. This shows that even if genuine differences amongst the three considered $U(1)'$ options once again appear, in particular for large sneutrino masses, all results are consistent with the SM to a good extent.

4.4 Neutralino dark matter

As shown in the above sections, the LSP can naturally be the lightest neutralino, that consists in UMSSM scenarios of an admixture of $\lambda_{\tilde{B}}$, $\lambda_{\tilde{W}}$ and $\lambda_{\tilde{Z}'}$ gauginos, as well as of higgsinos. Whether the LSP in a particular setup is able to yield the right relic abundance depends crucially on its composition. For a bino-dominated or a bino′-dominated neutralino, the LSP is a gauge singlet and it annihilates mainly through sfermion t-channel exchanges. As sfermions are heavy, the annihilation mechanism is often inefficient so that accommodating the observed relic density is difficult, unless one strongly relies on co-annihilations. The relic density can be more easily reproduced when the lightest neutralino is of a higgsino or wino nature, or a mixed state. If the LSP is higgsino-like, its mass is driven by the $\mu_{\rm eff}$ parameter, as is the mass of the lightest chargino and of the next-to-lightest neutralino. These three particles being almost degenerate, annihilations and co-annihilations easily occur so that DM could be underabundant if the LSP is too light [229]. In our setup the wino-like LSP is in contrast impossible to be realised due to the GUT relations that we have imposed in our scanning procedure.

Unlike for sneutrinos, the neutralino LSP mass is mainly determined by the $M_{1/2}$ and the $\mu_{\rm eff}$ parameters that also affect *all* the particle masses of the model. The LSP mass cannot be consequently varied independently of the rest of the spectrum, making an analysis based on specific benchmark configurations less straightforward than in the sneutrino LSP case. We therefore base our study on the results of our parameter space scan where all the constraints described in section 4.2.1 are imposed. Our results are given in Fig. 4.10 where we present the dependence of the DM relic density on the LSP mass. We correlate our findings with the value of the $U(1)'$ mixing angle θ_{E_6} (upper left panel), the magnitude of the LSP bino component (upper right panel), the value of the $\mu_{\rm eff}$ parameter (lower left panel) and the mass difference between the LSP and the NLSP (lower right panel). Accommodating the correct relic density yields a LSP mass of at least 300 GeV, which contrasts with sneutrino LSP scenarios where the mass of the latter is smaller. As expected, the lightest neutralino is mostly bino-like, and a higgsino component is only allowed for heavier LSP setups so that the co-annihilation rate turns out to be tamed. Viable DM scenarios also feature a small $\mu_{\rm eff}$ parameter lying in the $[-400, 400]$ GeV mass window, which allows the next-to-lightest neutralino to be higgsino-like and not too heavy, as emphasised in the lower right panel of the figure as it is often the NLSP. Co-annihilations are hence under good control, which guarantees a relic density in agreement with the observations. Our results also show that small differences are present for the different $U(1)'$ scenarios under consideration, the LSP mass being only in general slightly larger for $U(1)'_I$ models.

In Fig. 4.11, we include constraints that arise from DM direct detection experiments and correlate the proton-DM (upper left panel) and neutron-DM (upper right panel) spin-independent scattering cross section with the predicted relic density, including in addition information on the LSP mass for each point. This shows, together with the results of the lower right panel of the figure, that regardless of the LSP mass, there are always scenarios for which both the relic density and the direct detection constraints can be satisfied. We finally correlate, in the lower left panel of the figure, the relic density and the confidence level exclusion that can be obtained from the IceCube results on the neutrino flux. We observe that contrary to the sneutrino LSP case, here neutrino flux results play a role in constraining the UMSSM parameter space.

4.5 Collider signals

New physics models featuring a dark matter candidate can in general be equally tested with cosmology and collider probes and extra pieces of information can be obtained when both sources of constraints are considered in complementarily [230]. In the previous sections, we have discussed the DM phenomenology of UMSSM realisations in which the LSP is either the lightest sneutrino or the lightest neutralino, with the hope of getting handles allowing for the distinction of the gauge group structure. In this section, we focus on the potential searches that could be performed at the LHC, in particular when a part of the particle spectrum is light and when the high-luminosity LHC run is considered. To determine the signals to be searched for, we focus on a set of promising benchmarks obtained from our scan results for which all constraints are satisfied. This in particular concerns scenarios featuring a light sneutrino LSP. In order to evaluate the fiducial cross sections associated with various signals, we export the UMSSM to the UFO format [145] and make use of the MG5_aMC@NLO framework version 2.4.3 [144] to simulate hard-scattering LHC collisions. The QCD environment characteristic of hadronic collisions is simulated by means of the Pythia 8 program version 8.2.19 [231] and we rely on the Delphes 3 package version 3.3.2 [165] for the modelling of the response of a typical LHC detector. The resulting detector-level events are reconstructed by using the anti-k_T jet algorithm [167] as embedded in the FastJet library version 3.1.3 [166], and the reconstructed events are analysed within the MadAnalysis 5

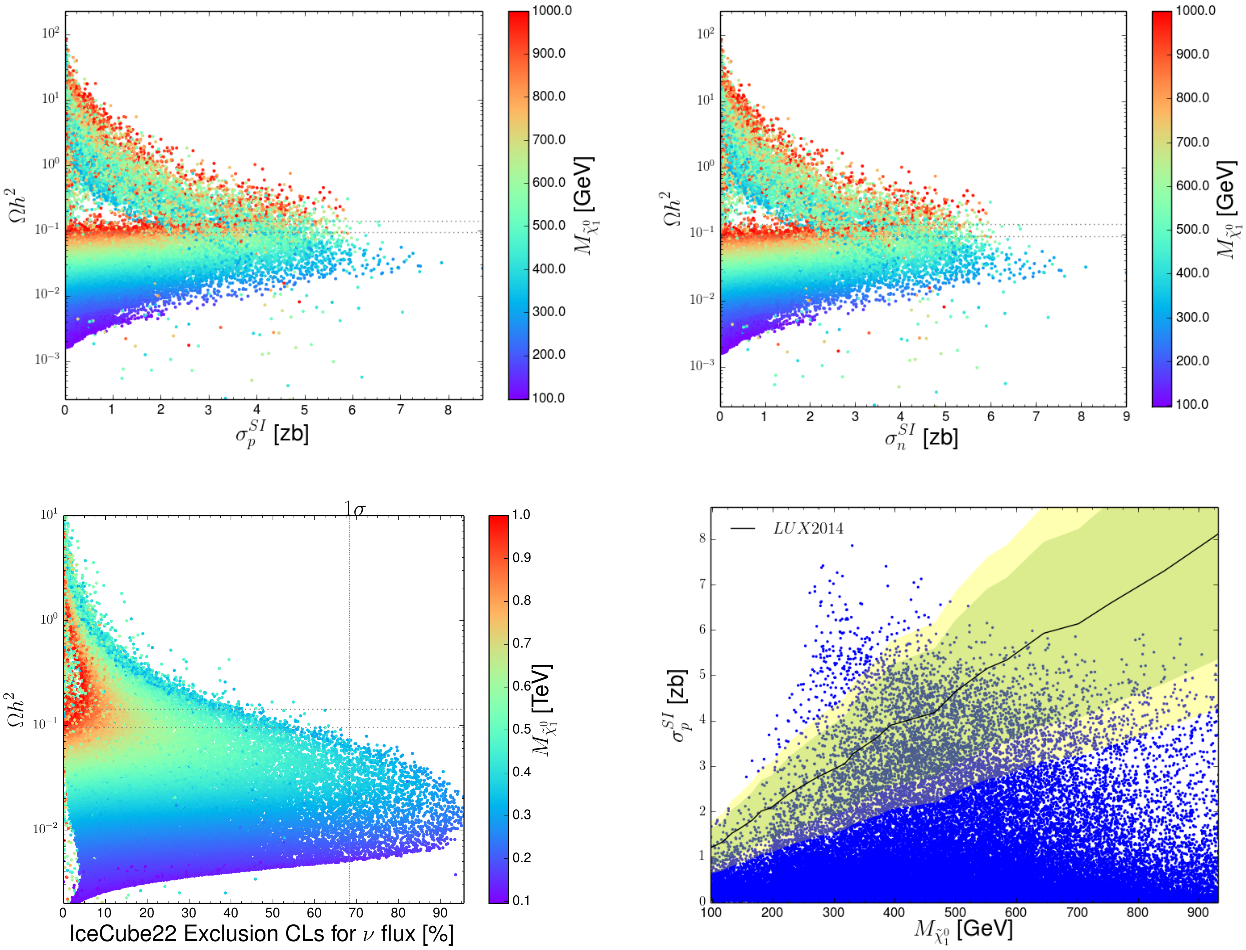

Figure 4.11: *Constraints on the UMSSM parameter space region in which the LSP is a neutralino that originate from DM direct detection. We present the dependence of the relic density on the neutralino mass and on the resulting spin-independent dark matter scattering cross section with protons (upper left panel) and neutrons (upper right panel) and on the possible exclusion that could be obtained from IceCube results (lower left panel). We also show the dependence of the spin-independent DM-proton scattering cross section on the neutralino mass, including the bound stemming from the LUX experiment (lower right panel).*

framework version 1.4.18 [232].

The best studied DM signatures at the LHC consist of the mono-X probes for which a certain amount of missing transverse energy (carried by one or more DM particles) is produced in association with a single energetic visible SM object. As in the case of other models, monojet signals are thought as the most promising due to the relative magnitude of the strong coupling with respect to the other gauge couplings. The corresponding rates are however very reduced in the case of a sneutrino LSP, in particular once one imposes a typical monojet selection that requires the presence of a jet with a large transverse momentum and a veto on final state leptons. Additionally, dark matter can also be produced together with an electroweak vector boson or a Z' boson radiated off the initial state. While the corresponding production cross section is expected to be smaller than the monojet one, the final state offers more freedom to reject the background and is thus worthy to be searched for. Moreover, if as in the UMSSM case, DM particles strongly couple to SM or extra gauge bosons, mono-vector boson production may be the dominant channel yielding DM production at the LHC. However, once all the constraints considered in the previous section are imposed, the remaining regions of the parameter space correspond to cross sections that are either negligible or too small relatively to the background cross sections.

Another way to probe phenomenologically viable UMSSM scenarios is to focus on sfermion pair production, and in particular on the production of the lighter third generation sfermions. The considered UMSSM scenarios feature heavy stops and sbottoms, so that third generation squark pair-production could be in principle easily tagged thanks to the subsequent presence of very hard final state objects. However, the associated production total rates are of the order of at most 1 fb. This makes any new physics contribution impossible to observe relative to the overwhelming SM background, even if advanced analysis techniques relying on the shape of the differential distributions are used. Moving on with the slepton sector, stau pair production is not expected to offer any extra handle on UMSSM-induced new physics, as the related rates are suppressed due to the electroweak nature of the process. The possible enhancement arising from the Z' contributions is in addition reduced given the low Z'-bosons branching ratios into sleptons (see Fig. 4.4).

Finally, we have studied chargino and neutralino pair-production, and in particular the associated production of one chargino and one neutralino that could be enhanced when the effective μ_{eff} parameter is small [233]. The subsequent associated signatures can contain one, two or more than two leptons, jets and missing energy. Fiducial cross sections of the order of the fb are obtained, which are nonetheless too small to be distinguished from the SM background even after relying on a judicious selection strategy.

The challenges of observing viable UMSSM models at colliders are not unique, and it turns out that scenarios that are in principle observable at colliders are disfavoured by cosmology, and that scenarios in agreement with cosmological and astrophysical data are out of reach of any present collider.

Chapter 5

Loopholes in Z' searches at the LHC: exploring supersymmetric and leptophobic scenarios

Although the discovery of the Higgs boson at the LHC has allowed for the completion of the particle spectrum of the Standard Model (SM), the issue of its extension still stands. Despite the experimental success in predicting most data observed so far, the SM indeed exhibits several limitations and shortcomings that motivate the study of beyond the Standard Model theories. Among those, supersymmetry, and in particular its minimal incarnation known as the MSSM, is one of the most appealing options. Unifying internal and external symmetries, supersymmetry provides a natural solution to the long-standing hierarchy problem, allows for gauge-coupling unification at high energies and predicts a stable particle that could address the problematics of Dark Matter. Despite these numerous motivations, no compelling evidence for supersymmetry has been found and the MSSM starts to be heavily constrained. Moreover, the MSSM suffers from severe fine-tuning issues related to the discovery of a SM-like Higgs boson, as well as the lack of any satisfactory explanation for the magnitude of the supersymmetric bilinear Higgs mass parameter μ that must unnaturally be of the order of the electroweak symmetry breaking scale.

As a consequence, arguments have been raised in favor of extending the MSSM superfield content by at least one singlet chiral superfield. Its scalar component can induce both supersymmetry breaking and dynamical generation of the μ term by getting a non-vanishing vacuum expectation value at the minimum of the scalar potential [206, 207, 208, 209, 210].

Such singlet superfields also appear under supersymmetric scenarios where the Standard Model gauge group is extended, the scalar singlet yielding the breaking of the additional gauge symmetry [189, 190]. This setup is furthermore motivated in a grand-unified scheme where a restricted set of high-dimensional representations are used to encompass all MSSM supermultiplets, and where all gauge couplings unify. In this context, the necessity of using representations of the unified gauge group automatically leads to the introduction of right-handed neutrino superfields, which consequently provides a solution for neutrino-mass generation, as well as vector-like fermions.

Among all GUTs, those based on gauge groups of rank 6, named E_6, have been extensively discussed as interesting possibilities [197, 190, 100]. In particular, the breaking pattern of E_6 to the electroweak symmetry results in the appearance of extra $U(1)'$ symmetries. From a bottom-up perspective, extending the MSSM with the introduction of an extra $U(1)'$ gauge group has numerous advantages, namely forbidding a too rapid proton decay without introducing an *ad hoc* discrete R-parity symmetry and making all field masses stable with respect to quantum corrections. Moreover, it is always possible to choose the $U(1)'$ field charges to ensure anomaly cancellation and gauge-coupling unification. Besides, the $U(1)'$ models do not suffer from the presence of cosmological domain walls, unlike theories like the Next-to-Minimal Supersymmetric Standard Model [191, 107].

While the spectrum of UMSSM models is altered from that of the MSSM, the most secure prediction emerging from the extended gauge symmetry consists of the existence of a novel neutral Z' boson, like in non-supersymmetric $U(1)'$ extensions of the SM. This makes the Z' boson a prime target for the LHC physics program, as the proof of its existence would constitute a promising indicator of a more general gauge structure. Any gauge group of rank greater than four (any group larger than $SU(5)$) indeed leads to the appearance of at least one extra neutral gauge boson. All current Z' analyses at the LHC are however guided by non-supersymmetric considerations in which the Z' boson only decays into SM particles [234, 235, 236, 237, 238]. Besides E_6-inspired Z', the experimental collaborations have also explored the so-called Sequential Standard Model (SSM), the simplest extension of the Standard Model, wherein Z' and possible W' bosons have the same couplings to fermions as the Z and W. This model is not theoretically motivated, but it is often used as a benchmark for the analyses, since the production cross section in the SSM just depends on the extra boson masses.

Along these lines, the ATLAS and CMS collaborations have searched for Z' bosons by investigating dilepton and dijet final states. In detail, by using high-mass dilepton data at 13 TeV, the ATLAS collaboration [239] set the mass exclusion limits $M_{Z'} > 4.5$ TeV in the SSM and $M_{Z'} > 3.8$-4.1 TeV in U$(1)'$ models, whereas CMS obtained $M_{Z'} > 4.0$ TeV (SSM) and $M_{Z'} > 3.5$ TeV (GUT-inspired models) [240]. For dijets, the limits are much milder and read $M_{Z'} > 2.1$-2.9 TeV (ATLAS) [241] and $M_{Z'} > 2.7$ TeV (CMS) [242][1].

In a UMSSM framework, the inclusion of the supersymmetric decay modes of the Z' bosons may nonetheless change these conclusions [245, 246, 247, 201, 200, 2]. Above all, the opening of new decay channels lowers the branching ratios into SM final states and therefore the Z' mass exclusion limits. In fact, Ref. [221] found an impact of about 200 GeV on the mass exclusion limits by comparing the 8 TeV ATLAS and CMS data on high-mass dileptons with UMSSM predictions for a benchmark point of the parameter space. Furthermore, in the UMSSM, a leptophobic Z' can yield the production of dilepton final states only through cascade decays into intermediate electroweakinos, which contrasts with the leptophobic non-supersymmetric case where this is simply not allowed [248]. The bounds on the Z'-boson mass and production cross section derived from the above-mentioned searches should then be revisited when more general theoretical contexts like the UMSSM or leptophobia are considered.

On different grounds, the hadronic environment at the LHC is so complex that new physics searches always rely on some simplifying assumptions in the form of the potential signals. For instance, most supersymmetry searches have been designed from the idea on how the MSSM could manifest itself in a typical LHC detector: they may hence be not suitable for given non-minimal supersymmetric realizations. In the UMSSM framework, which we focus on in this work, we consider Z'-boson signals that can potentially differ from the non-supersymmetric case. We restrict our analysis to leptonic Z' decay modes that are easier to explore, even if the expected signals are plagued by larger SM backgrounds. We additionally focus on UMSSM realizations in which the Z' boson is leptophobic, but where it could give rise to leptonic signatures via supersymmetric cascade decays into leptons and missing energy. This therefore offers an alternative opportunity to find both an extra gauge boson and supersymmetry from the study of the decays of a resonantly-produced colorless particle. This is one of the scenarios that we wish to investigate in this work, after imposing the most up-to-date constraints on the model. We hence aim at providing a clear roadmap for the discovery of unconventional leptophobic Z' bosons, such as those that could arise in

---

[1] It is important to note that these limits are recently updated. See ref. [243] for dijet resonances at 137 fb^{-1} and ref. [244] for dilepton resonances at 139 fb^{-1}.

Table 5.1: *Mixing angle* θ_{E_6} *for the most popular* $U(1)'$ *models. The value of* θ_{E_6} *is imposed to lie in the* $[-\pi, \pi]$ *range.*

Model	$U(1)'_\chi$	$U(1)'_\psi$	$U(1)'_\eta$	$U(1)'_S$	$U(1)'_I$	$U(1)'_N$
θ_{E_6}	-0.5π	0	-0.79π	-0.37π	0.71π	-0.08π

Table 5.2: $U(1)'$ *charges of the UMSSM quark (*Q*,* D*,* U*), lepton (*L*,* E*,* N*) and Higgs (*H_u*,* H_d*,* S*) supermultiplets for commonly studied anomaly-free* $U(1)'$ *groups that arise from the breaking of an* E_6 *symmetry.*

	$2\sqrt{10}Q'_\chi$	$2\sqrt{6}Q'_\psi$	$2\sqrt{15}Q'_\eta$	$2\sqrt{15}Q'_S$	$2Q'_I$	$2\sqrt{10}Q'_N$
Q, U, E	-1	1	-2	-1/2	0	1
L, D	3	1	1	4	-1	2
N	-5	1	-5	-5	1	0
H_u	2	-2	4	1	0	2
H_d	-2	-2	1	-7/2	1	-3
S	0	4	-5	5/2	-1	5

UMSSM scenarios and that escape detection when only considering standard LHC searches for extra gauge bosons.

Our work is organized as follows. In section 5.1, we briefly introduce $U(1)'$ supersymmetric models as when the gauge symmetry is designed as emerging from the breaking of an extended E_6 symmetry at the grand unification scale. We pay particular attention to the mass, mixing patterns and interactions of the extra neutral gauge boson and show under what conditions it could be made leptophobic. We finally set up the parameter-space region to be scanned over and proceed to its exploration in section 5.2, focusing on two different way to impose boundary conditions. In section 5.3, we concentrate on scenarios where the Z' boson does not directly decay into leptons and study its phenomenology at colliders, highlighting a preferred selection strategy that could lead to its discovery.

5.1 Z' bosons in $U(1)'$ supersymmetric models

5.1.1 Theoretical framework

There are different ways to implement a $U(1)'$ extension in the MSSM: one of the most commonly used parameterizations is inspired by grand-unified models, based on a rank-6 group E_6, where the symmetry-breaking scheme proceeds via multiple steps,

$$\begin{aligned} E_6 &\to SO(10) \otimes U(1)_\psi \to SU(5) \otimes U(1)_\chi \otimes U(1)_\psi \\ &\to SU(3)_C \otimes SU(2)_L \otimes U(1)_Y \otimes U(1)' \ . \end{aligned} \tag{5.1.1}$$

The $U(1)'$ symmetry that survives at the electroweak scale is taken as a linear combination of $U(1)_\chi$ and $U(1)_\psi$,

$$U(1)' = \cos\theta_{E_6} U(1)_\psi - \sin\theta_{E_6} U(1)_\chi \ , \tag{5.1.2}$$

where we have introduced the E_6 mixing angle θ_{E_6}. The neutral vector bosons associated with the $U(1)_\psi$ and $U(1)_\chi$ gauge groups are called the Z'_ψ and Z'_χ bosons, while a generic Z' is given by the mixing of these Z'_ψ and Z'_χ states, as in Eq. (5.1.2).

Different $U(1)'$ models can be classified according to the sole value of the θ_{E_6} mixing angle, and the charges Q' of the supermultiplets are fixed to ensure the theory to be anomaly-free. Six popular setups are summarized in Table 5.1, with the corresponding Q' charges listed in Table 5.2. In the notations of this last table, Q and L denote the left-handed weak doublets of quark and lepton fields, H_u and H_d the two weak doublets of Higgs fields, U and D the right-handed weak singlets of up-type and down-type quarks, E and N the right-handed weak singlets of charged leptons and neutrinos, and S a scalar singlet. In the case of supersymmetric extensions of the Standard Model, such as the MSSM, all fields in Table 5.2 must actually be understood as superfields containing also the supersymmetric partners of the fermions and Higgs bosons. In principle, the matter sector of E_6 should also feature vector-like exotic (s)quarks Q_D and $\bar{Q}_D$ which have the same $U(1)'$ charges as the H_u and H_d fields, respectively [197]. In the following, we assume that these exotic states are too heavy to be relevant at LHC energies and neglect them in our phenomenological analysis[2].

The Higgs supermultiplet content (H_u, H_d and S) is large enough to allow both for the breaking of $U(1)'$ via the scalar singlet field s, and of the electroweak symmetry through the neutral components of the scalar Higgs doublets h_u and h_d. All electrically-neutral Higgs fields indeed get non-vanishing vacuum expectation values at the minimum of the potential and carry non-trivial $U(1)'$ charges.

---

[2] Due to the requirement of the $SU(3)_c - SU(3)_c - U(1)'$ anomaly cancellation, these exotic quarks have weak isospin quantum numbers allowing for a superpotential interaction term involving ordinary quarks and inducing rapid proton decay. Their mass must thus be comparable to the GUT scale to prevent the proton from decaying too quickly [197].

In the grand–unified framework, the field content is organized into vector representations (**27**) of the E_6 group; the latter further branches as $\mathbf{27} = \mathbf{16} \oplus \overline{\mathbf{10}} \oplus \mathbf{1}$ into the irreducible representations of the $SO(10)$ subgroup that arises at the first step of the E_6 breaking scheme of Eq. (5.1.1). In the conventional field assignment, the representation **16** contains the left-handed quark and lepton supermultiplets (Q and L), as well as the right-handed quarks and leptons (U, D, E and N), while the Higgs fields (H_u and H_d) and the exotic quarks Q_D and $\bar{Q}_D$ are in the representation **10**. An alternative framework consists of having instead H_u and $\bar{Q}_D$ lying in the **16** and L and D in the **10** representation. According to whether one chooses the standard or unconventional assignment, the phenomenology of the Z' boson may be different. In the following, we shall adopt the standard $SO(10)$ representation choices, with the exotic quarks lying in the **10** representation. Nevertheless, the unconventional scenario can be easily recovered by redefining $\theta_{E_6} \to \theta_{E_6} + \arctan\sqrt{15}$ in Eq. (5.1.2) [249].

In principle, the Higgs fields in the **27** representation of E_6 should occur in three generations. However, as discussed in Refs. [183, 250, 251], it is always possible to perform a unitary transformation to a basis where only one generation of Higgs bosons gets a non-vanishing vacuum expectation value. The scalars with zero vacuum expectation values were called 'unHiggs' in Refs. [183, 250]. Through our analysis, we shall neglect the two generations of such states and focus on the 'true' Higgs bosons, which exhibit a non-zero vacuum expectation values and are denoted by H_u and H_d.

The **16** representation of $SO(10)$ is then decomposed in terms of those of $SU(5)$ as $\mathbf{16} = \mathbf{10} \oplus \overline{\mathbf{5}} \oplus \mathbf{1}$. The **10** representation of $SU(5)$ is suitable to include right-handed up-type quark and charged-lepton supermultiplets, together with the weak doublets of left-handed quarks, whereas the $\overline{\mathbf{5}}$ representation contains right-handed down quarks and left-handed lepton supermultiplets; the **1** representation includes right-handed (s)neutrinos [252]. The UMSSM superpotential is thus given, all flavor indices being omitted for clarity, by:

$$W_{\text{UMSSM}} = U\,\mathbf{Y}_u\,Q\,H_u - D\,\mathbf{Y}_d\,Q\,H_d - E\,\mathbf{Y}_e\,L\,H_d + N\,\mathbf{Y}_\nu\,L\,H_u + \lambda\,H_u\,H_d\,S\ .$$

The Yukawa interactions are encoded in a set of four 3×3 matrices in flavor space, $\mathbf{Y}_u$, $\mathbf{Y}_d$, $\mathbf{Y}_l$ and $\mathbf{Y}_\nu$, and the strength of the supersymmetric Higgs self-interactions is described by the λ parameter. After the breaking of the $U(1)'$ symmetry, this λ-term induces the dynamical generation of an effective μ-term (denoted μ_{eff} in the following) that allows for the resolution of the so-called MSSM μ-problem[3]. As supersymmetry has to be softly broken, we introduce

---

[3] μ_{eff} is related to λ and to the vacuum expectation value of the scalar singlet s via $\mu_{\text{eff}} = \lambda\langle s\rangle$.

in the Lagrangian explicit mass terms for all gaugino and scalar fields,

$$\begin{aligned}\mathcal{L}_{\rm soft}^{\rm (masses)} = & \frac{1}{2}\Big(M_1\lambda_{\tilde B}\!\cdot\!\lambda_{\tilde B} + M_2\lambda_{\tilde W}\!\cdot\!\lambda_{\tilde W} + M_3\lambda_{\tilde g}\!\cdot\!\lambda_{\tilde g} + M_4\lambda_{\tilde B'}\!\cdot\!\lambda_{\tilde B'} + \text{h.c.}\Big) - m_{H_d}^2 h_d^\dagger h_d \\ & - m_{H_u}^2 h_u^\dagger h_u - \frac{1}{2}m_s^2 s^2 - m_{\tilde q}^2 \tilde q^\dagger \tilde q - m_{\tilde d}^2 \tilde d^\dagger \tilde d - m_{\tilde u}^2 \tilde u^\dagger \tilde u - m_{\tilde l}^2 \tilde l^\dagger \tilde l - m_{\tilde e}^2 \tilde e^\dagger \tilde e - m_{\tilde\nu}^2 \tilde\nu^\dagger \tilde\nu \ ,\end{aligned}$$

where the $U(1)_Y$, $U(1)'$, $SU(2)_L$ and $SU(3)_c$ gaugino Weyl fermions are denoted by $\lambda_{\tilde B}$, $\lambda_{\tilde B'}$, $\lambda_{\tilde W}$ and $\lambda_{\tilde g}$, respectively, and where h_d, h_u, s, $\tilde q$, $\tilde d^\dagger$, $\tilde u^\dagger$, $\tilde l$, $\tilde e^\dagger$ and $\tilde\nu^\dagger$ are the scalar components of the H_d, H_u, S, Q, D, U, L, E and N superfields. The set of M_i and m_i parameters moreover denote the soft gaugino and scalar mass parameters, respectively.

Additional soft terms, related to trilinear scalar interactions, are also present and can be derived from the structure of the superpotential,

$$\mathcal{L}_{\rm soft}^{\rm (tril.)} = -A_\lambda\, s\, h_u\, h_d \,+ \tilde d^\dagger\, \mathbf{A}_d\, \tilde q\, h_d \,+ \tilde e^\dagger\, \mathbf{A}_e\, \tilde l\, h_d \,-\, \tilde u^\dagger\, \mathbf{A}_u\, \tilde q\, h_u \,-\, \tilde\nu^\dagger\, \mathbf{A}_\nu\, \tilde l\, h_u \,+ \text{h.c.} \ ,$$

where the $\mathbf{A}_e$, $\mathbf{A}_\nu$, $\mathbf{A}_d$ and $\mathbf{A}_u$ 3×3 matrices stand for the strengths of the soft Higgs-boson interactions with charged sleptons, sneutrinos, down-type squarks and up-type squarks, respectively. The A_λ parameter is finally related to the trilinear soft multi Higgs-boson coupling.

In order to calculate the sfermion masses, one would need to set up an explicit framework for supersymmetry breaking, such as a gauge-, gravity- or anomaly-mediated mechanisms, which goes beyond the goals of the present paper. We only recall that supersymmetry can be spontaneously broken if the so-called D-term and/or F-term in the scalar potential have non-zero vacuum expectation values. The F-terms are proportional to the SM particle masses, and are therefore important only for stop quarks, whereas D-terms are relevant for both light and heavy sfermions and contain contributions due to electroweak symmetry breaking and, in case of extension of the MSSM, to the Higgs bosons which break the extended symmetry [245, 201, 200]. Hereafter, we account for F- and D-term corrections to the sfermion masses, but do not present their explicit expressions, for the sake of brevity.

After the spontaneous breaking of the symmetry group down to electromagnetism, the W, Z and Z' bosons get massive and the photon stays massless. In general, for a $U(1)'$ extension of the SM, there is mixing between the Z and Z' eigenstates, parameterized by a mixing angle $\alpha_{ZZ'}$. However, electroweak precision data strongly constrain $\alpha_{ZZ'}$ to be very small [253]. At tree level, the squared masses of the Z and Z' bosons are given by:

$$\begin{aligned} M_Z^2 &= \frac{g_1^2+g_2^2}{2}\left(\langle h_u^0\rangle^2+\langle h_d^0\rangle^2\right) \\ M_{Z'}^2 &= g'^2\left({Q'_S}^2\langle s\rangle^2+{Q'_{H_u}}^2\langle h_u^0\rangle^2+{Q'_{H_d}}^2\langle h_d^0\rangle^2\right) , \end{aligned}$$

where h_d^0 and h_u^0 stand for the neutral components of the down-type and up-type Higgs fields h_d and h_u and g_1, g_2 and g' are the coupling constants of the $U(1)_Y$, $SU(2)_L$ and $U(1)'$ gauge groups, respectively. As discussed, *e.g.*, in Ref. [197], whenever the singlet s has a large vacuum expectation value (which contributes only to the Z' mass), as will be the case hereafter, $M_Z^2 \ll M_{Z'}^2$.

In the Higgs sector, as discussed above, one should deal with three generations of Higgs fields, although, in our chosen basis, only one generation (the so-called 'true' Higgs bosons) exhibits non-zero vacuum expectation values. Mass mixing matrices and mass eigenstates of the two generations of Higgs bosons with zero vacuum expectation values are thoroughly debated in [250]. In principle, because of the presence of these other states, one should impose further constraints on our scenario coming, e.g., from the current measurements of the (SM-like) neutral-Higgs production cross section and branching ratios, as well as from the exclusion limits on charged-Higgs bosons. In our work, however, such extra Higgs states and related constraints will be neglected.

In fact, after electroweak symmetry breaking, for each generation of Higgs fields, one is left with two charged and four neutral scalar bosons, namely one pseudoscalar and three neutral scalars, including a novel singlet-like scalar Higgs, inherited by the $U(1)'$ symmetry. In the following, we shall account for only one generation of Higgs bosons and denote by $H^\pm$ the charged bosons, h and H the MSSM-like neutral scalars, with h roughly corresponding to the Standard Model Higgs, A the pseudoscalar and H' the extra scalar associated with the $U(1)'$ gauge group.

As discussed, e.g., in Ref. [183], for $\langle s\rangle$ much larger than $\langle h_u^0\rangle$ and $\langle h_d^0\rangle$, diagonalizing the neutral Higgs mass matrix is straightforward and the singlet-like H' has mass $M_{H'}^2 \simeq g'^2{Q'_S}^2\langle s\rangle^2$, hence it is roughly degenerate with the Z', according to Eq. (5.1.3). The other neutral Higgs H has instead approximately the same mass as the pseudoscalar A and as the charged $H^\pm$: as a result, the heaviest scalar Higgs of the spectrum could be either H or H', depending on whether the Z' is lighter or heavier than A.

In the gaugino sector, with respect to the MSSM, one has two extra neutralinos, related to the supersymmetric partners of Z' and H' bosons, which yields a total of six $\tilde{\chi}_1^0, \ldots, \tilde{\chi}_6^0$ neutralino states. As discussed in Ref. [200], the new $\tilde{\chi}_5^0$ and $\tilde{\chi}_6^0$ eigenstates are often too heavy to contribute to the Z' phenomenology at the LHC. As the new Z' is electrically neutral, the chargino sector stays instead unchanged with respect to the MSSM.

On top of mass mixings, both $U(1)_Y$ and $U(1)'$ bosons are allowed to mix kinetically [254]. The corresponding Lagrangian reads, in terms of the gauge boson component fields,

$$\mathcal{L}_{\text{kin}} = -\frac{1}{4}\hat{B}^{\mu\nu}\hat{B}_{\mu\nu} - \frac{1}{4}\hat{Z}'^{\mu\nu}\hat{Z}'_{\mu\nu} - \frac{\sin\chi}{2}\hat{B}^{\mu\nu}\hat{Z}'_{\mu\nu} , \tag{5.1.3}$$

where $\hat{B}_{\mu\nu}$ and $\hat{Z}'_{\mu\nu}$ are the $U(1)_Y$ and $U(1)'$ boson field strength tensors, respectively, and χ is the kinetic mixing angle. In order to understand the physical implications of the kinetic mixing, it is necessary to diagonalize the field strengths, which is achieved via a $GL(2,\mathbb{R})$ rotation,

$$\begin{pmatrix} \hat{B}_\mu \\ \hat{Z}'_\mu \end{pmatrix} = \begin{pmatrix} 1 & -\tan\chi \\ 0 & \frac{1}{\cos\chi} \end{pmatrix} \begin{pmatrix} B_\mu \\ Z'_\mu \end{pmatrix} ,$$

where $\hat{B}_\mu$ and Z'_μ are the original $U(1)$ and $U(1)'$ gauge fields, with non-diagonal kinetic terms, while B_μ and Z'_μ have now canonical diagonal kinetic terms. As discussed in Refs. [254, 197], for $M_Z^2 \ll M_{Z'}^2$ and small values of χ, the impact of the kinetic mixing on the gauge boson masses is negligible. It nonetheless can have a significant effect on the coupling of the Z' boson with fermions. In fact, the interaction Lagrangian of the fields $\hat{B}_\mu$ and $\hat{Z}'_\mu$ with a generic fermion ψ_i, with charges Y_i and Q'_i under the $U(1)$ and $U(1)'$ groups, is given by

$$\mathcal{L}_{\text{int}} = -\bar{\psi}_i\gamma^\mu(g_1 Y_i \hat{B}_\mu + g' Q'_i \hat{Z}'_\mu)\psi_i ,$$

which can then be rewritten in terms of B_μ and Z'_μ as

$$\mathcal{L}_{\text{int}} = -\bar{\psi}_i\gamma^\mu(g_1 Y_i B_\mu + g' \bar{Q}_i Z'_\mu)\psi,$$

where

$$\bar{Q}_i = Q'_i \sec\chi - \frac{g_1}{g'} Y_i \tan\chi. \tag{5.1.4}$$

Leptophobic scenarios can hence be obtained requiring $\bar{Q}_L = \bar{Q}_E = 0$ [255, 256, 204]. Since $Y_L = -1/2$ and $Y_E = 1$, Eq. (5.1.4) dictates that leptophobia can be achieved only if $Q'_E = -2Q'_L$: this relation between the doublet and singlet leptonic charges is typical for the

Table 5.3: *Ranges over which we allow the parameters in Eq. (5.1.6) and Eq. (5.1.7) to vary. As discussed in the text, for coupling unification at GUT scale, only the quantities in the top panel are varied.*

Parameter	Scanned range	Parameter	Scanned range
M_0	$[0, 3]$ TeV	$\mu_{\rm eff}$	$[-2, 2]$ TeV
$M_{1/2}$	$[0, 5]$ TeV	A_λ	$[-7, 7]$ TeV
A_0	$[-3, 3]$ TeV	$M_{Z'}$	$[1.98, 5.2]$ TeV
$\tan\beta$	$[0, 60]$	θ_{E_6}	$[-\pi, \pi]$

Parameter	Scanned range	Parameter	Scanned range
$m^2_{\tilde q,\tilde u,\tilde d}$	$[0, 16]$ TeV^2	$M_{1,2,3,4}$	$[0, 3]$ TeV
$m^2_{\tilde e,\tilde l}$	$[0, 1]$ TeV^2	$m^2_{\tilde\nu}$	$[-6.8, 9]$ TeV^2

$U(1)'_\eta$ configuration, as shown in Table 5.2. Furthermore, if one assumes, as will be done in the following, the typical GUT-inspired relation between the $U(1)$ and $U(1)'$ couplings $g_1(M_{Z'})/g'(M_{Z'}) = \sqrt{3/5}$, then leptophobia requires the additional condition $\sin\chi \approx -0.3$. As a result, we expect leptophobic Z' models to naturally arise for E_6 mixing angles in the neighbourhood of

$$\theta_{E_6} \simeq \theta_\eta \pm n\pi, \quad n = 0, 1, 2, 3, \dots \ , \tag{5.1.5}$$

with the Z'-boson leptonic couplings being either exactly zero or very suppressed. In the following, we shall account for the kinetic mixing of $U(1)_Y$ and $U(1)'$ gauge groups, with the $U(1)'$ charges of all our matter fields given by Eq. (5.1.4).

5.1.2 Parameter-space scan and constraints

UMSSM theories rely on numerous free parameters so that simplifying assumptions are in order for a practical parameter-space exploration. Hereafter, we impose minimal flavor violation, so that all the flavor-violating parameters of the soft supersymmetry-breaking Lagrangian are considered as vanishing, and enforce unification boundary conditions on the remaining soft parameters.

In the first class of scenarios which we investigate, unification is assumed to occur at a very high scale $M_{\rm GUT} \approx \mathcal{O}(10^{16})$ GeV and all parameters are then run down to $M_{Z'}$ according to renormalization group evolution. More precisely, all gauge couplings are assumed to unify at a given high scale and the $U(1)'$ coupling is enforced to satisfy

$$g'(M_{\mathrm{GUT}}) = \sqrt{\frac{5}{3}}\, g_1(M_{\mathrm{GUT}}).$$

Furthermore, all scalar masses are set to a common value M_0, whilst all gaugino masses are taken equal to another universal mass $M_{1/2}$. All trilinear soft couplings are assumed to be proportional to the respective Yukawa coupling matrices with a universal proportionality factor A_0, so that

$$\mathbf{A}_i = \mathbf{Y}_i A_0 \qquad \text{for } i = e, \nu, d, u\ .$$

In the Higgs sector, we fix the values of the effective μ_{eff} parameter, the ratio of the vacuum expectation values of the neutral components of the two Higgs doublets $\tan\beta = v_u/v_d$, the trilinear soft coupling A_λ, as well as the Z' mass $M_{Z'}$. Finally, the diagonal entries of the neutrino Yukawa coupling matrices are set to a very small value, $\mathcal{O}(10^{-11})$, in such a way as to ignore the sneutrino soft trilinear interactions. The ensemble of free parameters considered in our exploration of the UMSSM parameter space is thus given by

$$\Big\{ M_0,\ M_{1/2},\ A_0,\ \tan\beta,\ \mu_{\mathrm{eff}},\ A_\lambda,\ M_{Z'},\ \theta_{E_6} \Big\}\ , \tag{5.1.6}$$

where we have additionally included the E_6 mixing angle θ_{E_6}. We vary those parameters over the ranges given in the top panel of Table 5.3.

In the second class of scenarios considered in this work, unification is imposed at the Z' mass scale. In this case, we just enforce the unification of the trilinear couplings as in Eq. (5.1.6) and set

$$g'(M_{Z'}) = \sqrt{\frac{5}{3}}\, g_1(M_{Z'})\ ,$$

all scalar and gaugino masses being kept free. The entire set of free parameters is thus here given by

$$\Big\{ m^2_{\tilde{q}},\ m^2_{\tilde{u}},\ m^2_{\tilde{d}},\ m^2_{\tilde{l}},\ m^2_{\tilde{e}},\ m^2_{\tilde{\nu}},\ M_1,\ M_2,\ M_3,\ M_4,\ A_0,\ \tan\beta,\ \mu_{\mathrm{eff}},\ A_\lambda,\ M_{Z'},\ \theta_{E_6} \Big\}\ , \tag{5.1.7}$$

with the ranges over which those parameters vary presented in Table 5.3.

In our scanning procedure, we analyze all possible anomaly-free UMSSM models derived from the breaking of an E_6 gauge symmetry. We generate the particle spectrum by making use of the SARAH code, version 4.6.0 [136], and its interface to SPHENO 3.3.8 [137].

Table 5.4: *Experimental constraints imposed within our scanning procedure in order to determine the parameter-space regions of interest.*

Observable	Constraints	Ref.	Observable	Constraints	Ref.
M_h	125.09 ± 3 GeV (theo)	[27]	$\chi^2(\hat{\mu})$	≤ 70	-
$\lvert\alpha_{ZZ'}\rvert$	$\mathcal{O}(10^{-3})$	[220]	$M_{\tilde{g}}$	> 1.75 TeV	[133]
$M_{\tilde{\chi}_2^0}$	> 62.4 GeV	[257]	$M_{\tilde{\chi}_3^0}$	> 99.9 GeV	[257]
$M_{\tilde{\chi}_4^0}$	> 116 GeV	[257]	$M_{\tilde{\chi}_i^\pm}$	> 103.5 GeV	[257]
$M_{\tilde{\tau}}$	> 81 GeV	[257]	$M_{\tilde{e}}$	> 107 GeV	[257]
$M_{\tilde{\mu}}$	> 94 GeV	[257]	$M_{\tilde{t}}$	> 900 GeV	[134]
$\mathrm{BR}(B_s^0 \to \mu^+\mu^-)$	$[1.1 \times 10^{-9}, 6.4 \times 10^{-9}]$	[123]	$\dfrac{\mathrm{BR}(B \to \tau\nu_\tau)}{\mathrm{BR}_{SM}(B \to \tau\nu_\tau)}$	$[0.15, 2.41]$	[122]
$\mathrm{BR}(B^0 \to X_s\gamma)$	$[2.99, 3.87] \times 10^{-4}$	[121]			

In order to test the phenomenological viability of the model, we compute various properties of the Higgs sector, such as the mass of the lightest Higgs state and the corresponding collider signal strengths by means of the HiggsBounds (version 4.3.1) and HiggsSignals (version 1.4.0) packages [138, 139]. The scan itself and the numerical analysis performed in this work have been achieved by interfacing all programs using also the pySLHA package, version 3.1.1 [146].

The parameter space is probed by using the Metropolis–Hasting sampling method, requiring consistency with the experimental bounds on masses and decay rates shown in Table 5.4. In particular, we require the mass of the Standard Model Higgs boson to agree with the measurements up to an uncertainty of 3 GeV, and the χ^2 fit of the available Higgs signal strengths is bounded to be smaller than the conservative value of 70. Other constraints, connected to the bounds on the masses of supersymmetric particles and on several flavor observables, are evaluated relying on the SPheno code. This includes in particular tests of the strict limits stemming from B-meson decays [123, 122, 134]. As for the supersymmetric sector, we enforce the LEP limits on slepton, chargino, and neutralino masses quoted in Ref. [257], while for gluinos and stops we implement the bounds set by CMS [133] and ATLAS [134], respectively.

5.2 Supersymmetric Z' Phenomenology

In this section, we analyze the phenomenology of the two classes of UMSSM scenarios introduced in section 5.1.2. In the subsequent section 5.3, specific configurations where the

Table 5.5: *g' values and dilepton branching ratios for commonly studied $U(1)'$ models with UMSSM parameters satisfying the constraints detailed in section 5.1.2. Quoted are $g'_{\rm min}$, the minimum value of $g'(M_{Z'})$, along with the corresponding spread $\Delta g'$ and the smallest possible branching ratio into leptons with (UMSSM) and without (USM) supersymmetric contributions to the Z' decays.*

Parameter	$U(1)'_\psi$	$U(1)'_\eta$	$U(1)'_I$	$U(1)'_N$
$g'_{\rm min}$	0.634	0.585	0.559	0.624
$\Delta g'$ [%]	0.9	7.8	6.8	1.4
$[{\rm BR}(Z' \to ll)]^{\rm min}_{\rm UMSSM}$ [%]	5.5	3.6	9.3	7.8
$[{\rm BR}(Z' \to ll)]^{\rm min}_{\rm USM}$ [%]	8.4	4.8	11.1	11.1

Z' boson is leptophobic by virtue of the kinetic mixing of $U(1)_Y$ and $U(1)'$ are in contrast investigated.

In order to apply the LHC constraints on the properties of Z' bosons, we calculate the Z' production cross section at Next-to-leading order (NLO) accuracy in QCD [258, 259]. This relies on the joint use of FeynRules version 2.3.27 [260] and the included NLOCT package [261], as well as FeynArts [262], for the automatic generation of a UFO library [145] containing both tree-level and counterterm vertices necessary at NLO. This UFO model is then used by MadGraph5_aMC@NLO (version 2.5.5) [144] for the numerical evaluation of the hard-scattering matrix elements, which are convoluted with the NLO set of NNPDF 2.3 parton distribution functions (PDF) [162]. Using the decay table provided by the SPheno package and assuming the narrow-width approximation, we compare our predictions with the ATLAS limits on Z' bosons in the dilepton mode [239] in order to estimate the impact of supersymmetric decay channels.

5.2.1 Scenarios With High-Scale Boundary Conditions

In this subsection, we focus on our first class of UMSSM scenarios where the proportionality between g' and g_1 is imposed at the GUT scale and where all free parameters in Eq. (5.1.6) are fixed at $M_{\rm GUT}$ and then evolved down to the Z' scale by means of renormalization group equations.

We have found that some parameter regions satisfying the constraints in Table 5.4 exist for a wide set of values of the E_6 mixing angle θ_{E_6}. The LHC collaborations typically use the rate $\sigma B \equiv \sigma(pp \to Z') \times {\rm BR}(Z' \to l^+l^-)$ to obtain the exclusion limits on the Z' mass. For the sake of exploring possible loopholes in the Z' searches, we are therefore

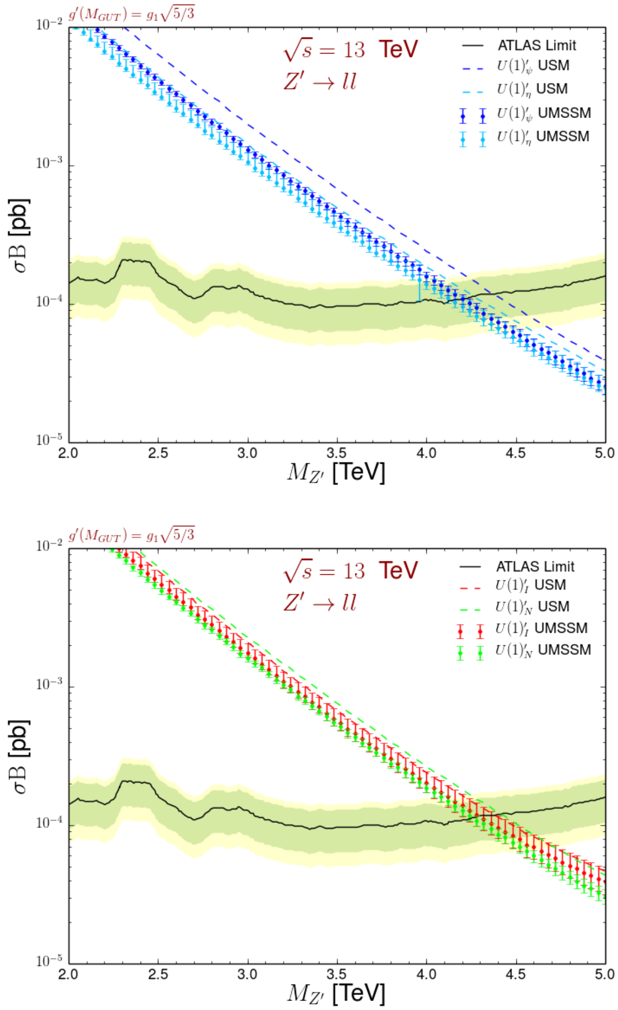

Figure 5.1: *Comparison of our predictions for the* $\sigma(pp \to Z') \times \mathrm{BR}(Z' \to ll)$ *product, in the scenario where the model boundary conditions are set at* $M_{\rm GUT}$*, with the ATLAS dilepton yield [239] at the* 1σ *(green) and* 2σ *(yellow) confidence levels. In the upper panel, we present the results for the* $U(1)'_\psi$ *and* $U(1)'_\eta$ *models, and in the lower panel we focus on the* $U(1)'_I$ *and* U'_N *models. The dots with error bands correspond to the UMSSM case, while the dashed lines do not include supersymmetry (USM). NLO corrections to* $\sigma(pp \to Z')$ *are accounted for in both cases and the spread in the UMSSM results includes the effects of the parameter scan as well as the theoretical error originating from scale and PDF variations.*

especially interested in scenarios which minimize the σB product, namely featuring small values of the g' coupling and of the BR($Z' \to l^+l^-$) branching ratio. In fact, when running the renormalization group equations, scanning the parameters in the ranges presented in Table 5.3, imposing the constraints of Table 5.4 and accounting for proper threshold matching conditions, $g'(M_{Z'})$ ends up with lying in a range $[g'_{\rm min}, g'_{\rm max}]$.

In Table 5.5 we quote, for a few $U(1)'$ models, the minimum value of g' at the $M_{Z'}$ scale and the spread $\Delta g'$, defined as

$$\Delta g' = 1 - \frac{g'_{\rm min}(M_{Z'})}{g'_{\rm max}(M_{Z'})}$$

and expressed as a percentage. The minimum branching fraction of Z' decays into dilepton final states, including supersymmetric channels (UMSSM) and without supersymmetry (USM) is also quoted.

In the table, we have discarded the models $U(1)'_\chi$ and $U(1)'_S$. As discussed, *e.g.*, in Refs. [201, 2], $U(1)'_\chi$ models are ill-defined in supersymmetry as it they typically lead to unphysical sfermion masses after adding to the soft masses the D-term contributions. As to $U(1)'_S$, it may be theoretically acceptable, but we were not able to find scenarios capable of satisfying the constraints of Table 5.4. From Table 5.5, we learn that the deviations of g' from $g'_{\rm min}$ are rather small, with $\Delta g'$ being of at most about 8%, but the impact of the inclusion of supersymmetric decays on the dilepton branching fraction is remarkable for most models. In the $U(1)'_\psi$ and $U(1)'_\eta$ scenarios, for example, BR($Z' \to ll$) decreases by about 35% and 25%, respectively, once decays into sfermions and gauginos are accounted for. Nevertheless, all models still exhibit substantial dilepton Z' decay rates, varying between 3% and 10%.

In Fig. 5.1 we compare the ATLAS limits on high-mass dileptons at the 1σ (green) and 2σ (yellow) levels with our predictions for σB, obtained in the context of $U(1)'_\psi$ and $U(1)'_\eta$ (upper panel), as well as $U(1)'_I$ and $U(1)'_N$ (lower panel) gauge groups, in the range 2 TeV $< M_{Z'} <$ 5 TeV. We consider both supersymmetric (markers with error bars) and non-supersymmetric cases (dashed lines) and include NLO QCD corrections to the production cross section $\sigma(pp \to Z')$. The error bars around the supersymmetric results include two contributions: first, they account for the spread covered in the scan and second, they include the theoretical uncertainties stemming from traditional scale and parton density variations in the NLO computation. We found that the latter uncertainty varies from 5% for Z' masses of about 2 TeV and goes up to 20% for $M_{Z'} \simeq$ 5 TeV. We observe that the impact of

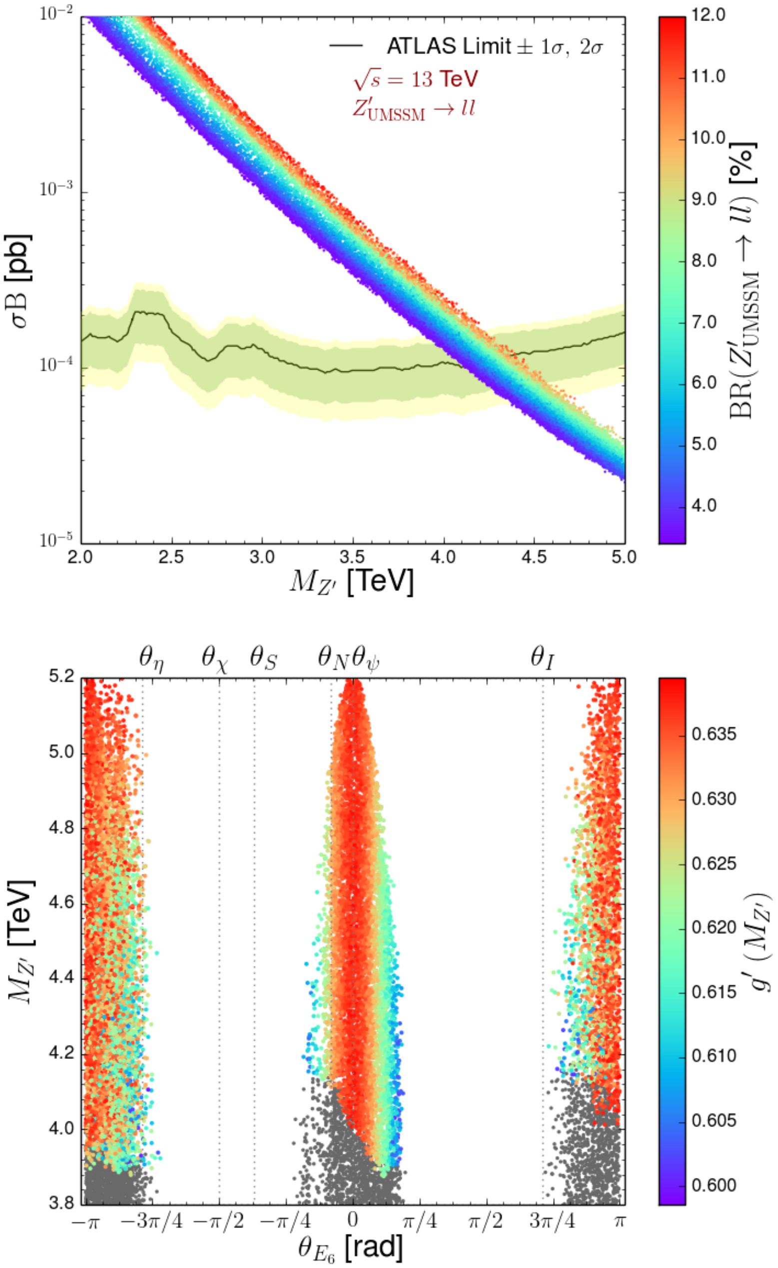

Figure 5.2: *In the upper panel, we compare the* σB *rate with ATLAS data, regardless of the specific* $U(1)'$ *group and emphasizing the values of the* $Z' \to ll$ *branching ratio. In the lower panel, we show the correlations between the* Z'*-boson mass and the* θ_{E_6} *mixing angle for all points satisfying the constraints detailed in section 5.1.2. Points that are excluded at the* 2σ *level by the recent ATLAS search for* Z' *in the dilepton mode [239] are shown in grey, whilst the value of the* $U(1)'$ *coupling strength is shown otherwise. Both figures refer to the scenario where couplings unify at* $M_{\rm GUT}$.

supersymmetric decays on the excluded $M_{Z'}$ values runs from about 100 GeV (Z'_η) to 200 GeV (Z'_ψ and Z'_N), while the errors on the Z'_I dilepton rate in the UMSSM are too large to discriminate it from the non-supersymmetric case. Overall, Z' bosons lighter than 4 TeV are still strongly disfavored by ATLAS data, regardless of the $U(1)'$ model.

In Fig. 5.2 (upper panel), we reexpress the same results by emphasizing the dependence of σB on the dilepton branching fraction, by superimposing the predictions of the different $U(1)'$ realizations, regardless of the actual θ_{E_6} mixing angle, and displaying the values of BR($Z' \to ll$) by means of different colors. We find that the dilepton rate varies between 4% and 12%, and that the yielded exclusion masses are roughly between 4 and 4.5 TeV.

In the lower panel of Fig. 5.2, we present instead the distribution of the allowed Z'-boson masses as a function of the E_6 mixing angle, with the value of the g' coupling for each scenario indicated by a color code. In order to determine the allowed regions, we first impose the experimental constraints in Table 5.4 and then the exclusion limits coming from the direct comparison with the ATLAS data in Fig. 5.1. The points ruled out by the ATLAS results are shown in grey. We observe, similarly to the findings of Ref. [2], that only $|\theta_{E_6}|$ values in the intervals $[0, \pi/4]$ and $[3/4\pi, \pi]$ can accommodate all the imposed experimental constraints. Outside of these regions, the $U(1)'$ charge of the extra singlet supermultiplet S is in fact close to zero so that either the SM-like Higgs boson or the Z' boson, or even both, are predicted to be too light with respect to current data. In particular, Fig. 5.2 (lower panel) dictates that models $U(1)'_\chi$ and $U(1)'_S$ are largely ruled out by the current data (see also the above discussion), while $U(1)'_I$ is only marginally consistent. As a whole, after adding the recent ATLAS constraints [239] (the grey points), it turns out once again that scenarios exhibiting a Z' boson lighter than 4 TeV can hardly ever be realized, the corresponding parameter-space regions getting more and more restricted.

5.2.2 Scenarios with Low-Scale Boundary Conditions

In this subsection, we focus on the second class of scenarios, wherein the input parameters, given in Eq. (5.1.7), are provided at the Z' mass scale and where the $U(1)'$ coupling reads

$$g'(M_{Z'}) = \sqrt{\frac{5}{3}}\, g_1(M_{Z'}) \approx 0.47 \ , \tag{5.2.1}$$

for all models satisfying the constraints imposed in section 5.1.2. Comparing Eq. (5.2.1) with the minimal values for $g'(M_{Z'})$ quoted in Table 5.5, we learn that, for low-scale boundary

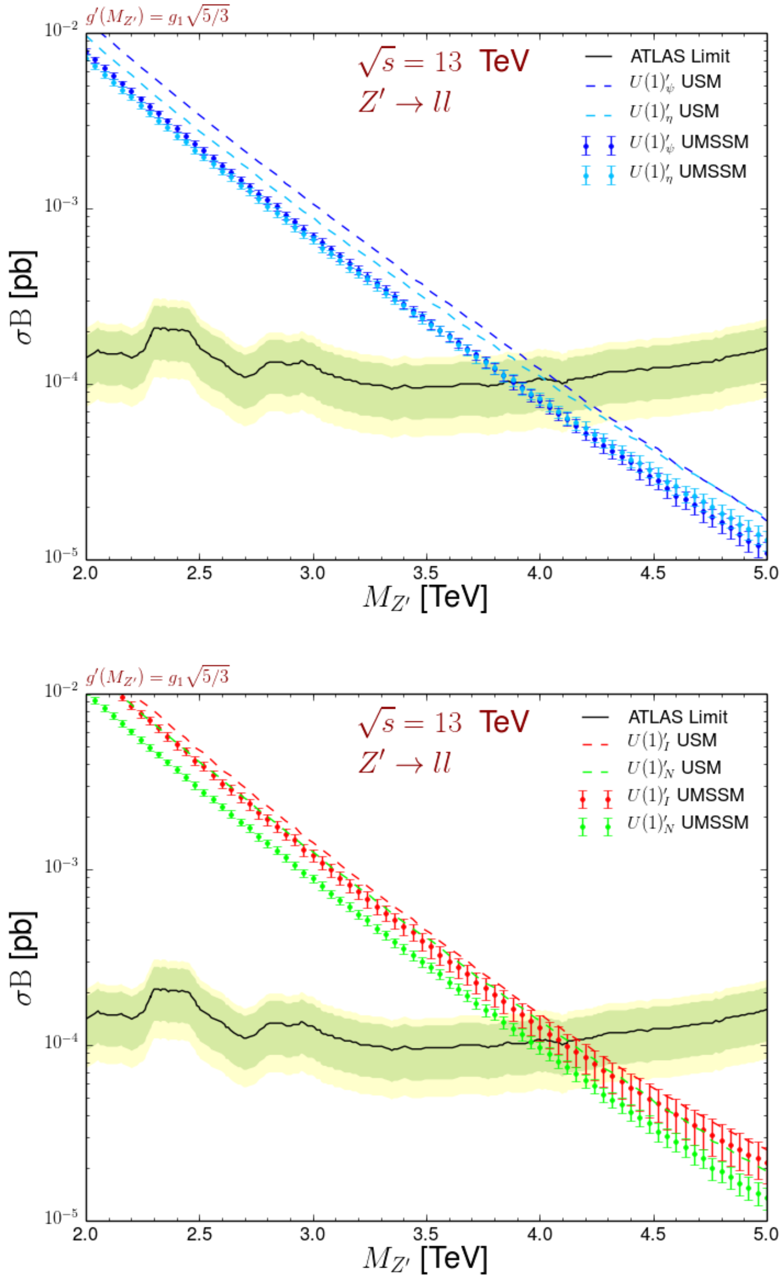

Figure 5.3: *As in Fig. 5.1, but for the scenario where the condition $g' = \sqrt{5/3}g_1$ is imposed at $M_{Z'}$.*

conditions, g' is substantially smaller. Therefore, the Z'-production cross section is lower than for scenarios where boundary conditions are provided at the GUT scale $M_{\rm GUT}$.

As a consequence, the inferred Z' mass exclusion limits are reduced by about 200–300 GeV with respect to the high-scale unification case, as can be seen in Fig. 5.3, where the ATLAS limits are compared with the UMSSM predictions for $U(1)'_\psi$, $U(1)'_\eta$ (upper panel), and $U(1)'_N$ and $U(1)'_I$ (lower panel) models. Since the g' value is roughly the same as in the non-supersymmetric case, the overall impact of the inclusion of supersymmetric decays is similar to that found in the high-scale boundary framework, namely a reduction of the bounds on the Z' boson mass by about 200 GeV. As observed for the other class of scenarios, the models with the highest impact of novel decay modes are the $U(1)'_\eta$ and $U(1)'_N$ ones, while the errors are too large to appreciate the effect of non-standard decays in σB for the $U(1)'_I$ case. Our analysis then confirms the finding of Ref. [221], which compared UMSSM predictions in the low-scale unification framework with 8 TeV LHC limits and obtained an effect of similar magnitude on the excluded masses.

As for the high-scale unification case, we present in Fig. 5.4 (upper panel) the comparison of σB with the ATLAS data, scanning through the whole parameter space and displaying in different color codes the values of BR($Z' \to ll$). Fig. 5.4 (lower panel) shows instead the correlations between the allowed $M_{Z'}$ values and θ_{E_6}, accounting for both indirect constraints and direct ATLAS exclusion limits, the latter given by the grey-shaded area. The results in Fig. 5.4 are qualitatively similar to those presented in Fig. 5.2. However, as anticipated before, the g' value is smaller, so that the ATLAS constraints on $M_{Z'}$ are milder and values of $M_{Z'} \gtrsim 3.6$ TeV are hence still allowed. Likewise, regarding specific $U(1)'$ models, $U(1)'_\chi$ and $U(1)'_S$ are ruled out, while the other setups are still permitted and worth to be further explored.

5.3 Leptophobic Z' Scenarios in UMSSM Models

The results presented in the previous section have shown that the inclusion of supersymmetric decays has a substantial effect on the Z' searches and exclusion limits, but nevertheless the ATLAS bounds originating from the dilepton channel strongly constrain any phenomenologically viable UMSSM realization. Furthermore, the very fact that the Z' boson has to be quite heavy impacts all sfermion masses through the $U(1)'$ D-terms, which may even lead to discarding some scenarios, such as $U(1)'_\chi$, as yielding unphysical sfermion spectra. All

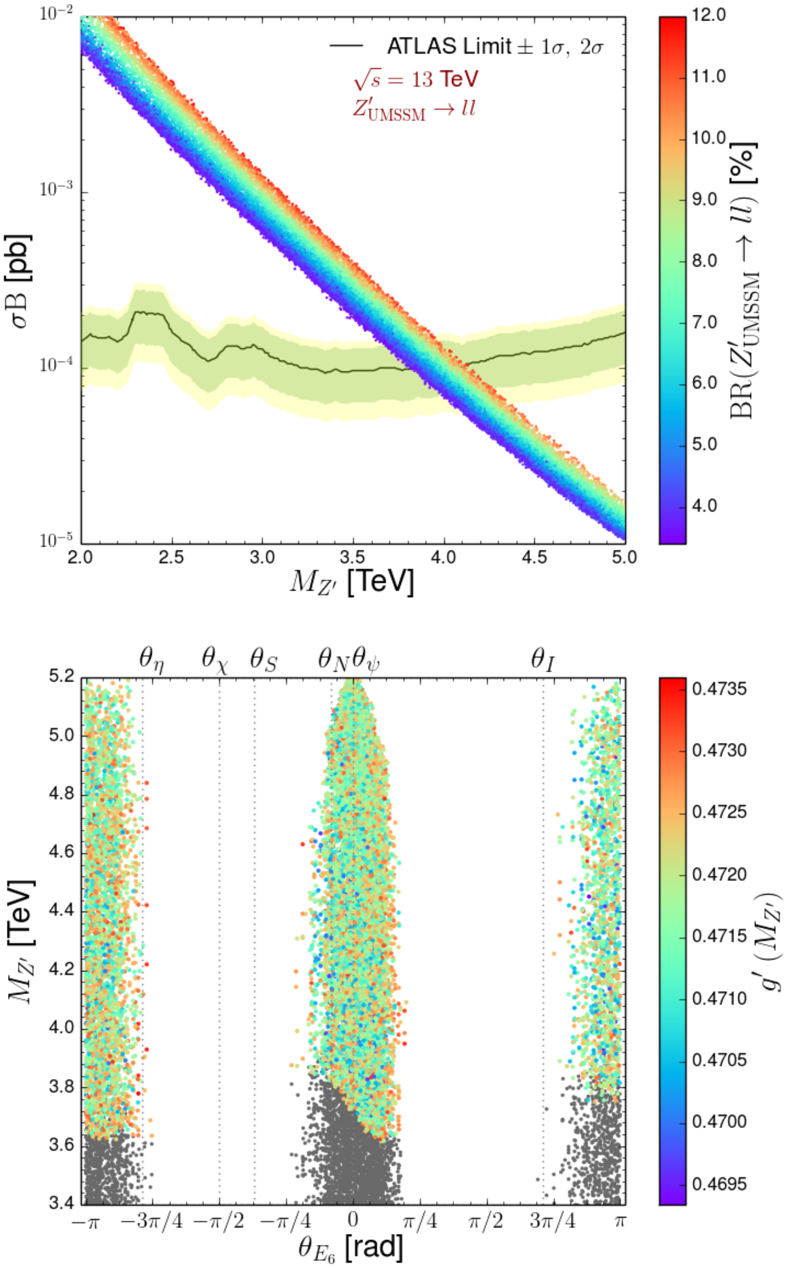

Figure 5.4: *As in Fig. 5.2, but for coupling unification at* $M_{Z'}$*.*

LHC constraints studied so far can, however, be evaded by enforcing the Z' boson to be leptophobic. In these scenarios, resonance searches in the dijet final state become the main probes of the new boson, Run II results for the top-antitop mode including the analysis of the full 2016 dataset being still not available. Dijet bounds are however much weaker, as described in Refs. [242, 241].

Before discussing the phenomenology of leptophobic Z' bosons within supersymmetry, in Fig. 5.5 we compare the CMS high-mass dijet yield from Ref. [242] with our predictions for $\sigma(pp \to Z') \times \mathrm{BR}(Z' \to q\bar{q})$, obtained after scanning the UMSSM parameters as described in Table 5.3 and imposing the constraints of Table 5.4, for scenarios with high-scale (upper panel) and low-scale (lower panel) boundary conditions. As in the dilepton channel, the production cross section is calculated at NLO and the values of the dijet branching ratios are characterized by different color codes. For the sake of consistency with the experimental analysis, the σB rate is multiplied by an acceptance factor A $\simeq 0.6$ and the fraction of $Z' \to t\bar{t}$ events is not included in the calculation.

From Fig. 5.5, one learns that the computed σBA is always below the CMS exclusion limits in the range 2 TeV $< M_{Z'} <$ 5 TeV at the 95% confidence level in both frameworks of coupling unification, once accounting for supersymmetric Z' decays. One can, therefore, envisage than even much lighter Z' bosons could be allowed by data when leptophobic UMSSM realizations, such as those introduced in section 5.1.1, are considered.

Hereafter we focus on the second class of UMSSM scenarios, *i.e.*, coupling unification at the $M_{Z'}$ scale, and add to the list of free parameters in Eq. (5.1.7) the sine of the kinetic mixing angle $\sin\chi$, defined through Eq. (5.1.4), that we allow to vary in the $[-1, 1]$ window. In principle, as thoroughly debated in Ref. [205], the kinetic mixing angle also affects the Dark Matter relic abundance, since the mass of the lightest supersymmetric particle (LSP), which in Ref. [205] can be either a right-handed neutrino or the lightest neutralino and in this paper is $\tilde{\chi}_1^0$, depends on the $U(1)'$ charges of the Higgs bosons, which have been modified according to Eq. (5.1.4) and are a function of $\sin\chi$[4]. Because of that, the authors of Ref. [205], besides applying the constraints due to collider physics, accounted for the upper bound on the relic density as well, relying on the Planck 2015 measurements [156]. The finding of Ref. [205] is that, although the mass of the LSP is indeed sensitive to $\sin\chi$ and, e.g., a heavy Dark Matter candidate is favored by small $|\sin\chi|$, a value of the relic density $\Omega h^2 \sim 0.1$, consistent with Ref. [156], can be achieved for any value of $\sin\chi$, and in particular for $|\sin\chi| \simeq 0.3$,

---

[4] Note that the kinetic mixing parameter k in Ref. [205] corresponds to our $\sin\chi$.

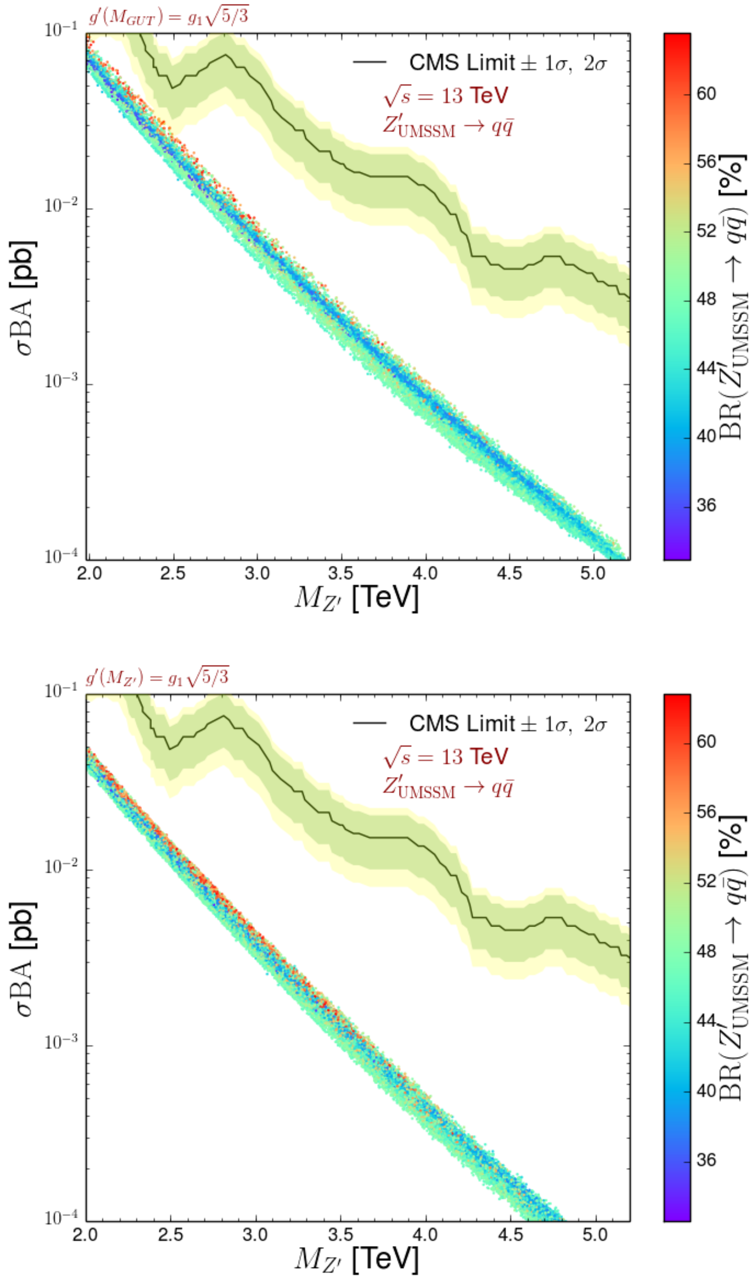

Figure 5.5: *Z' production cross section multiplied by the dijet branching ratio and by the acceptance* A $\simeq 0.6$*, for the first (upper panel) and second (lower panel) class of scenarios investigated in this work. We compare NLO QCD theoretical predictions to the bounds obtained by the CMS collaboration [242] at the* 1σ *(green) and* 2σ *(yellow) level. The actual Z' dijet branching ratio is indicated with the color code.*

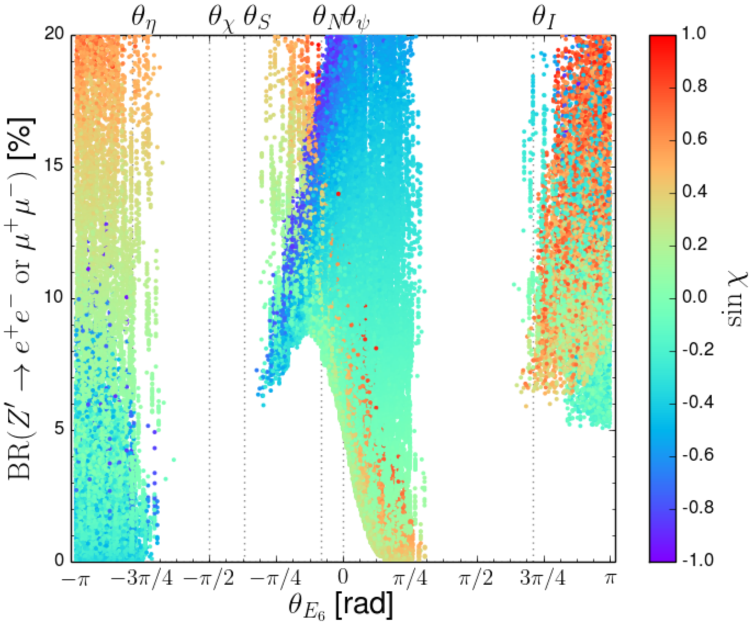

Figure 5.6: *Correlations between the Z'-boson branching ratio into a dilepton system and the θ_{E_6} mixing angle featured by all points satisfying the constraints detailed in section 5.1.2 and for UMSSM scenarios where the input parameters are fixed at the Z' mass scale (second class of considered scenarios). The value of the sine of the kinetic mixing angle* ($\sin\chi$) *is indicated by the color code.*

corresponding to a leptophobic Z'. In view of these results, we shall not impose further constraints, beyond those already discussed in the previous sections, and assume that any $\sin\chi$ can possibly be consistent with the Dark Matter relic density, including the values which make the Z' leptophobic.

In Fig. 5.6, we present the Z' dilepton branching ratio, scanning the parameter space as presented in Section 5.1.2, in terms of the mixing angle θ_{E_6} and $\sin\chi$. In agreement with Eq. (5.1.4), we realize that values of $\sin\chi$ around ± 0.3 can lead to leptophobia whenever the E_6 mixing angle obeys the condition in Eq. (5.1.5) and the $U(1)'$ charges fulfill the relation $\bar{Q}_E \approx \bar{Q}_L \approx 0$. In particular, the condition $\mathrm{BR}(Z' \to l^+l^-) \simeq 0$ can be achieved for $-\pi \lesssim \theta_{E_6} \lesssim -3\pi/4$, which includes the $U(1)'_\eta$ model, and for $\pi/8 \lesssim \theta_{E_6} \lesssim \pi/4$, hence in the neighborhood of $U(1)'_\psi$. The other $U(1)'$ symmetries are either ruled by the experimental data or, even in the most optimistic case, can hardly lead to dilepton rates below 5%.

Of course, these leptophobic scenarios cannot be constrained by standard Z'-boson searches in dimuons or dielectrons at the LHC, and novel strategies must be designed. In the following, we propose a selection potentially allowing to observe leptophobic light Z' bosons decaying through a supersymmetric cascade. As direct decays are forbidden, dilepton final states can arise from (Z'-mediated) chargino-pair production and subsequent decays into a charged lepton and missing energy via an intermediate W boson, possibly off-shell, namely $\tilde{\chi}_1^\pm \to (W^\pm \to l^\pm \nu_l)\ \tilde{\chi}_1^0$, $\tilde{\chi}_1^0$ being the lightest neutralino. However, for the points selected by our scan procedure, the off-shell contributions are typically either negligible (when the two-body decay channel is open) or not important enough to yield a sufficient number of signal events (when the $\tilde{\chi}_1^\pm \to W^\pm \tilde{\chi}_1^0$ decay is closed). We, therefore, design an analysis assuming the presence of intermediate on-shell W bosons, targeting thus UMSSM scenarios where the mass difference between the lightest chargino $\tilde{\chi}_1^\pm$ and the lightest neutralino $\tilde{\chi}_1^0$ is at least $M_W \simeq 80$ GeV. The signal process consists of the resonant production of a chargino pair, followed by the decay of each chargino into a charged lepton and missing energy,

$$pp \to Z' \to \tilde{\chi}_1^+ \tilde{\chi}_1^- \to l^+ l^- + \not{E}_T\ . \tag{5.3.1}$$

We focus on two optimistic signal benchmarks that are currently not excluded by data and with different $U(1)'$ properties. Both scenarios exhibit a Z' boson with a mass of about 2.5 TeV and charginos and neutralinos as light as possible, in order to maximize the branching ratios in Eq. (5.3.1), but with a mass splitting larger than M_W, in such a way to allow the transition $\tilde{\chi}_1^\pm \to \tilde{\chi}_1^0 W^\pm$ with real W bosons. The first scenario, that we denote

Table 5.6: *UMSSM parameters for the reference points* **BM I** *and* **BM II**.

Parameter	θ_{E_6}	$\tan\beta$	$\mu_{\rm eff}$ [GeV]	$M_{Z'}$ [TeV]	M_0 [TeV]	M_1 [GeV]
BM I	$-0.79\ \pi$	9.11	218.9	2.5	2.6	106.5
BM II	$0.2\ \pi$	16.08	345.3	2.5	1.9	186.7

Parameter	M_2 [GeV]	M_3 [TeV]	M_1' [GeV]	A_0 [TeV]	A_λ [TeV]	$\sin\chi$
BM I	230.0	3.6	198.9	2	5.9	-0.35
BM II	545.5	5.5	551.7	1.5	5.1	0.33

BM I, relies on a $U(1)'_\eta$ symmetry, namely $\theta_{E_6} = -0.79\pi$, since UMSSM scenarios based on this specific gauge symmetry can be made naturally leptophobic, as shown in Fig. 5.6. The second scenario, dubbed **BM II**, has instead a symmetry close to the $U(1)'_\psi$ setup, but with a larger mixing angle, *i.e.* $\theta_{E_6} = 0.2\pi$, so that a leptophobic Z' boson can still be realized (see again Fig. 5.6).

The UMSSM parameters for the two points are quoted in Table 5.6, while Table 5.7 and 5.8 contain the predicted masses for gluinos, squarks, sleptons, Higgses and gauginos in the reference points **BM I** and **BM II**, respectively. The branching ratios of the Z' in such representative points are listed in Table 5.9, omitting rates which are below 1%.

Table 5.6 shows that **BM II** features substantially larger values of $\tan\beta$, $\mu_{\rm eff}$ and of the gaugino masses M_1, M_2, M_3 and M_4, while M_0 and the trilinear couplings A_0 and A_λ are smaller than in **BM I**. Comparing Table 5.7 and 5.8, one learns that in **BM I** the squarks have masses between 3 and 4 TeV, while in **BM II** they are on average more than 1 TeV heavier. Charged sleptons in **BM II** are instead lighter than in **BM I**, unlike sneutrinos, whose masses vary between about 300 GeV and 1.7 TeV in **BM I** and between 660 GeV and 1.1 TeV in **BM II**. In the Higgs sector, with the exception of the SM-like h, all Higgs bosons have masses of a few TeV and are therefore too heavy to contribute to Z' decays for both benchmarks.

In particular, as anticipated, the singlet-like neutral boson H' has approximately the same mass as the Z', while H, A and $H^\pm$ are roughly degenerate, with mass about 3.37 TeV in **BM I** and 5.24 TeV in **BM II**. As for gauginos, as anticipated, the two novel neutralinos $\tilde\chi^0_5$ and $\tilde\chi^0_6$ have masses similar to $M_{Z'}$, thus too high to be relevant for Z' decays, while charginos and MSSM-like neutralinos are sufficiently light to possibly contribute to the Z' width. Overall, the electroweakino spectrum is more compressed in the reference point **BM I**. The mass splitting between $\tilde\chi^\pm_1$ and $\tilde\chi^0_1$ is in fact slightly above M_W in **BM I**, while it is

Table 5.7: *Masses of gluino, squarks, sleptons, Higgs and gauginos for the UMSSM benchmark point* **BM I**. $\tilde{q}_{1,2}$, $\tilde{l}_{1,2}$ *and* $\tilde{\nu}_{1,2}$ *are mass eigenstates and differ from the gauge eigenstates* $\tilde{q}_{L,R}$, $\tilde{\ell}_{L,R}$ *and* $\tilde{\nu}_{L,R}$ *by virtue of the mass mixing contributions that are relevant especially in the stop case. All masses are in GeV.*

$M_{\tilde{g}}$	$M_{\tilde{d}_1}$	$M_{\tilde{u}_1}$	$M_{\tilde{s}_1}$	$M_{\tilde{c}_1}$	$M_{\tilde{b}_1}$	$M_{\tilde{t}_1}$
3745.1	2988.8	2937.3	3380.3	3025.9	3380.4	3379.4
	$M_{\tilde{d}_2}$	$M_{\tilde{u}_2}$	$M_{\tilde{s}_2}$	$M_{\tilde{c}_2}$	$M_{\tilde{b}_2}$	$M_{\tilde{t}_2}$
	3525.2	3379.4	3541.2	3699.0	3541.2	3699.0
	$M_{\tilde{e}_1}$	$M_{\tilde{e}_2}$	$M_{\tilde{\mu}_1}$	$M_{\tilde{\mu}_2}$	$M_{\tilde{\tau}_1}$	$M_{\tilde{\tau}_2}$
	171.1	345.7	196.4	392.3	239.4	409.6
	$M_{\tilde{\nu}_{e,1}}$	$M_{\tilde{\nu}_{e,2}}$	$M_{\tilde{\nu}_{\mu,1}}$	$M_{\tilde{\nu}_{\mu,2}}$	$M_{\tilde{\nu}_{\tau,1}}$	$M_{\tilde{\nu}_{\tau,2}}$
	336.4	1663.1	384.1	1674.2	401.6	1683.6
M_h	M_H	$M_{H'}$	M_A	$M_{H^\pm}$	$M_{\tilde{\chi}_1^+}$	$M_{\tilde{\chi}_2^+}$
122.5	3371.5	2507.0	3371.5	3372.7	177.1	302.3
	$M_{\tilde{\chi}_1^0}$	$M_{\tilde{\chi}_2^0}$	$M_{\tilde{\chi}_3^0}$	$M_{\tilde{\chi}_4^0}$	$M_{\tilde{\chi}_5^0}$	$M_{\tilde{\chi}_6^0}$
	95.5	181.3	232.2	302.4	2405.1	2602.0

Table 5.8: *Same Table 5.7 but for the UMSSM benchmark point* **BM II**.

$M_{\tilde{g}}$	$M_{\tilde{d}_1}$	$M_{\tilde{u}_1}$	$M_{\tilde{s}_1}$	$M_{\tilde{c}_1}$	$M_{\tilde{b}_1}$	$M_{\tilde{t}_1}$
5669.3	4405.5	4141.5	4927.6	4418.1	4927.7	4926.9
	$M_{\tilde{d}_2}$	$M_{\tilde{u}_2}$	$M_{\tilde{s}_2}$	$M_{\tilde{c}_2}$	$M_{\tilde{b}_2}$	$M_{\tilde{t}_2}$
	5069.8	4927.0	5146.3	5117.1	5146.3	5117.1
	$M_{\tilde{e}_1}$	$M_{\tilde{e}_2}$	$M_{\tilde{\mu}_1}$	$M_{\tilde{\mu}_2}$	$M_{\tilde{\tau}_1}$	$M_{\tilde{\tau}_2}$
	665.1	871.5	679.2	1067.9	743.9	1075.6
	$M_{\tilde{\nu}_{e,1}}$	$M_{\tilde{\nu}_{e,2}}$	$M_{\tilde{\nu}_{\mu,1}}$	$M_{\tilde{\nu}_{\mu,2}}$	$M_{\tilde{\nu}_{\tau,1}}$	$M_{\tilde{\nu}_{\tau,2}}$
	660.4	1049.6	674.3	1079.4	739.3	1106.2
M_h	M_H	$M_{H'}$	M_A	$M_{H^\pm}$	$M_{\tilde{\chi}_1^+}$	$M_{\tilde{\chi}_2^+}$
127.4	5237.8	2498.2	5238.0	5238.8	343.8	593.5
	$M_{\tilde{\chi}_1^0}$	$M_{\tilde{\chi}_2^0}$	$M_{\tilde{\chi}_3^0}$	$M_{\tilde{\chi}_4^0}$	$M_{\tilde{\chi}_5^0}$	$M_{\tilde{\chi}_6^0}$
	178.1	346.9	360.0	593.2	2239.1	2785.9

Table 5.9: *Z' decay rates for the benchmark points* **BM I** *(second column) and* **BM II** *(third column). Branching ratios below 1% are omitted.*

Decay mode	BR [%] (**BM I**)	BR [%] (**BM II**)
$Z' \to \tilde{\chi}_1^+ \tilde{\chi}_1^-$	1.7	6.3
$Z' \to \tilde{\chi}_2^+ \tilde{\chi}_2^-$	2.1	-
$Z' \to \tilde{\chi}_1^\pm \tilde{\chi}_2^\mp$	3.9	-
$Z' \to \tilde{\chi}_2^0 \tilde{\chi}_2^0$	-	1.5
$Z' \to \tilde{\chi}_2^0 \tilde{\chi}_3^0$	1.7	3.3
$Z' \to \tilde{\chi}_3^0 \tilde{\chi}_3^0$	1.9	1.9
$Z' \to \tilde{\chi}_3^0 \tilde{\chi}_4^0$	2.2	-
$Z' \to \sum_i \tilde{\nu}_i \tilde{\nu}_i^\dagger$	-	1.6
$Z' \to hZ$	1.9	1.9
$Z' \to W^+W^-$	3.6	3.8
$Z' \to \sum_i d_i \bar{d}_i$	15.8	14.8
$Z' \to \sum_i u_i \bar{u}_i$	39.8	40.0
$Z' \to \sum_i \nu_i \bar{\nu}_i$	23.4	22.8

substantially larger than M_W, *i.e.* about 165 GeV, in the **BM II** framework. In both cases, the decay $\tilde{\chi}_1^\pm \to W^\pm \tilde{\chi}_1^0$ can occur through on-shell W-bosons and has a branching fraction of almost 100%.

Concerning the Z' branching ratios, Table 5.9 shows that the branching fraction of the Z' boson decay into a $\tilde{\chi}_1^+ \tilde{\chi}_1^-$ pair, entering in the process of Eq. (5.3.1), is of about 2% for the scenario **BM I** and 6% for the scenario **BM II**. **BM I** allows for substantial branching fractions into other combinations of chargino pairs, while both scenarios exhibit non-negligible rates into neutralino pairs, and the **BM II** scenario also includes decays into sneutrino pairs as well. The decay rates in pairs of the lightest neutralinos, possible candidates for Dark Matter, are instead suppressed in both reference points. As a whole, supersymmetric decays are responsible for 12% and 15% of the Z' width in the representative points **BM I** and **BM II**, respectively.

Once our representative configurations are set, we carry out a full Monte Carlo event simulation at the LHC, for a center-of-mass energy $\sqrt{s} = 14$ TeV. Hard-scattering signal events are generated with MadGraph5_aMC@NLO, the matrix elements being convoluted with the NLO set of NNPDF 2.3 parton densities. The production cross section is then $\sigma(pp \to Z') \simeq 120$ fb for both benchmarks. Parton showers and hadronization are simulated by means of the Pythia 8 program [231] (version 8.2.19), and the response of a typical LHC detector is modelled with the Delphes 3 package [165] (version 3.3.2), employing the

SNOWMASS parameterization [263, 264]. The resulting detector-level jets are reconstructed following the anti-k_T algorithm [167] with a radius parameter $R = 0.6$, as implemented in the FASTJET program (version 3.1.3) [166]. Moreover, we consider an average number of pile-up events of 140 and normalize our results to an integrated luminosity of 3000 fb^{-1}.

Regarding the backgrounds, we consider all processes leading to final states with two charged leptons and missing energy, such as vector-boson pairs VV, with V being a W-boson or a Z boson decaying leptonically. However, for the purpose of mimicking an actual experimental analysis, we account for processes yielding also jets which do not pass the acceptance cuts. Moreover, since our event simulation includes hadronization effects, we explore the possibility that background leptons originate from hadron decays as well. Overall, our backgrounds consist of single vector bosons (V) or vector-boson pairs (VV), possibly accompanied by jets, as well as $t\bar{t}$ and single-top events. In principle, even direct chargino production ($pp \to \chi_1^+\chi_1^- \to l^+l^- + \not{E}_T$) should be considered as a background to the supersymmetric Z' decays. Nevertheless, as pointed out in Ref. [200], the leptons produced in processes with direct charginos, unlike those coming from Z' events, are typically pretty soft or collinear to the beams. It is therefore quite easy to suppress the $pp \to \tilde{\chi}_1^+\tilde{\chi}_1^-$ background by setting suitable cuts on the lepton transverse momenta.

Lepton and jet candidates that are considered throughout our analysis must have transverse momenta p_T^l and p_T^j and pseudorapidities η^l and η^j satisfying

$$\begin{aligned} p_T^l &\geq 20 \text{ GeV} \qquad \text{and} \qquad |\eta^l| < 1.5 \ , \\ p_T^j &\geq 40 \text{ GeV} \qquad \text{and} \qquad |\eta^j| < 2.4 \ . \end{aligned} \tag{5.3.2}$$

Moreover, in our selection strategy, we reject lepton candidates that are not at an invariant angular distance, in the transverse plane, of at least 0.4 from a jet,

$$\Delta R(j,l) > 0.4 \ ,$$

and only focus on muons that are cleaner objects than electrons, in particular for the pseudorapidity region considered in Eq. (5.3.2). We finally enforce the considered muons to be isolated, so that the activity in a cone of radius $R = 0.4$ centered on each muon contains at most 15% of the muon p_T,

$$I_{\text{rel}}^{\mu} < 0.15 \ .$$

We select events featuring two well-separated muons, since the two signal leptons

Table 5.10: *Selection strategy aiming at observing a leptophobic UMSSM Z' boson decaying into a supersymmetric cascade. For each cut, we provide the expected number of surviving events for 3000 fb^{-1} of pp collisions at $\sqrt{s} = 14$ TeV for both background and signal benchmark scenarios* **BM I** *and* **BM II**. *We also quote the corresponding significances s and Z_A, as defined in Eq. (3.4), with 20% uncertainity.*

Step	Requirements	Background	**BM I**	**BM II**
0	Initial	1.7×10^{11}	8.8×10^3	1.9×10^4
1	$N^l = 2$	6.1×10^8	401	860
2	Electron veto	2.9×10^8	100	230
3	$\lvert\eta^l\rvert < 1.5$	1.7×10^8	76	170
4	$I^{\mu}_{\rm rel} < 0.15$	7.9×10^5	63	130
5	$\Delta R(l_1, l_2) > 2.5$	7.9×10^5	62	130
6	Jet veto	7.7×10^4	57	120
7	$p_T(l_1) > 300$ GeV	44	36	71
8	$p_T(l_2) > 200$ GeV	20	19	32
9	$\not{E}_T > 100$ GeV	10	14	27
		s	3.77σ	7.14σ
		Z_A	3.03σ	5.05σ

l_1 and l_2 are expected to originate from two different supersymmetric cascade decays, by requiring

$$N^l = 2 \qquad \text{and} \qquad \Delta R(l_1, l_2) > 2.5$$

and we veto the presence of jets, *i.e.*

$$N^j = 0 \ .$$

Furthermore, the two signal leptons are expected to be produced from the decay of a heavy Z' with a mass well above the TeV scale. We consequently impose the transverse momenta of the two leptons to fulfill

$$p_T(l_1) > 300 \text{ GeV} \qquad \text{and} \qquad p_T(l_2) > 200 \text{ GeV},$$

which are very efficient cuts to reduce the remaining SM background. We finally improve the sensitivity by requiring a large amount of missing energy,

$$\not{E}_T > 100 \text{ GeV},$$

as could be expected for a signal topology where several neutrinos and neutralinos escape the detector invisibly.

The corresponding cutflows are shown in Table 5.10, which illustrates that, for the two benchmark scenarios under consideration, background rejection is sufficiently important for observing the signal despite the low selection efficiencies. For other possible benchmark choices (not considered in this work) featuring a heavier Z', the smaller production total rate is expected to be compensated by a larger efficiency of the two selection cuts restricting the transverse momenta of the two selected leptons.

Denoting the number of selected signal and background events by S and $B \pm \sigma_B$, we make use of two standard criteria, labelled as s and Z_A, to define the LHC sensitivity to the leptophobic Z'-boson signal as defined in Eq. (3.4). In Eq. (3.4), s is the significance as defined by the CMS Collaboration in Ref. [265][5], whereas the second method (Z_A) is known to be more suitable (and conservative) when the number of background events is small [169]. The conclusions are however very similar in both cases, as can be seen from Table 5.10. For both significance definitions, we indeed find that the more compressed scenario **BM I** could lead to hints visible at the 3σ level, whilst the second scenario **BM II** is in principle observable at even more than 5σ. The largest LHC sensitivity to the latter scenario has a twofold origin. First, the Z'-induced chargino-pair production cross section is larger by virtue of a greater BR($Z' \to \tilde{\chi}_1^+ \chi_1^-$) branching ratio. Second, the heavier chargino mass typically induces harder leptons, the corresponding selection cuts being thus more efficient.

In the left panel of Fig. 5.7, we present the distribution in the transverse momentum of the leading muon l_1 after applying the first six cuts of Table 5.10. In the right panel of the figure, we in contrast show the transverse-momentum spectrum of the next-to-leading muon l_2 as resulting from the entire selection strategy. As for the $p_T(l_1)$ spectrum, all four considered backgrounds contribute at small p_T, while above 100 GeV the only surviving SM events originate from the production of VV and $t\bar{t}$ pairs. The signal spectra are rather broad and lie below the backgrounds at low $p_T(l_1)$, whereas, for $p_T(l_1) > 300$ GeV, both signals **BM I** and **BM II** start to be competitive with the background, yielding comparable numbers of events. For even larger transverse momenta, say $p_T(l_1) > 500$ GeV, muons coming from supersymmetric decays of a leptophobic Z' become dominant, especially in the reference point **BM II**. After all cuts are applied, the $p_T(l_2)$ distribution is explored (Fig. 5.7, right). All backgrounds are further suppressed and those due to single vector-boson and single-top production are negligible. The transverse momentum spectrum is thus

---

[5] Following Ref. [266], the denominator of s sums in quadrature the intrinsic statistical fluctuation of the background $\sqrt{B}$ and the uncertainty in the background σ_B, thus obtaining $s = S/\sqrt{(\sqrt{B})^2 + \sigma_B^2}$, leading to Eq. (3.4).

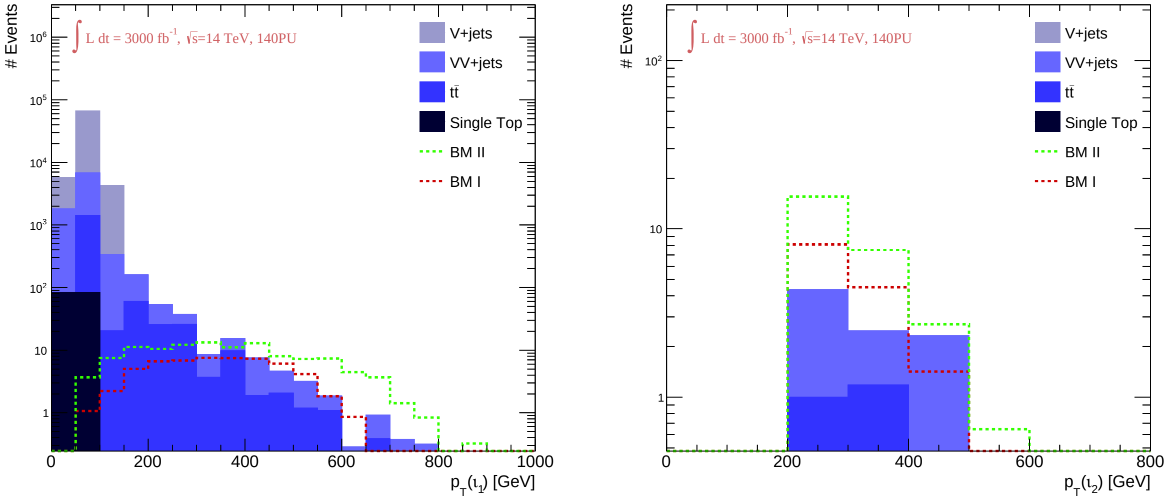

Figure 5.7: *Transverse momentum distribution of the leading muon* l_1 *after applying the first 6 cuts of Table 5.10 (left) and of the next-to-leading muon* l_2 *after applying all cuts (right) for both signal scenarios and the backgrounds.*

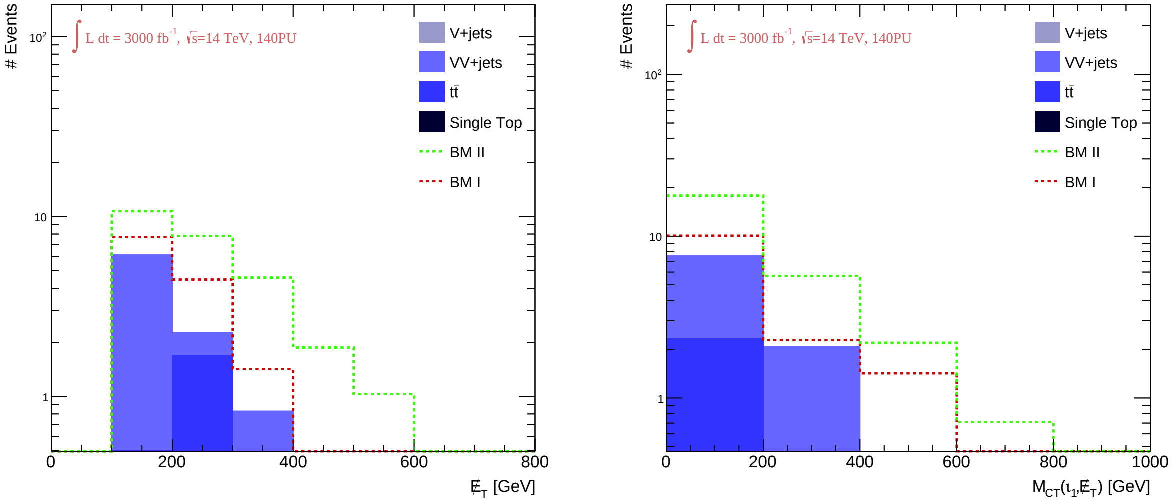

Figure 5.8: *Left: missing transverse energy spectrum for the different components of the background and the two signal benchmarks. Right: cotransverse mass distributions for muon* l_1 *and invisible particles leading to missing energy (neutralinos and neutrinos). All histograms are obtained after applying all the acceptance cuts discussed in the paper.*

substantial in the 200 GeV $< p_T(l_2) <$ 600 GeV range, with the **BM II** signal yielding the highest number of events through all p_T range and **BM I** being also quite remarkable, especially for 200 GeV $< p_T <$ 400 GeV. Overall, Fig. 5.7 (right) shows that the cuts which we have applied are rather efficient to discriminate the leptons in leptophobic Z' events from the Standard Model ones.

In Fig. 5.8 (left) we show the missing transverse energy, due to the lightest neutralinos $\tilde{\chi}_1^0$ in our signal and to neutrinos in the backgrounds, after all cuts are imposed. The $\not{E}_T$ spectra of our UMSSM benchmark scenarios are well above the backgrounds, once again limited to VV and $t\bar{t}$ pairs, through the whole $\not{E}_T$ range. The **BM II** configuration, in particular, is capable of yielding a few events up to $\not{E}_T \simeq$ 600 GeV, while, above 400 GeV, the backgrounds are basically all suppressed.

We have verified that any other transverse observable, such as the M_{T2} or M_{CT} variables defined in Refs. [267, 268, 269], are not useful for improving the considered selection strategy due to the too small mass difference between the lightest chargino and the lightest neutralino. The main features of the signal topology are in this case already captured by the requirements on the lepton transverse momenta and on the missing transverse energy.

This is illustrated in Fig. 5.8 (right), where we present the cotransverse mass M_{CT} distribution[6] for the leading muon l_1 and all particles contributing to the missing energy (lightest neutralinos and neutrinos). The M_{CT} spectrum is qualitatively comparable to the $\not{E}_T$ one. Both signals and backgrounds (VV and $t\bar{t}$) peak at similar values, although the number of events generated by Z' decays is always larger than for SM processes, and for $M_{CT} >$ 400 GeV only signal events survive. Designing an analysis with a possible extra cut on M_{CT} would lead to a reduction in the significance, as both S and B would be affected in the same way. Such a new selection may, however, increase the sensitivity for spectra featuring larger mass gaps. In this work, we nevertheless choose to focus on the lighter UMSSM particle spectra that are still not excluded so far and thus more relevant for the near future.

---

[6] Given two particles of transverse energies $E_{T,1}$ and $E_{T,2}$ and transverse momenta $\vec{p}_{T,1}$ and $\vec{p}_{T,2}$, the cotransverse mass is defined as $M_{CT}^2 = (E_{T,1} + E_{T,2})^2 - (\vec{p}_{T,1} + \vec{p}_{T,2})^2$ [269].

Chapter 6

Reinterpreting the results of the LHC with MadAnalysis 5: uncertainties and higher-luminosity estimates

The discovery of the Higgs boson has accomplished one of the long awaited objectives of the LHC physics programme and confirmed our understanding of the fundamental laws of nature. However, the concrete realisation of the electroweak symmetry breaking mechanism remains unexplained and no evidence for physics beyond the SM, whose existence is motivated by the SM theoretical inconsistencies and limitations, has emerged from data. There are two classes of possible explanations as to why the associated new particles and/or interactions have escaped detection so far. The first one is that the new states are too heavy and/or the new interactions too feeble to be observed with present collider reaches. Alternatively, new particles may be hiding just around the corner, but lie in a specific configuration (like being organised in a compressed spectrum) that renders their discovery challenging. The possible observation of any new phenomena therefore is the foremost goal of the future LHC runs, including in particular the LHC Run 3, to be started in two years, and the high-luminosity operations planned to begin in half a decade.

In order to investigate whether new physics could be present in existing data, several groups have developed and maintained public software dedicated to the reinterpretation of the results at the LHC [270, 271, 272, 273, 274]. In practice, these tools rely on predictions detailing how the different signal regions of given LHC analyses are populated to derive the potential of these searches for its observation. However, signal uncertainties are in general ignored by users in this procedure, although they could sometimes lead to incorrect interpretations [230]. With the limits on the masses of any hypothetical particle being pushed to higher and higher scales, the theoretical uncertainties related with the new physics signals can moreover sometimes be quite severe, in particular if the associated scale and Bjorken-x value lead to probing the parton densities in a regime in which they are poorly constrained [275].

On the other hand, it would be valuable to get estimates of the capabilities of the future runs of the LHC with respect to a given signal, possibly on the basis of the interpretation of the results of existing analyses of current data. Predictions in which the signal and the background are naively scaled up could hence be useful to obtain an initial guidance on the reach of future collider setups within new physics parameter spaces.

In this paper, we address the above mentioned issues by presenting an extension of the recasting capabilities of the MadAnalysis 5 platform [272, 276] so that signal theoretical and systematics uncertainties could be included in the recasting procedure. Moreover, we show how the reinterpretation results, with uncertainties included, could be correctly extrapolated to different luminosities to get insight on the sensitivity of the future LHC data on given signals.

As an illustration of these new features within concrete cases, we consider several classes of widely used simplified models. We first extract bounds on various model parameters from recent LHC results. Next, we study how those constraints are expected to evolve with the upcoming high-luminosity run of the LHC through a naive rescaling of the signal and background predictions. In practice, we make use of the recasting capabilities of MadAnalysis 5 and pay a special attention to the theoretical uncertainties.

We begin with a simplified model inspired by the MSSM in which the SM is complemented by a gluino and a neutralino, all other superpartners being assumed heavy and decoupled [277, 278]. Such a particle spectrum leads to a signature comprised of jets and missing transverse energy originating from the gluino decays into an invisible neutralino and quarks. We reinterpret the results of corresponding ATLAS searches for the signal in 36 fb^{-1} [173] and 139 fb^{-1} [279] of LHC data. We investigate the impact of the theory errors on the derived bounds at the nominal luminosity of the search, and extrapolate the findings to estimate the outcome of similar searches analysing 300 and 3000 fb^{-1} of LHC data. Secondly, we make use of these recent LHC searches to perform an equivalent exercise in the context of a simplified model in which the SM is extended by a single species of first generation squarks and a neutralino [277, 278]. Such a spectrum also leads to a new physics signature made of jets and missing transverse energy, although the squark colour triplet nature yields a signal featuring a smaller jet multiplicity. As the considered ATLAS study includes a large set of signal regions each dedicated to a different jet multiplicity, it is sensitive to this simplified model that has moreover not been covered the result interpretations performed in the experimental publication.

As a last example, we study the phenomenology of a simplified dark matter model in which a Dirac fermion dark matter candidate couples to the SM via interactions with an s-channel spin-1 mediator [280, 281]. This model is known to be reachable via standard LHC monojet and multijet plus missing transverse energy searches for dark matter. We extract up-to-date bounds on the model by reinterpreting the results of the ATLAS search of ref. [279] that analyses the full Run 2 ATLAS dataset. This search includes signal regions dedicated to both the monojet and the multijet plus missing energy signatures, so that it consists in an excellent probe for dark matter models. We focus on two specific configurations of our generic simplified models in which the mediator couples with the same strength to the dark and SM sectors. In the first case, we consider mediator couplings of a vector nature, whilst in the second case, we focus on axial-vector mediator couplings. We investigate how the bounds evolve with the luminosity for various dark matter and mediator masses and the nature of the new physics couplings.

The rest of this paper is organised as follows. We discuss the details of the recasting capabilities of MadAnalysis 5 in section 6.1, focusing not only on the new features that have been implemented in the context of this work, but also on how the code should be used for LHC recasting. We then apply it to extracting gluino and neutralino mass limits in section 6.2 for various luminosities of LHC data. We analyse the squark/neutralino simplified model in section 6.3 and perform our dark matter analysis in section 6.4.

6.1 LHC recasting with MadAnalysis 5

The MadAnalysis 5 package [232, 282] is a framework dedicated to new physics phenomenology. Whilst the first aim of the programme was to facilitate the design and the implementation of analyses targeting a given collider signal of physics beyond the Standard Model, and how to unravel it from the background, more recently it has been extended by LHC reinterpretation capabilities [272, 276]. This feature allows the user to derive the sensitivity of the LHC to any collider signal obtained by matching hard-scattering matrix elements with parton showers, based on the ensemble of analyses that have implemented in the MadAnalysis 5 public analysis database (PAD) [272][1]. For each of these analyses, the code simulates the experimental strategies (which includes both the simulation of the detector response and the selection) to predict the number of signal events that should populate the analysis signal regions. It then compares the results with both data and the SM expectation, so that conclusive statements could be drawn. As in all recasting codes relying on the same method [271, 273, 274], the uncertainty on the signal is ignored although it could be relevant [275].

With the release of MadAnalysis 5 version v1.8, the user has now the possibility to deal with various classes of signal uncertainties and to extrapolate any reinterpretation result to higher luminosities. This section documents all these new functionalities. section 6.1.1 briefly summarises how to install MadAnalysis 5, get the code running and download a local copy of its public analysis database. section 6.1.2 details how the code can be used to reinterpret the results of a specific LHC analysis. A more extensive and longer version of this information on MadAnalysis 5 installation and running procedures can be found in ref. [276]. Section 6.1.3 is dedicated to the new methods that have been developed in the context of this work, and which are available from MadAnalysis 5 version v1.8 onwards. We also introduce in this section several new optional features that can be used for the design of the analysis `.info` files. One such file accompanies each analysis of the database and contains information on the observation and the SM expectation of the different analysis signal regions. In section 6.1.4, we describe the corresponding modifications of the output format relevant for a recasting run of MadAnalysis 5.

6.1.1 Prerequisites and installation

MadAnalysis 5 is compatible with most recent Unix-based operating systems, and requires the GNU G++ or CLang compiler, a Python 2.7 installation (or more recent, but not a Python 3 one) and GMake. In order for the recasting functionalities to be enabled, the user must ensure that the SciPy library is present, as it allows for limit computations, and that the Delphes 3 package [165] is locally available within the MadAnalysis 5 installation. The latter, which requires the Root framework [283] and the FastJet programme [166], is internally called by MadAnalysis 5 to deal with the simulation of the response of the LHC

---

[1] See the webpage https://madanalysis.irmp.ucl.ac.be/wiki/PublicAnalysisDatabase.

detectors and to reconstruct the events. Moreover, reading compressed event files can only be performed if the ZLIB library is available.

The latest version of MADANALYSIS 5 can be downloaded from LAUNCHPAD[2], where it is provided as a tarball named `ma5_v<xxx>.tgz`, that contains all MADANALYSIS 5 source files (`<xxx>` standing for the version number). After unpacking the tarball, the code can be started by issuing in a shell

```
./bin/ma5 -R
```

where the `-R` options enforces the `reco` mode of MADANALYSIS 5, that is relevant for LHC recasting. The programme begins with checking the presence of all mandatory packages and determining which of the optional packages are available. The MADANALYSIS 5 command-line interface is then initialised and the user is prompted to type in commands.

In the case where any of the ZLIB or DELPHES 3 package would not be found by MADANALYSIS 5, they can be installed locally by typing, directly in the MADANALYSIS 5 interpreter,

```
install zlib
install delphes
```

Whilst ROOT can in principle be installed similarly, we recommend the user to handle this manually, following the instructions available on the ROOT website[3] Furthermore, all existing and validated recast LHC analyses in the MADANALYSIS 5 framework can be locally downloaded by typing in,

```
install PAD
install PADForMA5tune
```

The second command triggers the installation of older implemented analyses, that requires a (now disfavoured) `MA5tune` version of DELPHES 3. The latter can be installed by typing, in the MADANALYSIS 5 shell,

```
install delphesForMA5tune
```

---

[2] See the webpage `https://launchpad.net/madanalysis5`.

[3] See the webpage `https://root.cern.ch`.

6.1.2 Recasting LHC analyses with MadAnalysis 5

In this section, we rely on a generic example in which a user aims to estimate the sensitivity of a specific LHC analysis to a given signal with MadAnalysis 5. The analysis consists of one of the analyses available from the PAD and the signal is described by simulated events collected into a file that we call `events.hepmc.gz`. Such an event file includes the simulation of the considered hard-scattering process matched with parton showers, as well as the hadronisation of the final-state partons present in each of the showered events.

As mentioned above, MadAnalysis 5 has to be started in the `reco` mode,

```
./bin/ma5 -R
```

In a first step, the recasting mode of the programme has to be enabled and the event file, physically located at `<path-to-events.hepmc.gz>` on the user system, has to be imported. This is achieved by issuing the commands

```
set main.recast = on
import <path-to-events.hepmc.gz> as <label>
```

The second command defines a dataset identified by the label `<label>` that here solely includes the imported sample. Several event files can be imported and collected either under a unique dataset (by using the same `<label>` for each call to the `import` command) or split into different datasets (by employing different labels). When studying the signal under consideration, MadAnalysis 5 will run over all defined datasets and imported event files.

In addition, the user can activate the storage of the Root file(s) generated by Delphes 3 by issuing the command,

```
set main.recast.store_root = <status>
```

where `<status>` can take the `True` or `False` value, and directly provide a predefined recasting card (available on the system at `<path-to-a-card>`), through

```
set main.recast.card_path = <path-to-a-card>
```

In the case where no card is provided, MadAnalysis 5 creates a consistent new card with one entry for each of the available analyses. Such an entry is of the form

```
<tag> <type> <switch> <detector> # <comment>
```

The `<tag>` label corresponds to the filename of the C++ code associated with the considered analysis (located in the `Build/SampleAnalyzer/User/Analyzer` subdirectory of the PAD installation in `tools/PAD`), the `<type>` label indicates whether the PADForMA5tune (`v1.1`) or PAD (`v1.2`) recasting infrastructure should be used and the `<switch>` tag (to be set to `on` or `off`) drives whether the analysis has to be recast. The name of the Delphes 3 card to use (see the `Input/Cards` subdirectory of the PAD installation) is passed as `<detector>`, and `<comment>` consists of an optional comment (usually briefly describing the analysis).

The run is finally started by typing in the interpreter,

```
submit
```

Firstly, MadAnalysis 5 simulates the detector impact on the input events, for each of the necessary Delphes 3 cards according to the analyses that have been switched on in the recasting card. Next, the code derives how the different signal regions are populated by the signal events and finally computes, by means of the CL$_s$ prescription[284], the corresponding exclusion limits, signal region by signal region. This is achieved by a comparison of the results with the information on the SM background and data available from the different `info` files shipped with the PAD.

The output information is collected into a folder named `ANALYSIS_X`, where `X` stands for the next available positive integer (in terms of non-existing directories). On top of basic details about the run itself, this folder contains the recasting results that are located in the `ANALYSIS_X/Output` folder. The latter includes the `CLs_output_summary.dat` file that concisely summarises all the results of the run. A more extensive version of these results can be found in the set of subfolders named after the labels of the imported datasets. The `CLs_output_summary.dat` file contains one line for each signal region of each reinterpreted analysis, and this for each of the datasets under consideration. Each of these lines follows the format

```
<set> <tag> <SR> <exp> <obs> || <eff> <stat>
```

where the `<set>` and `<tag>` elements respectively consist in the names of the dataset and analysis relevant for the considered line of the output file. The `<SR>` entry relates to one of the analysis signal regions, the exact name being the one defined in the analysis C++ source code. The `<exp>` and `<obs>` quantities are the expected and observed cross-section values for which the signal modelled by the events stored within the dataset `<set>` is excluded by the signal region `<SR>` of the analysis `<tag>` at the 95% confidence level. In the former case, the code makes use of the SM expectation to predict the number of events populating the signal region `<SR>`, whilst in the latter case, data is used. Finally, the `<eff>` and `<stat>` entries respectively refer to the corresponding selection efficiency and the associated statistical error.

The user has the option to specify the cross section corresponding to the investigated signal by issuing, in the MadAnalysis 5 interpreter,

```
set <label>.xsection = <value>
```

prior to the call to the `submit` command. Following this syntax, `<label>` stands for one of the labels of the considered datasets and `<value>` for the associated cross-section value, in pb. In this case, the confidence level at which the analysed signal is excluded is included in the output summary file (before the double vertical line).

The `Output` folder additionally contains a specific subfolder for each of the defined datasets. Such a directory contains a file named `CLs_output.dat` that includes the same information as in the `CLs_output_summary.dat` file, following the same syntax, but restricted to a specific dataset. A second file encoded into the SAF format [232] and named `<label>.saf` (`<label>` being the dataset name) contains general information on the dataset organised according to an XML-like structure. The latter relies on three classes of elements, namely `<SampleGlobalInfo>`, `<FileInfo>` and `<SampleDetailedInfo>`. The first of these contains global information on the dataset, such as its cross section (`xsec`), the associated error (`xsec_err`), the number of events (`nev`) or the sum of the positive and negative event weights (`sum_w+` and `sum_w-`). The corresponding entry in the output file would read

```
<SampleGlobalInfo>
# xsec   xsec_error  nev    sum_w+  sum_w-
...       ...        ...    ...     ...
</SampleGlobalInfo>
```

where the numerical values have been omitted for clarity. The `<FileInfo>` element sequentially provides the paths to the different event files included in the dataset, while detailed information on each file is provided within the `<SampleDetailedInfo>` XML root element, in a similar manner as for the sample global information (with one line for each file).

Furthermore, the dataset output directory includes a `RecoEvents` folder dedicated to the storage of Delphes 3 output files (one file for each considered detector parameterisation), provided that the corresponding option has been turned on (see above), as well as one folder for each of the recast analyses. Each of these folders contains one SAF file listing all signal regions implemented in the associated analysis, as well as two subfolders `Cutflows` and `Histograms`. The former includes one SAF file for each signal region, and the latter a single file named `histos.saf`.

A cutflow is organised through XML-like elements, `<InitialCounter>` and `<Counter>` being used for the initial number of events and the results of each selection cut respectively. As depicted by the example below, in which all numbers have been omitted for clarity,

```
<Counter>
"my_cut_name"   # 1st cut
....    ....    # nentries
....    ....    # sum of weights
....    ....    # sum of weights^2
</Counter>
```

any of such elements includes a cut name as defined in the analysis C++ file (first line), the number of events passing the cut (second line), the weighted number of events passing the cut (third line) and the sum of the squared weights of all events passing the cut (last line). Moreover, the first (second) column refers to the positively-weighted (negatively-weighted) events only.

Histograms are all collected into the file `histos.saf`, that is also organised according to an XML-like structure relying on several `<Histo>` elements. Each of these corresponds to one of the histograms implemented in the analysis. A `<Histo>` element includes the definition of the histogram (provided within the `<Description>` element), general statistics (as part of the `<Statistics>` element) and the histogram data itself (within the `<Data>` element). The description of a histogram schematically reads

```
<Description>
"name"
# nbins   xmin           xmax
..      ...            ...
# Defined regions
...   # Region nr. 1
...   # Region nr. 2
</Description>
```

and is self-explanatory, all numbers having been replaced by dots. This moreover shows that a given histogram can be associated with several signal regions, provided they are indistinguishable at the moment the histogram is filled. Statistics are typically given as

```
<Statistics>
...  ...  # nevents
...  ...  # sum of event-weights over events
...  ...  # nentries
...  ...  # sum of event-weights over entries
...  ...  # sum weights^2
...  ...  # sum value*weight
...  ...  # sum value^2*weight
</Statistics>
```

which include information about the number of entries, the weighted number of entries, the variance, *etc.* Moreover, the contributions of the positively-weighted and negatively-weighted events are again split and provided within the first and second column respectively. The values of each bin are finally available from the `<Data>` element,

```
<Data>
...  ...    # underflow
...  ...    # bin 1 / 15
.
.
.
...  ...    # bin 15 / 15
...  ...    # overflow
</Data>
```

where all bin values are omitted and the two columns respectively refer to events with positive (first column) and negative (second column) weights. The underflow and overflow bins are also included.

To close this section, we detail below how limits on a given signal are derived by MadAnalysis 5, using the CL_s prescription. The output file generated by the code contains three numbers associated with those limits, the expected and observed cross sections excluded at the 95% confidence level, $\sigma_{95}^{\rm exp}$ and $\sigma_{95}^{\rm obs}$, as well as the confidence level at which the input signal is excluded. Those numbers are extracted on the basis of the information available from the `.info` file, shipped with each recast analysis and that contains, for each signal region, the number of expected SM events n_b, the associated error Δn_b and the observed number of events populating the signal region $n_{\rm obs}$. As said above, starting from the input event file, MadAnalysis 5 simulates the response of the LHC detector, applies the analysis selection, and estimates how the different signal regions are populated. In this way, for each signal region, the number of signal events n_s is known.

This enables the computation of the background-only and signal-plus-background probabilities $p_{\rm b}$ and $p_{\rm b+s}$ and to further derive the related CL$_s$ exclusion. In practice, the code considers a number of toy experiments (the default being 100000 that can be changed by issuing, in the MadAnalysis 5 interpreter and before the call to the `submit` method,

```
set main.recast.CLs_numofexps = <value>
```

where `<value>` stands for the desired number of toy experiments. For each toy experiment, the expected number of background events $N_{\rm b}$ is randomly chosen assuming that its distribution is Gaussian, with a mean $n_{\rm b}$ and a width $\Delta n_{\rm b}$. The corresponding probability density thus reads

$$f(N_b|n_b, \Delta n_b) = \frac{\exp\left\{-\frac{(N_b-n_b)^2}{2\Delta n_b^2}\right\}}{\Delta n_b\sqrt{2\pi}} \ . \tag{6.1.1}$$

Imposing $N_{\rm b} \geq 0$, the actual number of background events $\hat{N}_{\rm b}$ is randomly generated from the Poisson distribution

$$f(\hat{N}_b|N_b) = \frac{N_b^{\hat{N}_b} e^{-N_b}}{\hat{N}_b!} \ . \tag{6.1.2}$$

Accounting for the observation of $n_{\rm obs}$ events, $p_{\rm b}$ is defined as the percentile of score associated with $\hat{N}_{\rm b} \leq n_{\rm obs}$, which consists in the probability for the background to fluctuate as low as $n_{\rm obs}$.

The signal-plus-background probability $p_{\rm b+s}$ is computed similarly, assuming that the actual number of signal-plus-background events $\hat{N}_{\rm b} + \hat{N}_{\rm s}$ follows a Poisson distribution of parameter $n_{\rm s} + N_{\rm b}$ (after imposing this time that $N_{\rm b} + n_{\rm s} > 0$). The resulting CL$_s$ exclusion is then derived as

$$\text{CL}_s = \max\left(0, 1 - \frac{p_{\rm b+s}}{p_{\rm b}}\right) \ . \tag{6.1.3}$$

and $\sigma_{95}^{\rm obs}$ is calculated as above in a case where the number of signal events n_s is kept free. From the (derived) knowledge of the analysis selection efficiencies, MadAnalysis 5 can extract the upper allowed cross section value for which the signal is not excluded, *i.e.* $\sigma_{95}^{\rm obs}$.

The expected cross section excluded at the 95% confidence level, $\sigma_{95}^{\rm exp}$, is obtained by replacing $n_{\rm obs}$ by $n_{\rm b}$ in the above calculations.

6.1.3 Including signal uncertainties and extrapolation to higher luminosities

In the procedure described in the previous section, any error on the signal is ignored, both concerning the usual theory uncertainties (scale variations, parton densities) and the systematics, mostly stemming from more experimental aspects. In particular, with the constantly growing mass bounds on hypothetical new particles, the scale entering the relevant hard-scattering processes is larger and larger, so that theoretical errors could start to impact the derived limits in an important and non-negligible manner.

Starting from version v1.8 onwards, MadAnalysis 5 offers the user a way to account for both the theoretical and systematical errors on the signal when a limit calculation is performed. The scale and parton density (PDF) uncertainties can be entered, within the MadAnalysis 5 interpreter, similarly to the cross section associated with a given dataset (see section 6.1.2),

```
set <label>.xsection        = <xsec_val>
set <label>.scale_variation = <scale>
set <label>.pdf_variation   = <pdf>
```

where `<label>` stands for the label defining the signal dataset. In this case, the signal cross section σ_s is provided through the `xsection` attribute of the dataset, as described in the previous section, while the scale and parton density uncertainties $\Delta\sigma_{\rm scales}$ and $\Delta\sigma_{\rm PDF}$ are given through the `scale_variation` and `pdf_variation` attributes. The errors are symmetric with respect to the central value σ_s, and their value (given by `<scale>` and `<pdf>` in the above example) must be inputted as the absolute values of the relative errors on the cross section (*i.e.* as positive floating-point numbers). Asymmetric errors can also be provided, the upper and lower uncertainties being independently fixed by issuing, in the MadAnalysis 5 interpreter,

```
set <label>.scale_up_variation   = <scale_up>
set <label>.scale_down_variation = <scale_dn>
set <label>.pdf_up_variation     = <pdf_up>
```

```
set <label>.pdf_down_variation   = <pdf_dn>
```

Each error is again provided as a positive floating-point number and refers to the relative error on the cross section, in absolute value. On top of the computation of the confidence level at which the signal is excluded, MadAnalysis 5 additionally calculates the CL_s variation band associated with the scale uncertainties, as well as with the total theory uncertainties where both the scale and PDF contributions to the total error are added linearly. Such a behaviour can however be modified by issuing, in the interpreter

```
set main.recast.THerror_combination = <value>
```

where `<value>` can be set either to `quadratic` (the theory errors are added quadratically) or `linear` (default, the theory errors are added linearly). The CL_s band is then derived by allowing the signal cross section to vary within its error band, deriving the associated spread on $p_{\mathrm{b+s}}$.

The user can also specify one or more values for the level of systematics on the signal. This is achieved by issuing, in the command line interface,

```
set main.recast.add.systematics = <syst>
```

This command can be reissued as many times as needed, MadAnalysis 5 taking care of the limit calculation for each entered value independently. The level of systematics (`<syst>`) has to be given either as a floating-point number lying in the $[0, 1]$ range, or as a pair of floating-point numbers lying in the same interval. In the former case, the error is symmetric with respect to the central value σ_s, whilst in the latter case, it is asymmetric with the first value being associated with the upper error and the second one with the lower error.

In addition, we have also extended the code so that naive extrapolations for a different luminosity $\mathcal{L}_{\mathrm{new}}$ could be performed. This is achieved by typing, in the interpreter,

```
set main.recast.add.extrapolated_luminosity = <lumi>
```

Once again, the user has the possibility to reissue the command several times, so that the extrapolation will be performed for each luminosity `<lumi>` independently (where the value has to be provided in fb^{-1}). Those extrapolations assume that the signal and background selection efficiencies of a given region in a specific analysis are identical to those corresponding to the reference luminosity $\mathcal{L}_0$ initially considered. In this framework, the extrapolated number of background events n_b^{new} is related to n_b (the number of background events expected for the reference luminosity $\mathcal{L}_0$) as

$$n_b^{\rm new} = n_b \, \frac{\mathcal{L}_{\rm new}}{\mathcal{L}_0} \ , \tag{6.1.4}$$

that we assume equal to the extrapolated number of observed events,

$$n_{\rm obs}^{\rm new} = n_b^{\rm new} \ . \tag{6.1.5}$$

On the other hand, the associated uncertainties, $\Delta n_b^{\rm new}$, are derived from the relation

$$\Delta n_b^{\rm new} = \Delta_{b,{\rm syst}} \frac{\mathcal{L}_{\rm new}}{\mathcal{L}_0} \oplus \Delta_{b,{\rm stat}} \sqrt{\frac{\mathcal{L}_{\rm new}}{\mathcal{L}_0}} \ , \tag{6.1.6}$$

where the statistics and systematics components are added in quadrature. The systematics are extrapolated linearly, whilst the statistical uncertainties assume that the event counts follow a Poisson distribution. Such an extrapolation of the background error requires an access to the details of the background uncertainties. This is however not achievable within the XML `info` file format dedicated to the transfer of the background and data information to MadAnalysis 5 [272]. We therefore introduce two new XML elements to this format, namely `deltanb_stat` and `deltanb_syst`. These offer the user the option to implement his/her `info` file by either providing a unique combined value for the uncertainties (via the standard `deltanb` XML element) or by splitting them into their statistical and systematical components (via a joint use of the new `deltanb_stat` and `deltanb_syst` XML elements). In this way, a region element could be either implemented according to the old syntax, as in the schematic example below (with all numbers omitted),

```
<region type="signal" id="Region name">
<nobs>    ... </nobs>
<nb>      ... </nb>
<deltanb> ... </deltanb>
</region>
```

or following the new syntax, which would then read

```
<region type="signal" id="Region name">
<nobs>         ... </nobs>
<nb>           ... </nb>
<deltanb_stat> ... </deltanb_stat>
```

```
<deltanb_syst> ... </deltanb_syst>
</region>
```

Whilst the usage of the new syntax is encouraged, this new possibility for embedding the error information strongly depends on how the background uncertainties are provided in the experimental analysis notes. For this reason, as well as for backward-compatibility, MadAnalysis 5 supports both choices. If only a global error is provided, the user can freely choose how to scale the error (linearly or in a Poisson way), by typing in the interpreter,

```
set main.recast.error_extrapolation = <value>
```

where `<value>` has to be set either to `linear` or to `sqrt`. The user has also the choice to use a single floating-point number for the `<value>` parameter. In this case, the relative error on the number of background events at the new luminosity, $\Delta n_b^{\rm new}/n_b^{\rm new}$, is taken equal to this number. Finally, the user can provide a comma-separated pair of floating-point numbers κ_1 and κ_2, as in

```
set main.recast.error_extrapolation = <k1>,<k2>
```

The background error is here defined by

$$\left[\frac{\Delta n_b^{\rm new}}{n_b^{\rm new}}\right]^2 = \kappa_1^2 + \frac{\kappa_2^2}{n_b} \ , \tag{6.1.7}$$

where the two values provided by the user respectively control the systematical component of the uncertainties (`<k1>`, κ_1) and the statistical one (`<k2>`, κ_2). Finally, all extrapolations are based on expectations and not on observations, so that $n_{\rm obs}$ will be effectively replaced by the corresponding SM expectation $n_{\rm b}$.

6.1.4 Output format

MadAnalysis 5 propagates the information on the impact of the uncertainties all through the output file, which is then written in a format slightly extending the one presented in section 6.1.2. Starting with the summary file `CLs_output_summary.dat`, each line (corresponding to a given signal region of a given analysis) is now followed by information schematically written as

```
Scale var. band                [..., ...]
TH   error band                [..., ...]
```

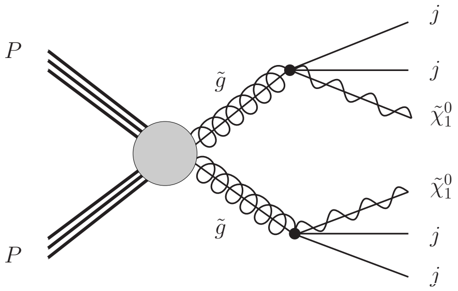

Figure 6.1: *Generic Feynman diagram associated with the production and decay of a pair of gluinos in the considered MSSM-inspired gluino simplified model. The figure has been produced with the help of the* JaxoDraw *package [35].*

```
+<lvl_up>%, -<lvl_dn>% syst    [..., ...]
```

The uncertainties on the exclusion stemming from scale variations are given in the first line, which is trivially omitted if the corresponding information on the signal cross section is not provided by the user. In the second line, MadAnalysis 5 adds either quadratically or linearly (according to the choice of the user) all theory errors, such a line being written only if at least one source of theory uncertainties is provided by the user. Finally, if the user inputted one or more options for the level of systematics, MadAnalysis 5 computes the band resulting from the combination of all errors and writes it into the output file (one line for each choice of level of systematics). In the above snippet, the user fixed an asymmetric level of systematics (for the sake of the example) indicated by the `<lvl_up>` and `<lvl_dn>` tags.

In cases where the band would have a vanishing size, the uncertainty information is not written to the output file. This could be due either to negligibly small uncertainties, to the fact that for the considered region, the signal is excluded regardless the level of systematics (at the 100% confidence level), or to the region not targeting the signal at all (the corresponding selection efficiency being close to zero).

The `CLs_output.dat` dataset-specific files present in the output subdirectory associated with each imported dataset all contain similar modifications. In case of extrapolations to different luminosities, copies of this file named `CLs_output_lumi_<lumi>.dat` are provided for each desired luminosity `<lumi>`.

6.2 Gluino and neutralino mass limits

To illustrate the usage of the new functionalities of MadAnalysis 5 introduced in the previous section, we perform several calculations in the context of a simplified model inspired by the MSSM. In this framework, all superpartners are heavy and decoupled, with the exception of the gluino $\tilde{g}$ and the lightest neutralino $\tilde{\chi}_1^0$, taken to be bino-like. Any given benchmark is thus defined by two parameters, namely the gluino and the neutralino masses $m_{\tilde{g}}$ and $m_{\tilde{\chi}_1^0}$. Such a new physics setup can typically manifest itself at the LHC through a signature made of a large hadronic activity and missing transverse energy. As shown by the schematic Feynman diagram of Fig. 6.1, such a signature originates from the production of a pair of gluinos, each of them promptly decaying into two jets and a neutralino (via virtual squark contributions).

We study the sensitivity of the LHC and its higher-luminosity upgrades to this signal by analysing state-of-the-art Monte Carlo simulations achieved by means of the MG5_aMC framework (version 2.6.6) [144], using the MSSM-NLO model implementation developed in ref. [275]. Hard-scattering matrix elements are generated at the NLO accuracy in QCD and convoluted with the NLO set of NNPDF 3.0 parton densities [285], as provided by the LHAPDF interface [286]. The gluino leading order (LO) decays are handled with the MadSpin [287] and MadWidth [288] packages. The resulting NLO matrix elements are then matched with Pythia parton showers and hadronisation (version 8.240) [231], following the MC@NLO method [289]. Our predictions include theoretical uncertainties stemming from the independent variations of the renormalisation and factorisation scales by a factor of two up and down relatively to the central scale, taken as half the sum of the transverse masses of the final-state particles, as well as from the parton densities extracted following the recommendations of ref. [290].

In the upper panel of Fig. 6.2, we present the total LO (red) and NLO (blue) gluino pair-production cross section for gluino masses ranging from 1 to 3 TeV, the error bars being associated with the quadratic sum of the scale and PDF uncertainties. The cross section central value is found to vary within the $100 - 0.001$ fb range when the gluino mass varies from 1 to 3 TeV, so that at least tens of gluino events could be expected even for a very heavy gluino benchmark at a high-luminosity upgrade of the LHC. We compare our predictions with the total rates traditionally employed by the ATLAS and CMS collaborations to extract gluino limits, as documented by the LHC Supersymmetry Cross Section Working Group [291]. Hence we include, in the first panel of Fig. 6.2, total gluino-pair pro-

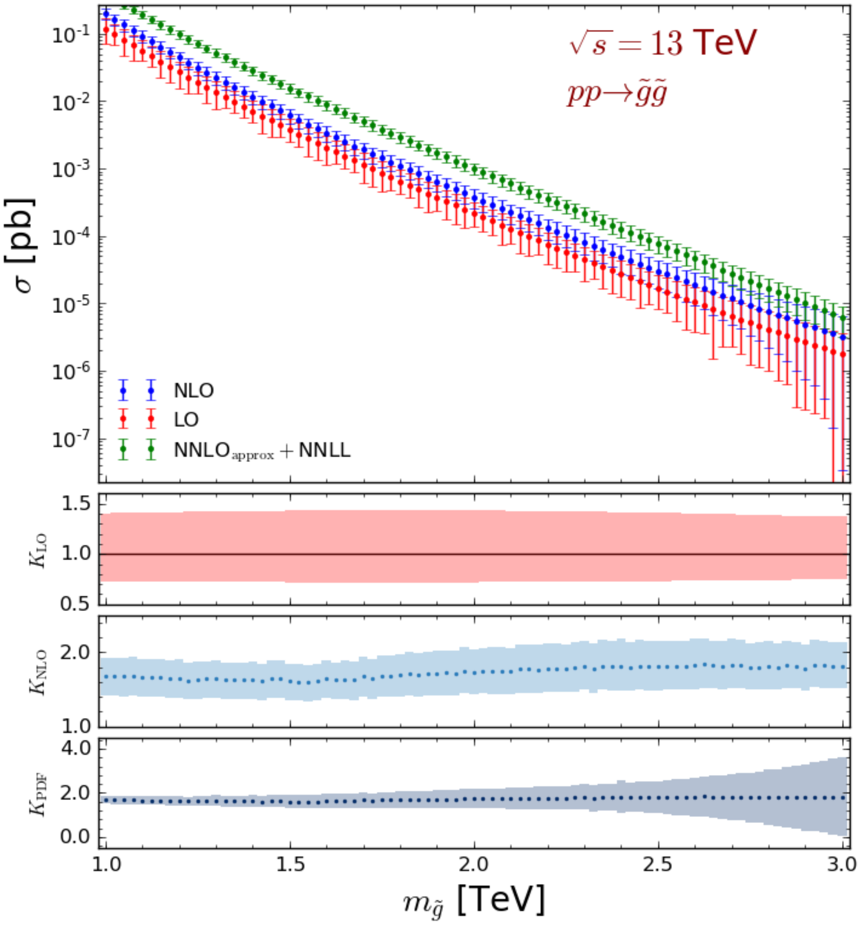

Figure 6.2: *Total LO (red), NLO (blue) and NNLO*$_{\rm approx}$*+NNLL (green) cross sections (upper panel) and K-factors (three lower panels, where the results are normalised to the LO central value) for gluino pair-production, at a centre-of-mass energy of* $\sqrt{s} = 13$ *TeV. In the upper panel, the error bands correspond to the quadratic sum of the scale and PDF uncertainties, whilst in the second and third panels, respectively, they refer to the scale uncertainties on the LO and NLO predictions. The last panel focuses on the PDF errors.*

duction cross sections matching approximate fixed-order results at next-to-next-to-leading order and threshold-resummed predictions at the next-to-next-to-leading logarithmic accuracy ($\mathrm{NNLO}_{\mathrm{approx}}$ + NNLL, in green). Following the PDF4LHC recommendations, those more accurate $\mathrm{NNLO}_{\mathrm{approx}}$+NNLL predictions are obtained by convoluting the partonic cross section with a combination of NLO CTEQ6.6M [292] and MSTW2008 [293] densities. This choice, together with the impact of the higher-order corrections, leads to $\mathrm{NNLO}_{\mathrm{approx}}$+NNLL results greater than our NLO predictions by a factor of about 2. While in the following we use NLO-accurate total rates (as the latter exist for any new physics model through a joint use of FeynRules [260], NLOCT [261] and MG5_aMC), we evaluate the impact of higher-order corrections whenever the relevant calculations exist, *i.e.* in this section and section 6.3.

With the second and third panels of the figure, we emphasise the significant reduction of the scale uncertainties at NLO by depicting the LO and NLO scale uncertainty bands respectively, the K_{LO} and K_{NLO} quantities, presented in the two subfigures, these being the LO and NLO cross sections normalised to the LO central value. Such better control in the theoretical predictions is one of the main motivations for relying on NLO simulations instead of on LO ones. In the lower panel of Fig. 6.2, we focus on the PDF uncertainties associated with the total rates and present the K_{PDF} quantity where the NLO result (with its PDF error band) is again shown relatively to the LO central result. We omit the corresponding LO curve, as it is similar to the NLO one, the same PDF set being used both at LO and NLO in order to avoid having to deal with the poor-quality LO NNPDF 3.0 fit [285]. Whilst the uncertainties are under good control over most of the probed mass range, the poor PDF constraints in the large Bjorken-x regime lead to predictions plagued by sizeable uncertainties for gluino heavier than about $2.6 - 2.7$ TeV. Finally, our results show that the NLO K-factor K_{NLO} is of about $1.6 - 1.7$, a typical value for a strong supersymmetric production process, and features a significant gluino mass dependence. The latter originates from the quark-antiquark contributions to the cross section that become relatively larger with respect to the gluon fusion ones with increasing Bjorken-x values [294].

We then predict, for several $(m_{\tilde{g}}, m_{\tilde{\chi}_1^0})$ configurations, how the signal events would populate the different signal regions of the ATLAS-SUSY-2016-07 search for supersymmetry [173]. In practice, we use the corresponding recast analysis as implemented in the MadAnalysis 5 public database [295], together with the appropriate Delphes 3 configuration for the simulation of the detector response. In this analysis, the ATLAS collaboration investigates the potential of a signature featuring multiple jets and missing transverse energy through two approaches. The first one relies on the so-called effective mass $M_{\mathrm{eff}}(N)$, a vari-

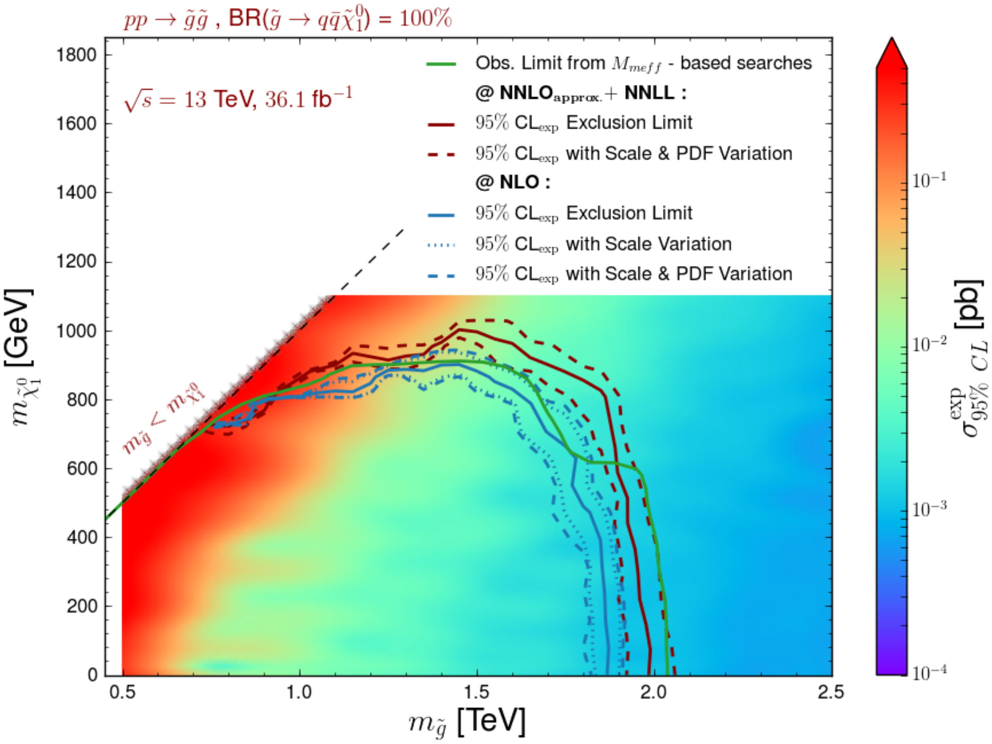

Figure 6.3: *Constraints on the gluino-neutralino simplified model under consideration, represented as 95% confidence level exclusion contours in the* $(m_{\tilde{g}}, m_{\tilde{\chi}_1^0})$ *plane. We compare the exclusion obtained with the ATLAS-SUSY-2016-07 reimplementation in the* MadAnalysis 5 *framework [295] when normalising the signal to NLO (blue) and to NNLO*$_{\text{approx}}$*+NNLL (red) with the official ATLAS results, extracted using the* M_{eff} *signal regions only [173] (solid green). Moreover, we include the uncertainty band on the* MadAnalysis 5 *results as originating from scale uncertainties (dotted) and from the quadratic combination of the scale and PDF uncertainties (dashed). The colour scheme represents the cross section value excluded at the 95% confidence level for each mass configuration.*

able defined as the scalar sum of the transverse momenta of the N leading jets and the missing transverse energy. The second one is based on the recursive jigsaw reconstruction technique [296]. Whilst all $M_{\rm eff}$-based signal regions have been implemented in MadAnalysis 5, the recursive jigsaw reconstruction ones have been ignored due to the lack of information allowing for their proper recasting. They are thus ignored in the following study as well.

Our results are presented in Fig. 6.3 in the form of exclusion contours in the $(m_{\tilde{g}}, m_{\tilde{\chi}_1^0})$ mass plane, to which we supplement the values of the signal cross section that are excluded at the 95% confidence level through a colour code. The exclusion contours and excluded cross sections at the 95% confidence level are extracted by means of Gaussian process regression with a conservative amount of data as implemented in the Excursion package [297].

We compare our predictions (the solid blue line), obtained with the setup described above, with the official ATLAS limits (the green line) as originating from the $M_{\rm eff}$-based signal region yielding the best expectation. ATLAS simulations are based on calculations at the LO accuracy in which samples of events describing final states featuring up to two extra jets are merged [298]. Moreover, the ATLAS results are normalised to NLO cross sections matched with threshold resummation at the next-to-leading logarithmic accuracy (NLO+NLL) [291]. The ATLAS setup therefore differs from ours both at the level of the differential distributions, as we model the properties of the second radiation jet solely at the level of the parton showers, and at the level of the total rates that are evaluated at the NLO matched with parton showers (NLO+PS) accuracy. This consequently results in MadAnalysis 5 limits slightly weaker than the ATLAS ones by about 10%, especially in the light neutralino mass regime.

With the goal of assessing the importance of the signal normalisation, we extract bounds on the model by making use of NNLO$_{\rm approx}$+NNLL rates (red contour) instead of NLO ones (blue contour), NNLO$_{\rm approx}$+NNLL predictions being the most precise estimates for gluino-pair production to date. While still different from what has been used in the ATLAS study, NLO-NLL and NNLO$_{\rm approx}$+ NNLL predictions are known to be consistent with each other when theory error bands are accounted for. This has been documented, in the case of a gluino simplified model in which all squarks are decoupled, by the LHC Supersymmetry Cross Section Working Group[4]. We observe a better agreement with the ATLAS results, showing the important role played by the new physics signal normalisation in the limit setting

---

[4] See the webpage `https://twiki.cern.ch/LHCPhysics/SUSYCrossSections13TeVgluglu`.

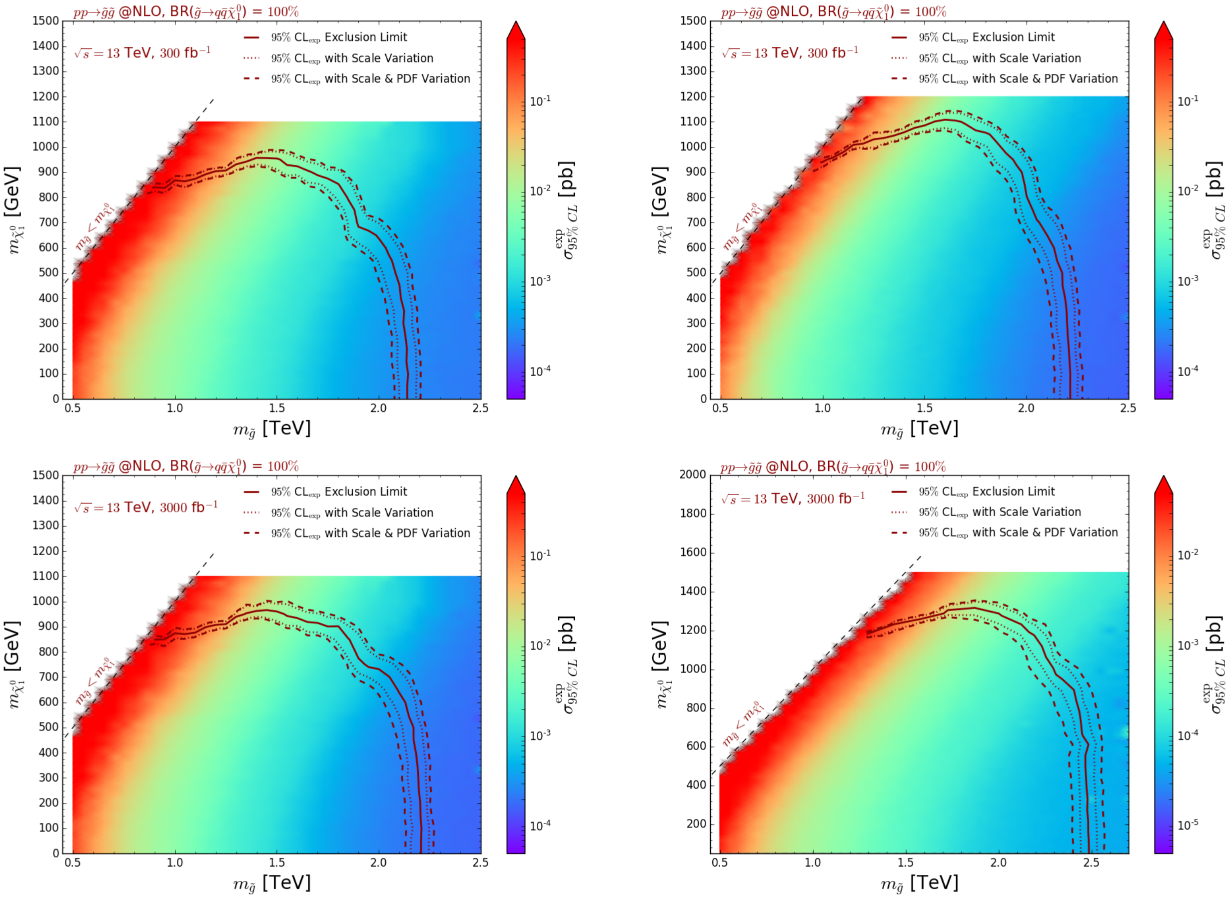

Figure 6.4: *Expected constraints on the gluino-neutralino simplified model under consideration, represented as 95% confidence level exclusion contours in the* $(m_{\tilde{g}}, m_{\tilde{\chi}_1^0})$ *plane. We present the exclusions derived by extrapolating with* MadAnalysis 5 *the expectation of the ATLAS-SUSY-2016-07 analysis for 36 fb*$^{-1}$ *of LHC collisions to 300 fb*$^{-1}$ *(upper) and 3000 fb*$^{-1}$ *(lower). In the left panel, we extrapolate the uncertainties on the background linearly (i.e. the errors are assumed to be dominated by the systematics) while in the right panel, we extrapolate them proportionally to the square root of the luminosity (i.e. the errors are assumed to be dominated by statistics). The colour scheme represents the cross section value excluded at the 95% confidence level for each mass configuration.*

procedure. Large differences of about 5% on the mass limits are nevertheless still noticeable, showing that not only the normalisation but also the shape of the distributions are important ingredients. The ATLAS-SUSY-2016-07 analysis indeed relies on the $M_{\rm eff}(N)$ variable that is particularly sensitive to the modelling of the second jet, as $N \geq 2$ for all the analysis signal regions. In our setup in which NLO matrix elements are matched with parton shower, the second jet properties are described at the leading-logarithmic accuracy, the presence of this jet in the event final state solely originating from parton showering. This constrats with ATLAS simulations in which LO matrix-element corrections are included as well, their final merged Monte Carlo signal samples including the contributions of LO matrix elements for gluino pair-production in association with two jets. This should motivate the usage of merged NLO samples matched with parton showers, so that predictions for observables sensitive to the sub-leading jet activity could be precisely achieved both for the shapes and the rates. The investigation of the actual impact of such an NLO multipartonic matrix element merging however goes beyond the scope of this work.

We also estimate in Fig. 6.3, the impact of the scale and PDF errors on the exclusion contours. For both MadAnalysis 5 predictions in which NLO (blue contour) and more precise $\text{NNLO}_{\text{approx}}$+NNLL (red contour) are used for the signal normalisation, we describe the effect of the scale uncertainties through dotted contours and the one of the combined scale and parton density uncertainties through dashed contour. It turns out that the uncertainties on the signal impacts the gluino mass limits by about 50 GeV in both cases, the effect being mostly dominated by scale variations. The reach of the considered ATLAS-SUSY-2016-07 analysis concerns gluino masses smaller than about 1.8 TeV. This corresponds to a mass range where the uncertainty on the predictions is dominated by the scale variations, as shown in Fig. 6.2. The latter indeed shows that the PDF errors (lower panel of the figure) are at the level of a few percents for $m_{\tilde{g}} < 1.8$ TeV, the parton density fits being under a very good control for the corresponding Bjorken-x values.

In order to estimate the reach of this ATLAS supersymmetry search in the context of the future runs of the LHC, we make use of the framework detailed in section 6.1.3 to extrapolate the results to 300 fb^{-1} and 3000 fb^{-1}. As the ATLAS note of ref. [173] does not include detailed and separate information on the systematical and statistical components of the uncertainties associated with the SM expectation in each signal region, we consider the two implemented options for their extrapolation to higher luminosities. More conservative, a linear extrapolation assumes that the error on the SM background is mostly dominated by its systematical component and scales proportionally to the luminosity (see the first term in

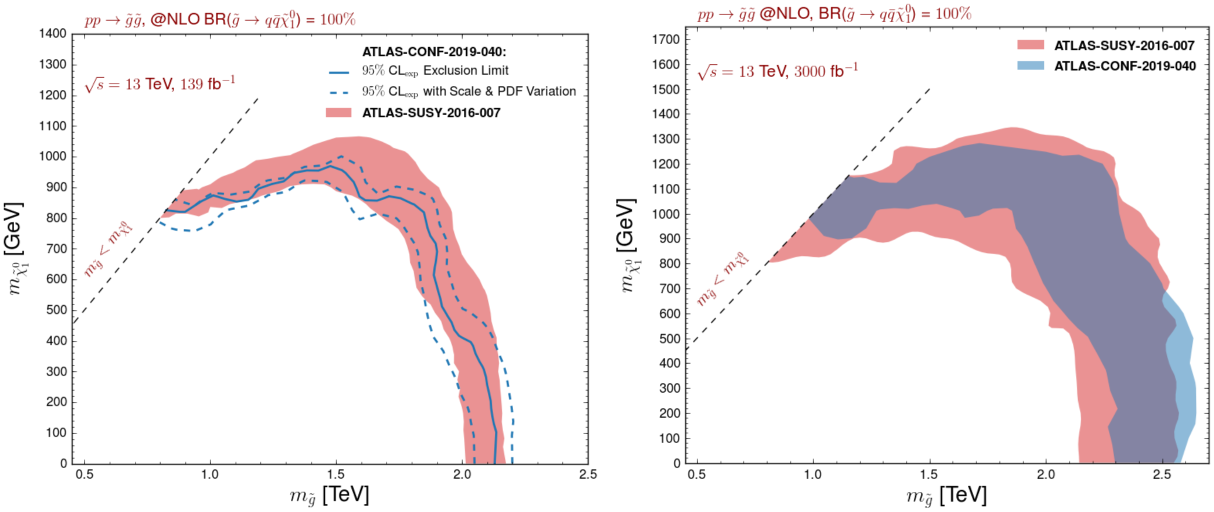

Figure 6.5: *Expected constraints on the gluino-neutralino simplified model under consideration, represented as 95% confidence level exclusion contours in the* $(m_{\tilde{g}}, m_{\tilde{\chi}_1^0})$ *plane for 139 fb*$^{-1}$ *(left) and 3000 fb*$^{-1}$ *(right) of proton-proton collisions at a centre-of-mass energy of 13 TeV. We compare predictions obtained by recasting the results of the ATLAS-CONF-2019-140 analysis (blue lines), which we then extrapolate to 3000 fb*$^{-1}$ *(filled blue area), with those obtained by extrapolating the expectation of the ATLAS-SUSY-2016-07 analysis of 36 fb*$^{-1}$ *of LHC data to 139 fb*$^{-1}$ *and 3000 fb*$^{-1}$ *(solid red areas). The parameter space regions spanned by the various contours correspond to including both the PDF and scale uncertainties. The extrapolations are moreover performed conservatively (see the text).*

Eq. (6.1.6)). More aggressive, an extrapolation in which the error scales proportionally to the square root of the luminosity (second term of Eq. (6.1.6)) considers that the background uncertainties are mainly of a statistical origin. The second option hence naively leads to a more important gain in sensitivity for higher luminosities, by definition. For all our predictions, we normalise the signal rates to NLO.

The results are presented in Fig. 6.4, first, by scaling the background uncertainties linearly to the luminosity (left panel, assuming that the background errors are dominated by the systematics), and second, by scaling them proportionally to the square root of the luminosity (right panel, assuming that the background errors are dominated by the statistical uncertainties). In all cases, we moreover assess the impact of the theory errors, the scale and PDF uncertainties being combined quadratically.

For an extrapolation to 300 fb^{-1} (upper subfigures), the gluino mass limits are pushed to $2.1 - 2.2$ TeV for a light bino-like neutralino with $m_{\tilde{\chi}_1^0} \lesssim 500$ GeV. The 36 fb^{-1} exclusion is then found to be improved by about $15 - 20\%$ (or $300 - 400$ GeV). For such a mass range, the error on the theoretical predictions is still dominated by the scale variations (see Fig. 6.2) and only mildly impacts the exclusion, the effects reaching a level of about 5%. Such a small effect on a mass limit is related to the behaviour of the cross section with the increasing gluino mass, that is only reduced by a factor of a few. Comparing the left and right upper figures, one can assess the impact of the different treatment for the extrapolation of the background uncertainties. In the parameter space region under discussion, the impact is mild, reaching roughly a level of about 5% on the gluino mass limit. Such a small effect originates from the small resulting difference on the background error, that is 3 times smaller in the more aggressive case. Correspondingly, this allows us to gain a factor of a 3 in cross section, or equivalently a few hundreds of GeV in terms of a mass reach.

For more compressed scenarios in which the neutralino is heavier ($m_{\tilde{\chi}_1^0} \gtrsim 800$ GeV) and the gluino lighter ($m_{\tilde{g}} \in [1, 1.7]$ TeV), the treatment of the background extrapolation has a quite severe impact on the bounds on the neutralino mass. A more conservative linear extrapolation of the background error does not yield any significant change comparatively to the 36 fb^{-1} case, neutralinos lighter than about 800 GeV being excluded. However, treating more aggressively the background uncertainties as being purely statistical, leads to an important increase in the bounds, neutralino masses ranging up to about 1 TeV becoming reachable. In those configurations, the spectra are more compressed and therefore more complicated to probe than for split configurations, consequently to the fact that the signal regions are less populated by the supersymmetry signals. A more precisely known background (with a relatively smaller uncertainty) is therefore crucial for being able to draw conclusive statements. As found in our results, any improvement, as little it is, can have a large impact.

In the lower subfigures, we present the results of an extrapolation to 3000 fb^{-1}. All above-described effects are emphasised to a larger extent. The differences in the treatment of the background uncertainties corresponding to knowing the background more accurately indeed now involve a factor of 10 in precision. A more interesting aspect concerns the theoretical predictions themselves that turn out to be known less and less precisely consequently to large parton density uncertainties. The limits indeed enter a regime in which large Bjorken-x are probed, which corresponds to PDF uncertainties contributing significantly to the total theory error. A better knowledge of the parton densities at large x and large scale is thus mandatory to keep our capacity to probe new physics in this regime.

We have verified that the obtained bounds were compatible with the naive extrapolations performed by the Collider Reach[5] platform that extracts naive limits of a given collider setup with respect to the reach of a second collider setup, rescaling the results of the later by ratio of partonic luminosities. For instance, an 1.8 TeV gluino excluded with 36 fb^{-1} of LHC collisions would correspond to a $2.4 - 2.7$ TeV exclusion at 300 fb^{-1}. This is in fair agreement with our findings, after accounting for the fact that Collider Reach uses the NNPDF 2.3 set of parton densities [162], a set of parton distribution functions whose fit only includes 2010 and 2011 LHC data, so that important differences are expected, particularly for large x-values.

Whilst our extrapolations rely on the reinterpretation of an ATLAS analysis of 36 fb^{-1} of LHC collisions, they are quite robust despite the small luminosity under consideration. Multijet plus missing transverse energy studies targeting a monojet-like topology (*i.e.* with a hard selection on the leading jet) are indeed limited by systematics [299], so that only mild improvements could be expected with a higher luminosity. This is what has been found in the results of Fig. 6.4, the bounds being improved by at most 20% in mass when going from 300 to 3000 fb^{-1}. This subsequently also implies that the expected sensitivity should be rather independent of the initially-analysed luminosity. We further demonstrate those considerations in Fig. 6.5.

In the left panel of the figure, we extrapolate the results of the ATLAS-SUSY-2016-07 analysis to the full Run 2 luminosity of 139 fb^{-1}, the theory errors being combined quadratically. In our extrapolation procedure, we have considered both that the background uncertainties are dominated by the systematics (linear scaling) and by the statistics (scaling proportional to the square root of the luminosity). The two set of results have been merged and presented as the unique envelope of the exclusion bands derived from the two extrapolation procedures. They could hence be seen as a conservative theory estimate for the LHC sensitivity at 139 fb^{-1}, when estimated from official 36 fb^{-1} results.

The ATLAS-SUSY-2016-07 analysis has been updated last summer as the ATLAS-CONF-2019-040 analysis [279], so that the most recent and stringent ATLAS limits on the considered gluino simplified model now encompass the analysis of the full LHC Run 2 dataset. On the other hand, the updated analysis has been recently added to the PAD [300], so that it can be used within the MadAnalysis 5 framework for reinterpretation studies. The corresponding 95% confidence level contour is shown on the left panel of Fig. 6.5 (solid blue line), together with the uncertainty band stemming from combining the scale and PDF un-

---

[5] See the webpage `http://collider-reach.web.cern.ch`.

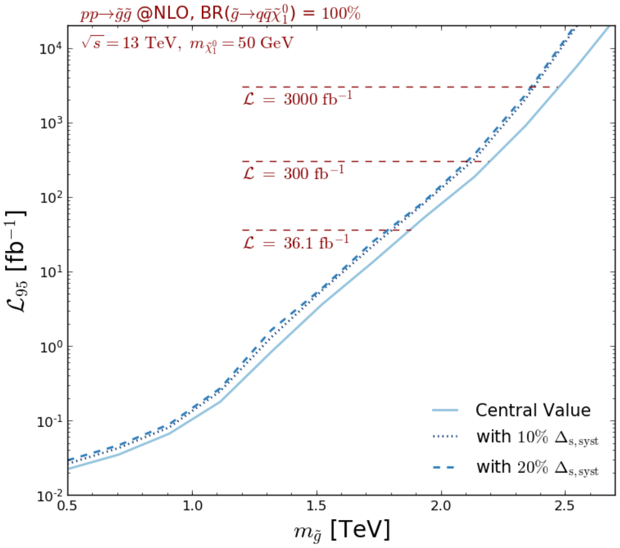

Figure 6.6: *Luminosity necessary to exclude, at the 95% confidence level, a given gluino-neutralino new physics setup with the ATLAS-SUSY-16-07 analysis. We fix the neutralino mass to* $m_{\tilde{\chi}_1^0} = 50$ *GeV, assume that the uncertainties on the background are dominated by their statistical component, and include systematical uncertainties on the signal of 0% (solid line), 10% (dotted line) and 20% (dashed line).*

certainties in quadrature. In addition, we also present predictions for the bounds as obtained from an extrapolations of early Run 2 results focusing on 36 fb^{-1} of LHC data. After accounting for the error bands, the two sets of constraints are found in good agreement, as expected.

On the right panel of Fig. 6.5, we consider the two ATLAS multijet plus missing transverse energy analyses that have been above-mentioned, namely the early LHC Run 2 ATLAS-SUSY-2016-07 analysis (36 fb^{-1}, red) and the full Run 2 ATLAS-CONF-2019-040 analysis (139 fb^{-1}, blue). We reinterpret their results with MadAnalysis 5, and extrapolate the predictions that have been obtained for the nominal luminosities of the two analyses to 3000 fb^{-1}. The contours shown on the figure are obtained as before, *i.e.* by considering independent scalings of the background assuming that it is either dominated by the systematical or by the statistical uncertainties. The envelopes of the two exclusion bands (including the theory errors) are then reported in the figure. The two solid areas presented on the figure are found to largely overlap and be consistent with each other.

In Fig. 6.6, we make use of the MadAnalysis 5 infrastructure to estimate, for various benchmark points, the luminosity $\mathcal{L}_{95}$ that is required to exclude the scenario at the 95% confidence level. We still consider the ATLAS-SUS-2016-07 analysis, fix the neutralino mass

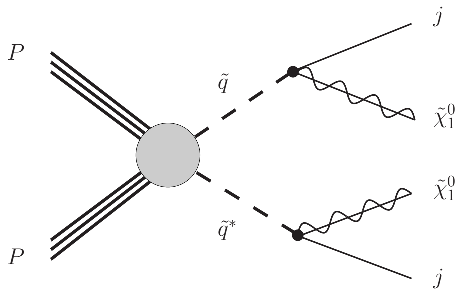

Figure 6.7: *Generic Feynman diagram associated with the production and decay of a pair of squarks in the considered MSSM-inspired squark simplified model. The figure has been produced with the help of the* JaxoDraw *package [35].*

to 50 GeV and let the gluino mass vary. We compute $\mathcal{L}_{95}$ for two choices of systematics on the signal (combined in both cases with the theory errors quadratically), namely 10% (dotted line) and 20% (dashed line), and compare the predictions with the central value where the signal is perfectly known (solid line). In those calculations, we scale the error on the background proportionally to the square root of the luminosity, as if it was mainly dominated by its statistical component. Our analysis first shows that light gluinos with masses smaller than about 1.5 TeV can be excluded with a luminosity $\mathcal{L}_{95}$ of a few fb^{-1}, as confirmed by the early Run 2 ATLAS search of ref. [171] that consists of the 3.2 fb^{-1} version of the ATLAS-SUSY-2016-07 analysis. The steep fall of the cross section with an increasing gluino mass moreover implies that the high-luminosity LHC reach of the analysis under consideration will be limited to gluinos of about 2.5 TeV, a bound that could be reduced by about 10% if the systematics on the signal are of about $10-20\%$. This order of magnitude has been found to agree with older ATLAS estimates [279].

6.3 Squark and neutralino mass limits

In this section, we consider a second class of simplified models inspired by the MSSM that is widely studied in the context of the LHC searches for new physics. As in section 6.2, all superpartners, except for two under investigation, are decoupled. This time, these are taken to be a squark and the lightest neutralino. In practice, we hence supplement the SM field content by one species of first generation squark $\tilde{q}$ and the lightest neutralino $\tilde{\chi}_1^0$, assumed to be bino-like. In this configuration, squarks can be pair-produced through standard QCD interactions, and then each decays into the lightest neutralino and an up quark, as illustrated

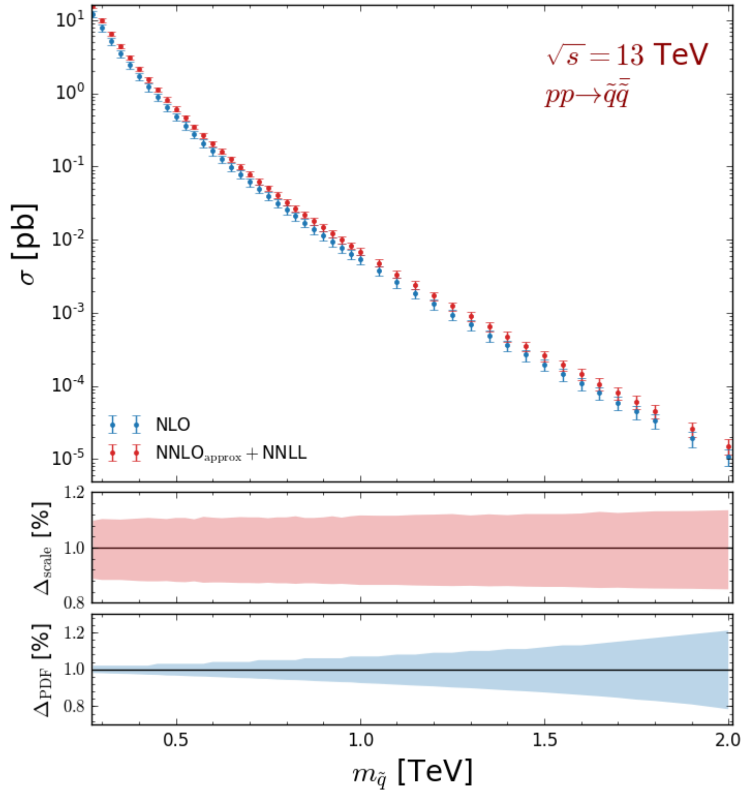

Figure 6.8: *Total NLO (blue) and approximate NNLO+NNLL (red) cross section (upper panel) for squark pair production in proton-proton collisions at a centre-of-mass energy of 13 TeV. The error bars represent the quadratic sum of the scale and PDF uncertainties. In the middle and lower panels of the figure, we report the NLO scale and PDF uncertainties respectively, after normalising the results to the central NLO cross section value.*

by the generic Feynman diagram of Fig. 6.7. Such a parton-level final state comprised of two quarks and two invisible neutralinos therefore manifests itself, after parton showering and hadronisation, as a multijet plus missing transverse energy topology.

The ATLAS analyses considered in section 6.2, targeting multijet plus missing energy signs of new physics, are therefore appropriate to put constraints on the model under consideration. Those analyses indeed include not only signal regions dedicated to probe final state featuring a large jet multiplicity (that are thus ideal to target the previously considered gluino simplified model), but also include signal regions targeting signals exhibiting a smaller jet multiplicity (that are thus excellent probes for the present squark simplified model). In the following, we only make use of the most recent search, ATLAS-CONF-2019-140 [279].

Making use of the same simulation setup as in section 6.2, we study the LHC sensitivity to this model after the full Run 2 and present the expectation of its high-luminosity

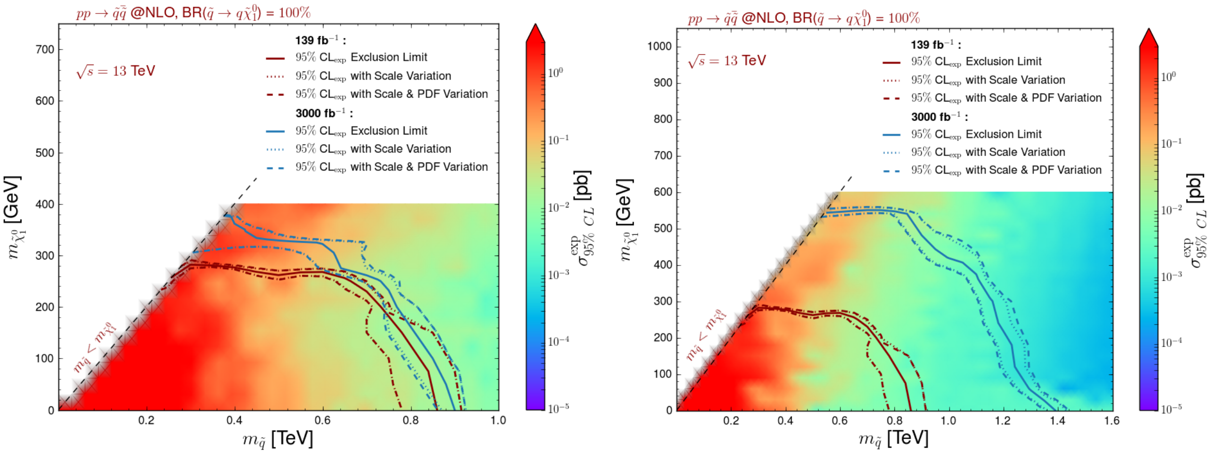

Figure 6.9: *Expected constraints on the squark-neutralino simplified model under consideration, represented as 95% confidence level exclusion contours in the* $(m_{\tilde{q}}, m_{\tilde{\chi}_1^0})$ *plane for 139 fb*$^{-1}$ *(red) and 3000 fb*$^{-1}$ *(blue) of proton-proton collisions at a centre-of-mass energy of 13 TeV. We derive those bounds with the ATLAS-CONF-2019-140 implementation in* MadAnalysis 5 *and extrapolate the uncertainties on the background as if they are systematically-dominated (left, scaling proportional to the luminosity) or statistically-dominated (right, scaling proportional to the sqare root of the luminosity).*

operation run. Our results are derived from simulations at the NLO+PS accuracy, so that our signal samples are normalised at the NLO accuracy. The rates that we employ in the following are depicted in the upper panel of Fig. 6.8, where we show total NLO-accurate squark-pair production cross sections as returned by MG5_aMC when using the MSSM implementation developed in ref. [275] and the NLO set of NNPDF 3.0 parton densities [285] (blue). Predictions are given for squark masses ranging from 250 GeV to 2 TeV and include theory errors that we estimate by adding scale and PDF uncertainties in quadrature. Those uncertainties are further described more precisely in the middle and lower panels of the figure, where they are given after normalising the results to the central NLO cross section value for each mass point.

We obtain cross sections that vary from 10 pb for $m_{\tilde{q}} \sim 250$ GeV to 0.01 fb for 2 TeV squarks. They are two orders of magnitude lower than in the gluino case for a specific mass value, as expected from the fact that squarks are scalars and are colour triplets and not octets. Scale uncertainties are found to be independent of the squark mass for the considered $m_{\tilde{q}}$ range, and are of about 15% (middle panel of the figure). In contrast, the PDF errors strongly depend on the squark mass $m_{\tilde{q}}$ (lower panel of the figure), as they are correlated with the associated Bjorken-x regime. They are of a few percents and thus subleading for small $m_{\tilde{q}}$ values, and grow for increasing squark masses, eventually reaching 20% for $m_{\tilde{q}} = 2$ TeV. For larger and larger x-values (and thus larger and larger $m_{\tilde{q}}$), the quark-antiquark contributions to the cross section play a bigger and bigger role. Simultaneously, the impact of the Bjorken-x regime in which the PDF sets are more poorly constrained by data gets more important.

As in section 6.2, we compare our predictions to the cross section values usually employed by the LHC collaborations (red curve), as reported by the LHC Supersymmetry Cross Section Working Group [291]. The latter are however only provided for a simplified model in which all squarks except the two stop squarks are mass-degenerate. We therefore normalise the NNLO$_{\text{approx}}$+NNLL results by an extra factor of 1/10, which should be a fair enough approximation for small squark masses. Nevertheless, as both NLO and NNLO$_{\text{approx}}$+NNLL predictions are consistent, we consider (exact) NLO rates in the following.

In Fig. 6.9, we reinterpret the results of the ATLAS-CONF-2019-040 analysis with MadAnalysis 5 and present the expected exclusion contours both at the nominal luminosity of 139 fb^{-1}, after extrapolating the findings to 3000 fb^{-1}, using for each point the region yielding the best expected sensitivity. Neutralino masses below about 300 GeV are currently (*i.e.* for a luminosity of 139 fb^{-1}) excluded, for squark masses ranging up to about 900 GeV. This may seem to contrast by a factor of about 2 with the current bounds on this class of simplified model set by the ATLAS collaboration [279]. This is however not surprising as the collaboration only interprets its results for a simplified model in which the superpartner spectrum exhibits 10 mass-denegerate left-handed and right-handed squarks (*i.e.* all squarks except the two stop squarks are degenerate). The corresponding signal cross sections are therefore about 10 times larger, so that much stronger limits could be extracted. In comparison with final Run 2 CMS results [301, 302] for which result interpretations both for eight mass-degenerate squarks and a single squark species are provided, we obtain more conservative bounds that are roughly 20% weaker in terms of excluded masses. When accounting for the uncertainty bands, our predictions agree with the experimental findings, as the uncertainty bands overlap.

Extrapolating the results to a luminosity of 3000 fb^{-1}, *i.e.* expected luminosity of the high-luminosity phase of the LHC, we obtain expected bounds which are improved quite a bit. The magnitude of the improvement is found strongly related to how the background uncertainties will be controlled, as visible by comparing the curves corresponding to 3000 fb^{-1} (blue) in the two panels of the figure. Assuming that the background is dominated by the systematics or the statistics change the results by more than 40%.

6.4 Sensitivity to simplified s-channel dark matter models

In this section, we investigate the sensitivity of the LHC to a simplified dark matter (DM) model. We assume that DM is described by a massive Dirac fermionic particle X that communicates with the Standard Model through the exchange of a spin-1 mediator Y. Motivated by models with an extended gauge group, we consider that the mediator couples only either to a pair of DM particles, or to a pair of SM fermions. Such a configuration is typical from the so-called s-channel dark matter models [280, 281]. In this class of scenarios, DM can only be pair-produced at colliders, from the scattering of a pair of SM quarks and through the s-channel exchange of the mediator.

The corresponding Lagrangian can generically be written as

$$\mathcal{L} = \mathcal{L}_{\rm SM} + \mathcal{L}_{\rm kin} + \bar{X}\gamma_\mu \big[g^V_X + g^A_X\gamma_5\big] X\ Y^\mu \quad + \sum_q \Big\{\bar{q}\gamma_\mu\big[g^V_q + g^A_q\gamma_5\big]q\Big\} Y^\mu$$

where $\mathcal{L}_{\rm SM}$ refers to the SM Lagrangian and $\mathcal{L}_{\rm kin}$ contains gauge-invariant kinetic and mass terms for all new fields. The next term includes the vector and axial-vector interactions of the mediator with DM, their strength being denoted by g^V_X and g^A_X respectively, and the last term focus on the mediator interactions with the SM quarks. The latter are assumed universal and flavour-independent, their strength being g^V_q and g^A_q in the vector and axial-vector case respectively, regardless of the quark flavour.

In our analysis, we focus on two further simplified scenarios originating from that model. In a first case (that we label **S1**), the mediator couplings are taken as of a vectorial nature, whilst in the second case (that we label **S2**), they are taken as of an axial-vectorial nature. In other words, the two scenarios are defined as

$$\textbf{S1}:\ \ g^A_q = g^A_X = 0\ ; \qquad \textbf{S2}:\ \ g^V_q = g^V_X = 0\ . \tag{6.4.1}$$

In order to study the sensitivity of the LHC to these two classes of scenarios, we make use of the publicly available[6] implementation of the model in the FeynRules package [260] introduced in ref. [280], as well as of the corresponding public UFO [145] library. As in the previous sections, hard scattering events are generated at the NLO accuracy in QCD with

---

[6] See the webpage `http://feynrules.irmp.ucl.ac.be/wiki/DMsimp`.

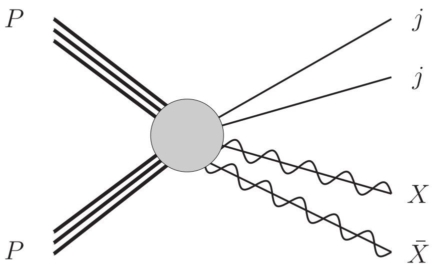

Figure 6.10: *Generic Feynman diagram associated with the production of a pair of dark matter particles X in association with two hard jets. The figure has been produced with the help of the* JaxoDraw *package [35].*

MG5_aMC [144] and then matched with parton showering and hadronisation as performed by Pythia [231]. In our simulations, the matrix elements are convoluted with the NLO set of NNPDF 3.0 parton densities [285]. We derive the LHC sensitivity to the model by considering the associated production of a pair of dark matter particles with jets, a signature targeted by the ATLAS-CONF-2019-040 analysis [279] introduced in the previous sections. This ATLAS study searches for new phenomena in a luminosity of 139 fb^{-1} of LHC data at a centre-of-mass energy of 13 TeV, investigating events featuring at least two hard jets and a potential subleading jet activity.

As the analysis selection requires at least two very hard jets, we consider as a hard-scattering process the production of a pair of DM particles with two hard jets, as sketched in Fig. 6.10. Moreover, we impose two conservative (with respect to the ATLAS analysis) generator-level selections. We constrain the transverse momentum of the hardest of the jets to satisfy $p_T > 150$ GeV, and the parton-level missing transverse energy (*i.e.* the transverse energy of the vector sum of the transverse momenta of the two DM particles) to fulfil $\not{E}_T >$ 150 GeV. Moreover, the reference renormalisation and factorisation scales are set to the mass of the mediator m_Y, and we estimate the associated uncertainties as usual, by independently varying the two scales by a factor of 2 up and down around the central scale choice.

We begin with considering a series of scenarios featuring light dark matter, *i.e.* with a dark matter mass m_X fixed to 100 GeV. The mediator mass is kept free to vary in the [0.3, 2] TeV range. In Table 6.1, we present the sensitivity of the ATLAS-CONF-2019-040 analysis to those scenarios, both at the nominal luminosity of 139 fb^{-1} and for the high-luminosity LHC run (with 3000 fb^{-1}). For each spectrum configuration, we show NLO signal cross sections (second and fifth columns for the **S1** and **S2** benchmarks respectively), as obtained following the simulation setup described above and for couplings obeying to Eq. (6.4.1). Moreover, those predictions are obtained after fixing the remaining non-vanishing free parameters to the reference values

$$\begin{aligned} \mathbf{S1}: g^V_q = 0.25\ ,\ g^V_X = 1\ ; \\ \mathbf{S2}: g^A_q = 0.25\ ,\ g^A_X = 1\ , \end{aligned} \tag{6.4.2}$$

which consist in one of the benchmarks studied by the LHC dark matter working group [281].

We first assess the LHC sensitivity to each point for the two considered luminosities in terms of the signal cross section that is reachable at the LHC σ_{95} (third and sixth columns of Table 6.1 for the **S1** and **S2** benchmarks respectively) by reinterpreting, with MadAnalysis 5, the results of the ATLAS-CONF-2019-040 analysis. Second, we translate the cross section limits that we have obtained into a bound on a universal new physics coupling strength g_{95} that is defined for scenarios in which

$$g_q = g_X\ . \tag{6.4.3}$$

Moreover, we provide the g_{95} limits together with the theory uncertainty stemming from scale and PDF variations (fourth and seventh column of the table). The most stringent bounds on the model originate from a single signal region of the analysis in which, the effective mass $M_{\rm eff}$ is imposed to be larger than 2.2 TeV. Such a cut is applied together with looser cuts on the jet properties, as compared with other signal regions featuring smaller effective masses.

For fixed vector couplings (**S1** scenarios), the NLO cross section $\sigma_{\rm NLO}$ decreases when the mediator mass increases and spans a range extending from about 450 fb for heavy mediators with a mass of about 2 TeV, to more than 10 pb for mediators lighter than 500 GeV. Those values and this steeply-falling behaviour are mainly driven by the heavy mass of the mediator as compared with the small dark matter mass. Larger cross sections are indeed obtained for smaller mediator masses as we lie closer to the resonant regime in which $m_Y \sim 2m_X$. The cross section that is expected to be excluded at the 95% confidence level also falls down with m_Y, although the slope is much flatter. Moreover, $\sigma_{95} < \sigma_{\rm NLO}$. Consequently, all scenarios defined by the coupling assumptions of Eq. (6.4.1) and Eq. (6.4.2) are excluded, already with the present full Run 2 luminosity.

Relaxing the coupling definitions of Eq. (6.4.2) and replacing it by the universal coupling constraint of Eq. (6.4.3), it turns out that couplings of 0.4–0.7 are excluded over the

Table 6.1: *Expected constraints on various light dark matter s-channel scenarios. The dark matter mass is fixed to* $m_X = 100$ *GeV and the couplings satisfy Eq. (6.4.1). Reference NLO cross sections (second and fifth columns) are provided for a case where the remaining free couplings are set as in Eq. (6.4.2), and can be compared with the 95% confidence level limits expected from the reinterpretation of the ATLAS-CONF-2019-040 analysis (third and sixth columns). Those bounds are also translated into a bound on the couplings for a* $g_q = g_X$ *configuration (fourth and seventh columns).*

	Vector couplings (**S1**)			Axial-vector couplings (**S2**)		
m_Y [TeV]	$\sigma_{\rm NLO}$ [pb]	σ_{95} [pb]	$\lvert g_{95}\rvert$	$\sigma_{\rm NLO}$ [pb]	σ_{95} [pb]	$\lvert g_{95}\rvert$
0.3	$19.45^{+35.4\%}_{-77.1\%}{}^{+1.2\%}_{-1.2\%}$	1.553(1.318)	$0.532^{+0.06}_{-0.07}$ $(0.510^{+0.06}_{-0.07})$	$9.21^{+30.9\%}_{-68.4\%}{}^{+1.2\%}_{-1.2\%}$	1.015(0.700)	$0.576^{+0.06}_{-0.07}$ $(0.525^{+0.05}_{-0.06})$
0.5	$12.19^{+15.5\%}_{-39.3\%}{}^{+1.1\%}_{-1.1\%}$	0.667(0.568)	$0.484^{+0.02}_{-0.04}$ $(0.465^{+0.02}_{-0.04})$	$9.73^{+15.8\%}_{-39.8\%}{}^{+1.3\%}_{-1.3\%}$	0.643(0.545)	$0.507^{+0.02}_{-0.04}$ $(0.486^{+0.02}_{-0.04})$
0.7	$7.05^{+10.3\%}_{-29.5\%}{}^{+1.2\%}_{-1.2\%}$	0.368(0.311)	$0.478^{+0.01}_{-0.03}$ $(0.458^{+0.01}_{-0.03})$	$6.41^{+9.2\%}_{-27.3\%}{}^{+1.3\%}_{-1.3\%}$	0.333(0.285)	$0.477^{+0.01}_{-0.03}$ $(0.459^{+0.01}_{-0.03})$
0.8	$5.37^{+8.3\%}_{-25.8\%}{}^{+1.4\%}_{-1.4\%}$	0.312(0.266)	$0.491^{+0.01}_{-0.03}$ $(0.472^{+0.01}_{-0.03})$	$5.22^{+6.3\%}_{-22.0\%}{}^{+1.2\%}_{-1.2\%}$	0.278(0.234)	$0.480^{+0.01}_{-0.02}$ $(0.460^{+0.01}_{-0.02})$
0.9	$4.15^{+6.1\%}_{-21.7\%}{}^{+1.3\%}_{-1.3\%}$	0.242(0.169)	$0.491^{+0.01}_{-0.02}$ $(0.449^{+0.01}_{-0.02})$	$4.13^{+5.5\%}_{-18.9\%}{}^{+1.3\%}_{-1.3\%}$	0.241(0.205)	$0.491^{+0.01}_{-0.02}$ $(0.472^{+0.01}_{-0.02})$
1.0	$3.30^{+5.2\%}_{-20.0\%}{}^{+1.6\%}_{-1.6\%}$	0.224(0.189)	$0.511^{+0.01}_{-0.02}$ $(0.490^{+0.01}_{-0.02})$	$3.39^{+4.7\%}_{-17.0\%}{}^{+1.6\%}_{-1.6\%}$	0.221(0.188)	$0.505^{+0.01}_{-0.02}$ $(0.485^{+0.01}_{-0.02})$
1.2	$2.16^{+4.0\%}_{-16.6\%}{}^{+1.7\%}_{-1.7\%}$	0.204(0.174)	$0.554^{+0.01}_{-0.02}$ $(0.533^{+0.01}_{-0.02})$	$2.17^{+3.9\%}_{-15.0\%}{}^{+1.7\%}_{-1.7\%}$	0.175(0.148)	$0.533^{+0.01}_{-0.02}$ $(0.511^{+0.01}_{-0.02})$
1.4	$1.44^{+3.7\%}_{-13.5\%}{}^{+2.3\%}_{-2.3\%}$	0.139(0.118)	$0.557^{+0.01}_{-0.02}$ $(0.535^{+0.01}_{-0.02})$	$1.42^{+2.5\%}_{-11.1\%}{}^{+1.9\%}_{-1.9\%}$	0.142(0.120)	$0.562^{+0.00}_{-0.01}$ $(0.539^{+0.00}_{-0.01})$
1.5	$1.15^{+2.9\%}_{-11.9\%}{}^{+2.1\%}_{-2.1\%}$	0.139(0.117)	$0.590^{+0.01}_{-0.02}$ $(0.566^{+0.01}_{-0.02})$	$1.15^{+2.6\%}_{-11.0\%}{}^{+2.3\%}_{-2.3\%}$	0.127(0.108)	$0.576^{+0.01}_{-0.02}$ $(0.554^{+0.00}_{-0.01})$
1.8	$0.63^{+2.1\%}_{-8.5\%}{}^{+2.5\%}_{-2.5\%}$	0.121(0.103)	$0.662^{+0.01}_{-0.01}$ $(0.636^{+0.01}_{-0.01})$	$0.66^{+1.9\%}_{-7.8\%}{}^{+2.6\%}_{-2.6\%}$	0.133(0.112)	$0.672^{+0.01}_{-0.01}$ $(0.643^{+0.01}_{-0.01})$
2.0	$0.44^{+2.1\%}_{-8.6\%}{}^{+2.9\%}_{-2.9\%}$	0.104(0.089)	$0.699^{+0.01}_{-0.02}$ $(0.671^{+0.01}_{-0.01})$	$0.44^{+1.6\%}_{-6.4\%}{}^{+3.1\%}_{-3.1\%}$	0.095(0.081)	$0.680^{+0.01}_{-0.01}$ $(0.653^{+0.01}_{-0.01})$

entire mass range, the best limits being obtained for scenarios featuring sub-TeV mediators and a spectrum such that one lies far enough from the resonant regime. In the latter case, the analysis is less sensitive as a consequence of the associated softer final state objects populating the signal events. The overall weak dependence of the excluded coupling on the mediator mass stems from various interplaying effects. First, the cross section has a quartic dependence on the couplings, so that a small coupling change leads to a large modification of the cross section. Second, there is a strong interplay between the mediator mass and the dark matter mass (*i.e.* if ones lies for enough from the resonant regime) and the kinematical configuration probed by the analysis cuts, especially for light mediators.

In the heavy-mediator regime, considering **S2** scenarios featuring axial-vector mediator couplings leads to very similar results. In this limit, the relevant matrix elements are insensitive to the mediator nature. On the contrary, when one approaches the resonant regime, significant changes arise: The cross section turns out to be suppressed relatively to the vector **S1** scenario. This originates from the impact of the threshold regime that plays a larger and larger role for smaller and smaller masses. At threshold, the pair of dark matter particles is organised into a ${}^3P_1$ state, and not into a ${}^3S_1$ configuration as in the **S1** scenario. Consequently, signal cross sections are relatively suppressed. The small increase in cross section for low m_Y values in the **S2** case hence stems from those threshold effects that are more and more tamed when one gets further from threshold, as well as from the cut on the leading jet of 150 GeV. As in the **S1** scenario, the entire mass range is excluded by the ATLAS-CONF-2019-040 analysis, which translates in the exclusion of couplings in the 0.4–0.7 ballpark for the considered mediator mass range.

Finally, those bounds are expected to only be sightly improved, by about 4–9%, after including 3000 fb^{-1} of data for both scenarios. This is related to the systematical dominance of the uncertainties on the background, as we have chosen to scale it under that assumption, so that more luminosity will not bring much compared with the Run 2 results. Moreover, we observe that the results are plagued by quite modest theoretical uncertainties at the g_{95} level (by virtue of the quartic dependence of the matrix element of the coupling).

In Table 6.2, we consider a new class of scenarios. This time, the mediator mass m_Y is fixed to 1.5 TeV and we vary the dark matter mass m_X from 200 to 900 GeV.

We first consider scenarios with couplings satisfying Eq. (6.4.1) and Eq. (6.4.2). We evaluate fiducial NLO cross sections for the different considered mass spectra (second and fifth columns of the table for the **S1** and **S2** cases respectively), after imposing the previously-

Table 6.2: *Same as Table 6.1, but for a scenario in which m_X is free and m_Y has been set to 1.5 TeV.*

	Vector coupling (**S1**)			Axial-vector coupling (**S2**)		
m_X [GeV]	σ_{NLO} [pb]	σ_{95} [pb]	$\lvert g_{95}\rvert$	σ_{NLO} [pb]	σ_{95} [pb]	$\lvert g_{95}\rvert$
200	$1.19^{+3.0\%}_{-12.2\%}{}^{+2.1\%}_{-2.1\%}$	0.149(0.126)	$0.595^{+0.006}_{-0.02}\ (0.571^{+0.005}_{-0.02})$	$1.11^{+2.5\%}_{-10.7\%}{}^{+2.2\%}_{-2.2\%}$	0.148(0.125)	$0.605^{+0.005}_{-0.02}\ (0.580^{+0.005}_{-0.01})$
350	$1.17^{+3.0\%}_{-12.5\%}{}^{+2.2\%}_{-2.2\%}$	0.115(0.098)	$0.560^{+0.005}_{-0.02}\ (0.538^{+0.005}_{-0.02})$	$0.85^{+2.5\%}_{-10.1\%}{}^{+2.1\%}_{-2.1\%}$	0.129(0.109)	$0.624^{+0.005}_{-0.02}\ (0.598^{+0.005}_{-0.01})$
500	$1.10^{+3.5\%}_{-12.6\%}{}^{+2.2\%}_{-2.2\%}$	0.143(0.122)	$0.601^{+0.006}_{-0.02}\ (0.577^{+0.006}_{-0.02})$	$0.51^{+2.7\%}_{-10.6\%}{}^{+2.2\%}_{-2.2\%}$	0.135(0.114)	$0.715^{+0.006}_{-0.02}\ (0.685^{+0.006}_{-0.02})$
650	$0.82^{+3.2\%}_{-13.2\%}{}^{+2.1\%}_{-2.1\%}$	0.149(0.127)	$0.653^{+0.006}_{-0.02}\ (0.627^{+0.006}_{-0.02})$	$0.15^{+2.7\%}_{-9.7\%}{}^{+2.4\%}_{-2.4\%}$	0.143(0.121)	$0.982^{+0.009}_{-0.02}\ (0.941^{+0.009}_{-0.02})$
800	$0.006^{+3.3\%}_{-13.8\%}{}^{+2.8\%}_{-2.8\%}$	0.131(0.110)	$2.171^{+0.02}_{-0.07}\ (2.075^{+0.02}_{-0.07})$	$0.0009^{+2.3\%}_{-11.4\%}{}^{+3.2\%}_{-3.2\%}$	0.121(0.104)	$3.456^{+0.03}_{-0.10}\ (3.322^{+0.03}_{-0.09})$
900	$0.001^{+3.5\%}_{-14.7\%}{}^{+3.5\%}_{-3.5\%}$	0.107(0.091)	$2.986^{+0.04}_{-0.10}\ (2.863^{+0.04}_{-0.10})$	$0.0002^{+3.1\%}_{-13.4\%}{}^{+3.5\%}_{-3.5\%}$	0.110(0.093)	$4.600^{+0.06}_{-0.15}\ (4.412^{+0.05}_{-0.14})$

mentioned cuts on the transverse momentum of the leading jet $p_T(j_1) > 150$ GeV and on the parton-level missing transverse energy $\not{E}_T > 150$ GeV. For both the **S1** and **S2** scenarios, the NLO predictions are found to decrease with the dark matter mass, paying the price of a phase-space suppression. The falling behaviour is found steeper once the dark matter mass is greater than half the mediator mass, as it has to be produced off-shell (*i.e.* for $m_Y > 2m_X$). Moreover, for given masses and couplings, **S1** cross sections (*i.e.* in the case of mediator vector couplings) are larger. This originates from the p-wave suppression of DM production through an axial-vector mediator (*i.e.* in the **S2** scenario), as already mentioned earlier in this section.

We then evaluate the cross section value σ_{95} that is excuded at the 95% confidence level (third and sixth columns of the table) by reinterpreting the results of the ATLAS-CONF-2019-040 analysis. We observe that small dark matter masses are excluded already with the full Run 2 dataset, cross sections as small as 100 fb being excluded regardless of the DM mass. Moving on with a scenario in which the couplings satisfy Eq. (6.4.1) and Eq. (6.4.3), we translate the bounds that we have obtained into bounds on a universal coupling. The latter is found to be of at most in the 0.5–0.7 range once one lies in a configuration below threshold ($2m_X < m_Y$), and is mostly unconstrained for larger DM mass values. As for the previous class of scenarios in which the DM mass was fixed and the mediator mass was varying, 3000 fb^{-1} will not improve the limits much, as the analysis being dominated by the systematics. We indeed expect an improvement on the bounds of at most 3-4%.

Chapter 7

Conclusion

This thesis focuses on extensions beyond the minimal supersymmetric realisations of the SM. Although MSSM provides extensive improvement in solving the widely known problems of the SM, we discussed its possible shortcomings and proposed extensions of its framework to complement its nature under GUT further.

First, we discussed a GUT-inspired vector-like extension of MSSM, utilising vector-like lepton and down-type quark doublet pair and a vector-like neutrino singlet pair. Alongside with neutralino LSP, such construction can lead to sneutrino LSP as well. Although additional fields give rise to vector-like supermultiplet mediated annihilation channels, it turns out that bino-(vector-like) neutralino DM is MSSM-like, due to the current experimental bounds on the τ'. Such annihilation process, in this scenario, is driven by bino-(vector-like) electron-selectron coupling, which is proportional to its corresponding hypercharge. This leads us to an annihilation cross-section proportional to Y^4, which is $(1/2)^4$. This largely suppresses the overall annihilation process. On the sneutrino front, although all arbitrary admixtures of it can be a DM candidate, we observed that vector-like left- and right doublet-like sneutrinos are excluded by cosmological data. This leads us to singlet like sneutrino, but such construction is hard to differentiate from other models with similar singlet-like sneutrinos. Having a new lepton generation, in such a framework accommodates interesting collider signals through boosted multilepton signature. We have demonstrated that pair production of vector-like τ' yields a highly distinguishable differential distribution at HL-LHC.

Secondly, we investigated gauge extensions in supersymmetric realisations. We focused on E_6 breaking through $SO(10) \otimes U(1)_\psi$ which further breaks into $SU(5) \otimes U(1)_\psi \otimes U(1)_\chi$. The existence of the R-parity violating terms in the Lagrangian, which typically arises from

$SU(5)$ breaking, are cancelled out with the extra $U(1)'$ charge structure of this model. The mixture between two extra $U(1)$'s naturally creates an extensive framework with different physical properties due to its gauge anomaly free structure. In addition to covering all matter sector of minimal supersymmetric extension of the SM (MSSM), this extended matter sector accommodates a right-handed neutrino superfield, which generates mass for neutrino sector and leads to an extra, viable dark matter candidate in addition to the MSSM-like neutralino dark matter. We investigated the parameter space that led to either one of the viable dark matter candidates and mapped their properties to $U(1)_\psi \otimes U(1)_\chi$ mixing angle. UMSSM framework also provides a unique heavy Z' boson which is strictly bounded by high-mass dileptonic and dijet resonance searches. Detailed analysis over the gauge breaking structure and addition of the supersymmetric particle decay channels have been shown to relax these bounds up to 300 GeV. Furthermore, introducing a kinetic mixing between $Z - Z'$ has been observed to create a leptophobic Z' which can only be bounded via relatively less stringent high-mass dijet resonances. We showed that it is possible to design analysis to detect this particle up to 7σ statistical significance in future collider experiments through supersymmetric cascade decays.

Finally, we studied the implications of theoretical uncertainties on expected limits coming from recasting the experimental analysis. We extended MadAnalysis 5 software functionalities to reinterpret the analyses using scale and PDF variations on the signal cross-section. Increasing mass bounds, especially PDF uncertainties, are more dominant in cross-section measurements. In particular, the high mass requirements on the supersymmetric particles pushes the analysis towards the large Bjorken-x regime where parton densities are poorly constrained. In addition to these, the scale variations on LO calculations constitute a significant source of theoretical uncertainties. We also integrated high luminosity predictability through extrapolating expected background and its uncertainty to the higher luminosities. We presented our results in three different simplified model scenarios where first we studied gluino exclusions at NLO precision and showed that combined uncertainties could reduce the mass bounds by several hundreds of GeV and we presented our high luminosity predictions. Then we exercised the same procedure on first-generation squark production where again we observe several few hundreds of GeV relaxation with respect to both ATLAS and CMS analyses. Finally, we discussed coupling sensitivity of simplified s-channel DM models coupled to the SM sector via a spin-1 mediator. We showed that depending on the nature of the mediator, which can either be vector or axial-vector mediator, the analysis sensitivity can change drastically with respect to the DM mass and the mass splitting between the mediator and the DM. We showed that the sensitivity could be improved up to 10% in HL-LHC.

This thesis can be taken as a pivotal point for future directions where one can take home multiple vital lessons. First and foremost, due to the empiric nature of the field, it is crucial to propose a theory that can also be tested by experimental collaborations. Such a proposal should have two crucial properties where first it must satisfy current experimental bounds. However, these bounds should not be taken blindly, as shown in chapter 6, depending on the nature of the theory or the construction of the phase-space and the severity of the theoretical uncertainties, these bounds can widely vary from the experimental results. Thus alongside case dependent testing, it is essential to provide the necessary toolset where the analysis can be duplicated or tested for other proposals. This employs the bare minimum requirement of our field.

In the very same chapter, we also showed the challenges in observing the compressed spectra. In chapter 5 and 3, we presented mainly boosted phase-spaces which can be observed via simple cut-and-count techniques due to the significant shift in high energy observables. However, since compressed spectra will only change the shape of differential-distributions, it is essential to develop different approaches to scrutinize that region in greater detail.

Last but not least, we studied various models which are attempting to describe different DM particles that can explain cosmological data. However, we only plainly show that such particles possibly exist beyond the current reach of our experimental capabilities, but we do not propose an experimental approach to observe and identify different properties of such particles in future collider experiments. Such an extension of the work proposed in this theses is essential to identify the nature of the DM through empiric data. Furthermore, this thesis presented dark matter candidates which are only produced by a process known as *freeze-out*. Such a scenario assumes that the DM has initially reached thermal equilibrium with other visible particles at the early universe. However, when the expansion rate of the universe becomes equal to the effective interaction rate between DM and the visible sector particles, the relic abundance stabilizes, "*freezes-out*". Another plausible scenario is the so-called *freeze-in*, where the coupling between visible sector particles and DM is very small, $\mathcal{O}(\leq 10^{-7})$. This prevents DM from reaching thermal equilibrium at the early universe and freeze-out can not happen. Such process results with feebly interacting particles (FIMPs) [303]. Alongside with various theoretical implications, FIMPs can cause unconventional signals in the detector. Due to the small coupling, a mediator that decays into such DM will be long-lived and can leave unique signatures on the tracker system of the detector. Depending on their decay length, these particles can decay within the tracker volume or beyond. The track signature is quantified via impact parameter, d_0. However, reconstruction and propagation of such tracks require crucial information such as the edge of the fiducial volume of the detector alongside with the intensity and the orientation of the magnetic field. Addition to the unique object reconstruction, these signals have atypical backgrounds such as fake-particle signatures coming from hadronic showers, cosmic muons or cavern radiations [304]. Thus it is quite challenging for theorists to reconstruct such particles within a good approximation. There is a wide range of studies using simple detector efficiencies to validate their theoretical models, but this is not an accurate approximation. Such analyses can be important for studies on freeze-in scenarios as well as theories with a compressed mass spectrum which can lead long-lived particles.

Bibliography

[1] J. Y. Araz, S. Banerjee, M. Frank, B. Fuks and A. Goudelis, *Dark matter and collider signals in an MSSM extension with vector-like multiplets*, *Phys. Rev.* **D98** (2018) 115009, [1810.07224].

[2] J. Y. Araz, M. Frank and B. Fuks, *Differentiating $U(1)'$ supersymmetric models with right sneutrino and neutralino dark matter*, *Phys. Rev.* **D96** (2017) 015017, [1705.01063].

[3] J. Y. Araz, G. Corcella, M. Frank and B. Fuks, *Loopholes in Z searches at the LHC: exploring supersymmetric and leptophobic scenarios*, *JHEP* **02** (2018) 092, [1711.06302].

[4] X. Cid Vidal et al., *Report from Working Group 3*, *CERN Yellow Rep. Monogr.* **7** (2019) 585–865, [1812.07831].

[5] J. Y. Araz, *Leptophobic Z' in supersymmetry and where to find them*, in *11th International Symposium on Quantum Theory and Symmetries (QTS2019) Montreal, Canada, July 1-5, 2019*, 2020. 2003.02177.

[6] J. Y. Araz, M. Frank and B. Fuks, *Reinterpreting the results of the LHC with MadAnalysis 5: uncertainties and higher-luminosity estimates*, 1910.11418.

[7] T. L. Heath, *A History of Greek Mathematics, Volume I: From Thales to Euclid.* Clarendon Press, 1921.

[8] D. F. Mansfield and N. Wildberger, *Plimpton 322 is babylonian exact sexagesimal trigonometry*, *Historia Mathematica* (2017) .

[9] G. W. F. Hegel and D. Forbes, *Lectures on the Philosophy of World History.* Cambridge Studies in the History and Theory of Politics. Cambridge University Press, 1975, 10.1017/CBO9781139167567.

[10] D. W. G. e. Patricia Curd, *The Oxford Handbook of Presocratic Philosophy.* Oxford Handbooks. Oxford University Press, 1 ed., 2008.

[11] E. Robson, *Neither sherlock holmes nor babylon: A reassessment of plimpton 322*, *Historia Mathematica* **28** (2001) 167 – 206.

[12] Herodotus, *The Histories.* Barnes & Noble Classics, 2005.

[13] J. Friberg, *Unexpected Links Between Egyptian and Babylonian Mathematics.* World Scientific Publishing Company, 2005.

[14] J. Friberg, *Amazing Traces of a Babylonian Origin in Greek Mathematics.* World Scientific Publishing Company, illustrated edition ed., 2007.

[15] D. Fowler and E. Robson, *Square root approximations in old babylonian mathematics: Ybc 7289 in context*, *Historia Mathematica* **25** (1998) 366 – 378.

[16] E. Robson, *Three old babylonian methods for dealing with "pythagorean" triangles*, *Journal of Cuneiform Studies* **49** (1997) 51–72.

[17] L. Brack-Bernsen and M. Brack, *Analyzing Shell Structure from Babylonian and Modern Times*, *International Journal of Modern Physics E* **13** (Jan., 2004) 247–260, [`physics/0310126`].

[18] A. Aaboe, *Episodes from the Early History of Mathematics (New Mathematical Library).* New Mathematical Library. The Mathematical Association of America, 1997.

[19] S. L. Glashow, *Partial-symmetries of weak interactions*, *Nuclear Physics* **22** (1961) 579 – 588.

[20] S. L. Glashow, J. Iliopoulos and L. Maiani, *Weak interactions with lepton-hadron symmetry*, *Phys. Rev.* **D2** (1970) 1285–1292.

[21] S. Weinberg, *A model of leptons*, *Phys. Rev. Lett.* **19** (Nov, 1967) 1264–1266.

[22] M. K. Gaillard, P. D. Grannis and F. J. Sciulli, *The Standard model of particle physics*, *Rev. Mod. Phys.* **71** (1999) S96–S111, [`hep-ph/9812285`].

[23] D. J. Gross and F. Wilczek, *Asymptotically free gauge theories. i*, *Phys. Rev. D* **8** (Nov, 1973) 3633–3652.

[24] D. J. Gross and F. Wilczek, *Asymptotically free gauge theories. ii*, *Phys. Rev. D* **9** (Feb, 1974) 980–993.

[25] H. D. Politzer, *Asymptotic freedom: An approach to strong interactions*, *Physics Reports* **14** (1974) 129 – 180.

[26] M. Kobayashi and T. Maskawa, *CP-Violation in the Renormalizable Theory of Weak Interaction*, *Progress of Theoretical Physics* **49** (02, 1973) 652–657.

[27] CMS collaboration, S. Chatrchyan et al., *Observation of a new boson at a mass of 125 GeV with the CMS experiment at the LHC*, *Phys. Lett.* **B716** (2012) 30–61, [`1207.7235`].

[28] ATLAS collaboration, G. Aad et al., *Observation of a new particle in the search for the standard model higgs boson with the atlas detector at the lhc*, *Phys.Lett.* **B716** (2012) 1–29, [`1207.7214`].

[29] J. Goldstone, *Field theories with superconductor solutions*, *Il Nuovo Cimento (1955-1965)* **19** (1961) 154–164.

[30] J. Goldstone, A. Salam and S. Weinberg, *Broken Symmetries*, *Phys. Rev.* **127** (1962) 965–970.

[31] P. W. Higgs, *Broken symmetries, massless particles and gauge fields*, *Phys. Lett.* **12** (1964) 132–133.

[32] F. Englert and R. Brout, *Broken symmetry and the mass of gauge vector mesons*, *Phys. Rev. Lett.* **13** (Aug, 1964) 321–323.

[33] P. W. Higgs, *Broken symmetries and the masses of gauge bosons*, *Phys. Rev. Lett.* **13** (Oct, 1964) 508–509.

[34] P. W. Higgs, *Spontaneous symmetry breakdown without massless bosons*, *Phys. Rev.* **145** (May, 1966) 1156–1163.

[35] D. Binosi, J. Collins, C. Kaufhold and L. Theussl, *JaxoDraw: A Graphical user interface for drawing Feynman diagrams. Version 2.0 release notes*, *Comput. Phys. Commun.* **180** (2009) 1709–1715, [`0811.4113`].

[36] SNO COLLABORATION collaboration, Q. R. Ahmad, R. C. Allen, T. C. Andersen, J. D. Anglin, G. Bühler, J. C. Barton et al., *Measurement of the rate of*

$\nu_e + d \to p + p + e^-$ *interactions produced by* ^8b *solar neutrinos at the sudbury neutrino observatory*, Phys. Rev. Lett. **87** (Jul, 2001) 071301.

[37] SNO Collaboration collaboration, Q. R. Ahmad, R. C. Allen, T. C. Andersen, J. D.Anglin, J. C. Barton, E. W. Beier et al., *Direct evidence for neutrino flavor transformation from neutral-current interactions in the sudbury neutrino observatory*, Phys. Rev. Lett. **89** (Jun, 2002) 011301.

[38] T2K collaboration, K. Abe et al., *Evidence of Electron Neutrino Appearance in a Muon Neutrino Beam*, Phys. Rev. **D88** (2013) 032002, [`1304.0841`].

[39] IceCube Collaboration collaboration, M. G. Aartsen, M. Ackermann, J. Adams, J. A. Aguilar, M. Ahlers, M. Ahrens et al., *Search for nonstandard neutrino interactions with icecube deepcore*, Phys. Rev. D **97** (Apr, 2018) 072009.

[40] Super-Kamiokande Collaboration collaboration, Y. Fukuda, T. Hayakawa, E. Ichihara, K. Inoue, K. Ishihara, H. Ishino et al., *Evidence for oscillation of atmospheric neutrinos*, Phys. Rev. Lett. **81** (Aug, 1998) 1562–1567.

[41] J. H. Christenson, J. W. Cronin, V. L. Fitch and R. Turlay, *Evidence for the* 2π *Decay of the* K_2^0 *Meson*, Phys. Rev. Lett. **13** (1964) 138–140.

[42] J. R. Fry, *CP violation and the standard model*, Reports on Progress in Physics **63** (jan, 2000) 117–169.

[43] A. D. Sakharov, *Violation ofCPin variance,casymmetry, and baryon asymmetry of the universe*, Soviet Physics Uspekhi **34** (may, 1991) 392–393.

[44] N. Jarosik, C. L. Bennett, J. Dunkley, B. Gold, M. R. Greason, M. Halpern et al., *Seven-year wilkinson microwave anisotropy probe (wmap) observations: Sky maps, systematic errors, and basic results*, The Astrophysical Journal Supplement Series **192** (Jan, 2011) 14.

[45] S. S. McGaugh, F. Lelli and J. M. Schombert, *Radial acceleration relation in rotationally supported galaxies*, Physical Review Letters **117** (Nov, 2016) .

[46] F. Zwicky, *On the masses of nebulae and of clusters of nebulae*, APJ **86** (Oct., 1937) 217.

[47] P. Tisserand, L. Le Guillou, C. Afonso, J. N. Albert, J. Andersen, R. Ansari et al., *Limits on the macho content of the galactic halo from the eros-2 survey of the magellanic clouds*, *Astronomy & Astrophysics* **469** (Apr, 2007) 387–404.

[48] D. Maity and P. Saha, *Connecting CMB anisotropy and cold dark matter phenomenology via reheating*, *Phys. Rev.* **D98** (2018) 103525, [`1801.03059`].

[49] C. North and S. Lowe, "planckapps." `https://github.com/chrisnorth/planckapps`, 2013.

[50] A. Stange and S. Willenbrock, *Yukawa correction to top quark production at the Tevatron*, *Phys. Rev.* **D48** (1993) 2054–2061, [`hep-ph/9302291`].

[51] Z. Sullivan, *Supersymmetric QCD correction to top quark production at the Tevatron*, *Phys. Rev.* **D56** (1997) 451–457, [`hep-ph/9611302`].

[52] H. Wang, C.-S. Li, H.-Y. Zhou and Y.-P. Kuang, *Supersymmetric QCD corrections to top quark pair production in photon-photon collision*, *Phys. Rev.* **D54** (1996) 4374–4379, [`hep-ph/9602332`].

[53] H.-Y. Zhou and C.-S. Li, *Supersymmetric electroweak corrections to top quark production at LHC*, *Commun. Theor. Phys.* **30** (1998) 465–470, [`hep-ph/9805372`].

[54] C. S. Li, R. J. Oakes and J. M. Yang, *Supersymmetric electroweak corrections to single top quark production at the Fermilab Tevatron*, *Phys. Rev.* **D55** (1997) 5780–5785, [`hep-ph/9611455`].

[55] E. Noether, *Invariante variationsprobleme, Nachrichten von der Gesellschaft der Wissenschaften zu Göttingen, Mathematisch-Physikalische Klasse* **1918** (1918) 235–257.

[56] T. Kaluza, *Zum Unitätsproblem in der Physik*. No. 966–972. Sitzungsber. Preuss. Akad. Wiss. Berlin. (Math. Phys.), 1921.

[57] F. Quevedo, S. Krippendorf and O. Schlotterer, *Cambridge Lectures on Supersymmetry and Extra Dimensions*, `1011.1491`.

[58] S. P. Martin, *A Supersymmetry primer*, `hep-ph/9709356`.

[59] B. Fuks, *Supersymmetry - When Theory Inspires Experimental Searches*. habilitation, U. Strasbourg, 2013. `1401.6277`.

[60] H. P. Nilles, *Supersymmetry, Supergravity and Particle Physics*, *Phys. Rept.* **110** (1984) 1–162.

[61] H. Haber and G. Kane, *The search for supersymmetry: Probing physics beyond the standard model*, *Physics Reports* **117** (1985) 75 – 263.

[62] R. K. Kaul, *Gauge hierarchy in a supersymmetric model*, *Physics Letters B* **109** (1982) 19 – 24.

[63] P. Langacker, *Precision tests of the Standard Model*, in *Frontiers of neutrino astrophysics. Proceedings, International Symposium, Takayama, Japan, October 19-22, 1992*, 1993. `hep-ph/9303304`.

[64] P. Langacker and M. Luo, *Implications of precision electroweak experiments for* m_t*,* ρ_0*,* $sin^2\theta_W$*, and grand unification*, *Phys. Rev. D* **44** (Aug, 1991) 817–822.

[65] S. Dimopoulos, S. Raby and F. Wilczek, *Supersymmetry and the scale of unification*, *Phys. Rev. D* **24** (Sep, 1981) 1681–1683.

[66] U. Amaldi, W. de Boer and H. Furstenau, *Comparison of grand unified theories with electroweak and strong coupling constants measured at LEP*, *Phys. Lett.* **B260** (1991) 447–455.

[67] M. Carena, S. Pokorski and C. E. M. Wagner, *On the unification of couplings in the minimal supersymmetric Standard Model*, *Nucl. Phys.* **B406** (1993) 59–89, [`hep-ph/9303202`].

[68] R. N. Mohapatra, *UNIFICATION AND SUPERSYMMETRY. THE FRONTIERS OF QUARK - LEPTON PHYSICS*. Springer, Berlin, 1986, 10.1007/978-1-4757-1928-4.

[69] S. Ferrara, J. R. Ellis and P. Van Nieuwenhuizen, eds., *UNIFICATION OF THE FUNDAMENTAL PARTICLE INTERACTIONS. PROCEEDINGS, EUROPHYSICS STUDY CONFERENCE, ERICE, ITALY, MARCH 17-24, 1980*, vol. 7, (New York, USA), Plenum, Plenum, 1980.

[70] D. S. M. Alves, J. Galloway, J. T. Ruderman and J. R. Walsh, *Running Electroweak Couplings as a Probe of New Physics*, *JHEP* **02** (2015) 007, [`1410.6810`].

[71] C. GIUNTI, C. W. KIM and U. W. LEE, *Running coupling constants and grand unification models*, *Modern Physics Letters A* **06** (1991) 1745–1755, [`https://doi.org/10.1142/S0217732391001883`].

[72] J. R. Ellis, J. S. Hagelin, D. V. Nanopoulos, K. A. Olive and M. Srednicki, *Supersymmetric Relics from the Big Bang*, *Nucl. Phys.* **B238** (1984) 453–476.

[73] J. Wess and B. Zumino, *Supergauge Transformations in Four-Dimensions*, *Nucl. Phys.* **B70** (1974) 39–50.

[74] J. F. Gunion, S. Dawson, H. E. Haber and G. L. Kane, *The Higgs hunter's guide*, vol. 80. Brookhaven Nat. Lab., Upton, NY, 1989.

[75] G. C. Branco, P. M. Ferreira, L. Lavoura, M. N. Rebelo, M. Sher and J. P. Silva, *Theory and phenomenology of two-Higgs-doublet models*, *Phys. Rept.* **516** (2012) 1–102, [`1106.0034`].

[76] J. Ellis, M. Fairbairn and P. Tunney, *Anomaly-Free Models for Flavour Anomalies*, *Eur. Phys. J.* **C78** (2018) 238, [`1705.03447`].

[77] S. Treiman, R. Jackiw, B. Zumino and E. Witten, *Current Algebra and Anomalies*. WORLD SCIENTIFIC, 1985, 10.1142/0131.

[78] T. P. Cheng and L. F. Li, *GAUGE THEORY OF ELEMENTARY PARTICLE PHYSICS*. 1984.

[79] A. Salam and J. A. Strathdee, *Supergauge Transformations*, *Nucl. Phys.* **B76** (1974) 477–482.

[80] S. Ferrara, J. Wess and B. Zumino, *Supergauge Multiplets and Superfields*, *Phys. Lett.* **51B** (1974) 239.

[81] G. 't Hooft, *Symmetry breaking through bell-jackiw anomalies*, *Phys. Rev. Lett.* **37** (Jul, 1976) 8–11.

[82] H. K. Dreiner, *An Introduction to explicit R-parity violation*, `hep-ph/9707435`.

[83] R. Barbier et al., *R-parity violating supersymmetry*, *Phys. Rept.* **420** (2005) 1–202, [`hep-ph/0406039`].

[84] E. Witten, *Dynamical breaking of supersymmetry*, *Nuclear Physics B* **188** (1981) 513 – 554.

[85] L. Girardello and M. Grisaru, *Soft breaking of supersymmetry*, *Nuclear Physics B* **194** (1982) 65 – 76.

[86] S. Dimopoulos and D. W. Sutter, *The Supersymmetric flavor problem*, *Nucl. Phys.* **B452** (1995) 496–512, [`hep-ph/9504415`].

[87] J. F. Gunion and H. E. Haber, *Errata for Higgs bosons in supersymmetric models: 1, 2 and 3*, `hep-ph/9301205`.

[88] M. Guchait, *Exact solution of the neutralino mass matrix*, *Zeitschrift für Physik C Particles and Fields* **57** (1993) 157–163.

[89] M. M. El Kheishen, A. A. Shafik and A. A. Aboshousha, *Analytic formulas for the neutralino masses and the neutralino mixing matrix*, *Phys. Rev. D* **45** (Jun, 1992) 4345–4348.

[90] J. L. Feng, *Naturalness and the Status of Supersymmetry*, *Ann. Rev. Nucl. Part. Sci.* **63** (2013) 351–382, [`1302.6587`].

[91] M. Dine, *Naturalness Under Stress*, *Ann. Rev. Nucl. Part. Sci.* **65** (2015) 43–62, [`1501.01035`].

[92] J. Dutta, P. Konar, S. Mondal, B. Mukhopadhyaya and S. K. Rai, *A Revisit to a Compressed Supersymmetric Spectrum with 125 GeV Higgs*, *JHEP* **01** (2016) 051, [`1511.09284`].

[93] R. Barbieri and G. F. Giudice, *Upper bounds on supersymmetric particle masses*, *Nucl. Phys. B* **306** (Aug, 1987) 63–76. 19 p.

[94] G. F. Giudice, *Naturally Speaking: The Naturalness Criterion and Physics at the LHC*, `0801.2562`.

[95] A. Grinbaum, *Which fine-tuning arguments are fine?*, *Found. Phys.* **42** (2012) 615–631, [`0903.4055`].

[96] R. Slansky, *Group theory for unified model building*, *Physics Reports* **79** (1981) 1 – 128.

[97] Robert E. Marshak, *Conceptual Foundations of Modern Particle Physics*. World Scientific, 1993.

[98] L. Ibáñez, *Locally supersymmetric su(5) grand unification*, *Physics Letters B* **118** (1982) 73 – 78.

[99] L. Ibáñez, *Intermediate mass scales in supersymmetric so(10) grand unification*, *Physics Letters B* **114** (1982) 243 – 246.

[100] F. Deppisch, A. Freitas, W. Porod and P. M. Zerwas, *Determining Heavy Mass Parameters in Supersymmetric SO(10) Models*, *Phys. Rev.* **D77** (2008) 075009, [`0712.0361`].

[101] F. F. Deppisch, N. Desai and T. E. Gonzalo, *Compressed and Split Spectra in Minimal SUSY SO(10)*, *Front.in Phys.* **2** (2014) 27, [`1403.2312`].

[102] L. Di Luzio, *Aspects of symmetry breaking in Grand Unified Theories*. PhD thesis, SISSA, Trieste, 2011. `1110.3210`.

[103] J. Erler, *Chiral models of weak scale supersymmetry*, *Nucl. Phys.* **B586** (2000) 73–91, [`hep-ph/0006051`].

[104] J. A. Casas, J. R. Espinosa and I. Hidalgo, *The MSSM fine tuning problem: A Way out*, *JHEP* **01** (2004) 008, [`hep-ph/0310137`].

[105] M. Dine, N. Seiberg and S. Thomas, *Higgs physics as a window beyond the MSSM (BMSSM)*, *Phys. Rev.* **D76** (2007) 095004, [`0707.0005`].

[106] C. Arina and N. Fornengo, *Sneutrino cold dark matter, a new analysis: Relic abundance and detection rates*, *JHEP* **11** (2007) 029, [`0709.4477`].

[107] U. Ellwanger, C. Hugonie and A. M. Teixeira, *The Next-to-Minimal Supersymmetric Standard Model*, *Phys. Rept.* **496** (2010) 1–77, [`0910.1785`].

[108] P. Batra, A. Delgado, D. E. Kaplan and T. M. P. Tait, *The Higgs mass bound in gauge extensions of the minimal supersymmetric standard model*, *JHEP* **02** (2004) 043, [`hep-ph/0309149`].

[109] K. S. Babu and R. N. Mohapatra, *Minimal Supersymmetric Left-Right Model*, *Phys. Lett.* **B668** (2008) 404–409, [`0807.0481`].

[110] S. P. Martin, *Extra vector-like matter and the lightest Higgs scalar boson mass in low-energy supersymmetry*, *Phys. Rev.* **D81** (2010) 035004, [`0910.2732`].

[111] M. Abdullah and J. L. Feng, *Reviving bino dark matter with vectorlike fourth generation particles*, *Phys. Rev.* **D93** (2016) 015006, [`1510.06089`].

[112] M. Abdullah, J. L. Feng, S. Iwamoto and B. Lillard, *Heavy bino dark matter and collider signals in the MSSM with vectorlike fourth-generation particles*, *Phys. Rev.* **D94** (2016) 095018, [`1608.00283`].

[113] LSND collaboration, C. Athanassopoulos et al., *Evidence for $\nu_\mu \to \nu_e$ neutrino oscillations from LSND*, *Phys. Rev. Lett.* **81** (1998) 1774–1777, [`nucl-ex/9709006`].

[114] MiniBooNE collaboration, A. A. Aguilar-Arevalo et al., *Improved Search for $\bar{\nu}_\mu \to \bar{\nu}_e$ Oscillations in the MiniBooNE Experiment*, *Phys. Rev. Lett.* **110** (2013) 161801, [`1303.2588`].

[115] T. Moroi and Y. Okada, *Radiative corrections to Higgs masses in the supersymmetric model with an extra family and antifamily*, *Mod. Phys. Lett.* **A7** (1992) 187–200.

[116] T. Moroi and Y. Okada, *Upper bound of the lightest neutral Higgs mass in extended supersymmetric Standard Models*, *Phys. Lett.* **B295** (1992) 73–78.

[117] K. S. Babu, I. Gogoladze and C. Kolda, *Perturbative unification and Higgs boson mass bounds*, `hep-ph/0410085`.

[118] K. S. Babu, I. Gogoladze, M. U. Rehman and Q. Shafi, *Higgs Boson Mass, Sparticle Spectrum and Little Hierarchy Problem in Extended MSSM*, *Phys. Rev.* **D78** (2008) 055017, [`0807.3055`].

[119] J. Ellis and K. A. Olive, *Supersymmetric Dark Matter Candidates*, `1001.3651`.

[120] Particle Data Group collaboration, C. Patrignani et al., *Review of Particle Physics*, *Chin. Phys.* **C40** (2016) 100001.

[121] Y. Amhis et al., *Averages of b-hadron, c-hadron, and τ-lepton properties as of summer 2016*, `1612.07233`.

[122] Heavy Flavor Averaging Group collaboration, D. Asner et al., *Averages of b-hadron, c-hadron, and τ-lepton properties*, `1010.1589`.

[123] LHCb collaboration, R. Aaij et al., *First Evidence for the Decay $B_s^0 \to \mu^+\mu^-$*, *Phys. Rev. Lett.* **110** (2013) 021801, [`1211.2674`].

[124] BaBar collaboration, B. Aubert et al., *Searches for Lepton Flavor Violation in the Decays $\tau \to e\gamma$ and $\tau \to \mu\gamma$*, Phys. Rev. Lett. **104** (2010) 021802, [0908.2381].

[125] Belle collaboration, Y. Miyazaki et al., *Search for lepton flavor violating τ^- decays into $\ell^-\eta$, $\ell^-\eta'$ and $\ell^-\pi^0$*, Phys. Lett. **B648** (2007) 341–350, [hep-ex/0703009].

[126] ATLAS collaboration, G. Aad et al., *Probing lepton flavour violation via neutrinoless $\tau \to 3\mu$ decays with the ATLAS detector*, Eur. Phys. J. **C76** (2016) 232, [1601.03567].

[127] T. Jubb, M. Kirk, A. Lenz and G. Tetlalmatzi-Xolocotzi, *On the ultimate precision of meson mixing observables*, Nucl. Phys. **B915** (2017) 431–453, [1603.07770].

[128] ATLAS collaboration, G. Aad et al., *Search for the lepton flavor violating decay $Z \to e\mu$ in pp collisions at $\sqrt{s} = 8$ TeV with the ATLAS detector*, Phys. Rev. **D90** (2014) 072010, [1408.5774].

[129] CMS collaboration, V. Khachatryan et al., *Search for lepton flavour violating decays of the Higgs boson to $e\tau$ and $e\mu$ in proton-proton collisions at $\sqrt{s} = 8$ TeV*, Phys. Lett. **B763** (2016) 472–500, [1607.03561].

[130] Gfitter Group collaboration, M. Baak, J. Cúth, J. Haller, A. Hoecker, R. Kogler, K. Mönig et al., *The global electroweak fit at NNLO and prospects for the LHC and ILC*, Eur. Phys. J. **C74** (2014) 3046, [1407.3792].

[131] D. Eriksson, J. Rathsman and O. Stal, *2HDMC: Two-Higgs-Doublet Model Calculator Physics and Manual*, Comput. Phys. Commun. **181** (2010) 189–205, [0902.0851].

[132] A. Ilnicka, M. Krawczyk and T. Robens, *Inert Doublet Model in light of LHC Run I and astrophysical data*, Phys. Rev. **D93** (2016) 055026, [1508.01671].

[133] CMS collaboration, V. Khachatryan et al., *Search for new physics with the M_{T2} variable in all-jets final states produced in pp collisions at $\sqrt{s} = 13$ TeV*, JHEP **10** (2016) 006, [1603.04053].

[134] ATLAS collaboration, M. Aaboud et al., *Search for top squarks in final states with one isolated lepton, jets, and missing transverse momentum in $\sqrt{s} = 13$ TeV pp collisions with the ATLAS detector*, Phys. Rev. **D94** (2016) 052009, [1606.03903].

[135] L3 collaboration, P. Achard et al., *Search for heavy neutral and charged leptons in e^+e^- annihilation at LEP*, Phys. Lett. **B517** (2001) 75–85, [hep-ex/0107015].

[136] F. Staub, *SARAH 4 : A tool for (not only SUSY) model builders*, *Comput. Phys. Commun.* **185** (2014) 1773–1790, [1309.7223].

[137] W. Porod and F. Staub, *SPheno 3.1: Extensions including flavour, CP-phases and models beyond the MSSM*, *Comput. Phys. Commun.* **183** (2012) 2458–2469, [1104.1573].

[138] P. Bechtle, O. Brein, S. Heinemeyer, G. Weiglein and K. E. Williams, *HiggsBounds: Confronting Arbitrary Higgs Sectors with Exclusion Bounds from LEP and the Tevatron*, *Comput. Phys. Commun.* **181** (2010) 138–167, [0811.4169].

[139] P. Bechtle, S. Heinemeyer, O. Stal, T. Stefaniak and G. Weiglein, *HiggsSignals: Confronting arbitrary Higgs sectors with measurements at the Tevatron and the LHC*, *Eur. Phys. J.* **C74** (2014) 2711, [1305.1933].

[140] R. V. Harlander, S. Liebler and H. Mantler, *SusHi: A program for the calculation of Higgs production in gluon fusion and bottom-quark annihilation in the Standard Model and the MSSM*, *Comput. Phys. Commun.* **184** (2013) 1605–1617, [1212.3249].

[141] *Monte Carlo Sampling Methods using Markov Chains and their Applications*, *Biometrika, Vol. 57, No. 1, p. 97-109, 1970* **57** (Apr., 1970) 97–109.

[142] G. Bélanger, F. Boudjema, A. Pukhov and A. Semenov, *micrOMEGAs4.1: two dark matter candidates*, *Comput. Phys. Commun.* **192** (2015) 322–329, [1407.6129].

[143] A. Belyaev, N. D. Christensen and A. Pukhov, *CalcHEP 3.4 for collider physics within and beyond the Standard Model*, *Comput. Phys. Commun.* **184** (2013) 1729–1769, [1207.6082].

[144] J. Alwall, R. Frederix, S. Frixione, V. Hirschi, F. Maltoni, O. Mattelaer et al., *The automated computation of tree-level and next-to-leading order differential cross sections, and their matching to parton shower simulations*, *JHEP* **07** (2014) 079, [1405.0301].

[145] C. Degrande, C. Duhr, B. Fuks, D. Grellscheid, O. Mattelaer and T. Reiter, *UFO - The Universal FeynRules Output*, *Comput. Phys. Commun.* **183** (2012) 1201–1214, [1108.2040].

[146] A. Buckley, *PySLHA: a Pythonic interface to SUSY Les Houches Accord data*, *Eur. Phys. J.* **C75** (2015) 467, [1305.4194].

[147] ALEPH collaboration, A. Heister et al., *Search for charginos nearly mass degenerate with the lightest neutralino in e+ e- collisions at center-of-mass energies up to 209-GeV*, *Phys. Lett.* **B533** (2002) 223–236, [`hep-ex/0203020`].

[148] DELPHI collaboration, J. Abdallah et al., *Searches for supersymmetric particles in e+ e- collisions up to 208-GeV and interpretation of the results within the MSSM*, *Eur. Phys. J.* **C31** (2003) 421–479, [`hep-ex/0311019`].

[149] L3 collaboration, M. Acciarri et al., *Search for charginos and neutralinos in e^+e^- collisions at $\sqrt{S}$ = 189-GeV*, *Phys. Lett.* **B472** (2000) 420–433, [`hep-ex/9910007`].

[150] OPAL collaboration, G. Abbiendi et al., *Search for chargino and neutralino production at s**(1/2) = 192-GeV to 209 GeV at LEP*, *Eur. Phys. J.* **C35** (2004) 1–20, [`hep-ex/0401026`].

[151] XENON collaboration, E. Aprile et al., *First Dark Matter Search Results from the XENON1T Experiment*, *Phys. Rev. Lett.* **119** (2017) 181301, [`1705.06655`].

[152] M. Perelstein and B. Shakya, *Fine-Tuning Implications of Direct Dark Matter Searches in the MSSM*, *JHEP* **10** (2011) 142, [`1107.5048`].

[153] M. Perelstein and B. Shakya, *XENON100 implications for naturalness in the MSSM, NMSSM, and λ-supersymmetry model*, *Phys. Rev.* **D88** (2013) 075003, [`1208.0833`].

[154] G. Belanger, C. Delaunay and A. Goudelis, *The Dark Side of Electroweak Naturalness Beyond the MSSM*, *JHEP* **04** (2015) 149, [`1412.1833`].

[155] S. Profumo, T. Stefaniak and L. Stephenson Haskins, *The Not-So-Well Tempered Neutralino*, *Phys. Rev.* **D96** (2017) 055018, [`1706.08537`].

[156] Planck collaboration, P. A. R. Ade et al., *Planck 2015 results. XIII. Cosmological parameters*, *Astron. Astrophys.* **594** (2016) A13, [`1502.01589`].

[157] A. Choudhury, L. Darmé, L. Roszkowski, E. M. Sessolo and S. Trojanowski, *Muon g - 2 and related phenomenology in constrained vector-like extensions of the MSSM*, *JHEP* **05** (2017) 072, [`1701.08778`].

[158] LUX collaboration, D. S. Akerib et al., *Improved Limits on Scattering of Weakly Interacting Massive Particles from Reanalysis of 2013 LUX Data*, *Phys. Rev. Lett.* **116** (2016) 161301, [`1512.03506`].

[159] M. Mitchell, B. Muftakhidinov, T. Winchen, Z. Jedrzejewski-Szmek and T. G. Badger, *engauge-digitizer: Support for smaller monitors*, Aug., 2016. 10.5281/zenodo.61108.

[160] XENON collaboration, E. Aprile et al., *Physics reach of the XENON1T dark matter experiment*, *JCAP* **1604** (2016) 027, [1512.07501].

[161] Fermi-LAT collaboration, M. Ackermann et al., *Searching for Dark Matter Annihilation from Milky Way Dwarf Spheroidal Galaxies with Six Years of Fermi Large Area Telescope Data*, *Phys. Rev. Lett.* **115** (2015) 231301, [1503.02641].

[162] R. D. Ball, V. Bertone, S. Carrazza, C. S. Deans, L. Del Debbio et al., *Parton distributions with LHC data*, *Nucl.Phys.* **B867** (2013) 244–289, [1207.1303].

[163] M. L. Mangano, M. Moretti, F. Piccinini and M. Treccani, *Matching matrix elements and shower evolution for top-quark production in hadronic collisions*, *JHEP* **01** (2007) 013, [hep-ph/0611129].

[164] T. Sjostrand, S. Mrenna and P. Z. Skands, *A Brief Introduction to PYTHIA 8.1*, *Comput. Phys. Commun.* **178** (2008) 852–867, [0710.3820].

[165] DELPHES 3 collaboration, J. de Favereau, C. Delaere, P. Demin, A. Giammanco, V. Lemaître, A. Mertens et al., *DELPHES 3, A modular framework for fast simulation of a generic collider experiment*, *JHEP* **02** (2014) 057, [1307.6346].

[166] M. Cacciari, G. P. Salam and G. Soyez, *FastJet User Manual*, *Eur. Phys. J.* **C72** (2012) 1896, [1111.6097].

[167] M. Cacciari, G. P. Salam and G. Soyez, *The Anti-k(t) jet clustering algorithm*, *JHEP* **04** (2008) 063, [0802.1189].

[168] CMS collaboration, S. Chatrchyan et al., *Identification of b-quark jets with the CMS experiment*, *JINST* **8** (2013) P04013, [1211.4462].

[169] G. Cowan, K. Cranmer, E. Gross and O. Vitells, *Asymptotic formulae for likelihood-based tests of new physics*, *Eur. Phys. J.* **C71** (2011) 1554, [1007.1727].

[170] ATLAS collaboration, M. Aaboud et al., *Search for new phenomena in final states with an energetic jet and large missing transverse momentum in pp collisions at* $\sqrt{s} = 13$ *TeV using the ATLAS detector*, *Phys. Rev.* **D94** (2016) 032005, [1604.07773].

[171] ATLAS collaboration, M. Aaboud et al., *Search for squarks and gluinos in final states with jets and missing transverse momentum at* $\sqrt{s}$ *= 13 TeV with the ATLAS detector*, *Eur. Phys. J.* **C76** (2016) 392, [1605.03814].

[172] ATLAS collaboration, M. Aaboud et al., *Search for dark matter and other new phenomena in events with an energetic jet and large missing transverse momentum using the ATLAS detector*, *JHEP* **01** (2018) 126, [1711.03301].

[173] ATLAS collaboration, M. Aaboud et al., *Search for squarks and gluinos in final states with jets and missing transverse momentum using 36 fb*$^{-1}$ *of* $\sqrt{s} = 13$ *TeV pp collision data with the ATLAS detector*, *Phys. Rev.* **D97** (2018) 112001, [1712.02332].

[174] CMS collaboration, A. M. Sirunyan et al., *Search for Evidence of the Type-III Seesaw Mechanism in Multilepton Final States in Proton-Proton Collisions at* $\sqrt{s} = 13$ TeV, *Phys. Rev. Lett.* **119** (2017) 221802, [1708.07962].

[175] CMS collaboration, *Search for vector-like leptons in multilepton final states in pp collisions at* $\sqrt{s} = 13$ TeV, CMS-PAS-EXO-18-005.

[176] ATLAS collaboration, M. Aaboud et al., *Search for supersymmetry in events with four or more leptons in* $\sqrt{s} = 13$ *TeV pp collisions with ATLAS*, *Phys. Rev.* **D98** (2018) 032009, [1804.03602].

[177] ATLAS collaboration, *Search for pair production of gluinos decaying via top or bottom squarks in events with b-jets and large missing transverse momentum in pp collisions at* $\sqrt{s} = 13$ *TeV with the ATLAS detector*, ATLAS-CONF-2016-052.

[178] ATLAS collaboration, *Search for squarks and gluinos in events with an isolated lepton, jets and missing transverse momentum at* $\sqrt{s}$ *= 13 TeV with the ATLAS detector*, ATLAS-CONF-2016-054.

[179] ATLAS collaboration, *Further searches for squarks and gluinos in final states with jets and missing transverse momentum at* $\sqrt{s}$ *=13 TeV with the ATLAS detector*, ATLAS-CONF-2016-078.

[180] L. J. Hall, D. Pinner and J. T. Ruderman, *A Natural SUSY Higgs Near 126 GeV*, *JHEP* **04** (2012) 131, [1112.2703].

[181] S. Cassel, D. M. Ghilencea, S. Kraml, A. Lessa and G. G. Ross, *Fine-tuning implications for complementary dark matter and LHC SUSY searches*, *JHEP* **05** (2011) 120, [1101.4664].

[182] H. Baer, V. Barger, D. Mickelson and M. Padeffke-Kirkland, *SUSY models under siege: LHC constraints and electroweak fine-tuning*, *Phys. Rev.* **D89** (2014) 115019, [1404.2277].

[183] J. L. Hewett and T. G. Rizzo, *Low-Energy Phenomenology of Superstring Inspired E(6) Models*, *Phys. Rept.* **183** (1989) 193.

[184] P. Langacker and J. Wang, *U(1)-prime symmetry breaking in supersymmetric E(6) models*, *Phys. Rev.* **D58** (1998) 115010, [hep-ph/9804428].

[185] C. T. Hill and E. H. Simmons, *Strong dynamics and electroweak symmetry breaking*, *Phys. Rept.* **381** (2003) 235–402, [hep-ph/0203079].

[186] N. Arkani-Hamed, A. G. Cohen, E. Katz and A. E. Nelson, *The Littlest Higgs*, *JHEP* **07** (2002) 034, [hep-ph/0206021].

[187] T. Han, H. E. Logan, B. McElrath and L.-T. Wang, *Phenomenology of the little Higgs model*, *Phys. Rev.* **D67** (2003) 095004, [hep-ph/0301040].

[188] I. Antoniadis, *A Possible new dimension at a few TeV*, *Phys. Lett.* **B246** (1990) 377–384.

[189] M. Cvetic, D. A. Demir, J. R. Espinosa, L. L. Everett and P. Langacker, *Electroweak breaking and the mu problem in supergravity models with an additional U(1)*, *Phys. Rev.* **D56** (1997) 2861, [hep-ph/9703317].

[190] D. A. Demir, G. L. Kane and T. T. Wang, *The Minimal U(1)' extension of the MSSM*, *Phys. Rev.* **D72** (2005) 015012, [hep-ph/0503290].

[191] J. R. Ellis, K. Enqvist, D. V. Nanopoulos, K. A. Olive, M. Quiros and F. Zwirner, *Problems for (2,0) Compactifications*, *Phys. Lett.* **B176** (1986) 403–408.

[192] P. Langacker and M. Plumacher, *Flavor changing effects in theories with a heavy Z' boson with family nonuniversal couplings*, *Phys. Rev.* **D62** (2000) 013006, [hep-ph/0001204].

[193] WMAP collaboration, G. Hinshaw et al., *Nine-Year Wilkinson Microwave Anisotropy Probe (WMAP) Observations: Cosmological Parameter Results*, *Astrophys. J. Suppl.* **208** (2013) 19, [1212.5226].

[194] PLANCK collaboration, P. A. R. Ade et al., *Planck 2013 results. XVI. Cosmological parameters*, *Astron. Astrophys.* **571** (2014) A16, [1303.5076].

[195] E. Ma, *Particle Dichotomy and Left-Right Decomposition of E(6) Superstring Models*, *Phys. Rev.* **D36** (1987) 274.

[196] S. W. Ham, E. J. Yoo and S. K. Oh, *Explicit CP violation in a MSSM with an extra U(1)-prime*, *Phys. Rev.* **D76** (2007) 015004, [`hep-ph/0703041`].

[197] P. Langacker, *The Physics of Heavy Z' Gauge Bosons*, *Rev. Mod. Phys.* **81** (2009) 1199–1228, [`0801.1345`].

[198] G. Bélanger, J. Da Silva, U. Laa and A. Pukhov, *Probing U(1) extensions of the MSSM at the LHC Run I and in dark matter searches*, *JHEP* **09** (2015) 151, [`1505.06243`].

[199] G. Belanger, J. Da Silva and A. Pukhov, *The Right-handed sneutrino as thermal dark matter in U(1) extensions of the MSSM*, *JCAP* **1112** (2011) 014, [`1110.2414`].

[200] G. Corcella, *Phenomenology of supersymmetric Z' decays at the Large Hadron Collider*, *Eur. Phys. J.* **C75** (2015) 264, [`1412.6831`].

[201] G. Corcella and S. Gentile, *Heavy Neutral Gauge Bosons at the LHC in an Extended MSSM*, *Nucl. Phys.* **B866** (2013) 293–336, [`1205.5780`].

[202] P. S. Bhupal Dev, S. Mondal, B. Mukhopadhyaya and S. Roy, *Phenomenology of Light Sneutrino Dark Matter in cMSSM/mSUGRA with Inverse Seesaw*, *JHEP* **09** (2012) 110, [`1207.6542`].

[203] V. Barger, D. Marfatia and A. Peterson, *LHC and dark matter signals of Z' bosons*, *Phys. Rev.* **D87** (2013) 015026, [`1206.6649`].

[204] C.-W. Chiang, T. Nomura and K. Yagyu, *Phenomenology of E_6-Inspired Leptophobic Z' Boson at the LHC*, *JHEP* **05** (2014) 106, [`1402.5579`].

[205] G. Bélanger, J. Da Silva and H. M. Tran, *Dark matter in U(1) extensions of the MSSM with gauge kinetic mixing*, `1703.03275`.

[206] J. E. Kim and H. P. Nilles, *The mu Problem and the Strong CP Problem*, *Phys. Lett.* **B138** (1984) 150.

[207] D. Suematsu and Y. Yamagishi, *Radiative symmetry breaking in a supersymmetric model with an extra U(1)*, *Int. J. Mod. Phys.* **A10** (1995) 4521–4536, [`hep-ph/9411239`].

[208] M. Cvetic and P. Langacker, *New gauge bosons from string models*, *Mod. Phys. Lett.* **A11** (1996) 1247–1262, [`hep-ph/9602424`].

[209] V. Jain and R. Shrock, *U(1)-A models of fermion masses without a mu problem*, `hep-ph/9507238`.

[210] D. A. Demir, *Two Higgs doublet models from TeV scale supersymmetric extra U(1) models*, *Phys. Rev.* **D59** (1999) 015002, [`hep-ph/9809358`].

[211] P. Minkowski, *$\mu \to e\gamma$ at a Rate of One Out of 10^9 Muon Decays?*, *Phys. Lett.* **B67** (1977) 421–428.

[212] R. N. Mohapatra and G. Senjanovic, *Neutrino Mass and Spontaneous Parity Violation*, *Phys. Rev. Lett.* **44** (1980) 912.

[213] J. Schechter and J. W. F. Valle, *Neutrino Masses in SU(2) x U(1) Theories*, *Phys. Rev.* **D22** (1980) 2227.

[214] J. Schechter and J. W. F. Valle, *Neutrino Decay and Spontaneous Violation of Lepton Number*, *Phys. Rev.* **D25** (1982) 774.

[215] J.-h. Kang, P. Langacker and T.-j. Li, *Neutrino masses in supersymmetric SU(3)(C) x SU(2)(L) x U(1)(Y) x U(1)-prime models*, *Phys. Rev.* **D71** (2005) 015012, [`hep-ph/0411404`].

[216] D. A. Demir and Y. Farzan, *Correlating mu parameter and right-handed neutrino masses in N=1 supergravity*, *JHEP* **03** (2006) 010, [`hep-ph/0601096`].

[217] D. A. Demir, L. L. Everett and P. Langacker, *Dirac Neutrino Masses from Generalized Supersymmetry Breaking*, *Phys. Rev. Lett.* **100** (2008) 091804, [`0712.1341`].

[218] S. Heinemeyer, O. Stal and G. Weiglein, *Interpreting the LHC Higgs Search Results in the MSSM*, *Phys. Lett.* **B710** (2012) 201–206, [`1112.3026`].

[219] G. G. Ross, K. Schmidt-Hoberg and F. Staub, *The Generalised NMSSM at One Loop: Fine Tuning and Phenomenology*, *JHEP* **08** (2012) 074, [`1205.1509`].

[220] J. Erler, P. Langacker, S. Munir and E. Rojas, *Improved Constraints on Z-prime Bosons from Electroweak Precision Data*, *JHEP* **08** (2009) 017, [`0906.2435`].

[221] G. Corcella, *Searching for supersymmetry in Z' decays*, *EPJ Web Conf.* **60** (2013) 18011, [1307.1040].

[222] LHC Higgs Cross Section Working Group collaboration, J. R. Andersen et al., *Handbook of LHC Higgs Cross Sections: 3. Higgs Properties*, 1307.1347.

[223] Muon g-2 collaboration, G. W. Bennett et al., *Final Report of the Muon E821 Anomalous Magnetic Moment Measurement at BNL*, *Phys. Rev.* **D73** (2006) 072003, [hep-ex/0602035].

[224] Muon g-2 collaboration, J. Grange et al., *Muon (g-2) Technical Design Report*, 1501.06858.

[225] J-PARC g-'2/EDM collaboration, N. Saito, *A novel precision measurement of muon g-2 and EDM at J-PARC*, *AIP Conf. Proc.* **1467** (2012) 45–56.

[226] WMAP collaboration, E. Komatsu et al., *Seven-Year Wilkinson Microwave Anisotropy Probe (WMAP) Observations: Cosmological Interpretation*, *Astrophys. J. Suppl.* **192** (2011) 18, [1001.4538].

[227] WMAP collaboration, D. N. Spergel et al., *Wilkinson Microwave Anisotropy Probe (WMAP) three year results: implications for cosmology*, *Astrophys. J. Suppl.* **170** (2007) 377, [astro-ph/0603449].

[228] IceCube collaboration, R. Abbasi et al., *Limits on a muon flux from neutralino annihilations in the Sun with the IceCube 22-string detector*, *Phys. Rev. Lett.* **102** (2009) 201302, [0902.2460].

[229] H. Baer, V. Barger and A. Mustafayev, *Implications of a 125 GeV Higgs scalar for LHC SUSY and neutralino dark matter searches*, *Phys. Rev.* **D85** (2012) 075010, [1112.3017].

[230] C. Arina et al., *A comprehensive approach to dark matter studies: exploration of simplified top-philic models*, *JHEP* **11** (2016) 111, [1605.09242].

[231] T. Sjöstrand, S. Ask, J. R. Christiansen, R. Corke, N. Desai, P. Ilten et al., *An Introduction to PYTHIA 8.2*, *Comput. Phys. Commun.* **191** (2015) 159–177, [1410.3012].

[232] E. Conte, B. Fuks and G. Serret, *MadAnalysis 5, A User-Friendly Framework for Collider Phenomenology*, *Comput. Phys. Commun.* **184** (2013) 222–256, [1206.1599].

[233] M. Frank, L. Selbuz and I. Turan, *Neutralino and Chargino Production in U(1)' at the LHC*, *Eur. Phys. J.* **C73** (2013) 2656, [1212.4428].

[234] F. del Aguila, J. de Blas and M. Perez-Victoria, *Electroweak Limits on General New Vector Bosons*, *JHEP* **09** (2010) 033, [1005.3998].

[235] E. Salvioni, G. Villadoro and F. Zwirner, *Minimal Z' models: Present bounds and early LHC reach*, *JHEP* **11** (2009) 068, [0909.1320].

[236] A. Leike, *The Phenomenology of extra neutral gauge bosons*, *Phys. Rept.* **317** (1999) 143–250, [hep-ph/9805494].

[237] M. Cvetic and S. Godfrey, *Discovery and identification of extra gauge bosons*, hep-ph/9504216.

[238] F. del Aguila, M. Cvetic and P. Langacker, *Determination of Z' gauge couplings to quarks and leptons at future hadron colliders*, *Phys. Rev.* **D48** (1993) R969–R973, [hep-ph/9303299].

[239] ATLAS collaboration, M. Aaboud et al., *Search for new high-mass phenomena in the dilepton final state using 36.1 fb^{-1} of proton-proton collision data at $\sqrt{s}$ = 13 TeV with the ATLAS detector*, 1707.02424.

[240] CMS collaboration, C. Collaboration, *Search for a high-mass resonance decaying into a dilepton final state in 13 fb^{-1} of pp collisions at* $\sqrt{s} = 13$ TeV, .

[241] ATLAS collaboration, M. Aaboud et al., *Search for new phenomena in dijet events using 37 fb^{-1} of pp collision data collected at $\sqrt{s}$ =13 TeV with the ATLAS detector*, *Phys. Rev.* **D96** (2017) 052004, [1703.09127].

[242] CMS collaboration, A. M. Sirunyan et al., *Search for dijet resonances in proton–proton collisions at $\sqrt{s}$ = 13 TeV and constraints on dark matter and other models*, *Phys. Lett.* **B769** (2017) 520–542, [1611.03568].

[243] CMS COLLABORATION collaboration, *A search for dijet resonances in proton-proton collisions at* $\sqrt{s} = 13$ TeV *with a new background prediction method*, Tech. Rep. CMS-PAS-EXO-19-012, CERN, Geneva, 2019.

[244] ATLAS collaboration, G. Aad et al., *Search for high-mass dilepton resonances using 139 fb^{-1} of pp collision data collected at $\sqrt{s}$ =13 TeV with the ATLAS detector*, *Phys. Lett.* **B796** (2019) 68–87, [1903.06248].

[245] T. Gherghetta, T. A. Kaeding and G. L. Kane, *Supersymmetric contributions to the decay of an extra Z boson*, Phys. Rev. **D57** (1998) 3178–3181, [`hep-ph/9701343`].

[246] M. Baumgart, T. Hartman, C. Kilic and L.-T. Wang, *Discovery and measurement of sleptons, binos, and winos with a Z'*, JHEP **11** (2007) 084, [`hep-ph/0608172`].

[247] C.-F. Chang, K. Cheung and T.-C. Yuan, *Supersymmetric Decays of the Z' Boson*, JHEP **09** (2011) 058, [`1107.1133`].

[248] F. del Aguila, M. Quiros and F. Zwirner, *On the Mass and the Signature of a New Z*, Nucl. Phys. **B284** (1987) 530–556.

[249] E. Nardi and T. G. Rizzo, *Identifying unconventional E(6) models at e+ e- colliders*, Phys. Rev. **D50** (1994) 203–209, [`hep-ph/9401260`].

[250] J. R. Ellis, D. V. Nanopoulos, S. T. Petcov and F. Zwirner, *Gauginos and Higgs Particles in Superstring Models*, Nucl. Phys. **B283** (1987) 93–110.

[251] H. Georgi and D. V. Nanopoulos, *Suppression of Flavor Changing Effects From Neutral Spinless Meson Exchange in Gauge Theories*, Phys. Lett. B **82** (1979) 95–96.

[252] R. Slansky, *Group Theory for Unified Model Building*, Phys. Rept. **79** (1981) 1–128.

[253] J. Erler, P. Langacker and T.-j. Li, *The Z - Z' mass hierarchy in a supersymmetric model with a secluded U(1) -prime breaking sector*, Phys. Rev. **D66** (2002) 015002, [`hep-ph/0205001`].

[254] K. S. Babu, C. F. Kolda and J. March-Russell, *Implications of generalized $Z - Z'$ mixing*, Phys. Rev. **D57** (1998) 6788–6792, [`hep-ph/9710441`].

[255] K. S. Babu, C. F. Kolda and J. March-Russell, *Leptophobic $U(1)'$s and the R(b) - R(c) crisis*, Phys. Rev. **D54** (1996) 4635–4647, [`hep-ph/9603212`].

[256] D. Suematsu, *Vacuum structure of the μ problem solvable extra $U(1)$ models*, Phys. Rev. **D59** (1999) 055017, [`hep-ph/9808409`].

[257] Particle Data Group collaboration, K. A. Olive et al., *Review of Particle Physics*, Chin. Phys. **C38** (2014) 090001.

[258] B. Fuks, M. Klasen, F. Ledroit, Q. Li and J. Morel, *Precision predictions for Z' - production at the CERN LHC: QCD matrix elements, parton showers, and joint resummation*, Nucl. Phys. **B797** (2008) 322–339, [`0711.0749`].

[259] B. Fuks and R. Ruiz, *A comprehensive framework for studying W' and Z' bosons at hadron colliders with automated jet veto resummation*, JHEP **05** (2017) 032, [`1701.05263`].

[260] A. Alloul, N. D. Christensen, C. Degrande, C. Duhr and B. Fuks, *FeynRules 2.0 - A complete toolbox for tree-level phenomenology*, Comput. Phys. Commun. **185** (2014) 2250–2300, [`1310.1921`].

[261] C. Degrande, *Automatic evaluation of UV and R2 terms for beyond the Standard Model Lagrangians: a proof-of-principle*, Comput. Phys. Commun. **197** (2015) 239–262, [`1406.3030`].

[262] T. Hahn, *Generating Feynman diagrams and amplitudes with FeynArts 3*, Comput. Phys. Commun. **140** (2001) 418–431, [`hep-ph/0012260`].

[263] J. Anderson et al., *Snowmass Energy Frontier Simulations*, in *Proceedings, Community Summer Study 2013: Snowmass on the Mississippi (CSS2013): Minneapolis, MN, USA, July 29-August 6, 2013*, 2013. `1309.1057`.

[264] A. Avetisyan et al., *Methods and Results for Standard Model Event Generation at $\sqrt{s}$ = 14 TeV, 33 TeV and 100 TeV Proton Colliders (A Snowmass Whitepaper)*, in *Proceedings, Community Summer Study 2013: Snowmass on the Mississippi (CSS2013): Minneapolis, MN, USA, July 29-August 6, 2013*, 2013. `1308.1636`.

[265] T. C. Collaboration, *CMS physics technical design report, volume II: Physics performance*, Journal of Physics G: Nuclear and Particle Physics **34** (apr, 2007) 995–1579.

[266] L. Lista, *Statistical Methods for Data Analysis in Particle Physics*, Lect. Notes Phys. **941** (2017) 1–257.

[267] C. G. Lester and D. J. Summers, *Measuring masses of semiinvisibly decaying particles pair produced at hadron colliders*, Phys. Lett. **B463** (1999) 99–103, [`hep-ph/9906349`].

[268] A. Barr, C. Lester and P. Stephens, *m_{T2}: The Truth behind the glamour*, J. Phys. **G29** (2003) 2343–2363, [`hep-ph/0304226`].

[269] D. R. Tovey, *On measuring the masses of pair-produced semi-invisibly decaying particles at hadron colliders*, JHEP **0804** (2008) 034, [`0802.2879`].

[270] S. Kraml, S. Kulkarni, U. Laa, A. Lessa, W. Magerl, D. Proschofsky-Spindler et al., *SModelS: a tool for interpreting simplified-model results from the LHC and its application to supersymmetry*, *Eur. Phys. J.* **C74** (2014) 2868, [`1312.4175`].

[271] M. Drees, H. Dreiner, D. Schmeier, J. Tattersall and J. S. Kim, *CheckMATE: Confronting your Favourite New Physics Model with LHC Data*, *Comput. Phys. Commun.* **187** (2015) 227–265, [`1312.2591`].

[272] B. Dumont, B. Fuks, S. Kraml, S. Bein, G. Chalons, E. Conte et al., *Toward a public analysis database for LHC new physics searches using MADANALYSIS 5*, *Eur. Phys. J.* **C75** (2015) 56, [`1407.3278`].

[273] A. Buckley, J. Butterworth, L. Lonnblad, D. Grellscheid, H. Hoeth, J. Monk et al., *Rivet user manual*, *Comput. Phys. Commun.* **184** (2013) 2803–2819, [`1003.0694`].

[274] GAMBIT collaboration, C. Balázs et al., *ColliderBit: a GAMBIT module for the calculation of high-energy collider observables and likelihoods*, *Eur. Phys. J.* **C77** (2017) 795, [`1705.07919`].

[275] S. Frixione, B. Fuks, V. Hirschi, K. Mawatari, H.-S. Shao, P. Sunder et al., *Automated simulations beyond the Standard Model: supersymmetry*, *JHEP* **12** (2019) 008, [`1907.04898`].

[276] E. Conte and B. Fuks, *Confronting new physics theories to LHC data with MADANALYSIS 5*, *Int. J. Mod. Phys.* **A33** (2018) 1830027, [`1808.00480`].

[277] J. Alwall, P. Schuster and N. Toro, *Simplified Models for a First Characterization of New Physics at the LHC*, *Phys. Rev. D* **79** (2009) 075020, [`0810.3921`].

[278] LHC NEW PHYSICS WORKING GROUP collaboration, D. Alves, *Simplified Models for LHC New Physics Searches*, *J. Phys. G* **39** (2012) 105005, [`1105.2838`].

[279] ATLAS collaboration, The ATLAS collaboration, *Search for squarks and gluinos in final states with jets and missing transverse momentum using 139 fb*$^{-1}$ *of* $\sqrt{s}$ *=13 TeV pp collision data with the ATLAS detector*, ATLAS-CONF-2019-040.

[280] M. Backović, M. Krämer, F. Maltoni, A. Martini, K. Mawatari and M. Pellen, *Higher-order QCD predictions for dark matter production at the LHC in simplified models with s-channel mediators*, *Eur. Phys. J. C* **75** (2015) 482, [`1508.05327`].

[281] D. Abercrombie et al., *Dark Matter Benchmark Models for Early LHC Run-2 Searches: Report of the ATLAS/CMS Dark Matter Forum*, *Phys. Dark Univ.* **27** (2020) 100371, [`1507.00966`].

[282] E. Conte, B. Dumont, B. Fuks and C. Wymant, *Designing and recasting LHC analyses with MadAnalysis 5*, *Eur. Phys. J.* **C74** (2014) 3103, [`1405.3982`].

[283] R. Brun and F. Rademakers, *ROOT: An object oriented data analysis framework*, *Nucl. Instrum. Meth.* **A389** (1997) 81–86.

[284] A. L. Read, *Presentation of search results: The CL(s) technique*, *J. Phys.* **G28** (2002) 2693–2704.

[285] NNPDF collaboration, R. D. Ball et al., *Parton distributions for the LHC Run II*, *JHEP* **04** (2015) 040, [`1410.8849`].

[286] A. Buckley, J. Ferrando, S. Lloyd, K. Nordström, B. Page, M. Rüfenacht et al., *LHAPDF6: parton density access in the LHC precision era*, *Eur. Phys. J.* **C75** (2015) 132, [`1412.7420`].

[287] P. Artoisenet, R. Frederix, O. Mattelaer and R. Rietkerk, *Automatic spin-entangled decays of heavy resonances in Monte Carlo simulations*, *JHEP* **03** (2013) 015, [`1212.3460`].

[288] J. Alwall, C. Duhr, B. Fuks, O. Mattelaer, D. G. Öztürk and C.-H. Shen, *Computing decay rates for new physics theories with FeynRules and MadGraph5_aMC@NLO*, *Comput. Phys. Commun.* **197** (2015) 312–323, [`1402.1178`].

[289] S. Frixione and B. R. Webber, *Matching NLO QCD computations and parton shower simulations*, *JHEP* **06** (2002) 029, [`hep-ph/0204244`].

[290] F. Demartin, S. Forte, E. Mariani, J. Rojo and A. Vicini, *The impact of PDF and alphas uncertainties on Higgs Production in gluon fusion at hadron colliders*, *Phys. Rev.* **D82** (2010) 014002, [`1004.0962`].

[291] C. Borschensky, M. Krämer, A. Kulesza, M. Mangano, S. Padhi, T. Plehn et al., *Squark and gluino production cross sections in pp collisions at $\sqrt{s}$ = 13, 14, 33 and 100 TeV*, *Eur. Phys. J.* **C74** (2014) 3174, [`1407.5066`].

[292] P. M. Nadolsky, H.-L. Lai, Q.-H. Cao, J. Huston, J. Pumplin, D. Stump et al., *Implications of CTEQ global analysis for collider observables*, *Phys. Rev.* **D78** (2008) 013004, [`0802.0007`].

[293] A. D. Martin, W. J. Stirling, R. S. Thorne and G. Watt, *Parton distributions for the LHC*, *Eur. Phys. J.* **C63** (2009) 189–285, [`0901.0002`].

[294] W. Beenakker, R. Hopker, M. Spira and P. M. Zerwas, *Squark and gluino production at hadron colliders*, *Nucl. Phys.* **B492** (1997) 51–103, [`hep-ph/9610490`].

[295] G. Chalons and H. Reyes-Gonzalez, *MadAnalysis 5 implementation of ATLAS-SUSY-16-07 (arXiv:1712.02332)*, 10.7484/INSPIREHEP.DATA.56DC.PPE2.

[296] P. Jackson and C. Rogan, *Recursive Jigsaw Reconstruction: HEP event analysis in the presence of kinematic and combinatoric ambiguities*, *Phys. Rev.* **D96** (2017) 112007, [`1705.10733`].

[297] L. Heinrich, G. Louppe and K. Cranmer, *diana-hep/excursion: Initial zenodo release*, 10.5281/zenodo.1634428.

[298] L. Lonnblad and S. Prestel, *Matching Tree-Level Matrix Elements with Interleaved Showers*, *JHEP* **03** (2012) 019, [`1109.4829`].

[299] S. Banerjee, D. Barducci, G. Bélanger, B. Fuks, A. Goudelis and B. Zaldivar, *Cornering pseudoscalar-mediated dark matter with the LHC and cosmology*, *JHEP* **07** (2017) 080, [`1705.02327`].

[300] F. Ambrogi, *MadAnalysis 5 recast of ATLAS-CONF-2019-040*, 10.7484/INSPIREHEP.DATA.45EF.23SB.

[301] CMS collaboration, A. M. Sirunyan et al., *Searches for physics beyond the standard model with the M_{T2} variable in hadronic final states with and without disappearing tracks in proton-proton collisions at $\sqrt{s} = 13$ TeV*, *Eur. Phys. J.* **C80** (2020) 3, [`1909.03460`].

[302] CMS collaboration, A. M. Sirunyan et al., *Search for supersymmetry in proton-proton collisions at 13 TeV in final states with jets and missing transverse momentum*, *JHEP* **10** (2019) 244, [`1908.04722`].

[303] N. Bernal, M. Heikinheimo, T. Tenkanen, K. Tuominen and V. Vaskonen, *The Dawn of FIMP Dark Matter: A Review of Models and Constraints*, *Int. J. Mod. Phys. A* **32** (2017) 1730023, [`1706.07442`].

[304] J. Alimena et al., *Searching for Long-Lived Particles beyond the Standard Model at the Large Hadron Collider*, `1903.04497`.